

# Manipulating Quantum Coherence in Solid State Systems

Edited by

Michael Edward Flatté  
and Ionel Trifea

NATO Science Series

# Manipulating Quantum Coherence in Solid State Systems

# NATO Science Series

*A Series presenting the results of scientific meetings supported under the NATO Science Programme.*

The Series is published by IOS Press, Amsterdam, and Springer in conjunction with the NATO Public Diplomacy Division

## *Sub-Series*

I. Life and Behavioural Sciences	IOS Press
II. Mathematics, Physics and Chemistry	Springer
III. Computer and Systems Science	IOS Press
IV. Earth and Environmental Sciences	Springer

The NATO Science Series continues the series of books published formerly as the NATO ASI Series.

The NATO Science Programme offers support for collaboration in civil science between scientists of countries of the Euro-Atlantic Partnership Council. The types of scientific meeting generally supported are "Advanced Study Institutes" and "Advanced Research Workshops", and the NATO Science Series collects together the results of these meetings. The meetings are co-organized bij scientists from NATO countries and scientists from NATO's Partner countries – countries of the CIS and Central and Eastern Europe.

**Advanced Study Institutes** are high-level tutorial courses offering in-depth study of latest advances in a field.

**Advanced Research Workshops** are expert meetings aimed at critical assessment of a field, and identification of directions for future action.

As a consequence of the restructuring of the NATO Science Programme in 1999, the NATO Science Series was re-organised to the four sub-series noted above. Please consult the following web sites for information on previous volumes published in the Series.

<http://www.nato.int/science>  
<http://www.springer.com>  
<http://www.iospress.nl>



**Series II: Mathematics, Physics and Chemistry – Vol. 244**

# Manipulating Quantum Coherence in Solid State Systems

edited by

**Michael E. Flatté**

University of Iowa, Iowa City,  
U.S.A.

and

**I. Tifrea**

Babeş-Bolyai University,  
Cluj Napoca, Romania



**Springer**

Published in cooperation with NATO Public Diplomacy Division

Proceedings of the NATO Advanced Study Institute on Manipulating  
Quantum Coherence in Solid State Systems  
Cluj-Napoca, Romania  
29 August–8 September 2005

A C.I.P. Catalogue record for this book is available from the Library of Congress.

---

ISBN 978-1-4020-6135-6 (PB)  
ISBN 978-1-4020-6134-9 (HB)  
ISBN 978-1-4020-6137-0 (e-book)

---

Published by Springer,  
P.O. Box 17, 3300 AA Dordrecht, The Netherlands.

[www.springer.com](http://www.springer.com)

*Printed on acid-free paper*

---

All Rights Reserved  
© 2007 Springer

No part of this work may be reproduced, stored in a retrieval system, or transmitted in any form or by any means, electronic, mechanical, photocopying, microfilming, recording or otherwise, without written permission from the Publisher, with the exception of any material supplied specifically for the purpose of being entered and executed on a computer system, for exclusive use by the purchaser of the work.

## PREFACE

The lectures at the NATO Advanced Study Institute “Manipulating Quantum Coherence in Solid State Systems” presented a fundamental introduction to three solid-state approaches to achieving quantum computation: semiconductor spin-based, semiconductor charge-based, and superconducting approaches. The purpose in bringing together lecturers and students in these disparate areas was to provide the opportunity for communication and cross-fertilization between these three areas, all focusing on the central goal of manipulating quantum coherence in solids. These proceedings present detailed introductions to the fundamentals of the first approach and the third approach, and as such bring together a fundamental pedagogical treatment of the two areas which have progressed the furthest towards realizing a scalable system of manipulable qubits.

Semiconductor spin-based approaches to quantum computation have made tremendous advances in the past several years. Individual spins have been successfully confined within self-assembled quantum dots and lithographically-formed quantum dots. Within the self-assembled quantum dots the spin lifetimes have been measured and shown to be longer than 1 ms at low temperature. Lithographic dots have been used to controllably reorient nuclear spins in order to lengthen the spin lifetimes. These exceptionally long spin lifetimes should permit many spin operations (qubit operations) within a decoherence time. Coherent spin transfer has also been demonstrated between two colloidal dots connected by polymer chains. Spins can be localized on dopant atoms, such as manganese atoms in gallium arsenide. These spins can be oriented, manipulated and detected with all-electrical means. Electrical techniques can also be used to manipulate nuclear spins, and eventually to drive nuclear magnetic resonance.

The four chapters in this area are based on the lectures presented at the ASI by M. E. Flatté, G. Vignale, I. Tifrea, and D. D. Awschalom, which progress from elementary considerations up to the challenges that must be overcome in the next few years to compete in the area of quantum computation with non-solid-state approaches. The first chapter provides an overview of several areas within this field, including spin transport and spin coherence times for ensembles of spins in bulk and quantum well materials, individual spin manipulation theory in ionic systems and quantum dots, and the application of spin-based quantum information to teleportation. The second chapter details the influence of many-body effects

on spin transport, including the exciting area of the spin Hall effect. The third chapter focuses on the use of electric fields to manipulate nuclear spin lifetimes via the hyperfine interaction with electron spins. The fourth chapter describes the electrical generation of spin polarization, the spin Hall effect, manipulation of spin via control of the  $g$  tensor, transport of spin coherence between quantum dots tethered by organic molecules, and the control of nuclear spin polarization with electric fields.

Superconducting approaches to quantum computation have demonstrated single qubits based on charge eigenstates as well as flux eigenstates. Each of these has strong possibilities for scalability, and visible Rabi flopping has been demonstrated in each case. Coupling between these qubits has been demonstrated, and the decoherence mechanisms for single qubits have been explored. The fifth and sixth chapters are based on the highly pedagogical lectures presented by M. Geller and F. Wilhelm at the ASI.

The NATO ASI was held in Cluj-Napoca, Romania from August 29 to September 8, 2005, and it was attended by 10 lecturers and 65 students from 17 different countries. In addition to the lectures, all students had the opportunity to orally present their own work in one of two special afternoon seminar sessions.

We would like to acknowledge the NATO Science Division, The National Science Foundation (USA), The Army Research Office (USA), and The Romanian Cultural Institute (ICR) for their financial contributions. Also, we would like to thank “Babeş-Bolyai” University and City Plaza Hotel for their hospitality.

Michael E. Flatté  
Ionel Tifrea

## CONTENTS

Preface	v
List of Participants	viii
M. E. Flatté/Semiconductor Spintronics for Quantum Computation	1
1    Introduction	1
2    Spin-Dependent Processes in Electrical Transport	2
3    Spin Coherence Times in Semiconductors	18
4    All-Electrical Control of Single Ion Spins in a Semiconductor	25
5    Single-Spin Manipulation in Quantum Dots	32
6    Spin-Selective Devices	42
7    Conclusion	45
G. Vignale/Many-body Effects in Spin-polarized Transport	53
1    Drift-Diffusion Theory for Charge	53
2    Drift-Diffusion Theory for Collinear Spins	55
3    Spin Coulomb Drag—An Introduction	57
4    Drift-Diffusion Theory—Continued	59
5    Simple Applications	62
6    Microscopic Theory of Spin Coulomb Drag	72
7    Experimental Observation of Spin Coulomb Drag	78
8    Spin Mass	81
9    Spin Hall Effect	86
10   Conclusion	93
Appendix	94
I. Tifrea/Nuclear Spin Dynamics in Semiconductor Nanostructures	97
1    Introduction	97
2    Hyperfine Interaction and Spin Relaxation Times	100
3    Dynamic Nuclear Polarization	106
4    Induced Magnetic Fields	112
5    Overhauser Frequency Shifts	116
6    Summary	120
Appendix	122
A    Table of Semiconductor Isotopes	122
B    Parabolic Quantum Wells	124

J. Berezovsky, W. H. Lau, S. Ghosh, J. Stephens, N. P. Stern, and D. D. Awschalom/Spin Coherence in Semiconductors	130
1    Introduction	130
2    Electrical Generation and Manipulation of Spin Polarization	135
3    The Spin Hall Effect	140
4    Spin Accumulation in Forward-Biased MnAs/GaAs Schottky Diodes	152
5    Spin Coherence in Quantum Dots	161
M. R. Geller, E. J. Pritchett, A. T. Sornborger, and F. K. Wilhelm/ Quantum Computing with Superconductors I: Architectures	171
1    Introduction	171
2    The Basic Qubits: Phase, Flux, and Charge	172
3    Fixed Linear Couplings	180
4    Tunable Couplings	184
5    Dynamic Couplings: Resonator Coupled Qubits	187
F. K. Wilhelm, M. J. Storcz, U. Hartmann, and M. R. Geller/ Superconducting Qubits II: Decoherence	195
1    Introduction	195
2    Single Qubit Decoherence	204
3    Beyond Bloch–Redfield	219
4    Decoherence in Coupled Qubits	227
5    Summary	229
Index	234

## LIST OF PARTICIPANTS

### LECTURERS

**Gerhard Abstreiter**, Technische Universität München, Germany  
**David D. Awschalom**, University of California, Santa Barbara, USA  
**Michael E. Flatté**, University of Iowa, USA (**co-director**)  
**Micheal Geller**, University of Georgia, USA  
**Leonid Glatzman**, University of Minnesota, USA  
**Ady Stern**, Weizmann Institute of Science, Israel  
**Seigo Tarucha**, University of Tokyo, Japan  
**Ionel Tifrea**, “Babeş-Bolyai” University, Romania (**co-director**)  
**Giovanni Vignale**, University of Missouri – Columbia, USA  
**Frank Wilhelm**, Ludwig-Maximilians Universität München, Germany

### STUDENTS

**Alex Matos Abiague**, Max-Planck Institut für Mikrostrukturphysik, Germany  
**Alexandru Aldea**, National Institute of Materials Physics, Romania  
**Reza Bakhtiari**, Scuola Normale Superiore Pisa, Italy  
**Igor Bejenari**, Institute of Applied Physics, Republic of Moldova  
**Jesse Berezovsky**, University of California, Santa Barbara, USA  
**Rafi Bistritzer**, Weizmann Institute of Science, Israel  
**Doru Bodea**, Max-Planck Institute for Physics of Complex Systems, Germany  
**Viorel Laurentiu Cartas**, University of Galati, Romania  
**Madalina Colci**, University of Illinois, USA  
**Benjamin J Cooley**, Penn State University, USA  
**Mircea Crisan**, “Babeş-Bolyai” University, Romania  
**Irene D’Amico**, University of York, United Kingdom  
**Ion Viorel Dinu**, National Institute of Materials Physics, Romania  
**Matthew F. Doty**, Naval Research Laboratory, USA  
**Vitalie Eremeev**, Institute of Applied Physics, Republic of Moldova  
**Peter Foldi**, University of Szeged, Hungary  
**Andreas Friedrich**, Institut für Theoretische Physik, Germany  
**Louis Gaudreau**, University of Sherbrooke, Canada

- Lachezar Georgiev**, Institute for Nuclear Research and Nuclear Energy, Bulgaria  
**Sayantani Ghosh**, University of California, Santa Barbara, USA  
**Lilach Goren**, Weizmann Institute of Science, Israel  
**Ioan Grosu**, “Babeş-Bolyai” University, Romania  
**Evelina Hankiewicz**, University of Missouri-Columbia, USA  
**Udo Hartmann**, Ludwig-Maximilians Universität München, Germany  
**Dominik Heiss**, Technische Universität München, Germany  
**Manuel Houzet**, CEA Grenoble, France  
**Orsolya Kálmán**, University of Szeged, Hungary  
**Erik Koop**, University of Groningen, The Netherlands  
**Wayne H. Lau**, University of California, Santa Barbara, USA  
**Lorenz Meier**, ETH Zurich and IBM Research, Switzerland  
**Igor Mekhov**, St. Petersburg State University, Russia  
**Romain Melet**, INSP Paris, France  
**Georgo Metalidis**, Max-Planck Institute of Microstructure Physics, Germany  
**Camil Mirestean**, “Babeş-Bolyai” University, Romania  
**Marian Nita**, National Institute of Materials Physics, Romania  
**George Pal**, Technische Universität Kaiserslautern, Germany  
**Traian Petisor**, Technical University Cluj, Romania  
**Joseph Pingenot**, University of Iowa, USA  
**Marco Polini**, Scuola Normale Superiore Pisa, Italy  
**Ioan Pop**, “Babeş-Bolyai” University, Romania  
**Emily Pritchett**, University of Georgia, USA  
**Guido Quax**, Technical University Eindhoven, The Netherlands  
**Guillermo Quinteiro**, Michigan State University, USA  
**Pedro J. Rizo**, University of Groningen, The Netherlands  
**Jennifer Robb**, Dalhousie University, Canada  
**Lucian Roiban**, “Babeş-Bolyai” University, Romania  
**Sebastian Roth**, Technische Universität München, Germany  
**Costel Sarbu**, “Babeş-Bolyai” University, Romania  
**Ioana Serban**, Ludwig-Maximilians Universität München, Germany  
**Roman Shchelushkin**, University of Science and Technology, Norway  
**Andrew Sornborger**, University of Georgia, USA  
**Oney O. Soykal**, University of Iowa, USA  
**Jason Stephens**, University of California, Santa Barbara, USA  
**Nathaniel Stern**, University of California, Santa Barbara, USA  
**Markus Storczyk**, Ludwig-Maximilians Universität München, Germany  
**Jan Suffczynski**, Warsaw University, Poland  
**Coriolan Tiusan**, Université Henri-Poincaré Nancy, France  
**Mugurel Tolea**, National Institute of Materials Physics, Romania  
**Mircea Teodor Trif**, “Babeş-Bolyai” University, Romania  
**Carmen Laura Tugulan**, “Babeş-Bolyai” University, Romania

**Romulus Flaviu Turcu**, “Babeş-Bolyai” University, Romania

**Mihai Vasilescu**, “Babeş-Bolyai” University, Romania

**Karel Vyborny**, Czech Academy of Sciences, Czech Republic

**Andreas Weichselbaum**, Ludwig-Maximilians Universität München, Germany

**Bernhard Wunsch**, University of Hamburg, Germany

# SEMICONDUCTOR SPINTRONICS FOR QUANTUM COMPUTATION

MICHAEL E. FLATTÉ ([michael\\_flatte@mailaps.org](mailto:michael_flatte@mailaps.org))

*Optical Science and Technology Center,*

*Department of Physics and Astronomy, and*

*Department of Electrical and Computer Engineering,*

*University of Iowa, Iowa City, IA 52242, USA*

**Abstract:** Encoding quantum information in spins embedded in semiconductors (electronic, ionic, or nuclear) offers several potential approaches towards solid-state quantum computation. Electronic spin transport, persistence and manipulation in nonmagnetic semiconductor materials, as well as the interaction of electronic spins with optics, are the fundamental properties reviewed here. The presentation focuses on the material properties important for implementing quantum computation, and on the characteristics that may lead more rapidly to scalable solutions for quantum information processing.

**Keywords:** spin coherence, spin dynamics, quantum computation, spin transport

## 1 Introduction

The range of proposed quantum-mechanical systems that can implement quantum computational algorithms continues to grow, and progress towards functional scalable devices appears rapid. An agreed set of criteria for such systems (Bennett and DiVincenzo, 2000) includes the initialization, evolution, and measurement of a set of entities that can be approximated as two-level systems (qubits). A universal quantum computer would have a selectable number of these qubits and a programmable arrangement of quantum gates (referred to as a quantum algorithm). An important distinction should be understood at the beginning between physical qubits and logical qubits. Physical qubits are elementary two-state systems, but information encoded simply in single physical qubits is highly susceptible to decoherence. Quantum error correction is possible if multiple physical qubits are used to encode a single logical, or coded, qubit (Preskill, 1998). The entanglement between the physical qubits that constitute a logical qubit permits a form of redundancy, and thus error correction, even though quantum information itself cannot be copied completely from one qubit to another. In order to implement any quantum algorithm it is sufficient to perform one-qubit and two-qubit operations on the logical qubits (Barenco et al., 1995).

A concrete realization of a solid-state quantum computation structure based on electron spins confined within quantum dots was proposed by Loss and DiVincenzo (1998). The single qubit operations could be implemented with local AC fields or by controlling the resonance frequencies of individual qubits. Two-qubit operations could be implemented by controlling the exchange interaction between two quantum dots with electric gates, and spin detection could be achieved through ferromagnetic nucleation. A similar proposal relying on nuclear spin qubits of donors in silicon appeared roughly simultaneously (Kane, 1998). Subsequent work has shown that in a solid-state environment with spins as logical qubits both one-qubit and two-qubit operations may require only one type of physical gate interaction, such as the exchange interaction (DiVincenzo et al., 2000; Levy, 2002; Petta et al., 2005). Reviews of these experimental pathways towards spin manipulation in quantum dots include Kouwenhoven et al. (2001) and Hanson et al. (2006).

The material presented here considers topics that may contribute to the implementation of quantum computation in solid-state spin-based systems in the future. Spin transport, the topic of section 2, and spin decoherence in electron spin ensembles, the topic of section 3, may play important roles in the efficient initialization of large arrays of spin-based qubits. The following section 4, on the electrical control of ionic spins in a semiconductor, shows quantum manipulation of ionic spins can be achieved without the use of any magnetic fields. The subsequent section 5 explores the spin-based properties of quantum dots, and the interaction of these spins with photons. Optical techniques can be used to probe the spin orientation and to manipulate the spins themselves. Section 6 describes a method for coupling quantum dot spins to individual photons within a microcavity (and the application of this method to teleportation). Section 7 presents some conclusions and topics for further development.

## 2 Spin-Dependent Processes in Electrical Transport

Initialization of multiple qubits within a quantum computer may require the transport of highly spin-polarized distributions across a material, followed by insertion of individual spins into localized regions such as quantum dots, or transfer of the spin information from the moving distribution to a set of localized spins. The applications of spin transport, however, also extend to a variety of possible information processing devices such as spin transistors (Datta and Das, 1990). The treatment presented here would also apply to the transport of spin polarized distributions in such systems.

The development of theories of spin transport initially followed in the footsteps of the broad and mature field of charge transport, by attempting to correlate physical regimes of spin transport with corresponding regimes of charge transport.

As the field of spin transport has become more mature the analogies have been further refined. A very helpful analogy has been to correlate the “two-channel” model for spin flow, which only tracks the spin polarization along a fixed quantization axis, with the two-band model for carrier flow in a semiconductor. Phenomena such as local charge neutrality and drift, which have been thoroughly explored for the two-band model for carrier flow in a semiconductor, can be transposed almost entirely to the transport of spin within the two-channel model. Most recently, with the treatment of many-body effects in spin-dependent transport, new regimes with no natural analogs in charge transport have been identified (Qi et al., 2006).

## 2.1 REGIMES OF CHARGE CURRENT FLOW

The most general description of the current associated with charge carriers would include the response of the full many-particle wave function to an applied electric field. A number of approximate schemes have been introduced to describe current flow with only a few parameters. Tremendous simplification, for example, can be achieved through the introduction of a local chemical potential. The key assumption behind this approximation is that the carriers in a particular spatial region are in equilibrium with other carriers in that region, but may be out of equilibrium with carriers elsewhere in the material. This assumption can be justified when the mean free path of carriers is shorter than the typical length scale of the region through which the carriers are traveling. In these circumstances, for carriers associated with a single band (and ignoring spin), the spatially-dependent distribution of the carriers can be summarized with two parameters: the local chemical potential  $\epsilon_\mu(\mathbf{r})$  measured relative to the electric potential, and the electric potential  $\phi(\mathbf{r})$ . Note that in this treatment the units of these two quantities are Volts.

The current  $\mathbf{J}$  can be then related directly to the local change in the total chemical potential  $\epsilon_\mu - \phi$ ,

$$\mathbf{J} = \sigma \nabla (\epsilon_\mu - \phi), \quad (1)$$

where  $\sigma$  is the conductivity. In principle the conductivity depends on  $\epsilon_\mu$  and thus must be found self-consistently. In semiconductors, which can sustain large deviations of the local charge density from equilibrium, it is convenient to separate the conductivity into the carrier density and mobility, as the mobility depends less sensitively on  $\epsilon_\mu$  than the carrier density.

Conservation of charge requires that in steady-state transport every electron passing in to an element of a circuit must pass out, and thus

$$\nabla \cdot \mathbf{J} = 0. \quad (2)$$

Solution of Eqs. (1) and (2) for the boundary conditions appropriate for a given voltage drop, along with a self-consistent solution for the conductivity, and

a self-consistent solution of the Poisson equation relating the electric field to the local variation of the charge density,

$$\nabla \cdot \mathbf{E} = -\frac{e}{\epsilon}(n - n_o), \quad (3)$$

will produce a full description of the current distribution in response to an applied voltage. In Eq. (3)  $n$  is the carrier density,  $n_o$  is the equilibrium carrier density,  $\mathbf{E}$  is the electric field,  $e$  is the magnitude of the electric charge, and  $\epsilon$  is the dielectric constant.

In lightly-doped semiconductors drift–diffusion equations are more commonly used than Eqs. (1)–(3). The drift–diffusion equations, however, are very closely related (Kittel and Kroemer, 1980), as illustrated here. Equation (2) permits the current to be written as the gradient of a scalar potential,  $\mathbf{J} = \nabla\xi$ , which can be written as Eq. (1). For nondegenerate carriers  $\epsilon_\mu = k_B T \ln(n/n_o)$ , and Eq. (1) can be written as

$$\mathbf{J} = \sigma\mathbf{E} + (\sigma kT/n)\nabla n = \sigma\mathbf{E} + eD\nabla n, \quad (4)$$

where  $k_B$  is Boltzmann’s constant,  $T$  is the temperature, and  $D$  is the diffusion constant. The far right expression of Eq. (4) also holds in the degenerate regime if  $n/n_o \ll 1$ . Thus one can use either the chemical potential expression or the drift–diffusion equations to calculate the current in a general situation.

The choice of using the quasichemical potential equations or the drift diffusion equations is made solely on convenience. Frequently quasichemical potentials are used when the carrier density is sufficiently high that the conductivity can be considered independent of the nonequilibrium spin-polarized carriers (as is the case in metals). Under these conditions Eq. (1) can be solved for the quasichemical potential with the appropriate boundary conditions (continuity of current, and a given voltage drop across the structure) and it is not necessary to consider the carrier density as a separate variable to be determined self-consistently. When the carrier density is low enough that a small change in carrier density markedly changes the conductivity of the material (as can be the case in semiconductors) then  $\sigma$  in Eq. (1) must be determined self-consistently, requiring solving for the carrier density in addition to the chemical potential and the electric field. In these situations it is easier to use drift–diffusion equations, which can be written without the chemical potential as a separate quantity to be determined.

In a set of regimes often termed “ballistic transport” the mean free path of carriers is longer than the typical length scale of the region through which the carriers are traveling, and the occupation of each state of band index  $j$  and momentum  $\mathbf{k}$  must be provided. In a further set of regimes often termed “mesoscopic transport”, the phase relationship between states of differing  $j$  and/or  $\mathbf{k}$  remains important during transport, and spatial interference between waves of differing  $\mathbf{k}$  is observed. One realization of this is the reorganization of carrier eigenstates from momentum states (which are no longer eigenstates) into new wave functions that are

coherent superpositions of different momentum states in one or more directions. For example, eigenstates of quantum wells are constructed from counterpropagating momentum states in the direction of carrier confinement. Many definitions of the terms ballistic and mesoscopic transport are used in the literature, so some will differ from those introduced above.

## 2.2 HOW DOES A SPIN CURRENT FLOW?

Spin currents can flow in magnetic and nonmagnetic materials, parallel to or perpendicular to an applied electric field, or even in the absence of a static applied electric field. A brief survey of spin current mechanisms will provide an introduction to the range of spin transport phenomena already demonstrated in solid-state materials.

One simple configuration for spin-current flow involves an applied electric field and a spin current flowing parallel to that field. This occurs naturally in magnetic materials due to the differing conductivity for spin-up and spin-down carriers. In the nondegenerate limit the conductivity would be

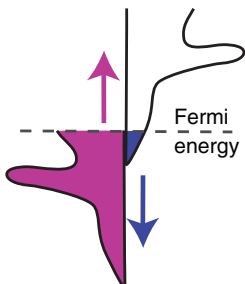
$$\sigma_{\uparrow(\downarrow)} = n_{\uparrow(\downarrow)} e \mu_{\uparrow(\downarrow)}, \quad (5)$$

and in the degenerate limit it would be

$$\sigma_{\uparrow(\downarrow)} = N_{\uparrow(\downarrow)}(E_{F,\uparrow(\downarrow)}) e^2 D_{\uparrow(\downarrow)}, \quad (6)$$

where the quantities introduced in section 2.1 have now been distinguished by spin direction (up or down). Shown in Figure 1a is an example of a spin-split electronic structure, as might be found in a magnetic material, with a different density of spin-up and spin-down carriers, as well as a different density of states for spin-up and spin-down carriers. It is likely in this situation that the diffusion

(a) *magnetic materials*



(b) *nonmagnetic materials*

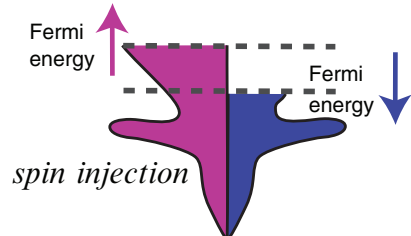


*Figure 1.* (a) Spin-split electronic structure, such as for a magnetic material. (b) Spin-degenerate electronic structure for a nonmagnetic material, but with additional nonequilibrium spin-polarized carriers that modify the conductivity and render it spin-dependent

constant for spin-up and spin-down carriers would also differ. Whether the degenerate or nondegenerate forms of the conductivity are appropriate, the conductivity of the two spin orientations will be different. In Figure 1a there is no spin-splitting of the chemical potential, so  $E_{F,\uparrow} = E_{F,\downarrow}$ . If the spin-resolved conductivities are spatially uniform this condition is preserved for the spatially-dependent spin-up and spin-down chemical potentials,

$$\phi_{\uparrow}(\mathbf{r}) = \phi_{\downarrow}(\mathbf{r}). \quad (7)$$

Once the conductivities vary spatially these chemical potentials may differ, and the chemical potentials and current flow for spin-up and spin-down carriers can be found independently within the two-channel model (Mott, 1936; Fert and Campbell, 1968).

In Figure 1b, by contrast, a nonmagnetic material is shown, but the chemical potential for spin-up carriers differs from that for spin-down carriers. This phenomenon, commonly referred to as “spin injection” can occur through the optical generation of spin-polarized carriers (Meier and Zachachrenya, 1984) (as described in section 2.5 and Chapter 4) or through flowing a current from a magnetic material through a nonmagnetic material (Aronov and Pikus, 1976; Johnson and Silsbee, 1988). Once the nonequilibrium density of spins has been generated, both the density of carriers and their density of states (and thus their conductivities) will depend on the carriers’ spin direction, and a spin current will flow in response to an applied electric field.

Another method of generating spin currents does not require an applied electric field, for it consists of optically generating a distribution of nonequilibrium carriers in which the spin-up carriers are moving in an opposite direction to the spin-down carriers, as shown in Figure 2. This can be performed by interfering two polarized optical pulses of differing photon energy in a semiconductor (Bhat and Sipe, 2000) and has been demonstrated in GaAs quantum wells (Stevens et al., 2003) and bulk ZnSe (Hübner et al., 2003). The current survives until scattering

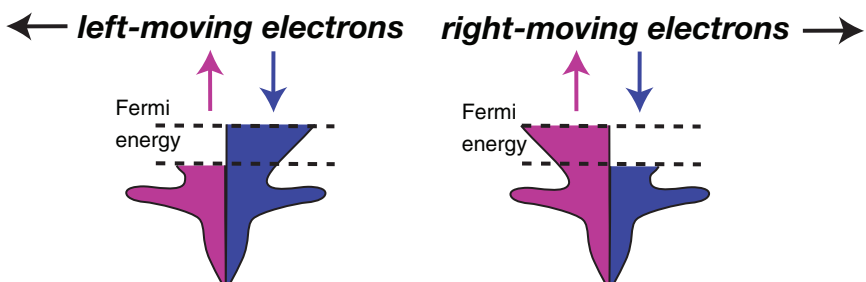


*Figure 2.* Electron distributions corresponding to the flow of ballistic spin current. An accumulation of spin-down left-moving electrons and spin-up right-moving electrons yields a spin current, even though overall there is no density difference between spin-up and spin-down carriers

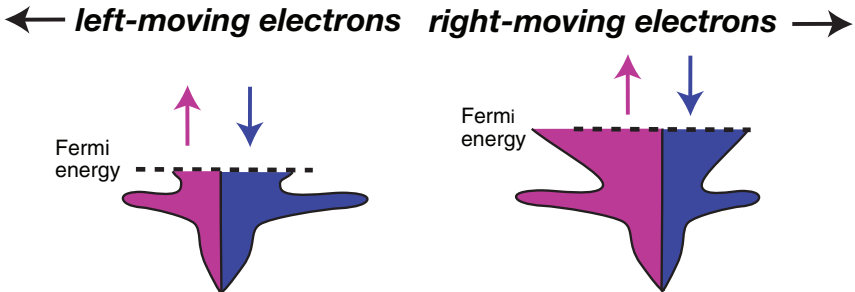


Figure 3. The spin-orbit interaction alters the density of states of spin-up and spin-down carriers according to whether the spin is parallel or antiparallel to the carrier momentum. When a current flows this produces a larger density of carriers of one spin than the other

of the ballistically-moving carriers eliminates the nonequilibrium distribution that produces the current.

Even without spin-selective differences in the occupation functions it is possible to generate a spin current. The presence of spin-orbit interaction in solids produces a different electronic structure for spin-up and spin-down carriers of the same momentum. Time-reversal invariance, however, will force

$$E_{\uparrow(\downarrow)}(\mathbf{k}) = E_{\downarrow(\uparrow)}(-\mathbf{k}), \quad (8)$$

where  $E_{\uparrow(\downarrow)}(\mathbf{k})$  is the energy of the spin-up (spin-down) carrier of momentum  $\mathbf{k}$ . A schematic spin-orbit correlated electronic structure is shown in Figure 3. When a diffusive charge current flows there are more carriers moving in the direction of the current than in the opposite direction, and as a result a greater occupation for one spin direction than the other (Edelstein, 1990).

Still other phenomena can produce spin currents. In the spin Hall effect (described in detail in Chapters 2 and 4) the flow of charge current in one direction yields a transverse spin current through asymmetries in the band structure or in the scattering of carriers from impurities.

## 2.3 PROCESSES MODIFYING SPIN MOTION IN SEMICONDUCTORS

Two principal characteristics modify spin current once it has started to flow. The first is the influence of internal magnetic fields and spin decoherence on the spin motion. In a magnetic material the internal fields are present at all times, and in a nonmagnetic material with inversion asymmetry such magnetic fields also exist once carriers begin to move. In a nonmagnetic material these magnetic fields originate from the electric fields of the crystal structure itself, relativistically transformed into the rest frame of the carrier. For a nonmagnetic inversion symmetric material these fields vanish, for inversion symmetry

$$E_{\uparrow(\downarrow)}(\mathbf{k}) = E_{\uparrow(\downarrow)}(-\mathbf{k}) \quad (9)$$

along with time-reversal symmetry, Eq. (8), produces degenerate eigenstates for the two spin directions,

$$E_{\uparrow}(\mathbf{k}) = E_{\downarrow}(\mathbf{k}). \quad (10)$$

As described in section 3 these internal magnetic fields provide the dominant contribution to spin relaxation and decoherence in nonmagnetic inversion-asymmetric semiconductors.

The second important effect on spin transport is the role of the charges associated with the moving spins. It should not be a surprise that charge interactions and spin properties are coupled to produce unexpected phenomena in transport, as magnetism in the solid state almost exclusively originates from the interplay between the Pauli exclusion principle and the Coulomb interaction itself.

## 2.4 MOTION OF SPIN DENSITY PACKETS IN SMALL ELECTRIC FIELDS

The transport of spin density packets in a semiconductor under conditions of small electric fields is closely related to the transport of charge polarization packets in semiconductors. So to begin consider the motion of a charge polarization packet in a semiconductor. This charge polarization packet corresponds to a nonequilibrium density of electrons  $n$  and/or holes  $p$  in a material with an equilibrium density of electrons  $n_o$  and holes  $p_o$ .

The current in such a two-band semiconductor is divided into an electron current and a hole current,

$$\mathbf{j}_e = ne\mu_e\mathbf{E} + eD_e\nabla n = \sigma_e\mathbf{E} + eD_e\nabla n, \quad (11)$$

$$\mathbf{j}_h = pe\mu_h\mathbf{E} - eD_h\nabla p = \sigma_h\mathbf{E} - eD_h\nabla p, \quad (12)$$

which must satisfy the continuity equations

$$-e\frac{\partial n}{\partial t} = -\nabla \cdot \mathbf{j}_e - eG + eRnp, \quad (13)$$

$$e\frac{\partial p}{\partial t} = -\nabla \cdot \mathbf{j}_h + eG - eRnp, \quad (14)$$

and the Poisson equation relating the local deviation from equilibrium of the charge densities to the electric field,

$$\nabla \cdot \mathbf{E} = -\frac{e}{\epsilon}(\Delta n - \Delta p). \quad (15)$$

Here  $\Delta n = n - n_o$  and  $\Delta p = p - p_o$ ,  $G$  is the generation rate for electron-hole pairs,  $R$  is their recombination rate and  $\epsilon$  is the dielectric constant.

Substituting the electron and hole currents into the continuity equations, neglecting the generation rate, assuming steady-state, and defining

$$Rnp = n/\tau_e = p/\tau_p, \quad (16)$$

yields

$$D_e \nabla^2 n - n \mu_e \nabla \cdot \mathbf{E} + \mu_e \nabla n \cdot \mathbf{E} = \frac{n}{\tau_e}, \quad (17)$$

$$D_h \nabla^2 p + p \mu_h \nabla \cdot \mathbf{E} - \mu_h \nabla p \cdot \mathbf{E} = \frac{p}{\tau_h}. \quad (18)$$

The middle term on the left-hand side will force the excess electrons and excess holes to move as a single packet, as  $\nabla \cdot \mathbf{E}$  is proportional to the deviation from local charge neutrality. A consistent solution to these two equations would not be found simply by setting  $\Delta n = \Delta p$ , however, for the diffusion constants and mobilities of the electrons and holes differ.

The physics of this situation is shown in Figure 4. The applied electric field will attempt to pull the electrons and holes in different directions, but that motion will generate a nonvanishing  $\Delta n - \Delta p$ , and thus an electric field that pulls the two carriers together. This space-charge field is shown in Figure 4. The response of the carriers to this field depends on the carrier mobility. The high-conductivity carriers will move more rapidly towards the low-conductivity carriers. To produce a single equation for the motion of the electrons and holes, without requiring  $\Delta n = \Delta p$ , multiply Eq. (17) by  $\sigma_h$ , Eq. (18) by  $\sigma_e$ , and then add them together. This eliminates the self-consistent electric field without requiring local charge neutrality, and produces

$$\sigma_h D_e \nabla^2 n + \sigma_e D_h \nabla^2 p + \sigma_h \mu_e \nabla n \cdot \mathbf{E} - \sigma_e \mu_h \nabla p \cdot \mathbf{E} = \sigma_h \frac{n}{\tau_e} + \sigma_e \frac{p}{\tau_h}. \quad (19)$$

Now the equation of motion of the packet can be found by allowing  $\Delta n = \Delta p$ . This approach allows us to work under conditions of *approximate* local charge

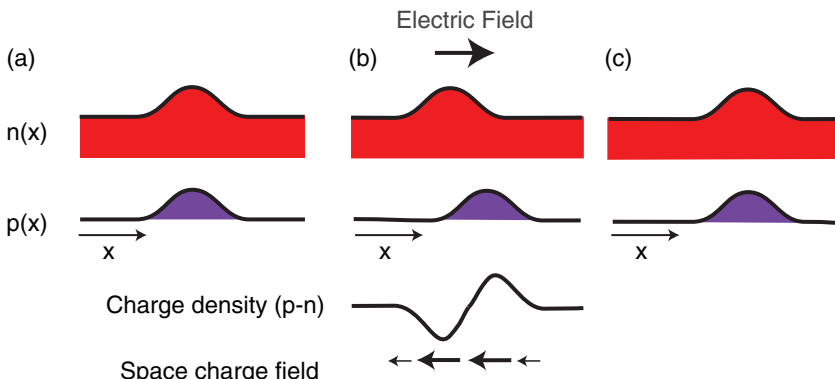


*Figure 4.* Motion of a charge polarization packet in an applied electric field. The electrons and holes wish to move in opposite directions, but the space-charge field pulls them together. The carriers with higher conductivity move towards those with lower conductivity, so the mobility and diffusion of the packet is determined by the minority carriers

neutrality without (incorrectly) ignoring all aspects of the space-charge field. The resulting charge polarization packet, with excess electrons and excess holes moving together, is characterized by an ambipolar diffusion constant and ambipolar mobility,

$$D_{\text{ambi}} \nabla^2 n + \mu_{\text{ambi}} \nabla n \cdot \mathbf{E} = \frac{\Delta n}{\tau_r}. \quad (20)$$

where

$$D_{\text{ambi}} = \frac{\sigma_h D_e + \sigma_e D_h}{\sigma_h + \sigma_e}, \quad \mu_{\text{ambi}} = \frac{\sigma_h \mu_e - \sigma_e \mu_h}{\sigma_h + \sigma_e}, \quad \tau_r = \tau_e = \tau_h. \quad (21)$$

The last equation in Eq. (21) also uses detailed balance to determine  $\tau_e = \tau_h$ . In the limit  $\sigma_e \gg \sigma_h$ ,  $D_{\text{ambi}} \sim D_h$  and  $\mu_{\text{ambi}} \sim \mu_h$ . This general result that the diffusion and mobility of the packet is dominated by the lower-conductivity species was the basis of the Shockley–Haynes measurement of the mobility and diffusion constant of minority carriers in germanium (Haynes and Shockley, 1951).

The same approach can be used to determine the mobility and diffusion constants of spin packets in semiconductors (Flatté and Byers, 2000), which explained some puzzling experimental results on the mobility of spin packets in GaAs (Kikkawa and Awschalom, 1999). To describe spin packets, distinct currents and densities for spin-up and spin-down carriers, for both electrons and holes, must be introduced. Drift-diffusion equations for carrier motion in a semiconductor describe the combined motion of spin-up and spin-down electrons and holes in the presence of electric and quasi-electric fields, including the effects of space charge fields on carrier motion (Awschalom et al., 2002). To include the possibility of spin imbalance in both the conduction and valence bands, four currents are required:

$$\mathbf{j}_{e\uparrow} = en_{\uparrow}\mu_{e\uparrow}\mathbf{E} + eD_{e\uparrow}\nabla n_{\uparrow}, \quad (22)$$

$$\mathbf{j}_{e\downarrow} = en_{\downarrow}\mu_{e\downarrow}\mathbf{E} + eD_{e\downarrow}\nabla n_{\downarrow}, \quad (23)$$

$$\mathbf{j}_{h\uparrow} = ep_{\uparrow}\mu_{h\uparrow}\mathbf{E} - eD_{h\uparrow}\nabla p_{\uparrow}, \quad (24)$$

$$\mathbf{j}_{h\downarrow} = ep_{\downarrow}\mu_{h\downarrow}\mathbf{E} - eD_{h\downarrow}\nabla p_{\downarrow}. \quad (25)$$

The evolution in time and space of these four currents and the electric field comes from the four continuity equations,

$$-e \frac{\partial n_{\uparrow}}{\partial t} = -\nabla \cdot \mathbf{j}_{e\uparrow} - e \frac{n_{\downarrow}}{\tau_{e\downarrow\uparrow}} + e \frac{n_{\uparrow}}{\tau_{e\uparrow\downarrow}} - eG_{e\uparrow} + eR_{\uparrow\downarrow}n_{\uparrow}p_{\downarrow} + eR_{\uparrow\uparrow}n_{\uparrow}p_{\uparrow}, \quad (26)$$

$$-e \frac{\partial n_{\downarrow}}{\partial t} = -\nabla \cdot \mathbf{j}_{e\downarrow} + e \frac{n_{\downarrow}}{\tau_{e\downarrow\uparrow}} - e \frac{n_{\uparrow}}{\tau_{e\uparrow\downarrow}} - eG_{e\downarrow} + eR_{\downarrow\uparrow}n_{\downarrow}p_{\uparrow} + eR_{\downarrow\downarrow}n_{\downarrow}p_{\downarrow}, \quad (27)$$

$$e \frac{\partial p_{\uparrow}}{\partial t} = -\nabla \cdot \mathbf{j}_{h\uparrow} + e \frac{p_{\downarrow}}{\tau_{h\downarrow\uparrow}} - e \frac{p_{\uparrow}}{\tau_{h\uparrow\downarrow}} + eG_{h\uparrow} - eR_{\downarrow\uparrow}n_{\downarrow}p_{\uparrow} - eR_{\uparrow\uparrow}n_{\uparrow}p_{\uparrow}, \quad (28)$$

$$e \frac{\partial p_{\downarrow}}{\partial t} = -\nabla \cdot \mathbf{j}_{h\downarrow} - e \frac{p_{\downarrow}}{\tau_{h\downarrow\uparrow}} + e \frac{p_{\uparrow}}{\tau_{h\uparrow\downarrow}} + eG_{h\downarrow} - eR_{\uparrow\downarrow}n_{\uparrow}p_{\downarrow} - eR_{\downarrow\downarrow}n_{\downarrow}p_{\downarrow}, \quad (29)$$

and the Poisson equation relating the local deviation from equilibrium of the charge densities to the electric field,

$$\nabla \cdot \mathbf{E} = -\frac{e}{\epsilon}(\Delta n_\uparrow + \Delta n_\downarrow - \Delta p_\uparrow - \Delta p_\downarrow). \quad (30)$$

Here  $\tau_{ess'}^{-1}$  and  $\tau_{hss'}^{-1}$  are rates for spin relaxation of electrons and holes respectively from spin  $s$  to spin  $s'$ ,  $G_{ns}$  are generation rates for carrier  $n$  and spin  $s$ ,  $R_{ss'}$  are the electron–hole pair recombination rates for an electron of spin  $s$  and hole of spin  $s'$ , and  $\epsilon$  is the dielectric constant. If the hole spins are unpolarized then Eqs. (28) and (29) can be replaced by a single one with  $p_\uparrow = p_\downarrow = p/2$ .

Under conditions of approximate local charge neutrality often these equations can be combined into a single one for a packet type with significant spin polarization, following the procedure used for the charge polarization packets. Shown in Figure 5 are such packets for a semiconductor lacking background doping. For the hole spin packet and electron spin packet the derivation follows through exactly as before for the charge polarization packet, but either the holes or the electrons are entirely spin polarized. The lifetime of the hole spin packet, however, is much shorter than of the charge polarization packet, for the hole spin lifetime is typically much shorter than the charge recombination lifetime (Meier and Zachachrenya, 1984; Uenoyama and Sham, 1990). Thus the hole spin packet decays into the charge polarization packet. The electron spin lifetime can be much longer than the charge recombination time, so in that regime the electron spin packet decays by electron–hole recombination. If the hole spin lifetime were very long, and recombination were 100% spin selective, then eventually the recombination of the electron spin packet might stop, but the short hole spin lifetime guarantees that any spin imbalance in the hole population generated during a

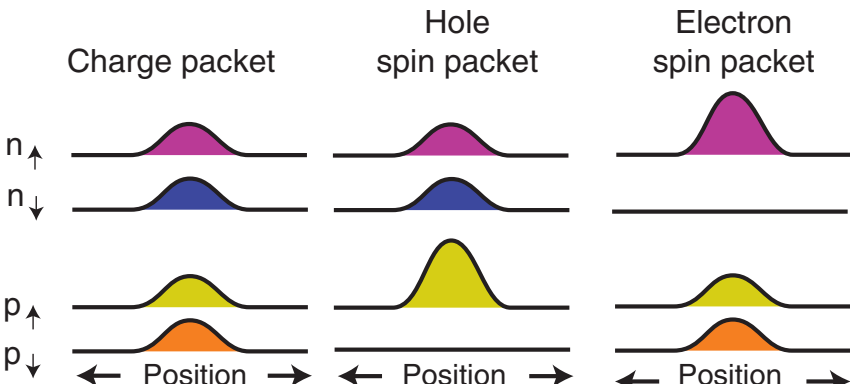


Figure 5. The packets of carriers possible in an undoped semiconductor require equal numbers of electrons and holes to maintain local charge neutrality. Thus packets of spin-polarized electrons (or holes) require a background of holes (or electrons)

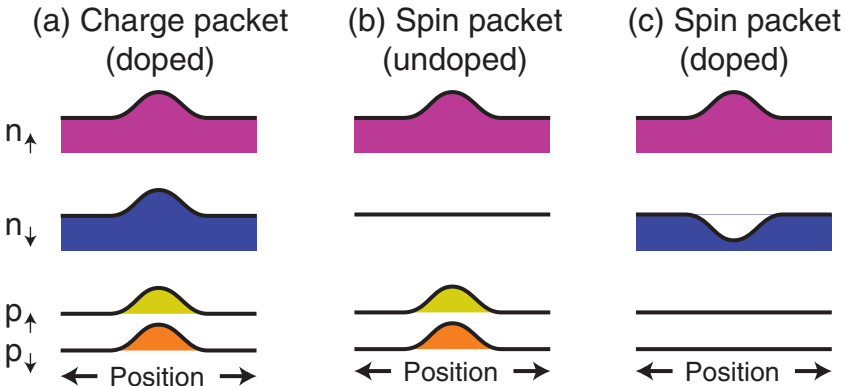


Figure 6. In the presence of a background of unpolarized electrons it is possible to satisfy local charge neutrality by removing opposite-spin-oriented electrons when adding spin-polarized electrons. Thus the mobility and diffusion of this packet is determined by the properties of the electrons, not the minority holes

spin-selective recombination process with spin-polarized electrons would decay away rapidly. Thus the lifetime of the electron spin packet is effectively the charge recombination time.

The situation changes considerably when the semiconductor has a background doping of carriers. As shown in Figure 6 it is now possible to maintain local charge neutrality by removing carriers from the background doping rather than adding carriers of the other species. Thus additional spin-up electrons can be compensated for by removing spin-down electrons. No holes are required. The two equations that play comparable roles in this case to Eqs. (13) and (14) are the two spin-resolved equations for the electrons, Eqs. (26) and (27), with  $p_\uparrow = p_\downarrow = 0$ .

The lifetime of the hole spin packet remains limited by the hole spin lifetime, but the lifetime of the electron spin packet is no longer limited by the carrier recombination lifetime. As holes no longer play a role in the decay of the packet, the lifetime of the electron spin packet is determined by the electron spin lifetime. Thus an electron spin packet in an n-doped semiconductor can persist for times orders of magnitude longer than for an electron spin packet in an undoped semiconductor, as seen in experimental observations in several semiconductor materials (Kikkawa et al., 1997; Kikkawa and Awschalom, 1998). Furthermore the diffusion constant and mobility of the packet will be those of the majority electrons rather than the minority holes (unlike the behavior of charge polarization packets). Following the derivation for charge polarization packets produces the following equation of motion for electron spin packets (Flatté and Byers, 2000; Yu and Flatté, 2002a, b),

$$D_s \nabla^2(n_\uparrow - n_\downarrow) + \mu_s \nabla(n_\uparrow - n_\downarrow) \cdot \mathbf{E} = \frac{(\Delta n_\uparrow - \Delta n_\downarrow)}{\tau_s} \quad (31)$$

with

$$D_s = \frac{\sigma_{e\uparrow} D_{e\downarrow} + \sigma_{e\downarrow} D_{e\uparrow}}{\sigma_{e\uparrow} + \sigma_{e\downarrow}}, \quad \mu_s = \frac{\sigma_{e\uparrow} \mu_{e\downarrow} - \sigma_{e\downarrow} \mu_{e\uparrow}}{\sigma_{e\uparrow} + \sigma_{e\downarrow}}, \quad \tau_s^{-1} = \tau_{e\downarrow\uparrow}^{-1} + \tau_{e\uparrow\downarrow}^{-1}. \quad (32)$$

As  $\tau_s$  denotes the decay of the magnetization, which is proportional to  $n_\uparrow - n_\downarrow$ , it is also correct to refer to  $\tau_s$  as  $T_1$  in the notation of nuclear magnetic resonance (Slichter, 1963). Some treatments in the literature use  $\tau_s$  to refer to  $\tau_{e\downarrow\uparrow}$  and  $\tau_{e\uparrow\downarrow}$ , which are considered to be equal. If  $\tau_s$  is defined this way then  $\tau_s = 2T_1$ .

The considerations described above also should apply to packet transport in 100% or nearly 100% spin-polarized semiconductor, such as n-doped ZnMnSe in a moderate magnetic field. In such materials it is not possible to construct a spin packet polarized parallel to the background carrier magnetization without both electrons and holes. For an antiparallel spin packet, however, the charge of an excess of spins (spin-down in Figure 7) is compensated for by a reduction in the number of spins oriented in the opposite direction. As with the electron spin packets above, the diffusion constant and mobility of the packet will be determined by the majority carriers rather than the minority carriers. So for the parallel spin packet Eqs. (21) apply whereas for the antiparallel spin packet Eqs. (32) hold.

In addition to the differences in the magnitude of the diffusion constants and mobilities between different packet types there is a difference in the ratios of the diffusion constant to the mobility for the different packets. This Einstein ratio ranges from  $kT/e$  to larger values, depending on the degree of degeneracy of the carriers. As electrons become degenerate at a much lower density than holes, the Einstein ratio will exceed unity by a significant amount at a much lower density for the electron spin packet in a doped semiconductor than in an undoped semiconductor. It can be very difficult to observe an Einstein ratio greater than unity in a semiconductor through the dynamics of charge polarization packets.

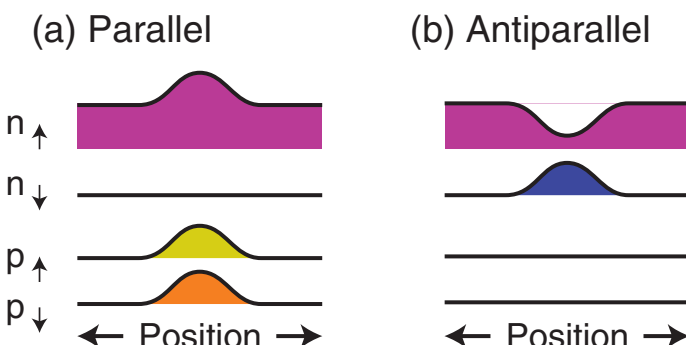


*Figure 7.* When there is a background of 100% spin-polarized electrons then the permissible spin packets are quite different for spins oriented parallel to or antiparallel to the background carrier spin direction. Parallel packets require minority holes whereas antiparallel packets can be constructed using only electrons

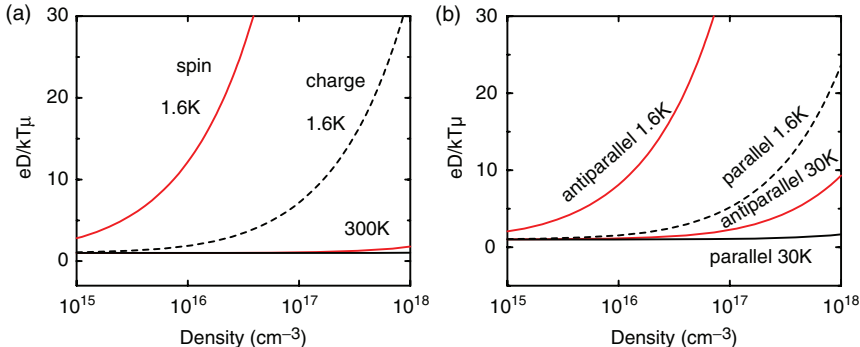


Figure 8. (a) The difference in the carrier which governs the mobility and diffusion constant of the spin and charge packets can be detected through the very different ratios of the diffusion constant to mobility. For spin packets the electrons play the principal role and the diffusion constant is much larger proportionally than the diffusion constant for the charge packet, whose motion is dominated by holes. (b) Similar behavior is seen for antiparallel and parallel spin packets. Reproduced with permission from Flatté and Byers (2000)

As their motion is determined by the minority carrier properties, it is required that the minority carriers be degenerate (which is much more unusual than having majority carriers degenerate). Shown in Figure 8 are the ratios of the diffusion constant to the mobility for spin and charge packets in GaAs as a function of density, and the same ratios in a 100% spin-polarized magnetic semiconductor. Here the properties of ZnSe have been assumed, as the magnetic semiconductor ZnMnSe can have nearly 100% spin-polarized carriers at low temperature and large magnetic field.

## 2.5 OPTICAL MEASUREMENTS OF SPIN DENSITY PACKET MOTION

Optical illumination of a semiconductor with circularly polarized light will generate spin-polarized electrons and holes through optical selection rules (Meier and Zachachrenya, 1984) as described in Chapter 4. Thus even though an electron spin packet can be constructed entirely from spin-up and spin-down electron density changes, without any holes, initially it may appear that such a packet could not be generated optically.

Shown in Figure 9 is a schematic of a process for generating the antiparallel electron spin packet in a 100% spin-polarized semiconductor. Initially circularly-polarized light generates 100% spin-polarized electrons (spin-up) and holes (spin-down). As described above, the spin lifetime for holes is considerably shorter than that of electrons, so very rapidly the holes lose their spin coherence. If the hole spin relaxation time is short compared to the electron–hole recombination time, and the electron spin lifetime is long compared to the electron–hole recombination time, then initially the optical disturbance evolves into a spin-polarized

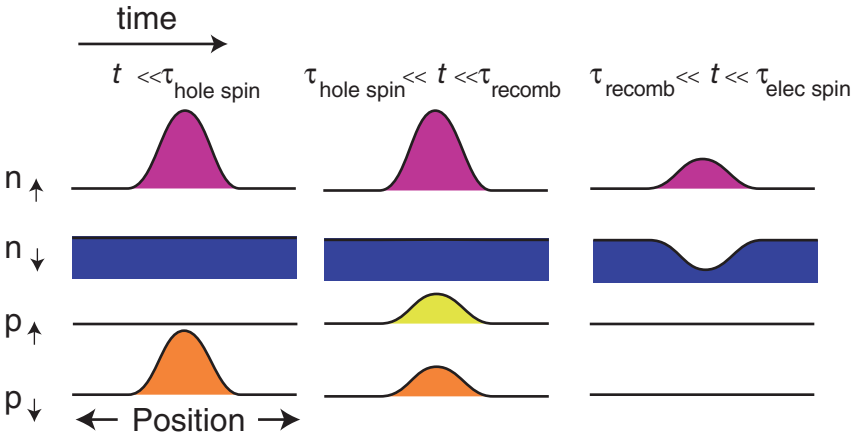


Figure 9. The initial optical generation of spin-polarized electrons and spin-polarized holes evolves, for times longer than the hole spin lifetime, to a population of spin-polarized electrons and unpolarized holes. That will then evolve, for times longer than the electron–hole recombination lifetime, to a pure electron spin packet. The electron spin packet then decays according to the electron spin lifetime (which is much longer than the electron–hole recombination time)

excess density of electrons and an unpolarized excess of holes. This can be considered the sum of a charge polarization packet and an electron spin packet. The charge polarization component will decay with a timescale of the carrier recombination time, leaving behind an electron spin packet with no excess holes. Thus even though the optical process generates equal numbers of electrons and holes, the eventual consequence of generating electron–hole pairs with circularly-polarized light is a pure electron spin disturbance.

## 2.6 IMPLICATIONS FOR SPIN INJECTION INTO SEMICONDUCTORS

Equation (31) can be written as

$$\nabla^2(n_\uparrow - n_\downarrow) + \frac{\mu_s}{D_s} \nabla(n_\uparrow - n_\downarrow) \cdot \mathbf{E} = \frac{(\Delta n_\uparrow - \Delta n_\downarrow)}{L^2}, \quad (33)$$

where  $L$  is the spin diffusion length in the limit  $\mathbf{E} = 0$ . When  $\mathbf{E} \neq 0$  the differential equation remains linear, but the spin diffusion length is modified from the zero-field limit. Suppose that a continuous spin imbalance is injected in a one-dimensional geometry at  $x = 0$ ,  $(n_\uparrow - n_\downarrow)|_0$ , and the electric field is along the  $-x$  direction, as shown in Figure 10a. The spin polarization will gradually decay in size as the distance from the point of injection increases and eventually go to zero at  $\pm\infty$ . The distribution of the spin polarization is described by

$$n_\uparrow - n_\downarrow = (n_\uparrow - n_\downarrow)|_0 \exp(-x/L_d), \quad x > 0, \quad (34)$$

$$n_\uparrow - n_\downarrow = (n_\uparrow - n_\downarrow)|_0 \exp(x/L_u), \quad x < 0, \quad (35)$$

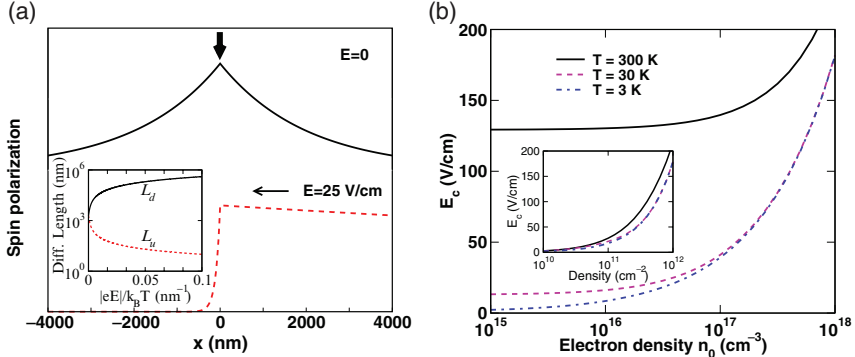


*Figure 10.* (a) Decay of spins away from an injection point parallel to and antiparallel to an applied electric field. A zero-field spin diffusion length of 2  $\mu\text{m}$ , nondegenerate electrons in GaAs at  $T = 3$  K has been assumed. The effect of a moderate electric field is to dramatically alter the decay length of the spins, both in the downstream and upstream directions. The inset shows the upstream and downstream spin diffusion lengths as a function of applied electric field. Reproduced with permission from Yu and Flatté (2002a). (b) The value of the applied electric field upon which the drift term is larger than the diffusion term in Eq. (31). Reproduced with permission from Yu and Flatté (2002b)

where the two quantities  $L_d$  and  $L_u$  are defined as the downstream (Aronov and Pikus, 1976) and upstream (Yu and Flatté, 2002a,b) spin diffusion lengths, respectively,

$$L_d = \left[ -\frac{|eE|}{2} \frac{\mu_s}{eD_s} + \sqrt{\left( \frac{|eE|}{2} \frac{\mu_s}{eD_s} \right)^2 + \frac{1}{L^2}} \right]^{-1}, \quad (36)$$

$$L_u = \left[ \frac{|eE|}{2} \frac{\mu_s}{eD_s} + \sqrt{\left( \frac{|eE|}{2} \frac{\mu_s}{eD_s} \right)^2 + \frac{1}{L^2}} \right]^{-1}, \quad (37)$$

and  $L_u L_d = L^2$ .

As shown in Figure 10, even for a small electric field of 25 V/cm at  $T = 3$  K the upstream and downstream spin diffusion lengths are very different from the zero-field spin diffusion length. To see if these effects would be important at room temperature,  $E_c$  from Figure 10b at a density of  $n = 10^{16} \text{ cm}^{-3}$  should be compared with typical lateral electric fields in devices. In order to maintain most of the spin polarization upon traversing a device with a typical spin lifetime of 100 ps, an estimate of 10 ps for the transit time appears reasonable. For a typical room-temperature mobility of  $5000 \text{ cm}^2/\text{Vs}$  for bulk GaAs it would require an electric field of 2000 V/cm to move a spin packet a typical device length of 1  $\mu\text{m}$  in 10 ps. This electric field is more than an order of magnitude larger than the  $\sim 100$  V/cm critical field at room temperature.

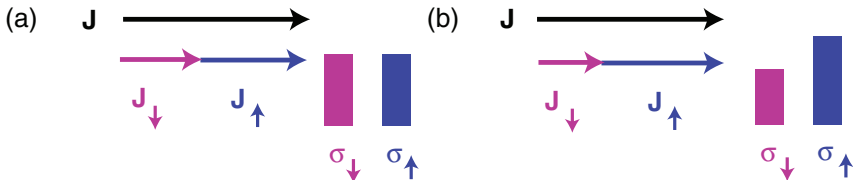


Figure 11. (a) When a spin-polarized current flows into a nonmagnetic semiconductor the initial conductivity is the same for spin-up and spin-down carriers. The excess carriers of one spin direction enlarge the conductivity for that spin direction, which permits a greater spin-polarized current to flow, leading to a larger spin injection efficiency in a feedback loop

The nature of spin transport in the drift regime has additional implications for the efficiency of spin injection from a ferromagnetic material into a semiconductor. An initial exploration of the efficiency of spin injection from a ferromagnetic metal into a semiconductor identified the conductivity difference between the two materials as a major impediment to highly efficient spin injection (Schmidt et al., 2000). Subsequent theoretical work found important exceptions to this analysis, particularly in the common case of a spin-dependent interface resistance (Rashba, 2000; Fert and Jaffrè, 2001; Smith and Silver, 2001). These calculations ignored the drift term in Eq. (31). The large enhancement of the downstream spin diffusion length pointed out by Aronov and Pikus (1976) would lead to greater spin injection throughout the bulk of the semiconductor, but does not directly indicate what the efficiency would be at the injection point.

Figure 11 indicates the physical effect of the drift term on the spin injection efficiency. Initially the conductivity of spin-up and spin-down carriers is the same. However, once spin-polarized current starts flowing into the semiconductor the conductivity of the injected spin direction increases and the conductivity of the other spin direction decreases (because of local charge neutrality). Shown in Figure 12 is the spin injection efficiency as a function of the electric field for several values of the ratio of the conductivity in the ferromagnet to the conductivity in the semiconductor. No matter what the conductivity of the ferromagnet is, the presence of the electric field dramatically enhances the spin injection efficiency relative to the zero-field value. A similar effect is seen in the presence of a spin-selective barrier. Here the effect of the drift term is to reduce the interface resistance required for high-efficiency spin injection.

## 2.7 SPIN TRANSPORT—CONCLUDING REMARKS

For each interesting regime of charge transport there appears to be an interesting regime of spin transport. The motion of charge polarization packets is governed by the behavior of space charge fields and the requirement to maintain approximate local charge neutrality. The same requirements are present for spin packets, although for spin packets it is not always necessary to have both carrier species

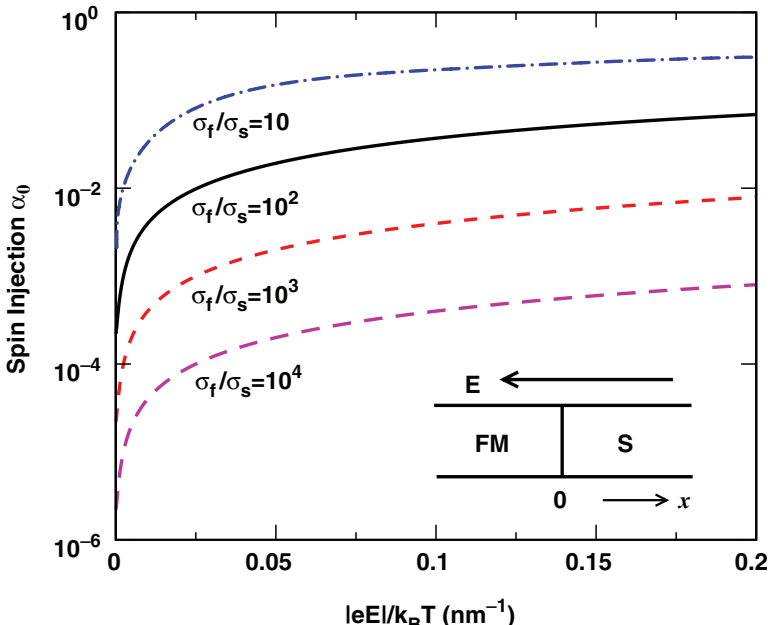


Figure 12. Spin injection efficiency as a function of applied electric field for several values of the ferromagnet/semiconductor conductivity ratio. Reproduced with permission from Yu and Flatté (2002a)

present to avoid excess charge. Thus the motion of spin packets can differ greatly from that of charge polarization packets. For nearly 100% spin-polarized magnetic semiconductors the nature of the packets differs depending on whether the excess spins are polarized parallel or antiparallel to the equilibrium carrier magnetization. These same constraints on spin motion from local charge neutrality lead to enhanced spin injection in the drift regime, where the downstream spin diffusion length is much larger than the zero-field spin diffusion length, and the upstream spin diffusion length (which influences spin injection efficiencies) is much smaller.

### 3 Spin Coherence Times in Semiconductors

A population of oriented spins in a nonmagnetic semiconductor represents a system out of thermal equilibrium, and the decay of such a nonequilibrium distribution will be characterized by spin coherence times. A physically unambiguous way of describing the evolution of that population can be achieved by distinguishing between a longitudinal spin coherence time (denoted  $T_1$  as in the nuclear magnetic resonance literature (Slichter, 1963)), which describes the decay of the population's magnetization parallel to an applied (and static) magnetic field, and a transverse spin coherence time, denoted  $T_2^*$ , describing the decay of the population's magnetization perpendicular to that magnetic field. The time  $T_2^*$

may differ from the transverse spin coherence time of an individual spin in the ensemble, denoted  $T_2$ , because of variability in the characteristics of the individual spins. If each of the spins in the ensemble has a different  $g$  factor, for example, the ensemble magnetization may disappear much more rapidly (due to different rates of spin precession) than the coherence of each individual spin. If there is spin exchange between members of this ensemble that have dephased relative to each other, then the dephased population becomes incoherent as well. This mechanism of dephasing followed by spin exchange (or other phenomena whereby the individual spin orientations are mixed within the ensemble) is known as precessional decoherence (Yafet, 1963).

The dominant mechanism for spin decoherence at and near room temperature in direct-gap zincblende semiconductors is a form of precessional decoherence. These materials are not inversion symmetric, and thus the energies of spin states are not degenerate at a given crystal momentum  $\mathbf{k}$ . This produces an effective internal magnetic field for each carrier depending on  $\mathbf{k}$ . The effective magnetic field changes sign when the momentum changes sign, so for stationary distributions the average internal magnetic field vanishes. As the value of this field is different at each value of  $\mathbf{k}$ , however, the spin orientations of an initially polarized distribution of spins will begin to precess relative to each other.

The rate of this precession can be quite fast, as a spin-splitting energy of just one meV would produce a precession frequency in the hundreds of GHz. Thus one might expect that spin coherence times would be extremely short in such materials. Despite this expectation the observed spin coherence times, as described in Chapter 4, can exceed 100 ns at low temperature. These much longer spin coherence times are made possible by the much more rapid momentum scattering times. In the simplest picture an orbital scattering event takes a carrier in the ensemble from a momentum  $\mathbf{k}$  to another momentum  $\mathbf{k}'$ , whose internal magnetic field has a different direction and magnitude. As the average internal magnetic field vanishes, it is as likely as not that the internal magnetic field will be pointing in the opposite direction. Thus instead of a coherent process of precession any specific carrier will undergo a random walk of spin precession, which is much less effective at spin reorientation (D'yakonov and Perel', 1972; Meier and Zachachrenya, 1984).

The spin-dependent electronic structure of bulk and quantum well structures has been calculated within the  $\mathbf{k} \cdot \mathbf{p}$  approach. For bulk semiconductors the approach is as follows. The wave functions at a general crystal momentum  $\mathbf{k}$  can be written as

$$\psi_{\mathbf{k}}(\mathbf{r}) = e^{i\mathbf{k}\cdot\mathbf{r}} u_{\mathbf{k}}(\mathbf{r}) = e^{i\mathbf{k}\cdot\mathbf{r}} \sum_n C_n u_n(\mathbf{r}). \quad (38)$$

The second portion of this equation denotes an expansion of the Bloch function at nonzero  $\mathbf{k}$  in terms of the Bloch functions at  $\mathbf{k} = 0$ . When the sum over  $n$  is complete then the representation in Eq. (38) is exact. In practice the sum over  $n$  is

restricted to a small number of nearby bands. An eight-band basis set (conduction, heavy hole, light hole and split off hole of both spin directions) is a common restricted set, and a 14 band basis set is also often used (Cardona et al., 1988), which includes the heavy electron, light electron and split off electron of both spin directions. The eight-band basis set is spherically symmetric unless diagonal terms in the Hamiltonian are introduced to break that symmetry. The 14-band basis set has intrinsic breaking of spherical symmetry (down to cubic) as well as breaking of inversion symmetry (which produces internal effective magnetic fields). Thus the 14-band basis set is a good choice for calculating spin-dependent properties in zincblende bulk and quantum well semiconductors (Lau et al., 2001; Winkler, 2003; Lau et al., 2004).

Application of the Hamiltonian

$$H = -\frac{\hbar^2}{2m} \nabla^2 + V(\mathbf{r}) \quad (39)$$

to the wave function in Eq. (38) produces three types of terms from the kinetic energy operator. The two spatial derivatives can both be applied to the plane wave, both to the Bloch function, or one can be applied to each. The result of this is

$$H\psi = e^{i\mathbf{k}\cdot\mathbf{r}} \sum_n \left( E_n + \frac{\hbar^2 k^2}{2m} \right) C_n u_n(\mathbf{r}) + e^{i\mathbf{k}\cdot\mathbf{r}} \sum_n C_n \frac{i\hbar\mathbf{k} \cdot \mathbf{p}}{m} u_n(\mathbf{r}), \quad (40)$$

where  $E_n$  are the energies of the Bloch functions

$$Hu_n(\mathbf{r}) = E_n u_n(\mathbf{r}). \quad (41)$$

The dominant contributions from the last term come from matrix elements between the Bloch functions.

### 3.1 SPIN COHERENCE TIMES IN BULK SEMICONDUCTORS

Shown in Figure 13a are calculated spin coherence times from Lau et al. (2001) for GaAs, InAs, and GaSb assuming that the mobility of the bulk material is dominated by ionized impurity scattering. The agreement with experimental measurements (Kikkawa and Awschalom, 1998) for GaAs at the higher temperatures is quite good, whereas for low temperatures other spin relaxation mechanisms are expected to dominate. There is good agreement for InAs with a room-temperature measurement (Boggess et al., 2000). The electron densities are  $10^{16} \text{ cm}^{-3}$  for GaAs,  $1.7 \times 10^{16} \text{ cm}^{-3}$  for InAs, and  $1.49 \times 10^{18} \text{ cm}^{-3}$  for GaSb. The difference in slope between GaSb and GaAs occurs because GaSb is degenerate for this density. The smaller spin coherence times in InAs and GaSb are due partly to the larger conduction spin splitting, which originates from a larger ratio of the spin-orbit coupling  $\Delta$  to the band gap  $E_g$  (see Cardona et al. (1988) for perturbative expansions of spin splittings). As the relevant electronic states are near the band edge,

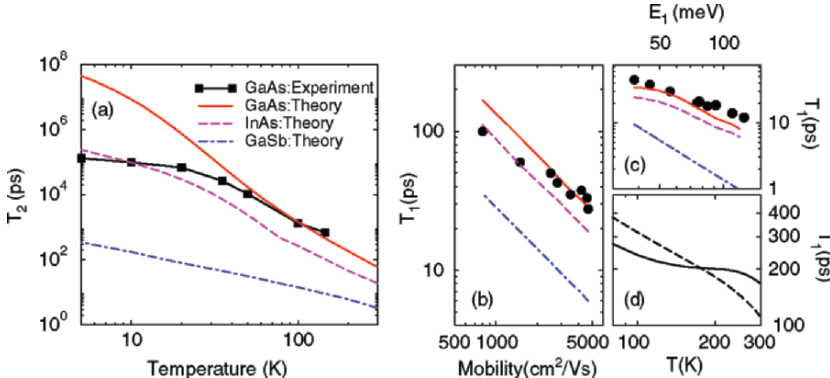


Figure 13. (a)  $T_2$ ,  $T_2^*$  in bulk III-V semiconductors as a function of temperature. Solid with squares and solid lines respectively represent the results of experiments on  $T_2^*$  (Kikkawa and Awschalom, 1998) and the non-perturbative theory for bulk GaAs with  $T_2 = T_2^*$  at the electron density  $n = 1.0 \times 10^{16} \text{ cm}^{-3}$ . Also shown are results for bulk InAs at  $n = 1.7 \times 10^{16} \text{ cm}^{-3}$  and bulk GaSb at  $n = 1.49 \times 10^{18} \text{ cm}^{-3}$ , which are indicated with dashed and dot-dashed lines respectively. Also shown is  $T_1$  as a function of (b) mobility, (c) confinement energy, and (d) temperature, for 75 Å GaAs/Al<sub>0.4</sub>Ga<sub>0.6</sub>As MQWs at room temperature. Closed circles represent the results of experiments (Terauchi et al., 1999). The non-perturbative theory results with mobility dominated by optical phonon scattering (solid lines) and with mobility dominated by neutral impurity scattering (dashed lines) are both shown, as well as the theory results from an approximate analytic expression (D'yakonov and Kachorovskii, 1986) (dot-dashed lines). Reproduced with permission from Lau et al. (2001)

perturbative expressions for the spin coherence times for these bulk semiconductors (D'yakonov and Perel', 1972; Meier and Zacharchenya, 1984) are identical to those obtained from the 14-band calculation within numerical accuracy. The agreement between calculated and measured spin coherence times in Figure 13a provides strong support for the dominance of the D'yakonov-Perel' mechanism of spin decoherence near room temperature. The model for spin relaxation for bulk semiconductors (D'yakonov and Perel', 1972) implies for these ensembles that  $T_2^* = T_2$  at small magnetic fields. These materials have cubic symmetry, so in this limit  $T_1 = T_2^* = T_2$  as well. This equality does not apply for nanostructures, for systems without a continuum of states (such as quantum dots), or for large magnetic fields.

### 3.2 SPIN COHERENCE TIMES IN QUANTUM WELLS

In a nanostructure the coefficients  $C_n$  in Eq. (40) become position-dependent, and turn into envelope functions. A proper calculation of the energies of the Bloch functions due to composition and strain is essential for a proper evaluation of the energies and wave functions for nanostructures. The results of calculations of  $T_1$  for GaAs quantum wells are shown in Figures 13b–d. The spin-dependent

electronic structure was obtained by writing the nanostructure electronic states as spatially-dependent linear combinations of the 14 states in the basis. The full Hamiltonian was then projected onto this restricted basis set, which produces a set of 14 coupled differential equations for the spatially-dependent coefficients of the basis states (generalized envelope functions) (Lau et al., 2001; Lau et al., 2004). These equations were then solved in Fourier space according to the method of Winkler and Rössler (Winkler and Rössler, 1993).

Experimental measurements (Terauchi et al., 1999) of  $T_1$  in 75 Å n-doped GaAs/Al<sub>0.4</sub>Ga<sub>0.6</sub>As MQWs at 300 K are indicated in Figure 13(b–c) with filled circles. The experimental results have been adjusted from Terauchi et al. (1999), for the authors defined an effective spin flip time for a single spin,  $\tau_s = 2T_1$ , and plotted their results for  $\tau_s$ . The D'yakonov and Kachorovskii (1986) calculation is an approximate analytic form for  $T_1$  (dot-dashed line in Figure 13b–d) and does not depend on the dominant contribution to the mobility. It differs from the experimental results by about a factor of 4. The more detailed theoretical calculations (Lau et al., 2001), shown as the solid line for a mobility dominated by optical phonon scattering, and the dashed line for a mobility dominated by neutral impurity scattering, are both in good agreement with the experimental results. For clean systems the mobility should be dominated by optical phonon scattering, which is closer to the experimental results than the other curve, whereas in dirty systems the mobility should be dominated by neutral impurity scattering, again closer to the experimental results for dirty systems. The spin coherence times have been calculated without any adjustable parameters, indicating that the theoretical understanding of the  $T_1$ ,  $T_2$ , and  $T_2^*$  times in these systems is now quite good.

### 3.3 SPIN DECOHERENCE FROM INTERFACE INVERSION ASYMMETRY

The source of the inversion asymmetry that produces the spin decoherence shown in Figure 13 is the inversion asymmetry of the bulk semiconductor constituents of the bulk or quantum well material. There are other possible sources of inversion asymmetry. The first is the presence of inversion symmetry breaking at the interfaces between two materials. Shown in Figure 14 are the interfaces between two materials, InAs and GaSb, which are both zincblende semiconductors, but which lack a common atom. As a result the interfaces must consist either of GaAs or InSb bonds (or some combination of the two), neither of which occur in the bulk of the material. The configurations for these two are shown in Figure 14.

In Figure 14a the configuration for a superlattice grown along the (001) orientation is shown. Here there is no mirror plane possible in the structure, no matter how the interfaces are grown. If the two types of interfaces (InAs on GaSb and GaSb on InAs) are grown with the same types of bonds (such as InSb) then the bonds at the two interfaces are rotated 90 degrees relative to each other, breaking the mirror symmetry. This additional inversion asymmetry can lead to much

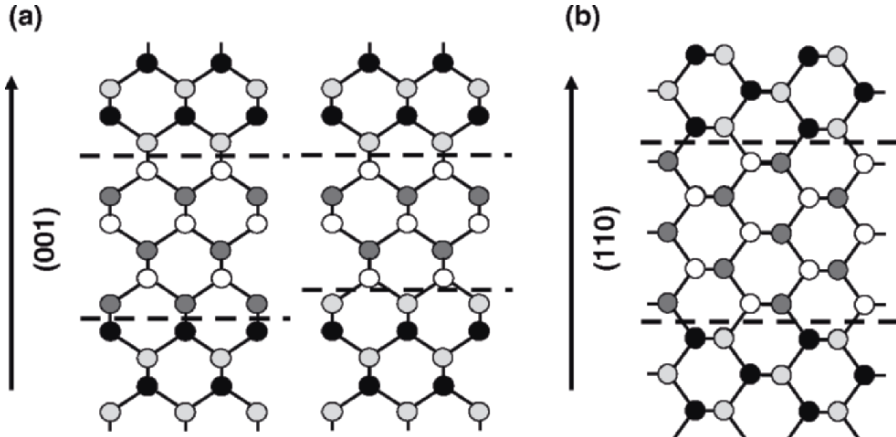


*Figure 14.* Schematic diagram of the interfaces in InAs/GaSb superlattices for (a): (001) and (b): (110) directions of growth. The shades indicate, in order of increasing darkness, Sb, In, Ga, As. Since InAs and GaSb have no atom in common, for (001) superlattices the interface potential is intrinsically asymmetric, referred to as NIA. The two types of bonding configurations for (001) superlattices are shown: different bond composition at the two interfaces (InSb and GaAs), or bonds of the same composition (InSb is shown) but different orientation. In contrast, for (110) no-common-atom superlattices, NIA is absent because the interfaces are mixed, containing equal numbers of both anions and cations, leading to a symmetric interface potential. Reproduced with permission from Hall et al. (2003a)

shorter spin coherence times than expected from calculations neglecting these interface bonds (Olesberg et al., 2001).

In Figure 14b the configuration for a superlattice grown along the (110) direction is shown. Here there is a mirror plane, and there is always a mix of GaAs and InSb bonds. The result of this higher symmetry is a much longer spin coherence time for (110) structures when the spins are oriented parallel to the (110) direction (D'yakonov and Kachorovskii, 1986; Ohno et al., 1999a; Lau and Flatté, 2002; Hall et al., 2003a).

### 3.4 TUNING SPIN COHERENCE WITH AN APPLIED ELECTRIC FIELD

The second source of inversion asymmetry is the presence of a graded composition or an applied electric field (Rashba, 1960; Bychkov and Rashba, 1984). A particularly useful characteristic of this source is that it is externally tunable. Due to the very long spin relaxation times in a (110) quantum well the spin relaxation times in such a system should be adjustable over several orders of magnitude if the electric field is applied parallel to the (110) direction (Lau and Flatté, 2002). Shown in Figure 15 are experimental results for a (110) GaAs/AlGaAs quantum well and a (110) InAs/AlSb multiple quantum well. In both cases the spin relaxation times are tunable when an electric field is applied. Theory predicts that

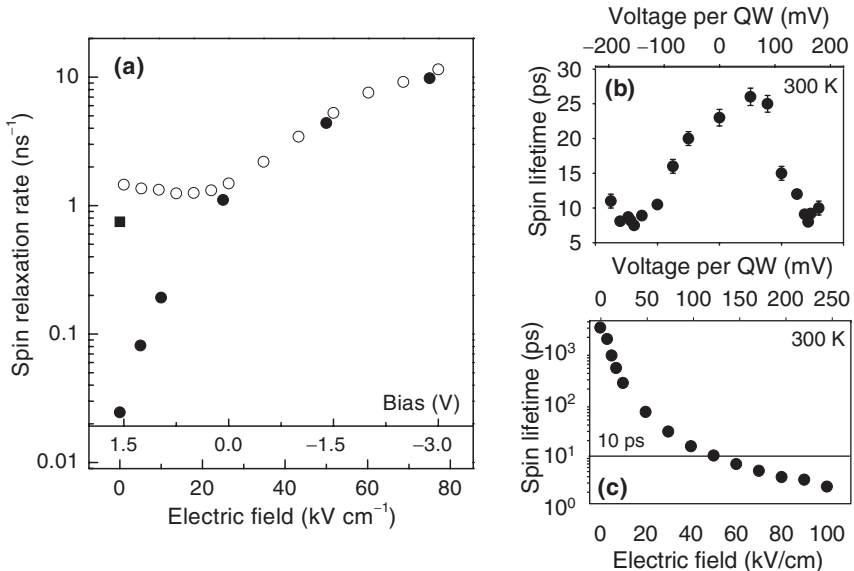


*Figure 15.* (a) Spin-dynamics: Measured spin relaxation rate vs bias voltage and corresponding electric field (open circles) for (110)-oriented *pin* mesa device at 170 K, compared with calculation for a symmetrical QW (solid circles) and for a QW with one two-monolayer graded interface (solid square) assuming electron mobility  $0.6 \text{ m}^2 \text{ V}^{-1} \text{ s}^{-1}$ . Reproduced with permission from Karimov et al. (2003). (b) Measured bias dependence of the spin relaxation time in a (110) InAs/AlSb multiple quantum well at 300 K. (c) Theoretical spin lifetimes vs bias calculated using a 14-band nonperturbative  $\mathbf{k} \cdot \mathbf{p}$  nanostructure model. Reproduced with permission from Hall et al. (2005)

the tuning range would be much larger than seen experimentally. The discrepancy for small applied electric fields probably occurs because the quantum wells are not completely symmetric, even in the absence of an applied electric field. Shown in Figure 15a is the spin relaxation rate for a quantum well with a non-symmetric (graded) interface, which appears similar to the experimental measurements.

### 3.5 SPIN COHERENCE—CONCLUDING REMARKS

The results shown in this section demonstrate that the understanding of spin coherence times in bulk and quantum well semiconductor is quite good. Quantitatively accurate spin coherence times can be calculated, including the effects of inversion asymmetry in the bulk material and in interface bonds. Even the tunable contribution from applied electric fields can be quantitatively calculated with considerable accuracy. This spin relaxation rate tuning has been proposed as a mechanism for switching spin transistors (Hall et al., 2003b; Hall and Flatté, 2006). Progress towards greater control of the spin relaxation times can be achieved by growing the quantum wells in a more symmetric fashion.

The physics of quantum dots can be quite different due to the quenching of all orbital motion, and the significant contribution of decoherence due to hyperfine interactions. In lithographic quantum dots these times have been directly observed (Petta et al., 2005). In self-assembled quantum dots very long  $T_1$  times have been observed at low temperature (Kroutvar et al., 2004). Results on long  $T_2$  times in such dots are presented in Chapter 4.

#### 4 All-Electrical Control of Single Ion Spins in a Semiconductor

Let us now begin to explore the properties of individual spins embedded in semiconductors. Sensitivity sufficient to measure the fluctuation of a single spin has been demonstrated using magnetic resonance force microscopy (Rugar et al., 2004), noise spectroscopy (Xiao et al., 2004), optical spectroscopy (Gruber et al., 1997; Jelezko et al., 2002), scanning tunneling microscopy (STM) (Manassen et al., 1989; Durkan and Welland, 2002; Heinrich et al., 2004), and quantum point contact conductivity (Elzerman et al., 2004). Proposed schemes to control a single spin in a solid state environment rely on magnetic resonance (Kane, 1998; Loss and DiVincenzo, 1998), optical manipulation (Imamoğlu et al., 1999; Quintero and Piermarocchi, 2005; Pryor and Flatté, 2006b), or the exchange interaction (DiVincenzo et al., 2000; Petta et al., 2005).

This section will explore the properties of ionic spins and the next section will investigate the properties of spins in quantum dots. Ionic spin states in solids have several attractive characteristics for fundamental studies of spin dynamics and for spin-based devices. An ionic spin system can be as uniform as a nuclear spin system, but also can permit spin manipulation on short time scales as in a quantum dot spin system. Controlling ionic single spins without any magnetic fields, using techniques in which electric fields play the typical role of magnetic fields, may provide a path to scalable quantum computation.

In Tang et al. (2006) an all-electrical scheme for ionic spin manipulation was proposed in which the role of magnetic fields in traditional electron spin resonance (ESR) was replaced by electric fields. In conventional ESR the energy splitting between different spin states, and the couplings between them, are controlled by magnetic fields because an electric field does not directly couple to the electron's spin. In a semiconductor crystal with tetrahedral symmetry and spin-orbit interaction (such as GaAs) a  $J = 1$  ion spin (such as that of Mn in GaAs) will be triply degenerate, however the energy splittings and the couplings between these states depend *linearly* on the *electric field* strength, allowing rapid all-electrical control. Thus all operations performed with magnetic fields in traditional ESR, can be performed with electrical techniques.

A specific proposed setup for manipulating a single ion spin from Tang et al. (2006) is shown in Figure 16. Tip-induced placement of Mn ions substituted

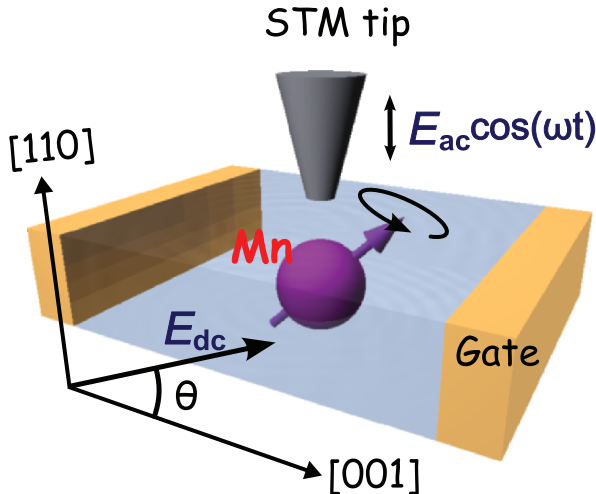


Figure 16. Proposed configuration for the electric resonances of a single Mn dopant in GaAs. A dc electric field  $\mathbf{E}_{dc}$  is applied via the electrical gates and the STM tip. The resonance is driven by an additional small ac field. Reproduced with permission from Tang et al. (2006)

for Ga in a GaAs sample has been demonstrated experimentally (Kitchen and Yazdani, 2005; Kitchen et al., 2006). Two gates are configured to apply an electric field along the [001] axis. The STM tip serves as the third gate for spin manipulation, and as a contact for initialization and detection. Taking advantage of the (110) natural cleavage plane (which lacks surface states), the applied electric field is confined in the (110) plane and the orientation is specified by the angle  $\theta$  from the [001] axis.

#### 4.1 PROPERTIES OF THE MN ION IN AN ELECTRIC FIELD

An isolated Mn atom has a half-filled  $3d$  shell and the spins of all five  $3d$  electrons are aligned (Hund's rule) to form a  $S = 5/2$  ground state. In GaAs a hole in the valence band compensates for the differing valences of Mn and Ga. The core spin-valence hole dynamics are described with the following effective spin Hamiltonian:

$$\mathcal{H}_{\text{spin}} = \alpha \mathbf{S} \cdot \mathbf{s} + \beta \mathbf{l} \cdot \mathbf{s}, \quad (42)$$

where  $\mathbf{l}$  and  $\mathbf{s}$  are the orbital angular momentum ( $l = 1$ ) and the spin of the bound hole respectively. Tight-binding calculations (Tang and Flatté, 2004) estimate the exchange coupling  $\alpha$  and the spin-orbit coupling  $\beta$  to be about 300 meV and -80 meV respectively. The exchange interaction binds the valence hole with spin antiparallel to the Mn core spin with a binding energy of 113 meV (Lee and Anderson, 1964). The spin-orbit interaction in GaAs configures

the orbital angular momentum of the hole parallel to its spin. The total angular momentum of the (Mn core + hole) complex is  $\mathbf{J} = \mathbf{S} + \mathbf{I} + \mathbf{s}$ , and the ground state of this complex has  $J = 1$  (both  $\mathbf{I}$  and  $\mathbf{s}$  are antiparallel to  $\mathbf{S}$ ), confirmed via ESR (Schneider et al., 1987). Tang et al. (2006)'s proposals for spin control involve energy scales smaller than  $\alpha$  or  $\beta$ , so only the lowest energy multiplet with  $J = 1$  is of interest here.

The degeneracy of the  $J = 1$  Mn ion can be substantially split by external electric fields, and the eigenstates depend strongly on the electric field direction. In Tang et al. (2006) this is the source both of state splitting (analogous to the static magnetic field in traditional ESR) and state coupling (analogous to the oscillating perpendicular magnetic field in traditional ESR). The electric-field-dependent Hamiltonian is

$$\mathcal{H}_I(\mathbf{E}) = \gamma [E_x(J_y J_z + J_z J_y) + \text{c.p.}], \quad (43)$$

where  $\mathbf{E}$  is an electric field, c.p. stands for cyclic permutation, and  $\{x, y, z\}$  stand for the three major axes of the cubic crystal. Note that this Hamiltonian does not break time-reversal symmetry, for the angular momentum operators  $\mathbf{J}$  always appear in pairs. The probability densities of the hole state found using tight-binding calculations and first-order perturbation theory (Tang et al., 2006) are  $\gamma = 6.4 \times 10^{-30}$  cm, corresponding to  $\gamma E = 160 \mu\text{eV}$  for  $E = 40 \text{ kV/cm}$ . This exceptionally large splitting is equivalent to that generated by applying a 1 Tesla magnetic field using the measured  $g$ -factor of 2.77 (Schneider et al., 1987). The linear dependence on electric field, critical to producing a large splitting, originates from the lack of inversion symmetry of the substituted ion in a tetrahedral host. The energy splittings from an electric field applied to bound states at inversion-symmetric sites in crystals, or electrons bound in atoms or ions in vacuum, would depend quadratically on the electric field and would be correspondingly much smaller. The other essential element causing this large splitting is the large ( $\sim 10 \text{\AA}$ ) Bohr radius of the bound valence hole (Tang and Flatté, 2004; Yakunin et al., 2004a). Recent progress in theory and scanning tunneling microscopy of Mn dopants in III–V semiconductors has confirmed the large spatial extent of the bound hole wavefunction (Arseev et al., 2003; Tang and Flatté, 2004; Yakunin et al., 2004a; Kitchen and Yazdani, 2005). Thus the response of the Mn wavefunction to electric fields is substantial compared to other ion levels associated with transition-metal (magnetic) dopants.

In the basis  $|X\rangle$ ,  $|Y\rangle$  and  $|Z\rangle$ , defined by  $J_a|\alpha\rangle = 0$ , Tang et al. (2006) write the Hamiltonian as

$$\mathcal{H}_I(\mathbf{E}) = -\gamma E \begin{pmatrix} 0 & \hat{E}_z & \hat{E}_y \\ \hat{E}_z & 0 & \hat{E}_x \\ \hat{E}_y & \hat{E}_x & 0 \end{pmatrix}. \quad (44)$$

The energy eigenvalues in units of  $\gamma E$  are the roots of the characteristic polynomial,

$$x^3 - x + 2\eta = 0, \quad (45)$$

where  $\eta = \hat{E}_x \hat{E}_y \hat{E}_z$ . A static electric field  $\mathbf{E}_{dc}$  splits all three eigenstates in energy except when the field is in the [111] direction (or equivalent), for which two of the eigenstates remain degenerate.

The energies of the three states are  $\xi_1 = (-\cos \theta - \sqrt{4 - 3 \cos^2 \theta})/2$ ,  $\xi_2 = (-\cos \theta + \sqrt{4 - 3 \cos^2 \theta})/2$ , and  $\xi_3 = \cos \theta$ , shown by the solid, dashed, and dotted curves respectively in Figure 17a. The eigenstate  $|\xi_3\rangle = |X - Y\rangle$  is independent of the electric field orientation. The independence of  $|\xi_3\rangle$  from  $\mathbf{E}$  motivates the construction of a pseudospin 1/2 from the other two states,  $|\xi_1\rangle$  and  $|\xi_2\rangle$ . These eigenstates can be written as  $|\xi_1\rangle = (\sin \Theta, \sin \Theta, \sqrt{2} \cos \Theta)$  and  $|\xi_2\rangle = (-\cos \Theta, -\cos \Theta, \sqrt{2} \sin \Theta)$ , where  $\Theta$  is the angle between  $|\xi_1\rangle$  and the  $|Z\rangle$  basis (Figure 17b). Note that all the eigenvectors are real because of time-reversal symmetry.

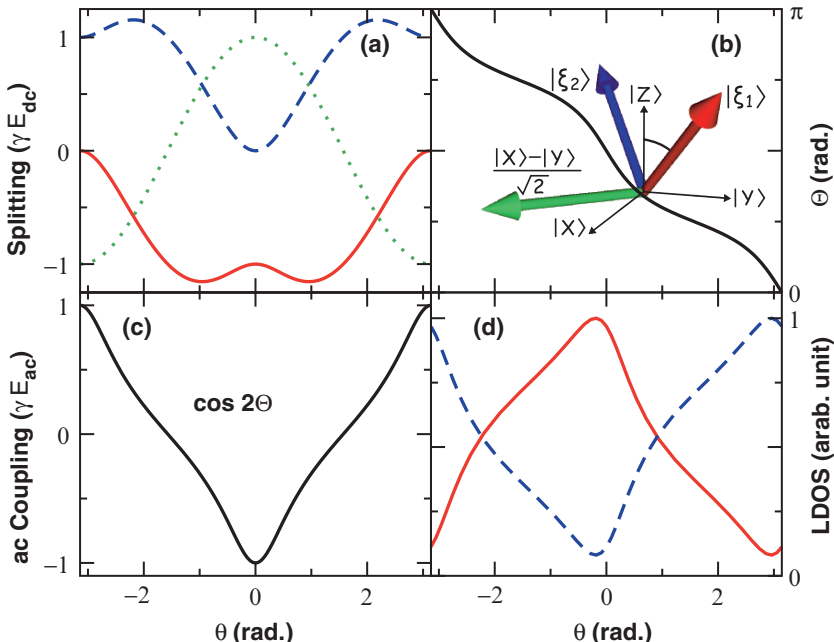


*Figure 17.* The ionic spin system as a function of the dc field orientation. (a) The energies of the  $J = 1$  states  $\xi_1$  (solid),  $\xi_2$  (dashed), and  $\xi_3$  (dotted). (b) The corresponding eigenvectors parametrized by the angle  $\Theta$ . (c) The coupling between  $|\xi_1\rangle$  and  $|\xi_2\rangle$  due to the ac field. (d) The scaled LDOS of the two possible final states  $|\xi_1\rangle$  (solid) and  $|\xi_2\rangle$  (dashed) probed four monoatomic layers directly above the Mn dopant. Reproduced with permission from Tang et al. (2006)

## 4.2 INITIALIZATION

Tang et al. (2006) suggest preparing the initial pseudospin state by applying an electric field to split the state energies, and allowing the hole to relax into the ground state. The electric field from the STM tip locally bends the bands of the semiconductor and permits ionization of the bound hole; this has been demonstrated for Mn in GaAs (Yakunin et al., 2004a, b). Rapid initialization of a high purity pseudospin state can be achieved by using the local band bending effect to move the two higher-energy levels ( $|\xi_2\rangle$ ,  $|\xi_3\rangle$ ) to the position shown in Figure 18a, so a hole in those states would ionize and be replaced by a hole in the lowest energy state ( $|\xi_1\rangle$ ). At a temperature of 0.5 K and a dc field of 100 kV/cm, the occupation of the next highest state ( $|\xi_2\rangle$ ) would be less than  $10^{-4}$ . Tang et al. (2006) chose  $E_{dc}$  such that  $|\theta| < (\pi - \tan^{-1} \sqrt{2})$ , so that  $|\xi_1\rangle$  (not  $|\xi_3\rangle$ ) is the ground state (see Figure 17(a)). Band bending also changes the effective radius of the bound hole wave function; gate voltages applied at the surface could thus control the coupling of two bound hole states in an analogous way to approaches in Loss and DiVincenzo (1998) and Kane (1998) for quantum dots and donor states.

## 4.3 MANIPULATION

In order to manipulate the initialized spins the tip-sample bias should be increased adiabatically (slower than  $\hbar/(\gamma E_{dc})$ ) to bring all three levels into the

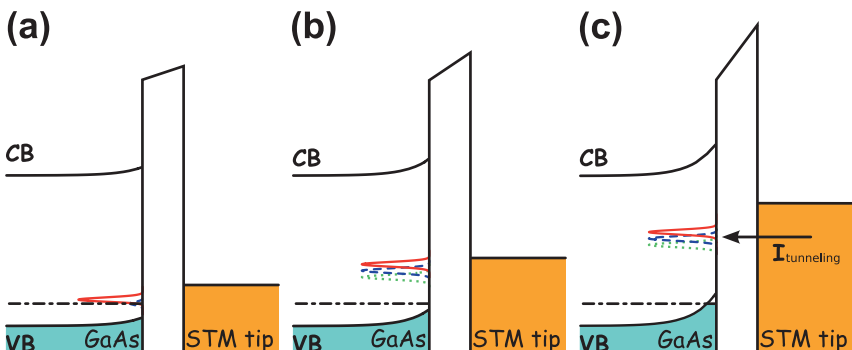


Figure 18. Schematics of controlling the spin states via local band bending. The dot-dashed lines show the chemical potential. Shaded regions are filled states. CB and VB label the conduction and valence bands of the semiconductor. (a) Initialization: For this voltage occupation of the  $|\xi_1\rangle$  state dominates. (b) Manipulation: Bring all the states into the gap, but control the bias voltage below the threshold where the current starts to tunnel through these states. The oscillating field ( $E_{ac}$ ) drives transitions between the  $|\xi_1\rangle$  and the  $|\xi_2\rangle$  states. (c) Detection: Bring the final state further into the gap, so that electrons can tunnel from the tip into the acceptor state. The final state is identified according to the amplitude of the tunneling current (Figure 17(d)). Reproduced with permission from Tang et al. (2006)

semiconductor's energy gap (see Figure 18b). This shift with bias is described for Mn in p-doped GaAs in (Yakunin et al., 2004a). The bias voltage has to be maintained below the critical value at which electrons start to tunnel directly through these levels, so that the transitions between these states remain coherent. Spin resonance can now be driven by applying a small oscillating electric field  $\mathbf{E}_{ac}(t)$  to the static field  $\mathbf{E}_{dc}$ . The Hamiltonian

$$\mathcal{H}_{\text{ESR}} = \mathcal{H}_I(\mathbf{E}_{dc}) + \mathcal{H}_I[\mathbf{E}_{ac}(t)]. \quad (46)$$

To have a well-defined pseudospin 1/2, constructed out of  $|\xi_1\rangle$  and  $|\xi_2\rangle$ , the coupling of these two states to  $|\xi_3\rangle$  must vanish. For the schematic in Figure 16 the oscillating field can be applied either along the [110] direction through the STM tip or along the [001] direction through the gates. Both choices leave  $|\xi_3\rangle$  unaffected and only couple  $|\xi_1\rangle$  and  $|\xi_2\rangle$  to each other. To see how the states are coupled by the ac field, Tang et al. (2006) wrote  $\mathcal{H}_I[\mathbf{E}_{ac}(t)]$  using the eigenstates of  $\mathcal{H}_I(\mathbf{E}_{dc})$  as a basis. For an ac field  $\mathbf{E}_{ac}(t)$  along the [110] direction,

$$\mathcal{H}_I[\mathbf{E}_{ac}(t)] = \gamma E_{ac} \cos(\omega t) \begin{pmatrix} -\sin 2\Theta & \cos 2\Theta & 0 \\ \cos 2\Theta & \sin 2\Theta & 0 \\ 0 & 0 & 0 \end{pmatrix}. \quad (47)$$

The off-diagonal term  $\cos 2\Theta$ , plotted in Figure 17c, shows how the coupling between the two coupled states changes with the field orientation. The coupling is maximized when the static field is completely along the [001] direction ( $\theta = 0$ ). Then the static and oscillating electric fields are perpendicular to each other, just as the static and oscillating magnetic fields are perpendicular to each other in traditional ESR. In the limit  $E_{ac} \ll E_{dc}$ , the diagonal term can be neglected and this configuration works just like conventional ESR. The Rabi frequency obtained from the standard Rabi formula is

$$\hbar\Omega = \frac{1}{2} \sqrt{(\gamma E_{ac} \cos 2\Theta)^2 + (\hbar\omega - \gamma E_{dc} \sqrt{4 - \cos^2 \theta})^2}. \quad (48)$$

For  $E_{ac} = E_{dc}/4 = 25$  kV/cm, and  $\Theta = \pi/2$ ,  $\Omega/2\pi = 12$  GHz, corresponding to a Rabi time of 80 ps. Ensemble spin coherence times  $T_2^*$  measured by traditional ESR in GaMnAs exceed 0.5 ns (several times the estimated Rabi time), and appear due to the inhomogeneous environments of Mn ions (Schneider et al., 1987); the  $T_2$ 's of individual spins are expected to be considerably longer. Hyperfine interactions, which significantly affect conduction electron spin coherence, are expected to be weak for Mn ions as the overlap of the valence  $p$  orbitals with the nucleus is small.

#### 4.4 DETECTION

High-fidelity determination of the orientation of the pseudospin can be achieved by measuring the total tunneling current through the final state with the STM (Tang and Flatté, 2005). When the tip-sample voltage is increased, and the semiconductor bands bend further (see Figure 18c), current starts to tunnel through the bound hole wavefunction state (Yakunin et al., 2004a, b) and the tunneling current is proportional to the probability density of the state at the STM tip location. The spatial structure of these  $J = 1$  states is highly anisotropic (Tang and Flatté, 2004; Yakunin et al., 2004a, b), which permits a visibility approaching 90%. Spatial averaging of the LDOS over a typical experimental 2 Å changes the visibility by only a few percent. Current measurement timescales can be very fast as STM experiments performed at 50 GHz have demonstrated (Steeves et al., 1998). So long as the tunneling current is small it is possible to neglect spin flip during the measurement.

Controllable coupling of two spins permits use of these Mn ions for quantum information processing. Estimates of the overlap of holes bound to two separated Mn ions (Tang and Flatté, 2004) indicate ~100 meV splittings of Mn pair states for ions separated by 12 Å along the  $(1\bar{1}0)$  direction. The overlap falls off for larger separations according to the ~13 Å wave function radius of the bound hole, so would be ~0.1 meV for two ions 10 nm apart. This overlap could be reduced, increased, or eliminated with a gate between the two ions (Kane, 1998; Loss and DiVincenzo, 1998). This overlap has been directly visualized recently with STM (Kitchen et al., 2006). By using single-Mn manipulations to put single-ion quantum information in the proper pair of single-Mn states, the Mn pair state splitting can be used to perform CNOT operations in an analogous way to how the singlet-triplet splitting is used for a CNOT with spin-1/2 qubits.

#### 4.5 IONIC SPIN MANIPULATION—CONCLUDING REMARKS

This section has outlined a concrete proposal, presented in Tang et al. (2006), for electrically initializing, manipulating, and detecting single pseudospin states of a magnetic dopant in a semiconductor. All-electrical spin manipulation should be possible for other impurities in tetrahedral semiconductors characterized by  $J > 1/2$  ground state spins (e.g. most transition metal ions in most tetrahedral semiconductors, or the nitrogen-vacancy center in diamond). In a future scalable architecture the STM tip would be replaced by a gate-controlled contact. The controlled resistance of that contact would permit alternation between the gate configuration for manipulation and the contact configuration for initialization and detection, all without moving parts. The [001] static electric field, here assumed to be implemented with gates, may also be replaced by an internal electric field from a doping gradient (such as in a  $p-n$  junction), or even a static strain

field. The Mn ions could be controllably placed within the surface relative to the contacts using current pulses from an STM tip as described in Kitchen and Yazdani (2005).

## 5 Single-Spin Manipulation in Quantum Dots

Quantum computation using spin in quantum dots has some complementary advantages to the ionic quantum computation approach described above. The growth of quantum dots, often by strain-nucleated approaches or mesa lithography, permits (through a choice of alloy composition, size and shape) a selection of many physical properties, including confinement energy, overlap and g factors. Quantum dots can also be defined by accumulation and depletion via gates in a two-dimensional electron gas. To evaluate the potential success of proposals for quantum dot quantum computation referred to in section 1 of this chapter it is first necessary to develop accurate methods of calculating the electronic structure of these quantum dots.

### 5.1 METHODS OF CALCULATING QUANTUM DOT ELECTRONIC STRUCTURE

The methods of calculating quantum dot electronic structure are very similar in perspective to those that have been developed for bulk electronic structures. Tight-binding methods use a basis related to the atomic orbitals on individual atomic positions within the crystal, and introduce hopping matrix elements. Pseudopotential techniques are constructed from the opposite limit of nearly free electrons, but still retain the atomistic nature of the lattice. Envelope function techniques hide the atomistic aspect by working in a basis of zone-center Bloch functions. As the spatial discretization of the envelope function techniques is not tied to the atomic positions, a much larger grid point spacing can be used, and the calculations can thus run much faster than either the tight-binding or pseudopotential techniques. Tight-binding and envelope-function techniques realized in a real-space basis commonly generate sparse matrices, so finding extremal eigenvalues for the Hamiltonian (such as the ground state energies of electrons and holes) can be performed extremely rapidly using the Lanczos algorithm.

In this section some results will be presented based on calculations for quantum dots that are performed as described in Pryor (1998). An eight-band envelope-function  $\mathbf{k} \cdot \mathbf{p}$  approach is used in a real-space finite-difference implementation. The strain is taken from linear continuum elasticity theory. The strain energy is evaluated within a finite difference approximation and is minimized using a conjugate gradient expansion. Hydrostatic, biaxial and shear deformation potentials are included. Shown in Figure 19 are band edges from quantum dots along the growth direction (Figure 19a) and along a direction perpendicular to the growth direction, passing through the base as shown in Figure 19b. The modification

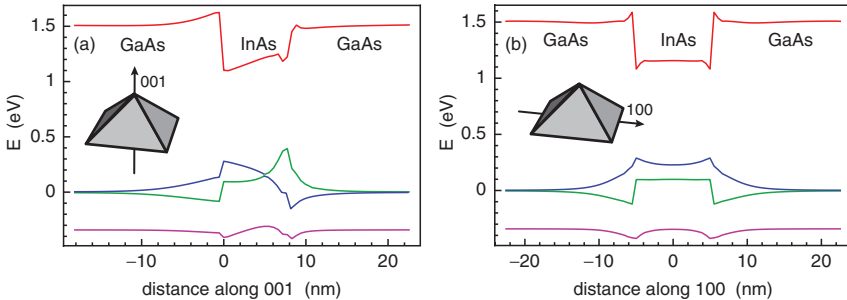


Figure 19. Band structure based on the local value of the strain in a pyramidal quantum dot. (a) Bands along the 001 direction, through the center of the island. (b) Bands along the 100 direction, through the base of the island. Reproduced with permission from Pryor (1998)

of the energies of the heavy and light holes, shown in Figure 19a, is an indication of the variation of the strain from biaxially tensile at the bottom of the dot to biaxially compressive at the top.

## 5.2 OPTICAL SELECTION RULES FOR QUANTUM DOTS

One of the first issues to address is the potential modification of the selection rules for quantum dots from the bulk or quantum well selection rules described in Chapter 4. These selection rules can help determine whether optical initialization or readout of a quantum dot quantum bit will be an effective approach. They will also help understand the properties of spin-light-emitting-diodes (spin-LED's) based on quantum dots. This may help optimize spin-LED's so they could be used to electrically initialize spins in quantum dots for quantum computation. Without a clear understanding of the selection rules one may not know if the polarization efficiency of an LED reflects the efficiency of spin transport and injection in the device, or simply the optical selection rules.

For hole spin injection into quantum wells for emission along the in-plane direction (Ohno et al., 1999b; Kohda et al., 2001; Johnston-Halperin et al., 2002; Young et al., 2002) the selection rules are somewhat controversial. Less is known about the shape and configuration of quantum dots than is known about quantum well structure, so one might worry whether it is possible to properly interpret the results from spin-LED's incorporating dots. Fortunately it is possible to calculate the spin-photon conversion efficiency of these dots, including the symmetry and strain of the dot material, and make quantitative statements about the selection rules for dots of definite size and shape.

Recent experiments (Chye et al., 2002) have demonstrated a spin-LED in which spin polarized carriers are injected into and recombine within InAs/GaAs self-assembled quantum dots (SAQDs). The emitted light is partially circularly

polarized, with the degree of polarization providing a measure of the spin in the SAQDs. The conversion of electron spin to photon polarization is filtered through the selection rules associated with the quantum well or dot. In Chye et al. (2002), spin polarized electrons or holes were injected along the [001] growth direction from a (Ga,Mn)As layer that was spin polarized along [110]. The light emitted along the [110] direction was found to be only  $\approx 1\%$  circularly polarized, suggesting a small spin polarization within the SAQD. However, due to the selection rule uncertainty, a small photon polarization does not necessarily mean that the spin polarization within the SAQD was small.

Pryor and Flatté (2003) calculated the circular polarization dependence of dipole recombination from spin polarized states within a self-assembled InAs/GaAs quantum dot to provide a measure of the efficiency with which spin polarized SAQD states are converted into circularly polarized photons. Calculations were done for a range of sizes and shapes. The polarization was independent of whether the injected spin polarized carriers are electrons or holes. The results showed that the SAQD geometry and emission direction strongly influenced the observed circular polarization, which varied from 0 to  $\approx 20\%$  (for 100% polarized carriers). For a lens-shaped SAQD there is a nonzero polarization for directions perpendicular to the growth direction only if the SAQD is elongated so as to break azimuthal symmetry. That elongation is indicated by  $e$ , which is the ratio of the semi-major to semi-minor axes of the dot footprint. Measuring along the growth direction, however, gives near unity conversion of spin to photon polarization, and is the least sensitive to uncertainties in SAQD geometry.

The situation considered by Pryor and Flatté (2003) had the electron spin polarized along a direction  $d$  and the emitted light observed along the same direction. The emitted light was characterized by its degree of polarization defined by

$$P_d = \frac{(I_d^+ - I_d^-)}{(I_d^+ + I_d^-)}, \quad (49)$$

where  $I_d^\pm$  is the intensity of light with  $\pm$  helicity. The InAs SAQD was taken to be an ellipsoidal cap, elongated along [110] and surrounded by GaAs.

Pryor and Flatté (2003) calculated ground state electron and hole wave functions using eight-band strain-dependent  $\mathbf{k}\cdot\mathbf{p}$  theory in the envelope approximation, by a method that has been described above (Pryor et al., 1997; Pryor, 1998). All wave functions were computed numerically on a real space grid with spacing set to the unstrained lattice constant of GaAs. Since strain and confinement split the HH/LH degeneracy, all levels are doubly degenerate, with states that may be denoted  $|\psi\rangle$  and  $T|\psi\rangle$ , which are time-reverses of each other. Because the wave functions were computed with a spin-independent Hamiltonian, the state  $|\psi\rangle$  has a random spin orientation. Spin polarized states were constructed by taking a linear combination of the states comprising the doublet, and adjusting the coefficient so

as to maximize the expectation value of the pseudospin operator projected onto a direction  $d$ . That is, the complex number  $a$  that maximizes

$$\frac{[\langle \psi | + a^* \langle \psi | T] \hat{\mathbf{d}} \cdot \mathbf{S} [|\psi\rangle + aT|\psi\rangle]}{(1 + |a|^2)} \quad (50)$$

was found, where the pseudospin operator in the eight-band model is given by

$$\mathbf{S} = \begin{pmatrix} \sigma_{\Gamma_6} & 0 & 0 \\ 0 & \mathbf{J}_{\Gamma_8} & 0 \\ 0 & 0 & \sigma_{\Gamma_7} \end{pmatrix} \quad (51)$$

and  $\sigma$  and  $\mathbf{J}$  are the spin-1/2 and spin-3/2 angular momentum operators respectively. The spin-polarized states found this way are the eigenstates in a small magnetic field oriented parallel to  $d$ , i.e. for  $\mathbf{B} < (mc/e\hbar)\Delta E$ , where  $\Delta E$  is the energy splitting of the top two orbital conduction states (for electrons) or valence states (for holes). For the systems considered the minimum  $\Delta E$  is 20 meV (for holes), thus  $\mathbf{B} < 100$  T. Coulomb interaction between the electron and hole does not appreciably change the results (Pryor and Flatté (2003) find a maximum change in the polarization of 0.05  $P$ ).

For spin-polarized electrons and unpolarized holes, the intensity for emission of circularly polarized light is given by

$$I_d^\pm = |\langle \psi_v | \hat{\epsilon}_d^\pm \cdot \mathbf{p} | \psi_c \rangle|^2 + |\langle \psi_v | T \hat{\epsilon}_d^\pm \cdot \mathbf{p} | \psi_c \rangle|^2, \quad (52)$$

where  $|\psi_v\rangle$  and  $|\psi_c\rangle$  are the conduction and valence states with spin oriented along  $\hat{\mathbf{d}}$ ,  $\mathbf{p}$  is the momentum operator, and  $\hat{\epsilon}_d^\pm$  is the circular polarization vector for  $\pm$  helicity with propagation along the direction  $d$ . The corresponding expression for spin polarized holes and unpolarized electrons is

$$I_d^\pm = |\langle \psi_v | \hat{\epsilon}_d^\pm \cdot \mathbf{p} | \psi_c \rangle|^2 + |\langle \psi_v | \hat{\epsilon}_d^\pm \cdot \mathbf{p} T | \psi_c \rangle|^2. \quad (53)$$

However, since  $T$  and  $\mathbf{p}$  anticommute, Eqs. (52) and (53) give identical results.

For axially symmetric dots ( $e = 1$ ) the polarization is zero, but increases as the dots become more elongated. The polarization also increases with increasing  $E_g$  with all other parameters held fixed. Finally, for a fixed elongation and fixed band gap, shorter dots have a larger polarization. Taken together, these indicate a general trend that the larger deviations from spherical symmetry result in larger polarization, whether comparing dimensions in the [110] vs [1̄10] or [001] vs [110].

The magnitude of the polarization is of great interest, since the experimentally observed polarizations were only on the order of 1%. For the geometries considered, Pryor and Flatté (2003) found  $P_{[110]} \lesssim 23\%$ . Assuming nominal values  $e = 1.2$ ,  $h = 2.3$ , and  $E_g = 1.25$  eV Figure 20 shows that for 100% polarized

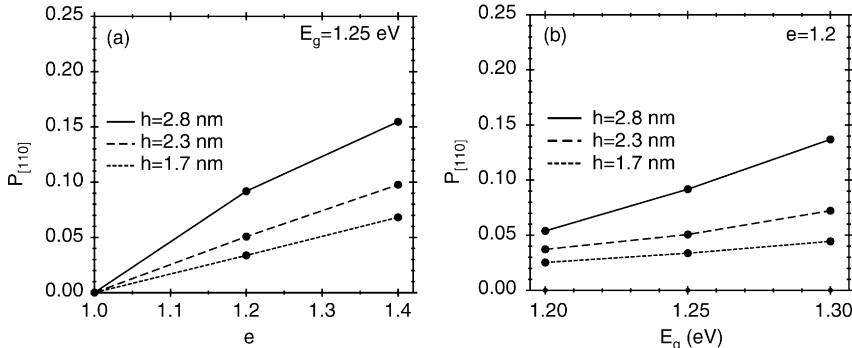


Figure 20. (a) Polarization along [110], as a function of elongation. (b) Polarization along [110], as a function of band gap. Reproduced with permission from Pryor and Flatté (2003)

carriers, the light should be 5% circular polarized. This value of 0.05 for the conversion efficiency suggests the observed 1% circular polarization (Chye et al., 2002) was generated by carriers that were  $(1/0.05)\% = 20\%$  polarized. As the polarization's dependence on elongation is roughly linear, an average elongation for a dot ensemble would produce an average polarization roughly given by Figure 20 as well.

### 5.3 THE RESPONSE OF QUANTUM DOT SPINS TO A MAGNETIC FIELD

The Landé  $g$  factor of electron and hole spins in quantum dots is also a topic of considerable interest. Confinement of the electrons and holes in the quantum dots modifies the  $g$  factors. As the confinement can be changed by an applied electric field the  $g$  factors can also be changed with a gate field. An experimental demonstration (Kato et al., 2003) of driving spin resonance with this effect in quantum wells suggests that single spins can also be manipulated in quantum dots this way. An elegant method of manipulating these spins utilizes the tensor nature of the  $g$  factor, and involves modifying the relative values of the tensor along different directions. The Hamiltonian for such a spin would be

$$H = \mu \mathbf{B} \cdot \mathbf{g} \cdot \mathbf{S} = \hbar \boldsymbol{\Omega} \cdot \mathbf{S}, \quad (54)$$

where  $\boldsymbol{\Omega} = \mathbf{B} \cdot \mathbf{g}$ . Thus even for a static applied magnetic field, if the components of the  $g$  tensor change in relative magnitude the precession vector for the spin  $\boldsymbol{\Omega}$  could alter its direction. Representing this as a static component to  $\boldsymbol{\Omega}$  and a time-dependent transverse component produces the same phenomenon of spin resonance that can be achieved with a time-dependent magnetic field and a static  $\mathbf{g}$ .

The electron  $g$  factor has been measured optically (Gupta et al., 1999; Bayer et al., 1999; Goñi et al., 2000; Tischler et al., 2002) and electrically (Kouwenhoven et al., 2001; Medeiros-Ribeiro et al., 2002; Hanson et al., 2003; Medeiros-Ribeiro

et al., 2003). For large dots (Darnhofer et al., 1994; Kouwenhoven et al., 2001; Hanson et al., 2003; Valín-Rodríguez et al., 2004), such as those defined lithographically (Kouwenhoven et al., 2001) or by electrical gates (Hanson et al., 2003), the magnetic fields of interest are usually large enough that the magnetic length is smaller than the dot diameter. In this limit the  $g$  factors are closely related to those of quantum wells, and theory (Valín-Rodríguez et al., 2004) appears to agree with experiment (Hanson et al., 2003). The theoretical situation is much less satisfactory for small dots—asymmetric structures grown by self assembly in the molecular beam epitaxy (MBE) growth process or spherical nanocrystals grown by chemical synthesis. Although several phenomena known to affect  $g$ -factors in quantum wells (Ivchenko and Pikus, 1997; Winkler, 2003) have been explored in quantum dots (Kiselev et al., 1998; Krasny et al., 2001; Nenashov et al., 2003; Prado et al., 2003; Rodina et al., 2003; Prado et al., 2004; Schrier and Birgitta Whaley, 2003), the electronic states in dots are discrete, and thus differ qualitatively from semiconductors with unbounded motion in one or more directions (Bimberg et al., 1998).

Semiconductor quantum dots also have fully coherent orbital electronic states with very long-lived spin coherence (Gupta et al., 1999), so the physics of their  $g$  factors is very different from that of metallic nanoparticles (Brouwer et al., 2000; Matveev et al., 2000; Petta and Ralph, 2002) (whose  $g$  factors are dominated by effects from incoherent orbital scattering and spin scattering). The orbital coherence of semiconductor quantum dot wavefunctions makes many dot properties, such as the sharply-peaked optical transitions, resemble those of atoms more than bulk semiconductors. If quantum dots are considered as “artificial atoms” and approached with techniques developed for magnetic atom dopants in solids (Van Vleck, 1932), then the relevant quantity is the ratio of the energy splitting between different angular momentum states to the spin-orbit interaction, and for a strong confining potential the  $g$  factor of dots should approach 2.

Pryor and Flatté (2006a) showed that the  $g$  factor of a ground state electron or hole in a quantum dot depends significantly on an atom-like property: the quenching of orbital angular momentum through quantum confinement. In bulk semiconductors the conduction-band  $g$  factor is (Roth et al., 1959),

$$g = 2 - \frac{2E_P\Delta}{3E_g(E_g + \Delta)}, \quad (55)$$

where  $E_g$  is the band gap,  $\Delta$  is the spin-orbit coupling,  $E_P = 2\langle S|P|X\rangle^2/m$  is the Kane energy involving S-like and P-like Bloch functions  $\langle S|$  and  $\langle X|$  respectively (Ivchenko and Pikus, 1997), and  $m$  is the free electron mass. For unstrained spherical InAs nanocrystals with hard wall boundary conditions only  $E_g$  changes, yet Eq. (55) is a very poor predictor of  $g$  factors in these dots (Figure 21). Similar conclusions can be obtained for InAs dots formed by self-assembly in MBE on

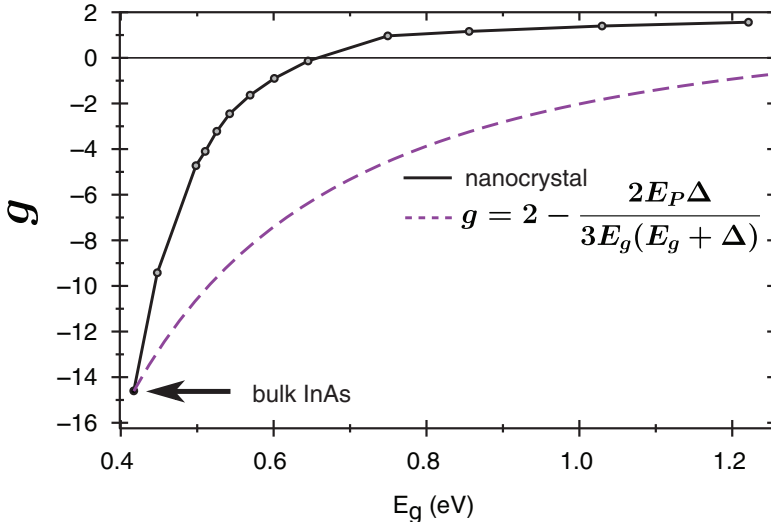


Figure 21. Electron  $g$  factor for a spherical unstrained InAs quantum dot embedded in vacuum. The dashed line indicates the result of Eq. (55) and the solid line the calculations in Pryor and Flatté (2006a). Reproduced with permission from Pryor and Flatté (2006a)

GaAs substrates (Pryor and Flatté, 2006a). Thus the bulk-like approach to  $g$  factors in these quantum dots, averaging the  $g$  factors over the dot and barrier material (Kiselev et al., 1998; Rodina et al., 2003), also fails. The competing influence of atom-like and bulk-like effects predict that the growth-direction electron  $g$  factor increases with increasing dot size, whereas considering only bulk-like effects leads to the opposite result. The results in Pryor and Flatté (2006a) agree with recent experiments on electron  $g$  factors (Medeiros-Ribeiro et al., 2003).

Pryor and Flatté (2006a) presented calculations of quantum dot  $g$  factors at  $T = 0$  K using eight-band strain dependent  $\mathbf{k} \cdot \mathbf{p}$  theory in the envelope approximation with finite differences on a real space grid (Pryor, 1998).  $g$  came from the spin splitting in a magnetic field of  $|B| = 0.1$  T and the sign of  $g$  from the spin direction of the lower energy state (parallel or anti-parallel to  $\vec{B}$ ). Material parameters were taken from Vurgaftman et al. (2001).

The magnetic field was included by coupling to both the envelope function and the electron spin. The envelope was coupled to  $\vec{B}$  by making all difference operators covariant using the standard prescription for introducing gauge fields on a lattice. For example,

$$\frac{\psi(\vec{r} + \epsilon\hat{x}) - \psi(\vec{r} - \epsilon\hat{x})}{2\epsilon} \rightarrow \frac{\psi(\vec{r} + \epsilon\hat{x})U_x(\vec{r}) - \psi(\vec{r} - \epsilon\hat{x})U_x^\dagger(\vec{r} - \epsilon\hat{x})}{2\epsilon}, \quad (56)$$

where  $\epsilon$  is the grid spacing and  $U_x(\vec{r})$  is the phase acquired by an electron hopping from the site at  $\vec{r}$  to the site at  $\vec{r} + \epsilon\hat{x}$ . The  $U$ 's were determined by

the requirement that transport around a plaquette produced the Aharonov–Bohm phase corresponding to the encircled flux, for example,

$$U_x(\vec{r})U_y(\vec{r} + \epsilon\hat{x})U_x^\dagger(\vec{r} + \epsilon\hat{y})U_y^\dagger(\vec{r}) = \exp(i\epsilon^2 B_\perp e/\hbar), \quad (57)$$

where  $B_\perp$  is the magnetic field component perpendicular to the plaquette. The electron spin was coupled to  $\vec{B}$  though a Pauli term for the Bloch functions, given by

$$H_s = \frac{\mu_B}{2} \vec{B} \cdot \begin{pmatrix} 2\vec{\sigma} & 0 & 0 \\ 0 & \frac{4}{3}\vec{J} & 0 \\ 0 & 0 & \frac{2}{3}\vec{\sigma} \end{pmatrix}, \quad (58)$$

where  $\mu_B$  is the Bohr magneton and  $\vec{\sigma}$  and  $\vec{J}$  are the spin matrices for spin 1/2 and 3/2 respectively. The  $g$  factors for the Bloch functions are 2,  $\frac{4}{3}$ , and  $\frac{2}{3}$  for the conduction, valence, and spin-orbit bands respectively. The Bloch function  $g$  factors are determined solely by the angular momentum of the Bloch states.

To see the origin of the discrepancy between the Roth expression of Eq. (55) and the results in Figure 21 consider the known origin of the effective  $g$  for conduction electrons in a bulk semiconductor (Roth et al., 1959). When a magnetic field is applied, the orbital part of the wavefunction is modified into Landau levels, corresponding to quantized orbital angular momentum along the axis of the magnetic field. In a single band model the Landau levels' orbital angular momentum comes from the envelope function alone. When the conduction and valence bands are coupled, there is also a contribution from the valence Bloch functions, which have a significant spin-orbit coupling. The Zeeman energy now splits the lowest Landau level into two spin-polarized Landau levels, one with spin parallel to the quantized orbital angular momentum and one antiparallel. Although the bare  $g = 2$  lowers the energy of the parallel spin state and raises that of the antiparallel state, the spin-orbit interaction preferentially aligns spin *antiparallel* to the orbital angular momentum. When that effect is absorbed into an effective  $g$ , it makes  $g < 2$ .

To isolate the effects of angular momentum quenching from those due to strain and spherical symmetry breaking Figure 21 shows results from unstrained spherical InAs nanocrystals (Pryor and Flatté, 2006a). The calculations were done with a high barrier (10 eV) to avoid any leakage of the wavefunction outside the dot. For large dots ( $E_g \sim 0.41$  eV) the calculation agrees with the bulk-like formula (Roth et al., 1959), however it rapidly diverges from Roth et al. (1959) for smaller dots; when the confinement energy equals the bulk band gap of InAs the deviation from  $g - 2$  predicted by Eq. (55) is six times larger than the actual value. Hole  $g$  factors for these nanocrystals show similar evidence of orbital angular momentum quenching. Note that the quenching of orbital angular momentum for the electron and hole states is compatible with the high fidelity selection rules for

generating spin-polarized carriers in dots with optical means (Pryor and Flatté, 2003), because the optical transitions connect states with specific angular momentum (valence and conduction) whereas the  $g$  factors probe how much angular momentum admixture is possible for  $B \neq 0$ .

#### 5.4 SPIN-AC STARK EFFECTS IN QUANTUM DOTS

The spin-AC Stark effect permits the optically controlled spin manipulation of individual spin states. Although it has been seen in atoms (Rosatzin et al., 1990), the much larger oscillator strengths of quantum dots should permit much larger effects. In a spin-selective AC Stark effect a quantum dot is illuminated with a single intense pulse of circularly-polarized nonresonant light. Such a pulse shifts the energies of dot states, and due to differing transition matrix elements the two spin states are shifted differently. Hence this pulse produces a splitting of the two lowest energy conduction states, even when they are coherently occupied by one electron (Pryor and Flatté, 2006b). The splitting of these two states (spin-up and spin-down) can be viewed as an optically-induced pseudo-magnetic field ( $\vec{B}_{eff}$ ) oriented along the propagation direction of the incident light. Direct application of this approach to quantum computing is clear, for one well-known physical realization of a single qubit operation is a magnetic field applied to a spin for a definite period of time. As this pseudo magnetic field can be applied in the absence of a real magnetic field, resonant oscillation of this precessing field is not required.

Spin-splittings of states in undoped CdSe quantum dots (Gupta and Awschalom, 2001; Gupta et al., 2002) and coherent manipulation of ensembles of spins in ZnMnSe quantum wells (Gupta et al., 2001) have been demonstrated experimentally. Early theoretical considerations of the AC Stark effect (Cohen-Tannoudji and Dupont-Roc, 1972; Combescot and Combescot, 1988; Cohen-Tannoudji et al., 1998), however, focused on non-spin-selective shifts of energy levels. Recently Pryor and Flatté (2006b) showed that the spin-AC Stark effect (1) produces coherent rotations of electron spin in quantum dots with one electron, (2) the rotation angle can exceed  $\pi$  for reasonable experimental parameters, and (3) the error rates are tolerable for quantum computation.

The AC Stark effect with unpolarized light is a nonlinear effect whereby light with photon energy tuned near to the absorption transition between two states induces a level repulsion between the two states (Cohen-Tannoudji and Dupont-Roc, 1972; Cohen-Tannoudji et al., 1998). In perturbation theory (Combescot and Combescot, 1988) this level repulsion depends on  $I f / \delta$ , where  $I$  is the light intensity,  $f$  is the oscillator strength of the transition, and  $\delta$  is the detuning of the photon energy from the transition energy. When circularly polarized light illuminates a transition from the first valence state pair to the first conduction

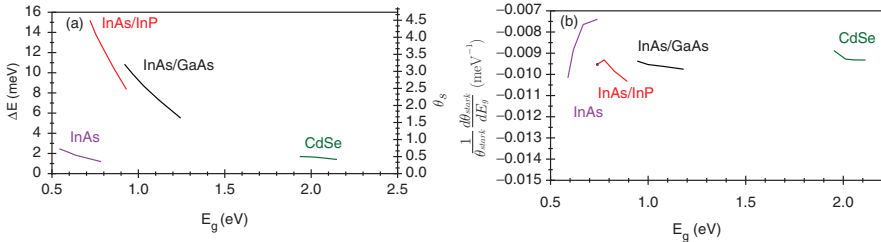


Figure 22. (a) Stark splittings as a function of the bandgap for a detuning of 30 meV for InAs, InAs/InP, InAs/GaAs, and CdSe quantum dots. The angle  $\theta_s = \Delta E \delta t / \hbar$  is for an incident 200 fs pulse with  $10^9$  W/cm<sup>2</sup>. (b) Sensitivity of  $\theta_s$  to variations in the bandgap as a function of bandgap for detuning of 100 meV. Reproduced with permission from Pryor and Flatté (2006b)

state pair in a crystal with spin-orbit interaction the oscillator strengths of the transitions differ considerably; this is the source of the effective spin splitting of the conduction state pair.

Pryor and Flatté (2006b) calculated optical Stark shifts non-perturbatively using a restricted basis of quantum dot wave functions calculated with eight-band  $k \cdot p$  theory in the envelope approximation. Because of the larger bandgap and lack of strain, CdSe calculations were performed with a single-band model for the conduction band, and a four-band model for the valence band. The CdSe calculations were done for the zincblende form, and all material parameters were taken from Madelung et al. (1982).

Pryor and Flatté (2006b) examined the effect of dot size on the spin splitting. Shown in Figure 22a are the splittings for a detuning of 30 meV for four systems. For spin manipulation it is useful to consider the precession angle associated with a light pulse of duration  $\delta t$ , given by  $\theta_s = \Delta E \delta t / \hbar$  where  $\Delta E$  is the Stark spin splitting between up and down conduction states. In the results that follow, the Stark splittings are given in meV along with the corresponding  $\theta_s$  for a 200 fs pulse with power density  $10^9$  W/cm<sup>2</sup>. The ~2 meV spin splitting seen in CdSe CQDs agrees with that measured experimentally in undoped dots (Gupta and Awschalom, 2001).

Bit errors may arise from a variety of sources, such as nonlinear effects and free-carrier excitation (Gupta et al., 2001). Pryor and Flatté (2006b) focused on bit errors due to a persistent problem with quantum dot systems, nonzero linewidths. For measurements on an ensemble of dots, inhomogeneities in the dot size will yield a different rotation angle for different dots. For a quantum computer, in which individual dots will be selected, the finite line width of an individual state will also cause some uncertainty in  $\theta_s$ . To address this question, Pryor and Flatté (2006b) calculated numerical estimates of

$$\frac{1}{\Delta E} \frac{\partial \Delta E(E_g, \hbar\omega)}{\partial E_g} = \frac{1}{\theta_s} \frac{\partial \theta_s(E_g, \hbar\omega)}{\partial E_g}, \quad (59)$$

as shown in Figure 22b for a detuning of 100 meV. The results of Figure 22b may be used to estimate the uncertainty in the rotation angle,  $\Delta\theta_s$ . For example, an ensemble measurement of InAs/InP dots with an inhomogeneous linewidth of 50 meV would give  $\Delta\theta_s \approx 0.5$  for a  $\pi$ -pulse, which should be sufficient to permit observation of a spin echo. For a single dot with a linewidth of 0.1 meV,  $\Delta\theta_s \approx 0.001$ , corresponding to a bit error rate of  $10^{-6}$ . This is sufficiently small for quantum error correction algorithms to apply (desirable error thresholds have been estimated (Preskill, 1998) at  $10^{-5} - 10^{-6}$ ).

## 6 Spin-Selective Devices

One of the important quantum information capabilities proposed and developed is the capability of teleporting quantum information. Leuenberger et al. (2005) proposed a teleportation scheme for an arbitrary number of electronic qubits that does not require an intermediate electronic qubit, or the use of external lasers to implement a phase gate. Instead of generating and measuring Bell states between the electronic qubits, this scheme relies on entangling both of the qubits with a single photon, yielding three-particle entanglement (a Greenberger–Horne–Zeilinger (GHZ) state (Greenberger et al., 1989)) of the qubit-photon-qubit Hilbert space. Any qubit that can be entangled with a photon can be used, but for specificity Leuenberger et al. (2005) considered qubits encoded in the electron spin of individual quantum dots. The establishment of spin–photon entanglement can then occur naturally through conditional Faraday rotation in a microcavity. The entanglement of the destination qubit and the photon can be performed first, and this photon can be retained at the origin before it is entangled with the origin qubit, thus this procedure is teleportation, not quantum transmission. The sending of the photon from the destination to the origin, after it is entangled with the destination qubit, is the step corresponding to the distribution of EPR pairs in teleportation. The EPR pairs of Leuenberger et al. (2005), however, are a hybrid consisting of an entangled electronic spin and photon polarization. Teleportation can then be implemented using only single-photon measurements: measurement of the polarization of the photon entangled with both qubits, and measurement of the spin orientation of the origin qubit via a single photon.

Described below in detail is the teleportation scheme of Leuenberger et al. (2005) for one qubit. Consider one excess electron in one quantum dot in a general single-spin state  $|\psi_e^{(1)}\rangle = \alpha|\uparrow\rangle + \beta|\downarrow\rangle$ , where the quantization axis is the  $z$  axis. The photon propagating in the  $-z$  direction is initially linearly polarized in the  $x$  direction, and interacts first with the destination spin, which is initialized parallel to  $x$ . Thus the destination spin–photon wavefunction initially is  $|\psi_{pe'}^{(1)}\rangle = |\leftrightarrow\rangle|\leftarrow'\rangle$ . The orientation of the spin affects the possible virtual processes excited by the photon, two of which are shown in Figure 23. For spin- $\uparrow$ , light of  $\sigma_{(z)}^+$  polarization

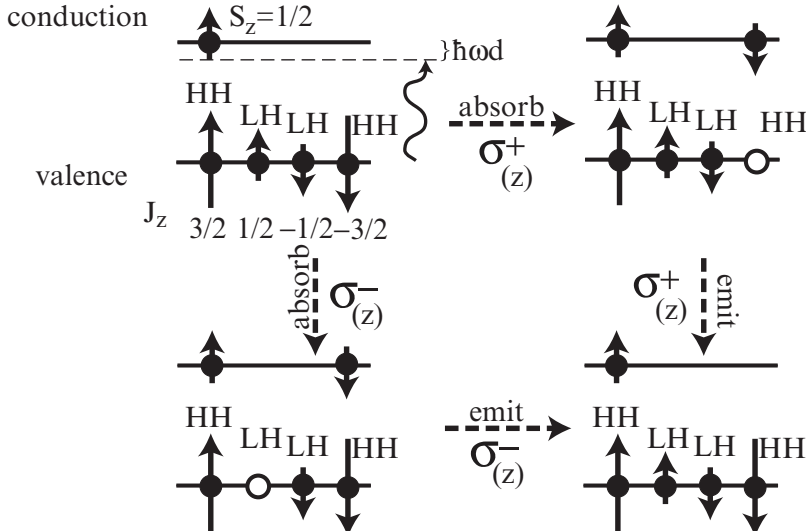


Figure 23. Selection rules for a photon propagating in the  $z$  direction and an excess spin- $\uparrow$  electron in the dot.  $\sigma_{(z)}^+$  can be virtually absorbed (upper right) by exciting an electron and a heavy hole, and  $\sigma_{(z)}^-$  by exciting an electron and a light hole (lower left).  $\hbar\omega_d$  is the detuning of the nonresonant photon from the transition energy. Reproduced with permission from Leuenberger et al. (2005)

excites an electron and heavy hole (upper right, Figure 23), and light of  $\sigma_{(z)}^-$  polarization excites an electron and a light hole (lower left, Figure 23). In both cases the selection rules and Pauli blocking force the light subsequently emitted from electron–hole recombination to have the same polarization as was absorbed, and the final occupations of electron states in the dot (lower right, Figure 23) are the same as the initial occupations. These virtual processes have different probabilities, however, and this leads to Faraday rotation: a phase shift  $e^{iS_0^{hh}}$  of  $\sigma_{(z)}^+$  and  $e^{iS_0^{lh}}$  of  $\sigma_{(z)}^-$ . If, however, the spin were  $\downarrow$  instead the phase shift of  $\sigma_{(z)}^+$  light would be  $e^{iS_0^{lh}}$  and of  $\sigma_{(z)}^-$  would be  $e^{iS_0^{hh}}$ . Thus there is a *conditional Faraday rotation* of the components of the electron–photon state depending on the photon polarization and spin orientation.

After the interaction of the initially unentangled photon with the spin in the quantum dot, the resulting electron–photon state is

$$\left| \psi_{pe'}^{(1)} \right\rangle = e^{iS_0^{hh}} \left| \psi_{hh}^{(1)} \right\rangle + e^{iS_0^{lh}} \left| \psi_{lh}^{(1)} \right\rangle, \quad (60)$$

where  $\left| \psi_{hh}^{(1)} \right\rangle = (\left| \sigma_{(z)}^+ \right\rangle |\uparrow'\rangle + \left| \sigma_{(z)}^- \right\rangle |\downarrow'\rangle)/2$  originates from the virtual process where a photon creates an electron and a heavy hole, and  $\left| \psi_{lh}^{(1)} \right\rangle = (\left| \sigma_{(z)}^- \right\rangle |\uparrow'\rangle + \left| \sigma_{(z)}^+ \right\rangle |\downarrow'\rangle)/2$  originates from the virtual process where the photon creates an

electron and a light hole. Both  $|\psi_{hh}^{(1)}\rangle$  and  $|\psi_{lh}^{(1)}\rangle$  are EPR states. The photon state  $|\varphi\rangle = \cos\varphi|leftrightarrow\rangle + \sin\varphi|up-down\rangle$  has a linear polarization rotated by  $\varphi$  around the  $z$  axis with respect to the state  $|leftrightarrow\rangle$  of linear polarization in the  $x$  direction, and can be written  $|\varphi\rangle = (e^{-i\varphi}|\sigma_{(z)}^+\rangle + e^{i\varphi}|\sigma_{(z)}^-\rangle)/\sqrt{2}$ . Consequently,

$$|\psi_{pe'}^{(1)}\rangle = \frac{e^{i(S_0^{hh}+S_0^{lh})/2}}{\sqrt{2}} (|-S_0/2\rangle|\uparrow'\rangle + |+S_0/2\rangle|\downarrow'\rangle), \quad (61)$$

where  $S_0 = S_0^{hh} - S_0^{lh}$ . Thus the spin–photon interaction produces a conditional single-photon Faraday rotation around the  $z$  axis by the angle  $\pm S_0/2$ . If  $S_0 = \pi/2$ , the linear polarization of the incoming photon is rotated  $-\pi/4$  by the spin up component, and at the same time is rotated  $+\pi/4$  by the spin down component, yielding two orthogonal photon polarizations. Thus  $|\psi_{pe'}^{(1)}\rangle = (|\nwarrow\rangle|\uparrow'\rangle + |\swarrow\rangle|\downarrow'\rangle)/\sqrt{2}$ , which is maximally entangled. In order to enhance the spin–photon interaction sufficiently to achieve  $S_0 = \pi/2$ , each quantum dot should be placed in its own microcavity. Using a switchable cavity permits the precise control of the Faraday rotation angle  $S_0/2$  necessary for high fidelity teleportation. After interacting with a spin at a destination ( $D'$ ) the photon is sent to an origin ( $D$ ), and can be retained as a resource for teleportation from  $D$  to  $D'$  until the spin at  $D'$  decoheres. For coherence times of 100 ns (Kikkawa and Awschalom, 1998) the maximum teleportation distance (determined by the speed of light) would be  $\sim 15$  m and for 10 ms (Kroutvar et al., 2004) it is  $1.5 \times 10^6$  m.

When it is time to teleport the spin at  $D$  to  $D'$  the photon is permitted to interact with the quantum dot at  $D$ , giving rise to a GHZ state in the hybrid spin–photon–spin system. After this interaction

$$\begin{aligned} |\psi_{epe'}^{(1)}\rangle = & e^{i(S_0^{hh}+S_0^{lh})/2} (\alpha|\uparrow\rangle|-S_0/2-\pi/4\rangle|\uparrow'\rangle + \alpha|\uparrow\rangle|-S_0/2+\pi/4\rangle|\downarrow'\rangle \\ & + \beta|\downarrow\rangle|+S_0/2-\pi/4\rangle|\uparrow'\rangle + \beta|\downarrow\rangle|+S_0/2+\pi/4\rangle|\downarrow'\rangle)/\sqrt{2}. \end{aligned} \quad (62)$$

Choosing  $S_0 = \pi/2$ ,

$$|\psi_{epe'}^{(1)}\rangle = [|\uparrow\rangle(-\alpha|\uparrow\rangle|\uparrow'\rangle + \beta|\downarrow\rangle|\downarrow'\rangle) + |\downarrow\rangle(\alpha|\uparrow\rangle|\downarrow'\rangle + \beta|\downarrow\rangle|\uparrow'\rangle)]/\sqrt{2}. \quad (63)$$

Changing to the  $S_x$  representation for the spin at  $D$  yields

$$\begin{aligned} |\psi_{epe'}^{(1)}\rangle = & \{|\uparrow\rangle[|\leftarrow\rangle(-\alpha|\uparrow'\rangle + \beta|\downarrow'\rangle) + |\rightarrow\rangle(-\alpha|\uparrow'\rangle - \beta|\downarrow'\rangle)] \\ & + |\downarrow\rangle[|\leftarrow\rangle(\beta|\uparrow'\rangle + \alpha|\downarrow'\rangle) + |\rightarrow\rangle(\beta|\uparrow'\rangle - \alpha|\downarrow'\rangle)]\}/\sqrt{2}. \end{aligned} \quad (64)$$

Performing the correct measurements completes the teleportation. If the linear polarization of the photon is measured first, then depending on the two initial spin orientations [see Eq. (63)], collapse of the wavefunction leaves the qubits

at  $D$  and at  $D'$  in one of the four Bell states. After performing a single-spin measurement in the  $x$  direction of the spin at  $D$  (which, as described below, can be done with a single photon), the spin state at  $D'$  is projected onto [see Eq. (64)]  $|\psi_{e1}^{(1)}\rangle = -\alpha|\uparrow'\rangle + \beta|\downarrow'\rangle$ ,  $|\psi_{e2}^{(1)}\rangle = -\alpha|\uparrow'\rangle - \beta|\downarrow'\rangle$ ,  $|\psi_{e3}^{(1)}\rangle = \beta|\uparrow'\rangle + \alpha|\downarrow'\rangle$ , or  $|\psi_{e4}^{(1)}\rangle = \beta|\uparrow'\rangle - \alpha|\downarrow'\rangle$  with equal probability. These projections correspond exactly to the states obtained in Bennett et al. (1993). After communicating classically the outcome of the measurement of the linear polarization of the photon and  $D$ 's spin orientation along  $S_x$  to  $D'$ , the original spin state of  $D$  can be reconstructed at  $D'$  and teleportation is complete. The same amount of classical communication (two bits) is required for this approach as was required in Bennett et al. (1993). However, no intermediate electronic qubit was required, and the measurements are simply performed with single photons.

Faraday rotation to entangle the photon and electron spin [Eq. (60)] also provides the way to measure the spin with a single photon. Leuenberger et al. (2005) assumes that the microcavities have an additional resonant mode at a different frequency for photons propagating in the  $x$  direction. Equation (60) shows that if the spin on the quantum dot points in the  $+x$  ( $-x$ ) direction, this incoming linearly polarized photon is converted into an outgoing circularly polarized photon  $\sigma_{(x)}^+$  ( $\sigma_{(x)}^-$ ). Measuring the circular polarization of the photon after it escapes yields the spin orientation along  $x$ . Electrical single-spin measurements at  $D$  could use instead a single electron transistor (SET), converting the spin information to charge information (Loss and DiVincenzo, 1998; Friesen et al., 2004). Each of the steps along the way could be performed with high fidelity (time-correlated single photon counting permits a counting efficiency close to one (Becker et al., 2001)).

## 7 Conclusion

This chapter has described several properties of spin that may be relevant to the successful achievement of high-fidelity quantum operations within a quantum computer. The transport and persistence of spin orientation in an ensemble has been described, which may assist in the preparation of highly oriented spins to initialize a quantum computer. Approaches to accurately calculate the spin-dependent electronic structure of bulk, quantum well, and quantum dot nanostructures have been described. Methods of initialization, manipulation, and detection of coherence in ionic degrees of freedom have been identified. The use of ionic spins may permit highly uniform systems of physical qubits to be generated. Techniques for initializing and optically manipulating spins in quantum dots have been presented, along with the physical origin of the Landé  $g$  factor in quantum dots.

At this point it appears too early to know what approach will most rapidly approach a scalable quantum computer in the solid state. Some approaches started

earlier, such as manipulation via the exchange interaction in lithographic quantum dots, are now making rapid progress (Petta et al., 2005). The seven years between the proposal of a quantum dot architecture for a quantum computer (Loss and DiVincenzo, 1998) and the successful observation of single-spin decoherence times in a quantum dot ( $T_2^*$ , as they were in a nuclear spin ensemble) (Petta et al., 2005) provides some indication of the potential time between proposal and successful demonstration in the field of solid-state quantum computation.

## Acknowledgments

I would like to acknowledge D. D. Awschalom, T. F. Boggess, K. C. Hall, W. H. Lau, J. Levy, M. Leuenberger, J. T. Olesberg, C. E. Pryor, J.-M. Tang, and Z. G. Yu. This work was supported in part by DARPA, ARO, and ONR.

## References

- Aronov, A. G. and Pikus, G. E. (1976) Spin injection into semiconductors, *Fiz. Tekh. Poluprovodn.* **10**, 1177–1179, [Sov. Phys. Semicond. **10**, 698–700 (1976)].
- Arseev, P. I., Maslova, N. S., Panov, V. I., Savinov, S. V., and van Haesendonck, C. (2003) Many-Particle Interaction in Tunneling Spectroscopy of Impurity States on the InAs(110) Surface, *Pis'ma Zh. Éksp. Teor. Fiz.* **77**, 202–207, [JETP Lett. **77**, 172 (2003)].
- Awschalom, D. D., Samarth, N., and Loss, D. (eds.) (2002) *Semiconductor Spintronics and Quantum Computation*, Heidelberg, Springer Verlag.
- Barenco, A., Bennett, C. H., Cleve, R., DiVincenzo, D. P., Margolus, N., Shor, P., Sleator, T., Smolin, J. A., and Weinfurter, H. (1995) Elementary gates for quantum computation, *Phys. Rev. A* **52**, 3457–3467.
- Bayer, M., Kuther, A., Forchel, A., Gorbunov, A., Timofeev, V. B., Schäfer, F., Reithmaier, J. P., Reinecke, T. L., and Walck, S. N. (1999) Electron and Hole g Factors and Exchange Interaction from Studies of the Exciton Fine Structure in  $In_{0.60}Ga_{0.40}As$  Quantum Dots, *Phys. Rev. Lett.* **82**, 1748–1751.
- Becker, W., Bergmann, A., Koenig, K., and Tirlapur, U. (2001) Picosecond fluorescence lifetime microscopy by TCSPC imaging, *Proc. SPIE* **4262**, 414–419.
- Bennett, C. H. and DiVincenzo, D. P. (2000) Quantum information and computation, *Nature* **404**, 247–255.
- Bennett, C. H., Brassard, G., Crépeau, C., Jozsa, R., Peres, A., and Wootters, W. K. (1993) Teleporting an unknown quantum state via dual classical and Einstein-Podolsky-Rosen channels, *Phys. Rev. Lett.* **70**, 1895–1899.
- Bhat, R. D. R. and Sipe, J. E. (2000) Optically Injected Spin Currents in Semiconductors, *Phys. Rev. Lett.* **85**, 5432–5435.
- Bimberg, D., Grundmann, M., and Ledentsov, N. N. (1998) *Quantum Dot Heterostructures*, New York, Wiley.
- Boggess, T. F., Olesberg, J. T., Yu, C., Flatté, M. E., and Lau, W. H. (2000) Room-temperature electron spin relaxation in bulk InAs, *Appl. Phys. Lett.* **77**, 1333–1335.
- Brouwer, P. W., Waintal, X., and Halperin, B. I. (2000) Fluctuating Spin g-Tensor in Small Metal Grains, *Phys. Rev. Lett.* **85**, 369–372.

- Bychkov, Y. A. and Rashba, E. I. (1984) Oscillatory effects and the magnetic susceptibility of carriers in inversion layers, *J. Phys. C* **17**, 6039–6045.
- Cardona, M., Christensen, N. E., and Fasol, G. (1988) Relativistic band structure and spin-orbit splitting of zinc-blende-type semiconductors, *Phys. Rev. B* **38**, 1806–1827.
- Chye, Y., White, M. E., Johnston-Halperin, E., Gerardot, B. D., Awschalom, D. D., and Petroff, P. M. (2002) Spin injection from (Ga,Mn)As into InAs quantum dots, *Phys. Rev. B* **66**, 201301.
- Cohen-Tannoudji, C. and Dupont-Roc, J. (1972) Experimental Study of Zeeman Light Shifts in Weak Magnetic Fields, *Phys. Rev. A* **5**, 968–984.
- Cohen-Tannoudji, C., Dupont-Roc, J., and Grynberg, G. (1998) *Atom-Photon Interactions*, New York, Wiley.
- Combescot, M. and Combescot, R. (1988) Excitonic Stark Shift: A Coupling to "Semivirtual" Biexcitons, *Phys. Rev. Lett.* **61**, 117–120.
- Darnhofer, T., Broido, D. A., and Rössler, U. (1994) Dipole spectra of holes in quantum dots, *Phys. Rev. B* **50**, 15412–15415.
- Datta, S. and Das, B. (1990) Electronic analog of the electro-optic modulator, *Appl. Phys. Lett.* **56**, 665–667.
- DiVincenzo, D. P., Bacon, D., Kempe, J., Burkard, G., and Whaley, K. B. (2000) Universal quantum computation with the exchange interaction, *Nature* **408**, 339–342.
- Durkan, C. and Welland, M. E. (2002) Electronic spin detection in molecules using scanning-tunneling-microscopy-assisted electron-spin resonance, *Appl. Phys. Lett.* **80**, 458–460.
- D'yakonov, M. I. and Kachorovskii, V. Y. (1986) Spin relaxation of two-dimensional electrons in noncentrosymmetric semiconductors, *Soviet Phys. Semiconductors* **20**, 110–112.
- D'yakonov, M. I. and Perel', V. I. (1972) Spin relaxation of conduction electrons in noncentrosymmetric semiconductors, *Soviet Phys. Solid State* **13**, 3023–3026.
- Edelstein, V. M. (1990) Spin polarization of conduction electrons induced by electric current in two-dimensional asymmetric electron systems, *Solid State Commun.* **73**, 233–235.
- Elzerman, J. M., Hanson, R., van Beveren, L. H. W., Witkamp, B., Vandersypen, L. M. K., and Kouwenhoven, L. P. (2004) Single-shot read-out of an individual electron spin in a quantum dot, *Nature* **430**, 431–435.
- Fert, A. and Campbell, I. A. (1968) Two-Current Conduction in Nickel, *Phys. Rev. Lett.* **21**, 1190–1192.
- Fert, A. and Jaffrè, H. (2001) Conditions for efficient spin injection from a ferromagnetic metal into a semiconductor, *Phys. Rev. B* **64**, 184420.
- Flatté, M. E. and Byers, J. M. (2000) Spin Diffusion in Semiconductors, *Phys. Rev. Lett.* **84**, 4220–4223.
- Friesen, M., Tahan, C., Joynt, R., and Eriksson, M. A. (2004) Spin Readout and Initialization in a Semiconductor Quantum Dot, *Phys. Rev. Lett.* **92**, 037901.
- Goñi, A. R., Born, H., Heitz, R., Hoffmann, A., Thomsen, C., Heinrichsdorff, F., and Bimberg, D. (2000) Magnetoluminescence Study of Annealing Effects on the Electronic Structure of Self-organized InGaAs/GaAs Quantum Dots, *Jpn J. Appl. Phys.* **39**, 3907–3914.
- Greenberger, D. M., Horna, M. A., and Zeilinger, A. (1989) Going Beyond Bell's Theorem, In *Bell's Theorem, Quantum Theory, and Conceptions of the Universe*, Dordrecht, Kluwer Academic, pp. 73–76.
- Gruber, A., Dräbenstedt, A., Tietz, C., Fleury, L., Wrachtrup, J., and von Borczyskowski, C. (1997) Scanning Confocal Optical Microscopy and Magnetic Resonance on Single Defect Centers, *Science* **276**, 2012–2014.
- Gupta, J. A. and Awschalom, D. D. (2001) Spin precession and the optical Stark effect in a semiconductor-doped glass, *Phys. Rev. B* **63**, 085303.

- Gupta, J. A., Awschalom, D. D., Peng, X., and Alivisatos, A. P. (1999) Spin coherence in semiconductor quantum dots, *Phys. Rev. B* **59**, R10421–R10424.
- Gupta, J. A., Knobel, R., Samarth, N., and Awschalom, D. D. (2001) Ultrafast manipulation of electron spin coherence, *Science* **292**, 2458–2561.
- Gupta, J. A., Awschalom, D. D., Efros, A. L., and Rodina, A. V. (2002) Spin dynamics in semiconductor nanocrystals, *Phys. Rev. B* **66**, 125307.
- Hall, K. and Flatté, M. E. (2006) Performance of a spin-based insulated gate field effect transistor, *Appl. Phys. Lett.* **88**, 162503.
- Hall, K., Gündođdu, K., Altunkaya, E., Lau, W. H., Flatté, M. E., Boggess, T. F., Zinck, J. J., Barvosa-Carter, W. B., and Skeith, S. L. (2003a) Spin relaxation in (110) and (001) InAs/GaSb superlattices, *Phys. Rev. B* **68**, 115311.
- Hall, K., Lau, W. H., Gündođdu, K., Flatté, M. E., and Boggess, T. F. (2003b) Nonmagnetic semiconductor spin transistor, *Appl. Phys. Lett.* **83**, 2937–2939.
- Hall, K., Gündođdu, K., Hicks, J. L., Kocabay, A. N., Flatté, M. E., Boggess, T. F., Holabird, K., Hunter, A., Chow, D. H., and Zinck, J. J. (2005) Room-temperature electric-field controlled spin dynamics in (110) InAs quantum wells, *Appl. Phys. Lett.* **86**, 202114.
- Hanson, R., Witkamp, B., Vandersypen, L. M. K., van Beveren, L. H. W., Elzerman, J. M., and Kouwenhoven, L. P. (2003) Zeeman Energy and Spin Relaxation in a One-Electron Quantum Dot, *Phys. Rev. Lett.* **91**, 196802.
- Hanson, R., Kouwenhoven, L. P., Petta, J. R., Tarucha, S., and Vandersypen, L. M. K. (2006) Spins in few-electron quantum dots, cond-mat/0610433.
- Haynes, J. R. and Shockley, W. (1951) The Mobility and Life of Injected Holes and Electrons in Germanium, *Phys. Rev.* **81**, 835–843.
- Heinrich, A. J., Gupta, J. A., Lutz, C. P., and Eigler, D. M. (2004) Single-atom spin-flip spectroscopy, *Science* **306**, 466–469.
- Hübner, J., Rühle, W. W., Klude, M., Hommel, D., Bhat, R. D. R., Sipe, J. E., and van Driel, H. M. (2003) Direct Observation of Optically Injected Spin-Polarized Currents in Semiconductors, *Phys. Rev. Lett.* **90**, 216601.
- Imamođlu, A., Awschalom, D. D., Burkard, G., DiVincenzo, D. P., Loss, D., Sherwin, M., and Small, A. (1999) Quantum Information Processing Using Quantum Dot Spins and Cavity QED, *Phys. Rev. Lett.* **83**, 4204–4207.
- Ivchenko, E. L. and Pikus, G. E. (1997) *Superlattices and Other Heterostructures*, New York, Springer.
- Jelezko, F., Popa, I., Gruber, A., Tietz, C., Wrachtrup, J., Nizovtsev, A., and Kilin, S. (2002) Single spin states in a defect center resolved by optical spectroscopy, *Appl. Phys. Lett.* **81**, 2160–2162.
- Johnson, M. and Silsbee, R. H. (1988) Spin-injection experiment, *Phys. Rev. B* **37**, 5326–5335.
- Johnston-Halperin, E., Lofgreen, D., Kawakami, R. K., Young, D. K., Coldren, L., Gossard, A. C., and Awschalom, D. D. (2002) Spin-polarized Zener tunneling in (Ga,Mn)As, *Phys. Rev. B* **65**, 041306.
- Kane, B. E. (1998) A silicon-based nuclear spin quantum computer, *Nature* **393**, 133–137.
- Karimov, O. Z., John, G. H., Harley, R. T., Lau, W. H., Flatté, M. E., Henini, M., and Airey, R. (2003) High temperature gate control of quantum well spin memory, *Phys. Rev. Lett.* **91**, 246601.
- Kato, Y., Myers, R. C., Gossard, A. C., Levy, J., and Awschalom, D. D. (2003) Gigahertz Electron Spin Manipulation Using Voltage-Controlled g-Tensor Modulation, *Science* **299**, 1201–1204.
- Kikkawa, J. M. and Awschalom, D. D. (1998) Resonant Spin Amplification in n-Type GaAs, *Phys. Rev. Lett.* **80**, 4313–4316.
- Kikkawa, J. M. and Awschalom, D. D. (1999) Lateral drag of spin coherence in gallium arsenide, *Nature* **397**, 139–141.

- Kikkawa, J. M., Smorchkova, I. P., Samarth, N., and Awschalom, D. D. (1997) Room-Temperature Spin Memory in Two-Dimensional Electron Gases, *Science* **277**, 1284–1287.
- Kiselev, A. A., Ivchenko, E. L., and Rössler, U. (1998) Electron g factor in one- and zero-dimensional semiconductor nanostructures, *Phys. Rev. B* **58**, 16353–16359.
- Kitchen, D. and Yazdani, A. (2005) Spatial Structure of a Single Mn Impurity State on GaAs (110) Surface, *J. of Supercond. and Nov. Mag.* **18**, 23–28.
- Kitchen, D., Richardella, A., Tang, J.-M., Flatté, M. E., and Yazdani, A. (2006) Atom-by-atom substitution of Mn in GaAs and Visualization of their hole-mediated interactions, *Nature* **442**, 436–439.
- Kittel, C. and Kroemer, H. (1980) *Thermal Physics*, New York, W. H. Freeman and Company.
- Kohda, M., Ohno, Y., Takamura, K., Matsukura, F., and Ohno, H. (2001) A Spin Esaki Diode, *Jpn. J. Appl. Phys. Part 2* **40**, L1274–L1276.
- Kouwenhoven, L. P., Austing, D. G., and Tarucha, S. (2001) Few-electron quantum dots, *Rep. Prog. Phys.* **64**, 701–736.
- Krasny, Y. P., Kovalenko, N. P., Krey, U., and Jacak, L. (2001) Paramagnetic-diamagnetic interplay in quantum dots for nonzero temperatures, *J. Phys. Cond. Mat.* **13**, 4341–4358.
- Kroutvar, M., Ducommun, Y., Heiss, D., Bichler, M., Schuh, D., Abstreiter, G., and Finley, J. J. (2004) Optically programmable electron spin memory using semiconductor quantum dots, *Nature* **432**, 81–84.
- Lau, W. H. and Flatté, M. E. (2002) Tunability of electron spin coherence in III-V quantum wells, *J. Appl. Phys.* **91**, 8682–8684.
- Lau, W. H., Olesberg, J. T., and Flatté, M. E. (2001) Electron-spin decoherence times in bulk and quantum well zinc-blende semiconductors, *Phys. Rev. B* **64**, 161301(R).
- Lau, W. H., Olesberg, J. T., and Flatté, M. E. (2004) Electronic structures and electron spin decoherence in (001)-grown layered zincblende semiconductors, cond-mat/0406201.
- Lee, T. C. and Anderson, W. W. (1964) Edge emission involving manganese impurities in GaAs at 4.2° K, *Solid State Commun.* **2**, 265–8.
- Leuenberger, M. N., Flatté, M. E., and Awschalom, D. D. (2005) Teleportation of electronic many-qubit states via single photons, *Phys. Rev. Lett.* **94**, 107401.
- Levy, J. (2002) Universal quantum computation with spin-1/2 pairs and Heisenberg exchange, *Phys. Rev. Lett.* **92**, 147902.
- Loss, D. and DiVincenzo, D. P. (1998) Quantum computation with quantum dots, *Phys. Rev. A* **57**, 120–126.
- Madelung, O., Schilz, M., and Weiss, H. (eds.) (1982) *Landolt-Börnstein, Numerical Data and Functional Relations in Science and Technology*, New York, Springer.
- Manassen, Y., Hamers, R. J., Demuth, J. E., and Castellano, Jr., A. J. (1989) Direct observation of the precession of individual paramagnetic spins on oxidized silicon surfaces, *Phys. Rev. Lett.* **62**, 2531–2534.
- Matveev, K. A., Glazman, L. I., and Larkin, A. I. (2000) g-Factors of Discrete Levels in Nanoparticles, *Phys. Rev. Lett.* **85**, 2789–2792.
- Medeiros-Ribeiro, G., Pinheiro, M. V. B., Pimentel, V. L., and Marega, E. (2002) Spin splitting of the electron ground states of InAs quantum dots, *Appl. Phys. Lett.* **80**, 4229–4231.
- Medeiros-Ribeiro, G., Ribeiro, E., and Westfahl, Jr., H. (2003) g-factor engineering and control in self-assembled quantum dots, *Appl. Phys. A* **77**, 725–729.
- Meier, F. and Zachachrenya, B. P. (1984) *Optical Orientation: Modern Problems in Condensed Matter Science*, Vol. 8, Amsterdam, North-Holland.
- Mott, N. F. (1936) The Electrical Conductivity of Transition Metals, *Proc. Royal Soc. of London A* **153**, 699–717.

- Nenashev, A. V., Dvurechenskii, A. V., and Zinovieva, A. F. (2003) Wave functions and  $g$  factor of holes in Ge/Si quantum dots, *Phys. Rev. B* **67**, 205301.
- Ohno, Y., Terauchi, R., Adachi, T., Matsukura, F., and Ohno, H. (1999a) Spin relaxation in GaAs(110) quantum wells, *Phys. Rev. Lett.* **83**, 4196–4199.
- Ohno, Y., Young, D. K., Beschoten, B., Matsukura, F., Ohno, H., and Awschalom, D. D. (1999b) Electrical spin injection in a ferromagnetic semiconductor heterostructure, *Nature (London)* **402**, 790–792.
- Olesberg, J. T., Lau, W. H., Flatté, M. E., Yu, C., Altunkaya, E., Shaw, E. M., Hasenberg, T. C., and Boggess, T. F. (2001) Interface contributions to spin relaxation in a short-period InAs/GaSb superlattice, *Phys. Rev. B* **64**, 201301(R).
- Petta, J. R. and Ralph, D. C. (2002) Measurements of Strongly Anisotropic  $g$  Factors for Spins in Single Quantum States, *Phys. Rev. Lett.* **89**, 156802.
- Petta, J. R., Johnson, A. C., Taylor, J. M., Laird, E. A., Yacoby, A., Lukin, M. D., Marcus, C. M., Hanson, M. P., and Gossard, A. C. (2005) Coherent Manipulation of Coupled Electron Spins in Semiconductor Quantum Dots, *Science* **309**, 2180–2184.
- Prado, S. J., Trallero-Giner, C., Alcalde, A. M., López-Richard, V., and Marques, G. E. (2003) Magneto-optical properties of nanocrystals: Zeeman splitting, *Phys. Rev. B* **67**, 165306.
- Prado, S. J., Trallero-Giner, C., López-Richard, V., Alcalde, A. M., and Marques, G. E. (2004) Zeeman effect and magnetic anomalies in narrow-gap semiconductor quantum dots, *Physica E* **20**, 286–289.
- Preskill, J. (1998) Fault Tolerant Quantum Computation, In H.-K. Lo, S. Popescu, and T. Spiller (eds.), *Introduction to quantum computation and information*, Singapore, World Scientific, pp. 213–269.
- Pryor, C. (1998) Eight-band calculations of strained InAs/GaAs quantum dots compared with one-, four-, and six-band approximations, *Phys. Rev. B* **57**, 7190–7195.
- Pryor, C., Pistol, M.-E., and Samuelson, L. (1997) Electronic structure of strained InP/Ga<sub>0.51</sub>In<sub>0.49</sub>P quantum dots, *Phys. Rev. B* **56**, 10404–10411.
- Pryor, C. E. and Flatté, M. E. (2003) Accuracy of Circular Polarization as a Measure of Spin Polarization in Quantum Dot Qubits, *Phys. Rev. Lett.* **91**, 257901.
- Pryor, C. E. and Flatté, M. E. (2006a) Landé  $g$  Factors and Orbital Momentum Quenching in Semiconductor Quantum Dots, *Phys. Rev. Lett.* **96**, 026804.
- Pryor, C. E. and Flatté, M. E. (2006b) Predicted ultrafast single qubit operations in semiconductor quantum dots, *Appl. Phys. Lett.* **88**, 233108.
- Qi, Y., Yu, Z.-G., and Flatté, M. E. (2006) Spin Gunn Effect, *Phys. Rev. Lett.* **96**, 026602.
- Quintero, G. F. and Piermarocchi, C. (2005) Entanglement and errors in the control of spins by optical coupling, *Phys. Rev. B* **72**, 045334.
- Rashba, E. I. (1960) Properties of semiconductors with an extremum loop I. Cyclotron and combinatorial resonance in a magnetic field perpendicular to the plane of the loop, *Soviet Phys. Solid State* **2**, 1109–1122.
- Rashba, E. I. (2000) Theory of electrical spin injection: Tunnel contacts as a solution of the conductivity mismatch problem, *Phys. Rev. B* **62**, R16267–R16270.
- Rodina, A. V., Efros, A. L., and Alekseev, A. Y. (2003) Effect of the surface on the electron quantum size levels and electron  $g$  factor in spherical semiconductor nanocrystals, *Phys. Rev. B* **67**, 155312.
- Rosatzin, M., Suter, D., and Mlynek, J. (1990) Light-shift-induced spin echoes in a  $J=1/2$  atomic ground state, *Phys. Rev. A* **42**, 1839–1841.
- Roth, L. M., Lax, B., and Zwerdling, S. (1959) Theory of Optical Magneto-Absorption Effects in Semiconductors, *Phys. Rev.* **114**, 90–104.

- Rugar, D., Budakian, R., Mamin, H. J., and Chui, B. W. (2004) Single spin detection by magnetic resonance force microscopy, *Nature* **430**, 329–332.
- Schmidt, G., Ferrand, D., Molenkamp, L. W., Filip, A. T., and van Wees, B. J. (2000) Fundamental obstacle for electrical spin injection from a ferromagnetic metal into a diffusive semiconductor, *Phys. Rev. B* **62**, R4790–R4793.
- Schneider, J., Kaufmann, U., Wilkening, W., and Baeumler, M. (1987) Electronic structure of the neutral manganese acceptor in gallium arsenide, *Phys. Rev. Lett.* **59**, 240–243.
- Schriger, J. and Birgitta Whaley, K. (2003) Tight-binding g-factor calculations of CdSe nanostructures, *Phys. Rev. B* **67**, 235301.
- Slichter, C. P. (1963) *Principles of Magnetic Resonance*, New York, Harper and Row.
- Smith, D. L. and Silver, R. N. (2001) Electrical spin injection into semiconductors, *Phys. Rev. B* **64**, 045323.
- Steeves, G. M., Elezzabi, A. Y., and Freeman, M. R. (1998) Nanometer-scale imaging with an ultrafast scanning tunneling microscope, *Appl. Phys. Lett.* **72**, 504–506.
- Stevens, M. J., Smirl, A. L., Bhat, R. D. R., Najmaie, A., Sipe, J. E., and van Driel, H. M. (2003) Quantum Interference Control of Ballistic Pure Spin Currents in Semiconductors, *Phys. Rev. Lett.* **90**, 136603.
- Tang, J.-M. and Flatté, M. E. (2004) Multiband tight-binding model of local magnetism in  $\text{Ga}_{1-x}\text{Mn}_x\text{As}$ , *Phys. Rev. Lett.* **92**, 047201.
- Tang, J.-M. and Flatté, M. E. (2005) Spin-orientation-dependent spatial structure of a magnetic acceptor state in a zincblende semiconductor, *Phys. Rev. B* **72**, 161315(R).
- Tang, J.-M., Levy, J., and Flatté, M. E. (2006) All-electrical control of single ion spins in a semiconductor, *Phys. Rev. Lett.* **97**, 106803.
- Terauchi, R., Ohno, Y., Adachi, T., Sato, A., Matsukura, F., Tackeuchi, A., and Ohno, H. (1999) Carrier Mobility Dependence of Electron Spin Relaxation in GaAs Quantum Wells, *Jpn. J. Appl. Phys. Pt. 1* **38**, 2549–2551.
- Tischler, J. G., Bracker, A. S., Gammon, D., and Park, D. (2002) Fine structure of trions and excitons in single GaAs quantum dots, *Phys. Rev. B* **66**, 081310.
- Uenoyama, T. and Sham, L. J. (1990) Hole relaxation and luminescence polarization in doped and undoped quantum wells, *Phys. Rev. Lett.* **64**, 3070–3073.
- Valín-Rodríguez, M., Puente, A., and Serra, L. (2004) Spin splitting and precession in quantum dots with spin-orbit coupling: The role of spatial deformation, *Phys. Rev. B* **69**, 085306.
- Van Vleck, J. H. (1932) *The Theory of Electric and Magnetic Susceptibilities*, New York, Oxford.
- Vurgaftman, I., Meyer, J. R., and Ram-Mohan, L. R. (2001) Band parameters for III–V compound semiconductors and their alloys, *J. Appl. Phys.* **89**, 5815–5875.
- Winkler, R. (2003) *Spin-orbit Coupling Effects in Two-Dimensional Electron and Hole Systems*, Berlin, Springer.
- Winkler, R. and Rössler, U. (1993) General approach to the envelope-function approximation based on a quadrature method, *Phys. Rev. B* **48**, 8918–8927.
- Xiao, M., Martin, I., Yablonovitch, E., and Jiang, H. W. (2004) Electrical detection of the spin resonance of a single electron in a silicon field-effect transistor, *Nature* **430**, 435–439.
- Yafet, Y. (1963) g Factors and Spin-Lattice Relaxation of Conduction Electrons, *Solid State Phys.* **14**, 2–98.
- Yakunin, A. M., Silov, A. Y., Koenraad, P. M., Roy, W. V., Boeck, J. D., and Wolter, J. H. (2004a) Imaging of the  $(\text{Mn}^{2+}3d^5 + \text{hole})$  complex in GaAs by cross-sectional scanning tunneling microscopy, *Physica E* **21**, 947–950.
- Yakunin, A. M., Silov, A. Y., Koenraad, P. M., Roy, W. V., Boeck, J. D., Wolter, J. H., Tang, J.-M., and Flatté, M. E. (2004b) Spatial structure of an individual Mn acceptor in GaAs, *Phys. Rev. Lett.* **92**, 216806.

- Young, D. K., Johnston-Halperin, E., and Awschalom, D. D. (2002) Anisotropic electrical spin injection in ferromagnetic semiconductor heterostructures, *Appl. Phys. Lett.* **80**, 1598–1600.
- Yu, Z. G. and Flatté, M. E. (2002a) Electric-field dependent spin diffusion and spin injection into semiconductors, *Phys. Rev. B* **66**, 201202.
- Yu, Z. G. and Flatté, M. E. (2002b) Spin diffusion and injection in semiconductor structures: Electric field effects, *Phys. Rev. B* **66**, 235302.

# MANY-BODY EFFECTS IN SPIN-POLARIZED TRANSPORT \*

GIOVANNI VIGNALE (vignaleg@missouri.edu)  
University of Missouri, Columbia, MO 65211, USA

**Abstract:** This chapter is about the role of electron–electron interactions in spin-polarized transport. It begins with a review of the drift–diffusion theory of spin transport in the presence of electron–electron interactions. The formulation of the theory differs from the usual noninteracting formulation due to the presence of off-diagonal elements in the resistivity, diffusion, and susceptibility matrices. The central concept of *spin Coulomb drag* (SCD) is introduced phenomenologically and is immediately applied to the study of spin-packet evolution and spin valve devices. I then review the microscopic theory of the SCD and the intimately related concept of *spin mass*. Recent experiments on the SCD are described. As a final application, the spin Hall conductivity of a doped semiconductor is calculated in the presence of electron–electron interactions.

**Keywords:** spin transport, spin Coulomb drag, spin valve devices, spin mass, spin Hall effect

## 1 Drift–Diffusion Theory for Charge

The drift–diffusion theory is an essential tool for the analysis of modern electronic devices (Streetman and Banerjee, 1980). Let us first review the theory for charge transport and then we will see how it is generalized to include the spin.

The electric current density,  $\mathbf{J}$ , in a metal or in a semiconductor is the sum of two pieces: the drift term, which is proportional to the electric field  $\mathbf{E}$ , and the diffusion term, which is proportional to the gradient of the carrier density  $n$ :

$$\mathbf{J} = \sigma \mathbf{E} - q D \nabla n , \quad (1)$$

where  $\sigma$  is the electric conductivity, and  $D$  is the diffusion constant.  $\mathbf{J}$  is related to the carrier current density,  $\mathbf{j}$ , by  $\mathbf{J} = q\mathbf{j}$ , where  $q$  is the charge of the carriers ( $q = -e$  for electrons,  $q = e$  for holes). Equation (1) is derived from the classical Boltzmann equation in the limit that the density and the external potentials are slowly varying on the scale of the mean free path.  $\sigma$  and  $D$  are connected by the Einstein relation,

$$\sigma = q^2 D \frac{\partial n(\mu_c)}{\partial \mu_c} , \quad (2)$$

where the *compressibility*  $\frac{\partial n(\mu_c)}{\partial \mu_c}$  (also known as thermodynamic density of states) is the derivative of the carrier density with respect to the local chemical potential

---

\*Work supported by NSF Grant No. DMR0313681

$\mu_c$ , i.e., the chemical potential measured from the bottom of the conduction band for electrons, or from the top of the valence band for holes. The electric field  $\mathbf{E}$  is determined by the Maxwell equation

$$\nabla \cdot \mathbf{E} = \frac{\rho}{\epsilon_0}, \quad (3)$$

where  $\rho$  is the net charge density of the mobile carriers plus the stationary background charges (e.g., the donors in an n-type doped semiconductor). Equations (1) and (2) can be combined to yield

$$\mathbf{J} = \sigma \left[ \mathbf{E} - \frac{\nabla \mu_c}{q} \right] = -\sigma \frac{\nabla \mu}{q}, \quad (4)$$

where the *electrochemical potential*  $\mu \equiv q\phi + \mu_c$  is the sum of the chemical potential  $\mu_c$  and the electrostatic potential energy  $q\phi$  ( $\phi$  is the electrostatic potential, related to the electric field by  $\mathbf{E} = -\nabla\phi$ ).

The second form of Eq. (4) reveals the physical content of the Einstein relation. Namely, the current vanishes when the electrochemical potential is constant in space, i.e., when the system is in equilibrium: for in that case the diffusion current due to the non-uniformity of the charge distribution is cancelled by the drift current due to the electric field.

The other fundamental property that is used in calculating the current and charge distributions is the local conservation of the electric charge, mathematically represented by the continuity equation

$$\nabla \cdot \mathbf{J} = -\frac{\partial \rho}{\partial t}. \quad (5)$$

Here  $\rho$  can be safely replaced by  $qn$  since the stationary charges do not contribute to the time derivative.

Equations (3)–(5) constitute a closed set of equations for the current and the charge distributions. In metals, these equations imply that any charge imbalance is effectively “screened out” over a microscopic length scale

$$\lambda = \left( \frac{e^2}{\epsilon_0} \frac{\partial n}{\partial \mu_c} \right)^{-1/2}. \quad (6)$$

The screening occurs during a very short time (dielectric relaxation time) rendering diffusion irrelevant. In doped semiconductors, due to the presence of carriers of opposite polarities (electrons and holes), density inhomogeneity can occur without breaking charge neutrality. Diffusion processes become then very important (Smith, 1978). We will see later that spin degrees of freedom allow normal metallic systems to behave in ways that are characteristic of bipolar systems.

The above discussion is quite general: the main physical assumption is the existence of a local relation between the current density and the gradient

of the electrochemical potential. Both quantum mechanics and many-body theory are needed for the determination of the homogeneous conductivity  $\sigma$  and the compressibility  $\chi_c \equiv \frac{\partial n}{\partial \mu_c}$ .  $\chi_c$  is strongly affected by quantum statistics and many-body correlation, and is accurately extracted from quantum Monte Carlo calculations (Giuliani and Vignale, 2005). The calculation of  $\sigma$  is more complex. At not too low temperatures,  $k_B T > \hbar/\tau$ , the interactions are ignorable since they do not change the total momentum. Impurities produce the Drude conductivity

$$\sigma = \frac{ne^2\tau}{m_b}, \quad (7)$$

where  $\tau$  is the elastic scattering time and  $m_b$  is the effective mass of the band. Phonons give contributions to the resistivity proportional to  $T$  or  $T^5$  in different regimes. Distinctive signatures of the Coulomb interaction arise only at very low temperature, with non-analyticities first pointed out by Altshuler and Aronov (1985). We will now show that much stronger interaction effects arise when the spin of the carriers is taken into account, when carriers of opposite spin orientations are allowed to move independently.

## 2 Drift-Diffusion Theory for Collinear Spins

Generalizing the drift-diffusion equations to take into account the spin degree of freedom is not as simple as it sounds. In fact, it has not yet been done in the general case of interacting electronic systems with *noncollinear* spin orientations. Here we will content ourselves with the simpler case in which one component of the spin (say the  $z$ -component) is conserved, or nearly conserved. Then spin up and spin down electrons can be regarded, in a first approximation, as two different species of carriers, like electrons and holes in semiconductors. Even in this simplest of treatments, however, we must allow for slow relaxation processes that flip the spin to establish the correct equilibrium polarization. These processes are the analogue of electron-hole recombination in semiconductors. What will *not* be allowed in our model is the possibility of an electron being in a coherent superposition of up and down spin. This is of course a serious restriction if one wants to study spin-orbit interaction effect, or the Zeeman coupling to a magnetic field of spatially varying direction. Fortunately, the restricted approach is sufficient to study the basic giant magneto-resistance (GMR) effect (Baibich et al., 1988) and the interaction corrections to it, as well as the spin Coulomb drag (SCD) effect (D'Amico and Vignale, 2000).

Assuming that spin-orbit interactions and noncollinear fields are negligible, we will now develop the two-component drift-diffusion theory for collinear spins. The generalization of Eq. (4) for electrons ( $q = -e$ ) with spin is

$$\mathbf{J}_\alpha = \sum_\beta \sigma_{\alpha\beta} \mathbf{E} + \sum_\beta e D_{\alpha\beta} \nabla n_\beta, \quad (8)$$

where  $\alpha$  and  $\beta$  are spin indices ( $= +1$  or  $-1$  for spin up or down, respectively),  $n_\beta$  is the density of  $\beta$ -spin electrons, and  $\sigma_{\alpha\beta}$ ,  $D_{\alpha\beta}$  are  $2 \times 2$  matrices, which generalize the homogeneous conductivity and the diffusion constant. The electric field does not have a spin index, since it couples in the same way to electrons of either spin orientation.  $\mathbf{J}_\uparrow$  and  $\mathbf{J}_\downarrow$  are the electric current densities associated with each spin orientation. The normal electric current is simply the sum  $\mathbf{J} = \mathbf{J}_\uparrow + \mathbf{J}_\downarrow$ , while the  $z$ -component of the spin current is  $\mathbf{J}_z = -\frac{\hbar}{2e}(\mathbf{J}_\uparrow - \mathbf{J}_\downarrow)$ . These currents satisfy a generalized form of the continuity equation

$$\nabla \cdot \mathbf{J}_\alpha = e \frac{\partial n_\alpha}{\partial t} + e \left( \frac{\delta n_\alpha}{\tau_{\alpha\bar{\alpha}}} - \frac{\delta n_{\bar{\alpha}}}{\tau_{\bar{\alpha}\alpha}} \right), \quad (9)$$

where the second term on the right hand side takes into account spin-flip processes. Here  $\delta n_\alpha \equiv n_\alpha - n_{0,\alpha}$  is the deviation of the density from its local equilibrium value,  $n_{0,\alpha}$ , and  $\frac{1}{\tau_{\alpha\bar{\alpha}}}$  is the rate at which  $\alpha$ -spin electrons are flipped to the  $\bar{\alpha} \equiv -\alpha$  state. Naturally, the two spin flip rates  $\frac{1}{\tau_{\alpha\bar{\alpha}}}$  and  $\frac{1}{\tau_{\bar{\alpha}\alpha}}$  are mutually related, as we will see later in this and in the next section.

The Einstein relation, Eq. (2), is readily generalized by noting that both currents  $\mathbf{J}_\uparrow$  and  $\mathbf{J}_\downarrow$  must vanish in a non-homogeneous equilibrium state. This requirement leads to the condition

$$\hat{\sigma} = e^2 \hat{D} \cdot \hat{\chi}, \quad (10)$$

where  $\hat{\sigma}$  and  $\hat{D}$  are shorthands for the  $2 \times 2$  matrices  $\sigma_{\alpha\beta}$  and  $D_{\alpha\beta}$ , and  $\hat{\chi}$  is a shorthand for the susceptibility matrix

$$\chi_{\alpha\beta} \equiv \frac{\partial n_\alpha}{\partial \mu_{c\beta}}, \quad (11)$$

which describes the response of the densities to independent variations of the chemical potentials of the two species (Giuliani and Vignale, 2005).

Another important connection between the susceptibility matrix  $\hat{\chi}$  and transport properties comes from the requirement that spin-flip processes do not change the equilibrium spin distribution. This means that a change in spin densities that merely reflects a shift in the common chemical potential of the two species must not contribute to the relaxation term on the right hand side of Eq. (9). Such a change in spin densities has the form  $\delta n_\uparrow = (\chi_{\uparrow\uparrow} + \chi_{\uparrow\downarrow})\delta\mu_c$  and  $\delta n_\downarrow = (\chi_{\downarrow\uparrow} + \chi_{\downarrow\downarrow})\delta\mu_c$ , where  $\delta\mu_c$  is the common shift in the chemical potential. This implies that (Hershfield and Zhao, 1997)

$$\frac{\chi_{\uparrow\uparrow} + \chi_{\uparrow\downarrow}}{\tau_{\uparrow\downarrow}} = \frac{\chi_{\downarrow\uparrow} + \chi_{\downarrow\downarrow}}{\tau_{\downarrow\uparrow}}. \quad (12)$$

We will make repeated use of this useful identity in the analysis of spin-polarized transport.

### 3 Spin Coulomb Drag—An Introduction

Before considering some applications of the drift–diffusion equations let us pause to discuss one of the most significant features of Eq. (8), namely the presence of the off-diagonal terms  $\sigma_{\uparrow\downarrow}$  and  $D_{\uparrow\downarrow}$  in  $\hat{\sigma}$  and  $\hat{D}$ . These terms arise primarily from the Coulomb interaction and are a manifestation of the *spin Coulomb drag* (SCD) (D’Amico and Vignale, 2000).

The nature of the Coulomb contribution to the off-diagonal conductivity can be easily understood at the phenomenological level. Let us write the equation of motion for the total momentum  $\mathbf{P}_\alpha$  (per unit volume) of the  $\alpha$ -spin component:

$$\dot{\mathbf{P}}_\alpha = -en_\alpha \mathbf{E}_\alpha + \mathbf{F}_{\alpha\bar{\alpha}} - \frac{\mathbf{P}_\alpha}{\tau_\alpha} + \frac{\mathbf{P}_{\bar{\alpha}}}{\tau'_\alpha}. \quad (13)$$

Here  $\mathbf{F}_{\alpha\bar{\alpha}}$  is the net force exerted by  $\bar{\alpha}$ -spins on  $\alpha$ -spins;  $\frac{\mathbf{P}_\alpha}{\tau_\alpha}$  is the rate of change of  $\mathbf{P}_\alpha$  due to electron-impurity collisions in which the electron is scattered out of its initial momentum state (with or without spin flip); finally  $\frac{\mathbf{P}_{\bar{\alpha}}}{\tau'_\alpha}$  is the rate of change of  $\mathbf{P}_\alpha$  due to electron-impurity collisions in which an electron of spin  $\bar{\alpha}$  is scattered into a state of spin  $\alpha$ .  $\tau_\alpha$  and  $\tau'_\alpha$  are *momentum* relaxation times and should not be confused with the spin–flip relaxation time  $\tau_{\alpha\bar{\alpha}}$  introduced in Eq. (9). Furthermore  $\tau_\alpha$  is largely dominated by non-spin–flip processes: it is basically the Drude scattering time.

From Newton’s third law one immediately sees that  $\mathbf{F}_{\alpha\bar{\alpha}} = -\mathbf{F}_{\bar{\alpha}\alpha}$ , and Galilean invariance requires that  $\mathbf{F}$  depend only on the relative drift velocity of the two spin species. This leaves us no choice but to write

$$\mathbf{F}_{\alpha\bar{\alpha}} = -\gamma m_b \frac{n_\alpha n_{\bar{\alpha}}}{n} (\mathbf{v}_\alpha - \mathbf{v}_{\bar{\alpha}}), \quad (14)$$

where  $\gamma$  is a positive coefficient, which we call *spin-drag coefficient*. Equations (13) and (14) form a closed set of linear equations for the homogeneous current densities  $\mathbf{J}_\alpha = -e \frac{\mathbf{P}_\alpha}{m_b}$ . For a periodic electric field of angular frequency  $\omega$  their solution yields the homogeneous resistivity matrix  $\hat{\rho}(\omega) = \hat{\sigma}^{-1}(\omega)$  in the following form:

$$\hat{\rho}(\omega) = \begin{pmatrix} -i\omega \frac{m_b}{e^2 n_\uparrow} + \frac{m_b}{n_\uparrow e^2 \tau_\uparrow} + \frac{n_\downarrow}{n_\uparrow} \frac{m_b}{ne^2} \gamma & -\frac{m_b}{n_\uparrow e^2 \tau'_\uparrow} - \frac{m_b}{ne^2} \gamma \\ -\frac{m_b}{n_\downarrow e^2 \tau'_\downarrow} - \frac{m_b}{ne^2} \gamma & -i\omega \frac{m_b}{e^2 n_\downarrow} + \frac{m_b}{n_\downarrow e^2 \tau_\downarrow} + \frac{n_\uparrow}{n_\downarrow} \frac{m_b}{ne^2} \gamma \end{pmatrix}. \quad (15)$$

Several features of this matrix are worth commenting. First, the matrix is symmetric, as it must be, because  $n_\uparrow \tau'_\uparrow = n_\downarrow \tau'_\downarrow$  (a fact that will be verified explicitly at the end of this section). Second, the off-diagonal elements are *negative*. This makes perfect sense once it is understood that  $\rho_{\uparrow\downarrow}$  is the electric field induced in the up-spin channel by a current flowing in the down-spin channel *when the up-spin*

current is zero. Since a down-spin current in the positive direction tends to drag along the up-spins, a negative electric field is needed to maintain the zero value of the up-spin current. There is no limit, in principle, on how large the absolute value of  $\rho_{\uparrow\downarrow}$  can be. The only physical restriction is that the *eigenvalues* of the real part of the resistivity matrix be positive to ensure positivity of dissipation. Finally, observe that the spin drag coefficient appears both in the diagonal and in the off-diagonal elements of the resistivity: this ensures that spin drag effect is absent when up- and down-spin electrons move with the same drift velocity, i.e., when  $\frac{J_\uparrow}{n_\uparrow} = \frac{J_\downarrow}{n_\downarrow}$ .

Looking at Eq. (15) we see that the off-diagonal resistivity has contributions not only from the SCD but also from spin-flip processes. What about the relative importance of these two contributions? At very low temperature spin flip processes win because in this limit the Coulomb scattering is suppressed by phase space restrictions (Pauli's exclusion principle), and  $\gamma$  tends to zero as  $T^2$  (see section 6). On the other hand  $\frac{1}{\tau}$  is generally very small for two reasons: first, the spin-orbit interactions that are responsible for spin-flips are weak, as is evidenced by the long spin relaxation times  $\tau_s \sim 50$  ns and spin diffusion lengths  $L_s \sim 200$   $\mu\text{m}$  (Kikkawa et al., 1997; Kikkawa and Awschalom, 1998); second, the spin-flip scattering process does not effectively transfer momentum between the two spin channels. To understand the second point consider a down-spin electron that collides with an impurity and is thereby scattered into the up-spin stream (Figure 1). Such an electron is almost equally likely to be moving in any direction after the collision, and therefore does not significantly contribute to the up-spin current. So taking  $\tau' \sim 500$  ns (10 times longer than the spin relaxation time) and the peak value of  $\frac{1}{\gamma} \sim 1$  ps (of the order of the Drude scattering time) at temperatures of the order of the Fermi energy  $T_F$  ( $\sim 300$  K in doped

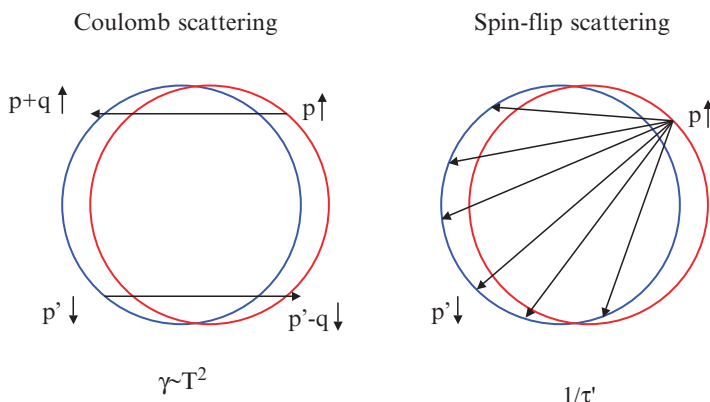


Figure 1. Momentum transfer between opposite spin channels: Coulomb scattering vs spin-flip processes

semiconductors of current interest) we estimate that the Coulomb contribution will dominate the off-diagonal resistivity for  $T > 10^{-3}T_F \sim 0.3$  K.

An explicit expression for  $\frac{1}{\tau'_\alpha}$  can be obtained from the analysis of the collision integral in the Boltzmann equation. This expression has the form

$$\frac{1}{\tau'_\alpha} = -\frac{1}{n_{\bar{\alpha}}} \sum_{\mathbf{k}\mathbf{k}'} f'_0(\epsilon_{k\alpha}) W_{\mathbf{k}\alpha, \mathbf{k}'\bar{\alpha}}^{sf} \mathbf{k} \cdot \mathbf{k}' \delta(\epsilon_{k\alpha} - \epsilon_{k'\bar{\alpha}}), \quad (16)$$

where  $W_{\mathbf{k}\alpha, \mathbf{k}'\bar{\alpha}}^{sf}$  is the scattering probability from state  $\mathbf{k}\alpha$  to state  $\mathbf{k}'\bar{\alpha}$ , and  $f'_0(\epsilon_{k\alpha})$  is the derivative of the equilibrium distribution with respect to the single-particle energy  $\epsilon_{k\alpha}$ . Notice that  $\frac{1}{\tau'}$  vanishes for short-ranged scatterers, i.e., when  $W^{sf}$  is independent of  $\mathbf{k}$  and  $\mathbf{k}'$ . From this expression we can also see that  $\frac{n_\uparrow}{\tau'_\uparrow} = \frac{n_\downarrow}{\tau'_\downarrow}$  and hence  $n_\uparrow \tau'_\uparrow = n_\downarrow \tau'_\downarrow$ , as required for the symmetry of the resistivity matrix (15).

The corresponding expression for the spin drag coefficient  $\gamma$  is

$$\begin{aligned} \gamma = \frac{n}{n_\alpha n_{\bar{\alpha}}} \sum_{\mathbf{k}\mathbf{k}'} W_{\mathbf{k}\alpha, \mathbf{p}\bar{\alpha}; \mathbf{k}'\alpha, \mathbf{p}'\bar{\alpha}}^C & \frac{(\mathbf{k} - \mathbf{k}')^2}{4mk_B T} f_{0\alpha}(\epsilon_k) f_{0\bar{\alpha}}(\epsilon_p) f_{0\alpha}(-\epsilon_{k'}) f_{0\bar{\alpha}}(-\epsilon_{p'}) \\ & \times \delta_{\mathbf{k}+\mathbf{p}, \mathbf{k}'+\mathbf{p}'} \delta(\epsilon_{k\alpha} + \epsilon_{p\bar{\alpha}} - \epsilon_{k'\alpha} - \epsilon_{p'\bar{\alpha}}), \end{aligned} \quad (17)$$

where  $W_{\mathbf{k}\alpha, \mathbf{p}\bar{\alpha}; \mathbf{k}'\alpha, \mathbf{p}'\bar{\alpha}}^C$  is the probability that two electrons with momenta and spins  $\mathbf{k}\alpha$  and  $\mathbf{p}\bar{\alpha}$  scatter into states  $\mathbf{k}'\alpha$  and  $\mathbf{p}'\bar{\alpha}$ . This expression will come handy in section 9, when we discuss the spin Hall effect in the presence of interactions.

## 4 Drift-Diffusion Theory—Continued

Most applications of the drift-diffusion theory start from the *drift-diffusion equation*, which is obtained by substituting Eq. (8) in the continuity equation (9), and then making use of Eq. (3) to express the divergence of the electric field in terms of the net electric charge density  $\rho$ . This gives the following two equations (one for each  $\alpha$ ):

$$\frac{\sigma_\alpha \rho}{\epsilon_0 e} + \nabla \sigma_\alpha \cdot \mathbf{E} + \sum_\beta D_{\alpha\beta} \nabla^2 n_\beta = \frac{\partial n_\alpha}{\partial t} + \left( \frac{\delta n_\alpha}{\tau_{\alpha\bar{\alpha}}} - \frac{\delta n_{\bar{\alpha}}}{\tau_{\bar{\alpha}\alpha}} \right), \quad (18)$$

where we have defined

$$\sigma_\alpha \equiv \sigma_{\alpha\alpha} + \sigma_{\alpha\bar{\alpha}}. \quad (19)$$

Notice that we have dropped a term  $\sum_\beta \nabla D_{\alpha\beta} \cdot \nabla n_\beta$  from the left hand side of this equation: this is justified only if the density is slowly varying, so that the product of the two gradients is negligible.

The first term on the left hand side (known as the *space-charge term*), plays an important role in the equation. If we assume, as normally is the case, that the system is electrically neutral at equilibrium, then we have

$$\rho = -e(\delta n_\uparrow + \delta n_\downarrow) . \quad (20)$$

The dielectric relaxation time  $\tau_d = \frac{\epsilon_0}{\sigma}$  (roughly the time it takes a local charge accumulation to spread out) is much shorter than all other relaxation times. Therefore the space charge term is huge unless  $\rho$  is very nearly zero. This implies that on a timescale longer than  $\tau_d$  the system can be considered neutral ( $\delta n_\uparrow = -\delta n_\downarrow$ ) and only the difference of the two densities

$$\delta m \equiv \delta n_\uparrow - \delta n_\downarrow$$

needs to be calculated. In order to take advantage of this fact we multiply Eq. (18) by  $\alpha\sigma_\alpha$  and sum over  $\alpha$ : this eliminates the space charge term. Then and only then are we allowed to set  $\delta n_\uparrow = -\delta n_\downarrow = \frac{\delta m}{2}$ . The result is the drift-diffusion equation for the spin density

$$\frac{\partial \delta m}{\partial t} = -\frac{\delta m}{\tau_s} + D_s \nabla^2 \delta m + \mu_s \mathbf{E} \cdot \nabla \delta m , \quad (21)$$

where

$$\begin{aligned} \frac{1}{\tau_s} &= \frac{1}{\tau_{\uparrow\uparrow}} + \frac{1}{\tau_{\downarrow\downarrow}} && \text{(spin relaxation time)}, \\ D_s &= \frac{\sigma_\downarrow D_\uparrow + \sigma_\uparrow D_\downarrow}{\sigma_\uparrow + \sigma_\downarrow} && \text{(spin diffusion constant)}, \\ \mu_s &= \frac{\sigma_\downarrow \tilde{\mu}_\uparrow + \sigma_\uparrow \tilde{\mu}_\downarrow}{\sigma_\uparrow + \sigma_\downarrow} && \text{(mobility)} . \end{aligned} \quad (22)$$

The notation is summarized in Table 1.

The largest effect of the electron-electron interaction is to enforce charge neutrality, which allows us to derive an equation for the spin density alone. Because up- and down-spin densities are “tied together” by the charge neutrality condition, the spin diffusion constant  $D_s$  turns out to be a weighted average of the diffusion

TABLE 1. Summary of notation for the drift-diffusion equation in the presence of electron-electron interactions

$D_\uparrow = D_{\uparrow\uparrow} - D_{\uparrow\downarrow}$	$\tilde{\mu}_\uparrow = \tilde{\mu}_{\uparrow\uparrow} - \tilde{\mu}_{\uparrow\downarrow}$
$D_\downarrow = D_{\downarrow\downarrow} - D_{\downarrow\uparrow}$	$\tilde{\mu}_\downarrow = \tilde{\mu}_{\downarrow\downarrow} - \tilde{\mu}_{\downarrow\uparrow}$
$\sigma_\alpha \equiv \sum_\beta \sigma_{\alpha\beta}$	$\tilde{\mu}_{\alpha\beta} \equiv \frac{\partial \sigma_\alpha}{\partial n_\beta}$

constants of each spin. The weight factor for each species is the conductivity of the other species (Smith, 1978). This means that in a spin polarized system the diffusion constant of the minority spins will dominate, since it is weighted by the large conductivity of the majority spins. Similarly, the effective mobility is dominated by the mobility of the minority spins. Just as the speed of a fleet is limited by the speed of its slowest ship, the diffusion constant and the mobility of a spin packet are controlled by the mobility of its slowest component.

The other many-body effect is of course the SCD, which is responsible for the off-diagonal contributions to  $D_{\uparrow}$  and  $D_{\downarrow}$ , shown in Table 1.

Equation (18) can be solved by standard methods. For a spin packet that is initially localized at the origin ( $\delta m(\mathbf{r}, 0) = \Delta M \delta(\mathbf{r})$ ) one has

$$\delta m(\mathbf{r}, t) = \Delta M e^{-t/\tau_s} \frac{e^{-|\mathbf{r} + \mu_s \mathbf{E} t|^2 / 4D_s t}}{(4\pi D_s t)^{3/2}}, \quad (23)$$

i.e., a Gaussian of width  $(D_s t)^{1/2}$ , whose center drifts with a velocity  $\mathbf{v}_d = -\mu_s \mathbf{E}$ , and whose total strength decays as  $e^{-t/\tau_s}$ . An application of this formula to optically induced spin packets will be presented in the next section.

The elimination of the space-charge term in Eq. (18) followed by the imposition of the charge-neutrality condition is a convenient approximation when the primary interest is the spin density. However, in the analysis of electronic devices, one is often interested in the spatial dependence of the electrochemical potentials  $\mu_\alpha = -e\phi + \mu_{c,\alpha}$ , which determine the current through the equation

$$\hat{\mathbf{J}} = -\hat{\sigma} \cdot \nabla \hat{\mu}. \quad (24)$$

(Here  $\hat{\mathbf{J}}$  and  $\hat{\mu}$  denote the column vectors  $\begin{pmatrix} \mathbf{J}_\uparrow \\ \mathbf{J}_\downarrow \end{pmatrix}$  and  $\begin{pmatrix} \mu_\uparrow \\ \mu_\downarrow \end{pmatrix}$ , respectively, and the dot denotes the usual matrix product). In such cases the spin-channel projected theory is not recommended, because even a tiny violation of local charge neutrality can give rise to large differences in the electrochemical potentials of the two species, and hence in the electric currents.

A simple theoretical treatment can still be developed under the assumption that the deviation of the electrochemical potential from its uniform equilibrium value is small. Then, in the linear approximation, the deviation of the density from local equilibrium is given by

$$\delta n_\alpha = \sum_\beta \chi_{\alpha\beta} \delta \mu_{c,\beta} = \sum_\beta \chi_{\alpha\beta} (\delta \mu_\beta + e \delta \phi), \quad (25)$$

where  $\delta \mu_\alpha$  is the deviation of the full electrochemical potential from equilibrium, and  $\delta \phi$  is the change in electric potential. Making use of this relation it is possible to rewrite Eq. (18) as an equation for the electrochemical potentials. The calculation is simpler in the limit of weak electric field, for in that case the  $\nabla \sigma \cdot \mathbf{E}$  term

can be neglected. Then, after simple transformations which are described in the Appendix we arrive at the useful equation

$$\nabla^2 \begin{pmatrix} \delta\mu_\uparrow \\ \delta\mu_\downarrow \end{pmatrix} = \hat{\chi}^{-1} \cdot \begin{pmatrix} \frac{1}{\tilde{D}_\uparrow \tau_{\uparrow\downarrow}} & -\frac{1}{\tilde{D}_\uparrow \tau_{\uparrow\uparrow}} \\ -\frac{1}{\tilde{D}_\downarrow \tau_{\uparrow\downarrow}} & \frac{1}{\tilde{D}_\downarrow \tau_{\downarrow\downarrow}} \end{pmatrix} \cdot \hat{\chi} \cdot \begin{pmatrix} \delta\mu_\uparrow \\ \delta\mu_\downarrow \end{pmatrix}, \quad (26)$$

where

$$\tilde{D}_\uparrow \equiv \frac{1}{(\hat{D}^{-1})_{\uparrow\uparrow} - (\hat{D}^{-1})_{\uparrow\downarrow}}, \quad \tilde{D}_\downarrow \equiv \frac{1}{(\hat{D}^{-1})_{\downarrow\downarrow} - (\hat{D}^{-1})_{\downarrow\uparrow}}. \quad (27)$$

Notice that in this equation the space-charge effect is included in the electric part of the electrochemical potential. In the next section we will illustrate the use of this equation in the analysis of spin-valve devices. For the time being we notice that the matrix

$$\Gamma = \hat{\chi}^{-1} \cdot \begin{pmatrix} \frac{1}{\tilde{D}_\uparrow \tau_{\uparrow\downarrow}} & -\frac{1}{\tilde{D}_\uparrow \tau_{\uparrow\uparrow}} \\ -\frac{1}{\tilde{D}_\downarrow \tau_{\uparrow\downarrow}} & \frac{1}{\tilde{D}_\downarrow \tau_{\downarrow\downarrow}} \end{pmatrix} \cdot \hat{\chi}, \quad (28)$$

appearing on the right hand side of (26) has two eigenvalues: one is 0 and the other is

$$\frac{1}{L_s^2} \equiv \frac{1}{\tilde{D}_\uparrow \tau_{\uparrow\downarrow}} + \frac{1}{\tilde{D}_\downarrow \tau_{\downarrow\uparrow}}, \quad (29)$$

where  $L_s$  is the spin diffusion length. The existence of the eigenvalue 0 is a direct consequence of the identity (12): the associated right eigenvector is  $\begin{pmatrix} 1 \\ 1 \end{pmatrix}$ , which corresponds to the conserved electric charge mode. The second eigenvalue (29) follows from the fact that the trace of a matrix is the sum of its eigenvalues. The right eigenvector associated with this eigenvalue is easily shown to be proportional to  $\begin{pmatrix} \sigma_\downarrow \\ -\sigma_\uparrow \end{pmatrix}$  or, equivalently

$$\begin{pmatrix} 1/\sigma_\uparrow \\ -1/\sigma_\downarrow \end{pmatrix}, \quad (30)$$

which is the spin mode. We will make heavy use of these eigenvectors in the analysis of spin-valve devices.

## 5 Simple Applications

### 5.1 SPIN PACKET DIFFUSION

Spin packets can be injected by shining circularly polarized light on doped as well as undoped GaAs. Their time evolution can be monitored by measuring the Faraday-rotation angle of linearly polarized probe light at different times (Kikkawa and Awschalom, 1998; Kikkawa and Awschalom, 1999).

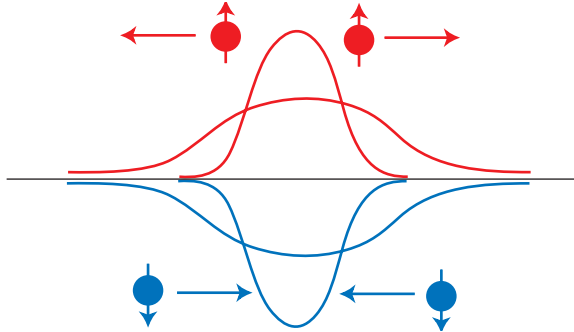


Figure 2. Diffusion of a spin packet entails oppositely directed flows of up- and down-spin electrons

Figure 2 illustrates the typical structure of a spin packet in a doped semiconductor – an excess of spin up electrons neutralized by an equal deficiency of spin-down electrons. Such packets offer an ideal testing ground for the spin drift–diffusion equation (21) and its solution, Eq. (23). The calculations are particularly simple in the spin-unpolarized case since all the matrices have equal diagonal elements and equal off-diagonal elements. For example, the resistivity matrix is

$$\hat{\rho} = \rho_D \begin{pmatrix} 2 + \gamma\tau & -\gamma\tau \\ -\gamma\tau & 2 + \gamma\tau \end{pmatrix}, \quad (31)$$

where  $\rho_D$  is the usual Drude resistivity and the scattering time  $\tau$  is spin-independent. Its inverse, the conductivity matrix is

$$\hat{\sigma} = \frac{ne^2\tau}{4m_b(1 + \gamma\tau)} \begin{pmatrix} 2 + \gamma\tau & \gamma\tau \\ \gamma\tau & 2 + \gamma\tau \end{pmatrix}. \quad (32)$$

The susceptibility matrix  $\hat{\chi}$  has a similar structure, with  $\chi_{\uparrow\uparrow} = \chi_{\downarrow\downarrow}$  and  $\chi_{\uparrow\downarrow} = \chi_{\downarrow\uparrow}$ . We introduce the spin susceptibility

$$\chi_s \equiv \chi_{\uparrow\uparrow} - \chi_{\uparrow\downarrow} - \chi_{\downarrow\uparrow} + \chi_{\downarrow\downarrow} = 2(\chi_{\uparrow\uparrow} - \chi_{\uparrow\downarrow}). \quad (33)$$

Then making use of the Einstein relation (10) we obtain (D’Amico and Vignale, 2001)

$$D_s = D_{\uparrow\uparrow} - D_{\uparrow\downarrow} = \frac{\sigma_{\uparrow\uparrow} - \sigma_{\uparrow\downarrow}}{e^2(\chi_{\uparrow\uparrow} - \chi_{\uparrow\downarrow})} = \frac{n\tau}{m_b\chi_s(1 + \gamma\tau)}. \quad (34)$$

A similar calculation leads to the conclusion that the spin-packet mobility  $\mu_s$  is unrenormalized by Coulomb interactions, i.e., we have

$$\mu_s = \frac{e\tau}{m_b}. \quad (35)$$

The physical meaning of these equations is quite clear. The spin diffusion constant is renormalized by Coulomb interactions in two different ways: through the spin Coulomb drag coefficient  $\gamma$  (see Figure 2 and its caption) and through the renormalization of the spin susceptibility.

The formula for  $D_s$  should be compared to the well-known formula that expresses the *electrical diffusion constant*,  $D_c$ , in terms of the electrical conductivity and the proper electronic compressibility  $\chi_c \equiv 2(\chi_{\uparrow\uparrow} + \chi_{\uparrow\downarrow})$ :

$$D_c = \frac{\sigma_D}{e^2 \chi_c} = \frac{n\tau}{m_b \chi_c}. \quad (36)$$

The ratio between the two diffusion constants is

$$\frac{D_s}{D_c} = \frac{\chi_c / \chi_s}{1 + \gamma\tau}. \quad (37)$$

Notice that there is no limit to how large the SCD renormalization can get as the electron mobility increases, i.e., as  $\tau$  tends to infinity. The reason for this is that in the limit of infinite mobility the diffusion constant approaches the finite “intrinsic” limit

$$D_s \xrightarrow{\tau \rightarrow \infty} D_{s,i} = \frac{n}{m_b \chi_s \gamma} \quad (38)$$

instead of growing indefinitely as it would in a noninteracting system. This intrinsic limit is large but not unreachable in high-mobility doped GaAs.<sup>1</sup>

As for the ratio  $\chi_c / \chi_s$ , its value is well known from quantum Monte Carlo studies of the homogeneous electron liquid. This ratio tends to 1 in the noninteracting limit (with both  $\chi_c$  and  $\chi_s$  tending to the density of states at the Fermi surface), and it is also 1 to first order in the Coulomb interaction. Differences between  $\chi_c$  and  $\chi_s$  are due to the existence of a finite  $\chi_{\uparrow\downarrow}$ , which appears only to second order in the Coulomb interaction.<sup>2</sup> The correlation effects that are responsible for  $\chi_{\uparrow\downarrow}$  enhance the compressibility while reducing the spin-susceptibility: therefore  $\chi_c / \chi_s$  is larger than 1, but typically only by a few percent at the densities of interest.<sup>3</sup>

Optical measurements of the spin diffusion constant have recently been done by Kikkawa and Awschalom (1998) and Weber and Awschalom (2005). The

<sup>1</sup>Of course, this assumes that  $\gamma$  is nonzero. This in turn requires a finite temperature, implying that other mechanisms, such as electron–phonon scattering, would prevent in practice the diffusion constant from diverging.

<sup>2</sup>In Landau’s theory of Fermi liquids one has

$$\frac{\chi_c}{\chi_s} = \frac{1 + F_0^a}{1 + F_0^s}, \quad (39)$$

where  $F_0^s$  and  $F_0^a$  are the phenomenological Landau parameters with angular momentum  $\ell = 0$  in the spin and density channels, respectively.

<sup>3</sup>However, the spin susceptibility will diverge at the onset of ferromagnetism in the electron liquid. Accordingly, the spin diffusion constant should vanish at the ferromagnetic transition.

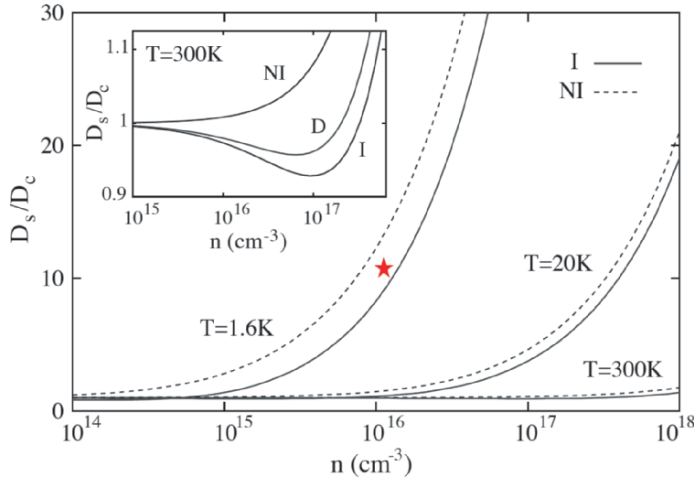


*Figure 3.* Theoretically calculated spin-diffusion constant (in units of the classical diffusion constant  $D_{class}$ ) for n-doped GaAs at three different temperatures. The results for the interacting system (I) are plotted as solid lines, and are lower than the results for the non-interacting system (NI, dashed lines). The star is the experimental point measured by Kikkawa and Awschalom (1999) at  $T = 1.6$  K. Inset shows the relative importance of SCD and spin-susceptibility enhancement at 300 K. The curve labelled “D” shows the effect of the SCD alone

second set of measurements focused specifically on the spin diffusion constant in high mobility samples and will be discussed extensively in section 7, after the microscopic theory of  $\gamma$  is presented in section 6.

Figure 3 shows the numerically calculated spin diffusion constant for n-type doped GaAs as a function of doping density at three different temperatures. The SCD coefficient  $\gamma$  was obtained from the semi-analytical microscopic theory of section 6. The mobility was taken to be  $3 \times 10^3 \text{ cm}^2/\text{Vs}$ —a value appropriate for the experiments at 1.6 K.  $D_s$  is expressed in units of the classical diffusion constant  $D_{class} = \frac{n k_B T}{4\pi \hbar n_1}$ , where  $k_B$  is the Boltzmann constant. The graph also shows the experimental point from the paper of Kikkawa and Awschalom (1999) at  $T = 1.6$  K.

There was initially some surprise at the large value of  $D_s$  (about 10 times the classical value). This is now well understood to be a consequence of the degenerate character of the carriers in these high density samples. As emphasized by Flatté and Byers (2000), electron doping is essential to achieve good spin-packet mobility: in an undoped sample the spin-packet would inevitably include a hole component in the valence band, with drastic reduction of the mobility.

Figure 3 shows that interaction effects are relatively small ( $\sim 20\%$ ) at the chosen value of the mobility. Indeed the intrinsic  $D_s$  at  $n = 10^{16} \text{ cm}^{-3}$  and  $T = 1.6$  K is of the order of  $10^4 \text{ cm}^2/\text{s}$ , more than a thousand times larger than the reported value of  $D_s$ : this is a clear indication that disorder is the main

diffusion-limiting mechanism in these samples. As expected, both the spin drag and the spin susceptibility reduce  $D_s$ , and the first effect appears to dominate at room temperature: this is demonstrated in the inset where the curve calculated including SCD only is found to be very close to the curve that includes both SCD and the spin susceptibility enhancement.

## 5.2 SPIN VALVE DEVICE AND SPIN INJECTION

Figure 4 shows schematically the structure of a spin valve device. A nonmagnetic doped semiconductor is sandwiched between two ferromagnetic metallic electrodes (Baibich et al., 1988; Valet and Fert, 1993; Schmidt et al., 2000, 2001). An electric field is applied across the structure by means of a battery connected to the electrodes. The resistance of this device depends significantly on the relative orientation of the magnetizations in the two electrodes—this is the GMR effect in the current-perpendicular-to-plane (CPP) configuration. Our objective is to calculate this dependence, as well as the values of the spin currents and the spin accumulations at the metal-semiconductor interfaces—all including the effect of the spin Coulomb drag. I first discuss the device within the framework of Eq. (26), which is valid for weak electric field. At the end of this section I will show how the conclusions of this analysis must be modified in order to take into account a strong electric field (Yu and Flatté, 2002). The calculations that follow are based on the following assumptions (Vignale, 2005): (i) the SCD is appreciable only in the semiconductor region; (ii) the semiconductor region is essentially paramagnetic; (iii) the conductivity of the ferromagnetic electrodes  $\hat{\sigma}^f$ , is purely diagonal and strongly dependent on the spin polarization  $p \equiv \frac{n_\uparrow - n_\downarrow}{n_\uparrow + n_\downarrow}$ . Thus we have

$$\sigma_{\uparrow\uparrow}^f = \frac{1+p}{2} \sigma^f, \quad \sigma_{\downarrow\downarrow}^f = \frac{1-p}{2} \sigma^f, \quad \sigma_{\uparrow\downarrow}^f = 0, \text{ or, more compactly,}$$

$$\hat{\sigma}_f = \begin{pmatrix} \frac{1+p}{2} \sigma^f & 0 \\ 0 & \frac{1-p}{2} \sigma^f \end{pmatrix}, \quad (40)$$

where  $\sigma^f$  is the total electrical conductivity for both spin channels.

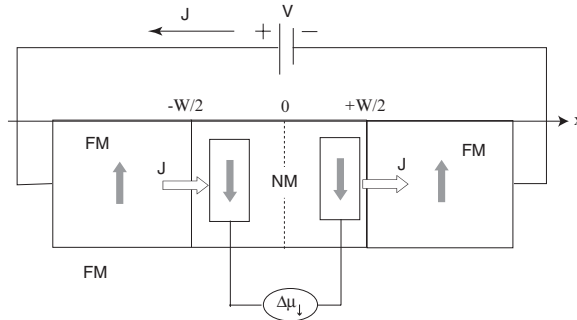


Figure 4. Schematics of a spin valve device

Equation (26) is now written for each of the three homogeneous sections of the device:

$$\frac{d^2\mu_\alpha(x)}{dx^2} = \sum_\beta \Gamma_{\alpha\beta}\mu_\beta(x), \quad (41)$$

where the matrix  $\hat{\Gamma}$  has, in each section, the eigenvectors  $\begin{pmatrix} 1 \\ 1 \end{pmatrix}$  (with eigenvalue 0) and  $\begin{pmatrix} 1/\sigma_\uparrow \\ -1/\sigma_\downarrow \end{pmatrix}$  (with eigenvalue  $\frac{1}{L_s^2}$ ), with the values of the parameters appropriate for that section of the device. Recall that  $\mu_\alpha$  in Eq. (41) includes the electrostatic potential due to the battery: its value must therefore vary from  $-\frac{eV}{2}$  at  $x = -\infty$  to  $\frac{eV}{2}$  at  $x = \infty$ , where  $V$  is the potential difference supplied by the battery.

In the case of parallel magnetizations in the two electrodes the solution for  $\mu(x)$  is odd under inversion about the center  $x = 0$ :  $\mu_\alpha(x) = -\mu_\alpha(-x)$  and vanishes at  $x = 0$ . Furthermore, it must be finite and continuous at the metal–semiconductor interfaces, which we put at  $x = \pm W/2$ . Its derivative must be continuous too. The solution that satisfies all these condition is (for  $x < 0$ ) (Vignale and D’Amico, 2003; Vignale, 2005)

$$\begin{pmatrix} \mu_\uparrow \\ \mu_\downarrow \end{pmatrix} = \begin{cases} \frac{eJW}{\sigma^f} \left[ \left[ -\frac{C_0}{2} + \left( \frac{1}{2} + \frac{x}{W} \right) \right] \begin{pmatrix} 1 \\ 1 \end{pmatrix} + 2C_1 e^{\frac{W/2+x}{L^f}} \begin{pmatrix} (1+p)^{-1} \\ -(1-p)^{-1} \end{pmatrix} \right], & x < -\frac{W}{2}, \\ \frac{eJW}{\sigma^s} \left[ \frac{x}{W} \begin{pmatrix} 1 \\ 1 \end{pmatrix} + 2C_2 \sinh\left(\frac{x}{L^s}\right) \begin{pmatrix} 1 \\ -1 \end{pmatrix} \right], & -\frac{W}{2} \leq x \leq 0, \end{cases} \quad (42)$$

where  $J$  is the charge current,  $\sigma^f$  and  $\sigma^s$  are the conductivities of the ferromagnetic ( $f$ ) electrodes and of the semiconductor, and  $L^f$  and  $L^s$  the spin diffusion lengths in the electrodes and in the semiconductor, respectively. Notice that the continuity of the charge current,  $J$ , is already built in Eq. (42). The value of the conserved current is determined by the boundary condition  $\mu_\alpha(\pm\infty) = \pm eV$ . The three constants  $C_0$ ,  $C_1$ , and  $C_2$  are determined from the continuity of the two electrochemical potentials and of the spin current  $j_\uparrow(x) - j_\downarrow(x)$  at  $x = -W/2$ . Their explicit forms are easily found to be

$$\begin{aligned} C_0 &= \frac{\sigma^f}{\sigma^s} + \frac{2p^2}{\mathcal{D}} \sinh\left(\frac{W}{2L^s}\right), \\ C_1 &= -\frac{p(1-p^2)}{2\mathcal{D}} \sinh\left(\frac{W}{2L^s}\right), \\ C_2 &= \frac{p\sigma^s}{2\sigma^f \mathcal{D}}, \end{aligned} \quad (43)$$

with

$$\mathcal{D} = \frac{W(1-p^2)}{L^f} \sinh\left(\frac{W}{2L^s}\right) + \frac{W\sigma^s}{L^s\sigma^f} \frac{1}{1+\gamma\tau} \cosh\left(\frac{W}{2L^s}\right). \quad (44)$$

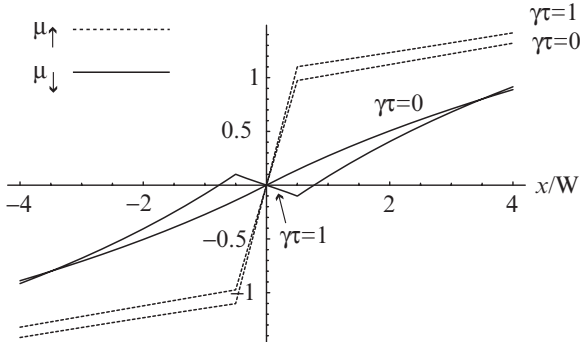


Figure 5. Electrochemical potentials  $\mu_\uparrow/eJ$  and  $\mu_\downarrow/eJ$  for the spin valve device of Fig. 4 in the case of parallel alignment of the electrodes. We assume  $\sigma^f/\sigma^s = 10$ ,  $L_s = 2W$ ,  $L_f = 4W$  and  $p = 0.99$ .  $x$  is in units of  $W$  and  $\mu_\uparrow/eJ$ —a resistivity—is in units of  $1/\sigma^s$

As mentioned above, the solution for  $x > 0$  is obtained by means of the symmetry relation  $\mu_\sigma(x) = -\mu_\sigma(-x)$ . Notice how the SCD renormalization factor  $1 + \gamma\tau$  enters these expressions only at one place, namely in the expression for  $\mathcal{D}$ .

The behavior of the solution is shown in Figure 5. Far from the interface both  $\mu_\uparrow$  and  $\mu_\downarrow$  vary linearly, with slope  $\frac{eJ}{\sigma^f}$ . This slope is the electric field times  $e$ . Near the interfaces (typically within distances  $L_s$  and  $L_f$  of it) the behaviors of the two chemical potentials begin to differ qualitatively. The majority spin potentials remains more or less constant within the metallic regions, but the minority spin potentials change more rapidly, indicating an accumulation of down-spin electrons on the left interface and a depletion of down-spin electrons at the right interface. (This is not surprising when you think that the electronic current flows from right to left, implying that the electrons that enter the left electrode come from a region in which they are equally likely to have their spin oriented in either direction.)

Let us now look at the electrochemical potentials inside the semiconductor region ( $|x| < W/2$ ). Consider the noninteracting case ( $\gamma = 0$ ) first. The slopes of the up-spin chemical potential is greatly increased and overcomes the slope of the down-spin chemical potential. In particular, the slopes at the geometric center of the device are

$$\begin{aligned} E_\uparrow(0) &= \frac{J}{\sigma^s} + \frac{JWp}{L^s \sigma^f \mathcal{D}} \\ E_\downarrow(0) &= \frac{J}{\sigma^s} - \frac{JWp}{L^s \sigma^f \mathcal{D}}, \end{aligned} \quad (45)$$

so the up-spin field is larger than the down-spin field, but the difference is very small if  $\sigma^f \gg \sigma^s$ . This is known as the *conductivity mismatch problem* (Schmidt et al., 2000). It implies that the spin polarization of the current in the semiconductor will be extremely small if the conductivity of the semiconductor is much smaller than that of the ferromagnetic electrodes. One way to make up for this

is to increase the spin polarization of the electrodes or the spin diffusion lengths to the point that the first term in  $\mathcal{D}$  becomes negligible with respect to the second, and we have  $\mathcal{D} \approx \frac{W}{L_s} \frac{\sigma^s}{\sigma^f} \frac{1}{1+\gamma\tau}$ . Then the electrochemical fields at the center of the device are approximately given by

$$\begin{aligned} E_{\uparrow}(0) &\approx \frac{Jp}{\sigma^s} [1 + p(1 + \gamma\tau)] \\ E_{\downarrow}(0) &\approx \frac{Jp}{\sigma^s} [1 - p(1 + \gamma\tau)] . \end{aligned} \quad (46)$$

In this case the difference between the electrochemical fields is large and can support a significant spin polarization of the current.

In the absence of SCD we see that  $E_{\downarrow}(0) \rightarrow 0$  for  $p \rightarrow 1$ , indicating that in this limit only up-spin electrons flow through the device, as intuition suggests. But when SCD is taken into account something strange happens: now  $E_{\downarrow}(0)$  becomes negative if  $p > \frac{1}{1+\gamma\tau}$ . At first sight this seems absurd, because we know that no spin-down current must flow for  $p \approx 1$ . But in the presence of SCD the spin-down current is determined by both  $E_{\uparrow}$  and  $E_{\downarrow}$ . The negative value of  $E_{\downarrow}$  is needed precisely to cancel the effect of the positive  $E_{\uparrow}$ , which drags the down-spin electrons along with the up-spin electrons. The experimental observation of a negative electrochemical field acting on the spin down electrons would provide unambiguous evidence for the SCD. The second equation (46) shows that this change in sign can occur at relatively small values of  $p$ , provided  $\gamma\tau$  is large. Realistic values of  $\gamma\tau$  will be discussed in the next section.

One can also ask how the SCD affects the spin injection efficiency  $\beta \equiv \frac{J_{\uparrow}-J_{\downarrow}}{J_p}$ . A simple calculation gives

$$\beta = \frac{1}{1 + (1 - p^2) \frac{L_s \sigma^f}{L_f \sigma^s} (1 + \gamma\tau)} . \quad (47)$$

For  $p$  very close to 1 it is easy to see that the efficiency remains close to 100%, and is essentially unaffected by the SCD. For smaller values of  $p$ , however, the SCD considerably reduces the efficiency of spin injection. This is shown in Figure 6 where  $\beta$  is plotted as a function of the ratio  $\frac{\sigma_{\downarrow}}{\sigma^f} = \frac{1}{4} \frac{\gamma\tau}{1+\gamma\tau}$ .

Let us now consider the electrical resistance of the spin valve device. Far from the interfaces the electrochemical potentials of the two spin orientations tend to common values  $\mu_- = -\frac{eJW(C_0-1)}{2\sigma^f} + \frac{eJx}{\sigma^f}$  for  $x \rightarrow -\infty$  and  $\mu_+ = +\frac{eJW(C_0-1)}{2\sigma^f} + \frac{eJx}{\sigma^f}$  for  $x \rightarrow +\infty$ . The difference between these two asymptotic behaviors is  $e$  times the voltage drop due to the presence of the semiconductor layer. Hence, the resistance of our device (per unit cross-sectional area) is given by

$$R_p = R_c(p) + R^s + \frac{2Wp^2}{\mathcal{D}\sigma^f} \sinh\left(\frac{W}{2L_s}\right), \quad (48)$$

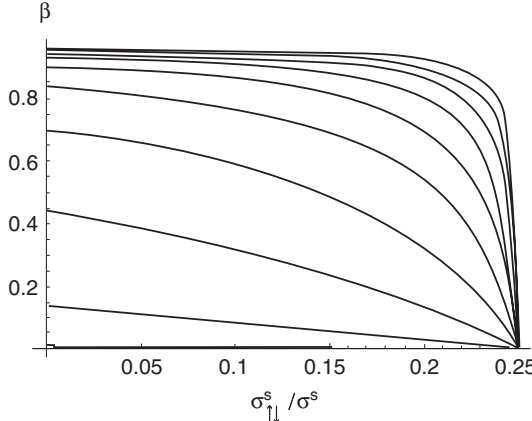


Figure 6. Effect of SCD on spin injection efficiency in the spin valve device for different values of the polarization  $p$  of the electrodes. Here  $p = 1 - 0.1/n^4$  with  $n$  ranging from 1 (bottom curve) to 10 (top curve) in steps of 1. The parameters (other than  $p$ ) are the same as in the caption of Fig. 5

where  $R_c(p)$  is the combined resistance of the electrodes and the external wires, and  $R^s = \frac{W}{\sigma^s}$  is the ordinary resistance of the semiconductor. The last term on the right hand side of this equation arises from the spin accumulations at the interfaces between the electrodes and the semiconductor.

In order to calculate the magnetoresistance one must compare this resistance with that of a similar device in which the two ferromagnetic electrodes are magnetized in opposite directions. The solution for the electrochemical potentials in this second case has the form (Vignale, 2005)

$$\begin{pmatrix} \mu_\uparrow \\ \mu_\downarrow \end{pmatrix} = \begin{cases} \frac{eJW}{\sigma^f} \left\{ \left[ -\frac{C'_0}{2} + \left( \frac{1}{2} + \frac{x}{W} \right) \right] \begin{pmatrix} 1 \\ 1 \end{pmatrix} + 2C'_1 e^{\frac{W/2+x}{L^f}} \begin{pmatrix} (1+p)^{-1} \\ -(1-p)^{-1} \end{pmatrix} \right\}, & x < -\frac{W}{2}, \\ \frac{eJW}{\sigma^s} \left\{ \frac{x}{W} \begin{pmatrix} 1 \\ 1 \end{pmatrix} - 2C'_2 \cosh\left(\frac{x}{L^s}\right) \begin{pmatrix} 1 \\ -1 \end{pmatrix} \right\}, & -\frac{W}{2} \leq x \leq 0, \end{cases} \quad (49)$$

where the constants  $C'_0 - C'_2$  are given by

$$\begin{aligned} C'_0 &= \frac{\sigma^f}{\sigma^s} + \frac{2p^2}{\mathcal{D}'} \cosh\left(\frac{W}{2L^s}\right), \\ C'_1 &= -\frac{p(1-p^2)}{2\mathcal{D}'} \cosh\left(\frac{W}{2L^s}\right), \\ C'_2 &= \frac{p\sigma^s}{2\sigma^f \mathcal{D}'}, \end{aligned} \quad (50)$$

and

$$\mathcal{D}' = \frac{W(1-p^2)}{L^f} \cosh\left(\frac{W}{2L^s}\right) + \frac{W\sigma^s}{L^s\sigma^f} \frac{1}{1+\gamma\tau} \sinh\left(\frac{W}{2L^s}\right). \quad (51)$$

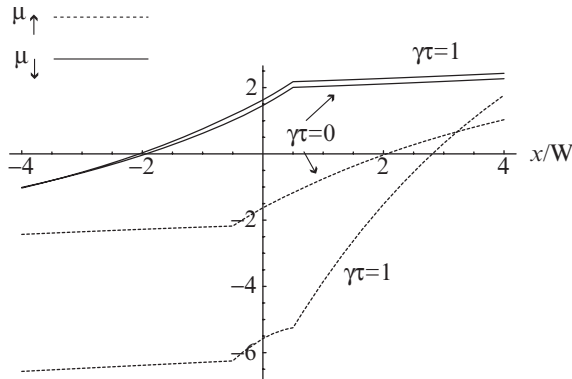


Figure 7. Electrochemical potentials of the spin valve device of Fig. 4 in the case of antiparallel alignment of the electrodes. The parameters and the units are the same as in the caption of Fig. 5

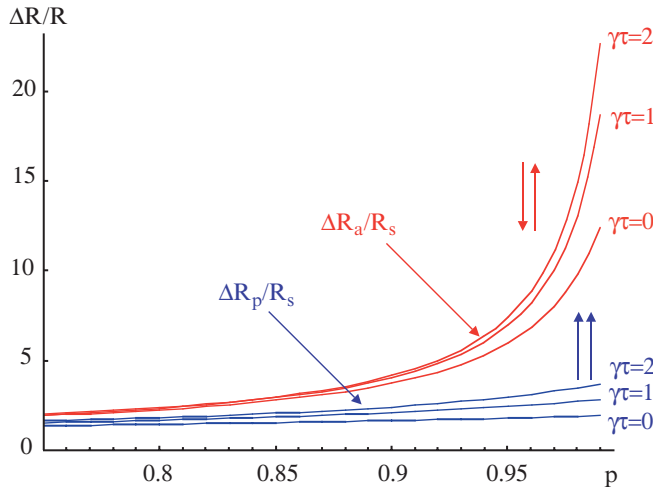


Figure 8. Comparison of spin-accumulation resistance for parallel and antiparallel alignment of the electrodes for different values of the spin drag coefficient  $\gamma$

The solution for  $x > 0$  is obtained by means of the symmetry relation  $\mu_\sigma(x) = -\mu_{-\sigma}(-x)$ . A representative plot of  $\mu_\uparrow$  and  $\mu_\downarrow$  is shown in Figure 7.

From this solution, following the same procedure used in the case of parallel magnetizations of the electrodes, we obtain a resistance per unit area

$$R_a = R_c(p) + R^s + \frac{2Wp^2}{\mathcal{D}'\sigma^f} \sinh\left(\frac{W}{2L^s}\right). \quad (52)$$

The magnetoresistance is given by the difference  $R_a - R_p$ . Figure 8 compares the behavior of the spin-accumulation contributions to  $R_p$  and  $R_a$  (i.e. the last terms

on the right hand sides of Eqs. (48) and (52)) as functions of  $p$  for different values of  $\gamma\tau$ . Clearly, the effect of  $\gamma\tau$  becomes significant only for large polarizations, but what is interesting is that the resistance in the antiferromagnetic channel is enhanced much more than in the ferromagnetic channel. Hence the GMR effect is strongly enhanced by the SCD when the polarization of the electrodes approaches 100%.

Our analysis of the spin valve device thus far has been based on the assumption that the electric field is weak. Recently Yu and Flatté (2002) have questioned this assumption, and analyzed the current characteristics of the device for large electric field based on the complete diffusion equation (21). They have shown that in a typical doped semiconductor even a modest electric field of 1 V/cm is “large”, and its main effect is to create two different spin diffusion lengths, one shorter and one longer than the zero-field spin diffusion length, one “upstream” and one “downstream” the electric field. Details of this study are presented in the chapter by Flatté in this book. Subsequently the effect of the electric field has been carefully studied by D’Amico (2004), with inclusion of the SCD in both the degenerate and nondegenerate regimes. Here it suffices to say that the net effect of the electric field on the spin injection coefficient  $\beta$  (see Eq. (47)) is to replace  $L^s$  in Eq. (47) by the shorter “upstream” diffusion length

$$\frac{1}{L_u} = \left\{ \frac{eE}{2k_B T} + \sqrt{\left( \frac{eE}{2k_B T} \right)^2 + \left( \frac{1}{L^s} \right)^2} \right\}^{-1}. \quad (53)$$

The effect of the SCD is still entirely contained in the  $1+\gamma\tau$  factor of that equation.

## 6 Microscopic Theory of Spin Coulomb Drag

We have seen that in order to set up and solve the drift-diffusion equations we need to know the homogeneous conductivity matrix  $\hat{\sigma}$  and the homogeneous susceptibility matrix  $\hat{\chi}$ : the Einstein relation (10) does all the rest. The susceptibility matrix is an equilibrium property which has been calculated by quantum Monte Carlo. For the conductivity, however, we do not have such a luxury and must resort to approximations.

As discussed in section 3 a key quantity is the spin drag coefficient  $\gamma$ . It turns out that this can be obtained quite easily by a simple Fermi golden rule calculation in which the matrix element of the electron-electron interaction between plane wave states near the Fermi surface is taken to be  $\frac{v_q}{\epsilon(q,0)}$ , where  $v_q$  is the Fourier transform of the Coulomb interaction ( $=\frac{2\pi e^2}{\epsilon_b q}$  in two dimensions,  $\frac{4\pi e^2}{\epsilon_b q^2}$  in three dimensions),  $\epsilon_b$  is the background dielectric constant, and  $\epsilon(q,0)$

is the contribution of the doped electrons to the static dielectric constant. More complicated effects are simply neglected.<sup>4</sup>

To build a more general formalism we resort to the Kubo formula for the conductivity:

$$\sigma_{\alpha\beta}(\omega) = -\frac{1}{i\omega} \frac{e^2}{m_b} \left( n_\alpha \delta_{\alpha\beta} + \frac{\langle\langle \mathbf{P}_\alpha; \mathbf{P}_\beta \rangle\rangle_\omega}{m} \right), \quad (54)$$

where the symbol

$$\langle\langle A; B \rangle\rangle_\omega = -\frac{i}{\hbar V} \int_0^\infty \langle [A(t), B(0)] \rangle e^{i\omega t} dt \quad (55)$$

represents the retarded linear response function for the expectation value of an observable  $A$  to a perturbation that couples linearly to the observable  $B$ . Here  $A(t) = e^{iHt/\hbar} A(0) e^{-iHt/\hbar}$  is the time evolution of the operator  $A$  under the Hamiltonian  $H$  which includes electron-electron interactions, but not the coupling to the external electric field.  $[A(t), B(0)]$  denotes the commutator of  $A(t)$  and  $B(0)$ , and  $\langle \dots \rangle$  denotes the equilibrium average of the quantity within brackets. In Eq. (54)  $\mathbf{P}_\alpha$  is the total momentum associated with the  $\alpha$ -spin component of the electron gas, that is

$$\mathbf{P}_\alpha \equiv \sum_{i=1}^N \mathbf{p}_i \frac{1 + \alpha \sigma_{z,i}}{2}, \quad (56)$$

where  $\mathbf{p}_i$  is the momentum of the  $i$ -th electron and  $\frac{\hbar}{2}\sigma_{z,i}$  is the  $z$ -component of the spin of the  $i$ -th electron.  $V$  is the total volume of the electron gas (or the area in two dimensions).

An immediate problem in the evaluation of Eq. (54) is that the quantity  $\langle\langle \mathbf{P}_\alpha; \mathbf{P}_\beta \rangle\rangle_\omega$  vanishes for a clean translationally invariant system without electron-electron interactions,<sup>5</sup> but jumps to a finite value ( $-nm\delta_{\alpha\beta}$  at  $\omega = 0$ ) as soon as an infinitesimal amount of disorder is introduced into the system. This is because in the zero frequency limit the  $\langle\langle \mathbf{P}_\alpha; \mathbf{P}_\beta \rangle\rangle_\omega$  of Eq. (54) must cancel the free-electron pole coming from the first term (we assume that the system is not a superconductor!). This is nice, but it also means that perturbation theory with respect to disorder must necessarily fail at frequencies  $\omega \ll \frac{1}{\tau}$  where  $\tau$  is the electron-impurity mean collision time.

<sup>4</sup>One of the effects that are neglected in the naive theory is the exchange correction to the scattering rate. This arises because the scattering takes place not between single plane wave states but between Slater determinants of plane waves. Fortunately, in this case, there is no exchange effect in leading order, since the primary scattering process involves two electrons of opposite spins, which are effectively made distinguishable by their different spin.

<sup>5</sup>This is an immediate consequence of the general theorem according to which the linear response function  $\langle\langle A; B \rangle\rangle_\omega$  is zero if either  $A$  or  $B$  are constants of the motion with Hamiltonian  $H$ . In the absence of impurities the total momentum of either spin in any direction is conserved.

The trick by which we handle this problem is to calculate  $\sigma_{\alpha\beta}(\omega)$  at a frequency  $\omega \gg \frac{1}{\tau}$  where perturbation theory is applicable, i.e., where the second term of Eq. (54) is much smaller than the first (D'Amico and Vignale, 2000). Then we can invert the conductivity matrix to first order in  $\langle\langle \mathbf{P}_\alpha; \mathbf{P}_\beta \rangle\rangle_\omega$  to find the resistivity matrix,

$$\rho_{\alpha\beta}(\omega) = -\frac{i\omega m_b}{e^2} \left( \frac{\delta_{\alpha\beta}}{n_\alpha} - \frac{1}{n_\alpha} \frac{\langle\langle \mathbf{P}_\uparrow; \mathbf{P}_\downarrow \rangle\rangle_\omega}{m_b} \frac{1}{n_\beta} \right). \quad (57)$$

Admittedly, this formula is valid only for  $\omega \gg \frac{1}{\tau}$ , but in the limit  $\frac{1}{\tau} \rightarrow 0$  (which means in practice  $\frac{1}{\tau}$  much smaller than all other energy scales, including the temperature and the Fermi energy) we can assume that the resistivity does not vary significantly between  $\omega = 0$  and  $\omega = \frac{1}{\tau}$  (this is because the resistivity, unlike the conductivity, has no pole at  $\omega = -\frac{i}{\tau}$ ). Then Eq. (57) is a good starting point for the calculation of both the ordinary electron–impurity resistivity and the spin drag resistivity.

From this point on we focus on the latter. Thus, we select the  $\uparrow\downarrow$  matrix element of  $\hat{\rho}$ ,

$$\rho_{\uparrow\downarrow}(\omega) = \frac{i\omega}{e^2} \frac{\langle\langle \mathbf{P}_\uparrow; \mathbf{P}_\downarrow \rangle\rangle_\omega}{n_\uparrow n_\downarrow}, \quad (58)$$

and make use of the equations of motion

$$\begin{aligned} \langle\langle A; B \rangle\rangle_\omega &= \frac{1}{\omega} (\langle\langle [A, B] \rangle + i\langle\langle \dot{A}; B \rangle\rangle_\omega), \\ &= \frac{1}{\omega} (\langle\langle [A, B] \rangle - i\langle\langle A; \dot{B} \rangle\rangle_\omega), \end{aligned} \quad (59)$$

(where  $\dot{A} \equiv -i[A, H]$  is the time derivative of  $A$ ) twice to arrive at

$$\rho_{\uparrow\downarrow}(\omega) = \frac{i}{e^2 n_\uparrow n_\downarrow} \frac{\langle\langle \dot{\mathbf{P}}_\uparrow; \dot{\mathbf{P}}_\downarrow \rangle\rangle_\omega + i\langle\langle \dot{\mathbf{P}}_\uparrow, \mathbf{P}_\downarrow \rangle\rangle_\omega}{\omega}. \quad (60)$$

Notice that  $\dot{\mathbf{P}}_\alpha$  is the net force,  $\mathbf{F}_\alpha$ , acting on electrons of spin  $\alpha$ . Its explicit expression is

$$\mathbf{F}_\alpha \equiv \dot{\mathbf{P}}_\alpha = -\frac{i}{V} \sum_{\mathbf{q}} \mathbf{q} v_q n_{\bar{\alpha}} n_{-\mathbf{q}\alpha} - \frac{i}{V} \sum_{\mathbf{q}} \mathbf{q} v_q^{ei} n_{\mathbf{q}}^i n_{-\mathbf{q}\alpha}, \quad (61)$$

where the first term on the right hand side is the force exerted on spin  $\alpha$  electrons by electrons of the opposite spin orientation  $\bar{\alpha}$  (the net force exerted by spin  $\alpha$  electrons on themselves vanishes, by Newton's third law), and the second term is the force exerted on the same electrons by impurities. The operators  $n_{\mathbf{q}\alpha}$  represent the Fourier components of the density fluctuation for spin  $\alpha$  while  $n_{\mathbf{q}}^i$

is the Fourier component of the density of impurity (a  $c$ -number), and  $v_q^{ei}$  is the Fourier transform of the electron-impurity potential.

The average of the commutator  $[\hat{\mathbf{P}}_\uparrow, \hat{\mathbf{P}}_\downarrow]$  in Eq. (60) is purely imaginary, since the commutator of two hermitian operators is anti-hermitian. This term therefore does not contribute to the real part of the spin drag resistivity which is finally given by

$$\Re e \rho_{\uparrow\downarrow}(\omega) = -\frac{1}{e^2 n_{\uparrow} n_{\downarrow}} \Im m \frac{\langle\langle \mathbf{F}_\uparrow; \mathbf{F}_\downarrow \rangle\rangle_\omega}{\omega} \equiv -\frac{m_b \gamma(\omega)}{ne^2}. \quad (62)$$

When the expression (61) for the force is substituted in this expression three types of terms are generated: Coulomb–Coulomb terms, Coulomb–impurity terms, and impurity–impurity terms. The Coulomb–Coulomb terms are proportional to  $|v_q|^2$ , while the remaining two types of terms are both proportional (in leading order) to  $v_q |v_q^{ei}|^2$ . The Coulomb–impurity term is proportional to  $v_q |v_q^{ei}|^2$  because the random electron–impurity potential must enter with at least two powers to survive disorder averaging. And the impurity–impurity term is also proportional to  $v_q |v_q^{ei}|^2$  because the average  $\langle n_{-\mathbf{q}\uparrow} n_{\mathbf{q}\downarrow} \rangle$  vanishes in the absence of Coulomb interactions.

A careful examination of the last two terms (D’Amico and Vignale, 2000), shows that they cancel out exactly to the leading order  $v_q |v_q^{ei}|^2$ . So, in a homogeneous system, there is no first-order contribution to the SCD from the Coulomb interaction. The first nonvanishing term is of second-order in the electron–electron interaction (coming from the Coulomb–Coulomb term) and has the following form:

$$\Re e \rho_{\uparrow\downarrow}(\omega) = \frac{1}{n_{\uparrow} n_{\downarrow} e^2 \omega \mathcal{V}^2} \sum_{\mathbf{q}\mathbf{q}'} \frac{\mathbf{q} \cdot \mathbf{q}'}{3} v_q v_{q'} \Im m \langle\langle n_{-\mathbf{q}\uparrow} n_{\mathbf{q}\downarrow}; n_{\mathbf{q}'\uparrow} n_{-\mathbf{q}'\downarrow} \rangle\rangle_\omega. \quad (63)$$

This does not explicitly depend on impurity scattering and can be calculated in the “clean” limit.<sup>6</sup>

Equation (63) is still a very complex formula, depending as it does on the spectrum of the four-point response function  $\langle\langle n_{-\mathbf{q}\uparrow} n_{\mathbf{q}\downarrow}; n_{\mathbf{q}'\uparrow} n_{-\mathbf{q}'\downarrow} \rangle\rangle_\omega$ , but it is amenable to approximations. First of all, since there are two  $v_q$ s already in evidence in Eq. (63) one can do a meaningful lowest-order calculation by calculating the four-point spectrum in the noninteracting approximation. This can be done exactly and results in the convolution of two noninteracting density fluctuation spectra  $\Im m \chi_{0\uparrow}(q, \omega)$  and  $\Im m \chi_{0\downarrow}(q, \omega)$ , where  $\chi_{0\alpha}(q, \omega)$  is the well-known Lindhard

---

<sup>6</sup>It must be stressed that the present theory holds at the level of the Drude–Boltzmann approximation defined by Eq. (58), which is the result of interchanging the natural order of the  $\omega \rightarrow 0$  limit and the weak scattering limit. A more sophisticated treatment of quantum effects in electron–impurity scattering (I. V. Gornyi and Khveshchenko, 1999) suggests that the spin drag would be even larger than predicted by the present theory at temperatures  $k_B T \ll \hbar/\tau$ . The temperature range in which these quantum corrections are important shrinks to zero in the limit of weak impurity scattering.

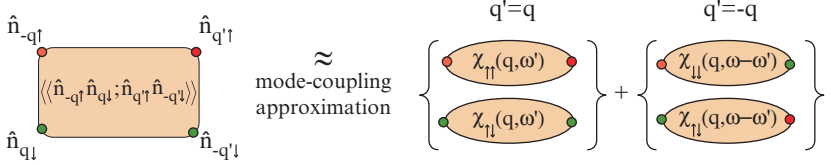


Figure 9. Mode-coupling approximation for the four-point response function of Eq. (64)

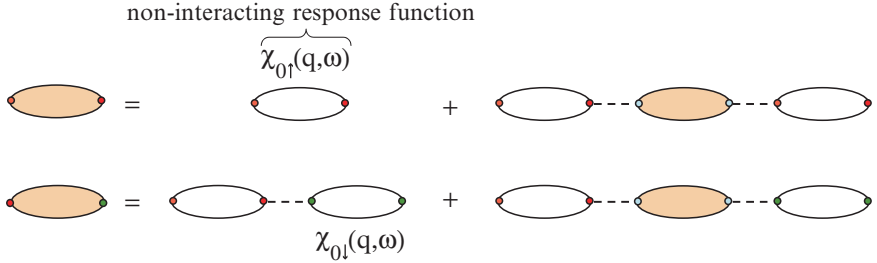


Figure 10. Diagrammatic expansion of the RPA response functions

function of the free-electron gas. Unfortunately, the long-range of the Coulomb interaction (i.e., the divergence of  $v_q$  for  $q \rightarrow 0$ ) prevents us from getting a finite answer from this approach. One needs to go to infinite order in the Coulomb interaction and replace  $v_q$  by the screened interaction  $\frac{v_q}{\epsilon(q, 0)}$ . A better approximation is the random-phase approximation (RPA) which is described schematically in Figures 9 and 10.

The result of this approximation is

$$\begin{aligned} \Re e \rho_{\uparrow\downarrow}(\omega, T) &= \frac{\hbar^2}{n_\uparrow n_\downarrow V e^2} \sum_{\mathbf{q}} \frac{q^2 v_q^2}{d} \frac{(e^{-\hbar\omega/k_B T} - 1)}{\omega} \\ &\times \int_{-\infty}^{\infty} \frac{d\omega'}{\pi} \frac{[\chi''_{\uparrow\uparrow}(q, \omega') \chi''_{\downarrow\downarrow}(q, \omega - \omega') - \chi''_{\uparrow\downarrow}(q, \omega') \chi''_{\downarrow\uparrow}(q, \omega - \omega')]}{(e^{-\hbar\omega'/k_B T} - 1)(e^{-\hbar(\omega - \omega')/k_B T} - 1)}, \end{aligned} \quad (64)$$

where  $d$  is the number of dimensions, and  $\chi''_{\uparrow\uparrow}$ ,  $\chi''_{\uparrow\downarrow}$ ,  $\chi''_{\downarrow\downarrow}$  are the imaginary parts of the RPA response functions given the box of Figure 10. In the d.c. limit  $\omega \rightarrow 0$  this seemingly complicated expression reduces to

$$\rho_{\uparrow\downarrow}(T) = \frac{\hbar^2}{4n_\uparrow n_\downarrow k_B T V e^2} \sum_{\mathbf{q}} \frac{q^2 v_q^2}{d} \int_0^\infty \frac{d\omega'}{\pi} \frac{\Im m \chi_{0\uparrow}(q, \omega') \Im m \chi_{0\downarrow}(q, \omega')}{|\epsilon(q, \omega')|^2 \sinh^2(\hbar\omega'/2k_B T)}, \quad (65)$$

where  $\epsilon(q, \omega)$  is the RPA dielectric function.

This formula is essentially the same that was obtained in the study of the ordinary Coulomb drag between currents flowing in adjacent electronic layers (Zheng and MacDonald, 1993; Rojo, 1999). The only difference is that the Lindhard functions in it refer to the two different spin components of the electron liquid in the same layer. For this reason the effect is considerably stronger than the ordinary Coulomb drag and the scattering of individual quasiparticle plays the dominant role (plasmon exchange between the two layers is more important in ordinary Coulomb drag in bilayers, because the effective interaction between electrons in the two layer is rapidly suppressed at large momentum transfers  $q \sim \Lambda^{-1}$ , where  $\Lambda$  is the distance between the layers).

It is immediately evident from Eq. (65) that: (i)  $\rho_{\uparrow\downarrow}(T)$  is proportional to  $T^2$  at low temperature (this is because the integral over  $\omega'$  is cutoff by the hyperbolic sine at  $\omega' \sim k_B T$ , and  $\Im m \chi_{0,\alpha}(q, \omega)$  is proportional to  $\omega$  for small  $\omega$ ); (ii) the formula becomes exact in the high-density limit. This expression has been calculated carefully in several limits and different regimes (D'Amico and Vignale, 2000, 2002, 2003; Flensberg et al., 2001). The general qualitative results are shown in the Figures 11–13.

A general purpose formula for  $\rho_{\uparrow\downarrow}(T)$ , which is valid both at high temperature and low temperature in a two-dimensional electron gas is given in Eqs. (12) and (13) of D'Amico and Vignale (2003).

D'Amico and Vignale (2002) also examined the case in which one of the two components is degenerate, while the other is classical. Surprisingly, the result is in this limit independent of the vanishing concentration of minority spins—a counterintuitive result which reminds us of the fact that the viscosity of a classical ideal gas is independent of its density—a fact first noted by Maxwell (Huang, 1963).

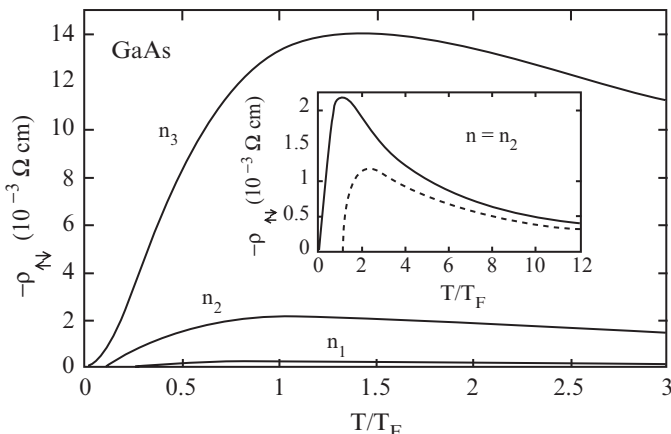


Figure 11. Calculated spin transresistivity in 3D at densities  $n_1 = 1.5 \times 10^{18} \text{ cm}^{-3}$ ,  $n_2 = 1.5 \times 10^{17} \text{ cm}^{-3}$ , and  $n_3 = 1.5 \times 10^{16} \text{ cm}^{-3}$

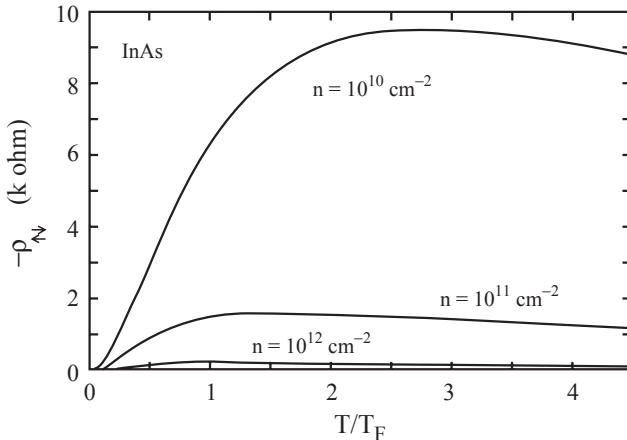


Figure 12. Calculated spin transresistivity in 2D

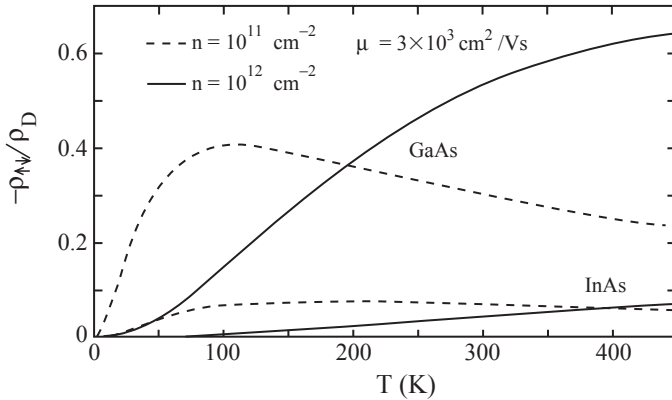


Figure 13. Comparison between spin transresistivity and ordinary Drude resistivity in 2D. The mobility is  $\mu = 3 \times 10^3 \text{ cm}^2/\text{Vs}$

## 7 Experimental Observation of Spin Coulomb Drag

According to Eq. (34), the spin drag coefficient  $\gamma$  can be experimentally determined from a measurement of the spin diffusion constant. Such a measurement has recently been done by Weber and Awschalom (2005), who made use of the transient spin-grating technique to monitor the time evolution of the spin density. A periodic spin density can be induced in an n-type doped GaAs sample by letting two linearly polarized light beams coming from different directions interfere on the surface of the sample. The interference produces a spatially varying pattern of polarization, i.e., a *spin grating*, with alternating regions of left-handed and right-handed circular polarization separated by linearly polarized regions. The spin density is optically induced in the regions of circular polarization, and its

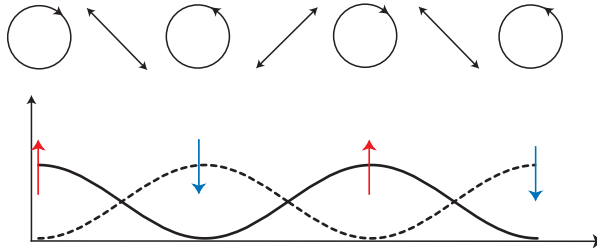


Figure 14. Pattern of light (top) and spin polarization (bottom) in a spin grating

direction depends on the handedness of the polarization (see Figure 14). At the initial time  $t = 0$  the pump light is turned off and the subsequent time evolution of the spin density is then monitored on a picosecond timescale by means of Kerr spectroscopy—a technique in which one determines the amplitude of the spin density modulation from the rotation of the plane of polarization of the light diffracted from the spin grating. The initial rate of decay of the spin grating amplitude  $\gamma_q$  (immediately after the pump light is turned off) depends on the wave vector  $q$  of the grating in the following manner:  $\gamma_q = \frac{1}{\tau_s} + D_s q^2$ , where  $\tau_s$  is the spin density relaxation time and  $D_s$  is the spin diffusion constant. Therefore, the slope of the  $\gamma_q$  vs  $q^2$  graph yields  $D_s$ . Figure 15 shows the results of the measurement for  $D_s$  (open circles) and for the noninteracting electrical diffusion constant  $D_c^{(0)}$ , which differs from the exact diffusion constant of Eq. (36) because the interacting compressibility  $\chi_c$  is replaced by the non-interacting compressibility  $\chi_c^{(0)}$  ( $\chi_c^{(0)}$  is equal to the density of states at the Fermi surface,  $N(0) = \frac{m_b}{\pi \hbar^2}$  for the two-dimensional electron gas, and also to the non-interacting spin susceptibility  $\chi_s^0$ ).

It is immediately seen that  $D_s$  is considerably smaller than  $D_c^0$ . According to the formulas of section 5.1 the ratio  $D_s/D_c^{(0)}$  is given by

$$\frac{D_s}{D_c^{(0)}} = \frac{\chi_s^{(0)} / \chi_s}{1 + \gamma \tau}. \quad (66)$$

The reduced value of  $D_s$  could arise in principle from two different mechanisms: (i) The exchange-driven enhancement of the spin susceptibility and (ii) the spin drag coefficient  $\gamma$ . However, at the density of the present experiment the spin susceptibility enhancement (known from quantum Monte Carlo calculations) is at most a few percent (Giuliani and Vignale, 2005). Therefore, the large reduction of  $D_s$  must be almost entirely ascribed to the spin drag coefficient. The effect of the latter is amplified by the large mobility of the sample: notice that the spin diffusion constant is of the order of  $1000 \text{ cm}^2/\text{s}$ , more than a thousand times larger than the spin diffusion constant observed in the samples of (Kikkawa and Awschalom, 1999). This supports the view that these samples are close to the intrinsic limit, where the primary limitation to  $D_s$  comes from electron-electron scattering.

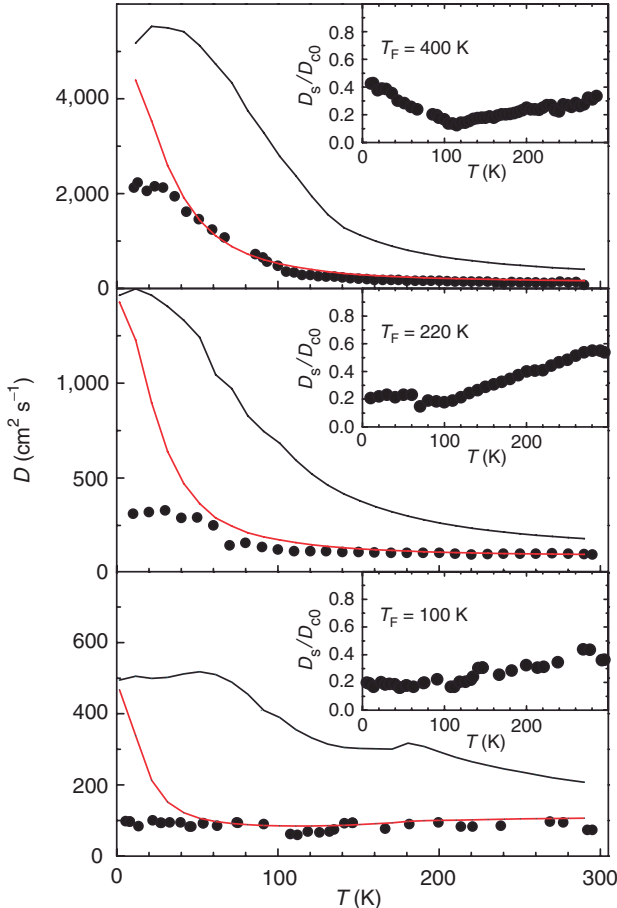


Figure 15. Experimentally determined spin diffusion constant (dots) and its theoretically calculated value (D'Amico and Vignale, 2003) (lower solid line). Also shown the non-interacting electrical diffusion constant  $D_c^{(0)}$  (upper solid line), and the ratio  $\frac{D_s}{D_c^{(0)}}$  (insets). From Weber and Awschalom (2005), with permission

The lower solid line in Figure 15 represents the theoretical prediction for  $D_s$  based on  $\gamma$  calculated as a function of temperature (D'Amico and Vignale, 2003) and plotted in Figure 12. Notice that there are no adjustable parameters. The agreement is excellent, except at the lowest temperature, where the experimental data saturate to a constant value, apparently due to the practical difficulty of further lowering the electronic temperature. The lower panel of the same figure shows the spin-channel resistivity obtained from  $D_s$  according to Eq. (10),  $\rho_s = 1/e^2 N(0) D_s$ , where again we use the noninteracting approximation for the spin susceptibility,  $\chi_s = N(0)$ . The agreement with the theoretically calculated value is very satisfactory.

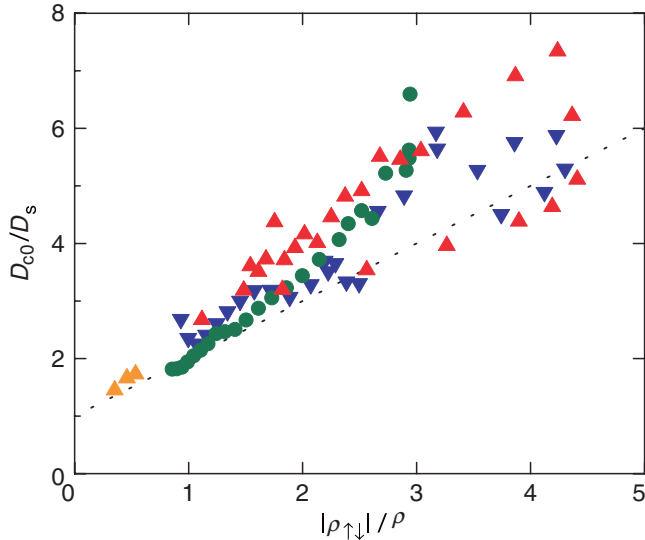


Figure 16. Ratio of noninteracting charge diffusion constant to spin diffusion constant vs spin drag coefficient  $|\rho_{\uparrow\downarrow}|/\rho = \gamma\tau$  in three different samples. From Weber and Awschalom (2005), with permission

Finally, Figure 16 shows how the experimental results for the ratio  $\frac{D_s}{D_c^{(0)}}$  line up as functions of  $|\rho_{\uparrow\downarrow}|/\rho = \gamma\tau$  in three different samples, characterized by different Fermi temperatures  $T_F$ . For each sample and each temperature  $\frac{D_s}{D_c^{(0)}}$  is determined by experiment and  $\gamma\tau$  comes from the theory. If the theory is correct all the points in the  $\frac{D_s}{D_c^{(0)}} - \gamma\tau$  plane must fall on a straight line  $1 + \gamma\tau$ . The fact that they do—albeit with some scatter—provides convincing evidence that the observed value of  $D_s$  is primarily controlled by the SCD coefficient  $\gamma$ .

## 8 Spin Mass

We now turn our attention to a less known aspect of the many-body theory of spin-polarized transport. Let us go back to the phenomenological equations of motion for the spin momentum,  $\mathbf{P}_\alpha$ , Eqs. (13) and (14). Thus far we have assumed that the current densities are related to the spin momentum by the relation  $\mathbf{J}_\alpha = -e \frac{\mathbf{P}_\alpha}{m_b V}$ . But, how do we know that? In other words, how do we know that the effective mass that should be used to relate the momentum to the current is just the noninteracting band mass  $m_b$ ? In the presence of electron-electron interactions this is a nontrivial question, as can be seen from the following argument.

A quasiparticle state in a Fermi liquid is an eigenstate of total momentum and spin, but not separately of  $\mathbf{P}_\uparrow$  and  $\mathbf{P}_\downarrow$  (nor, for that matter, of the Hamiltonian). Let us denote by  $|\mathbf{p}\sigma\rangle$  the state that contains just one quasiparticle of momentum  $\mathbf{p}$  and spin  $\sigma$ . In a noninteracting system the quasiparticle is a real particle and

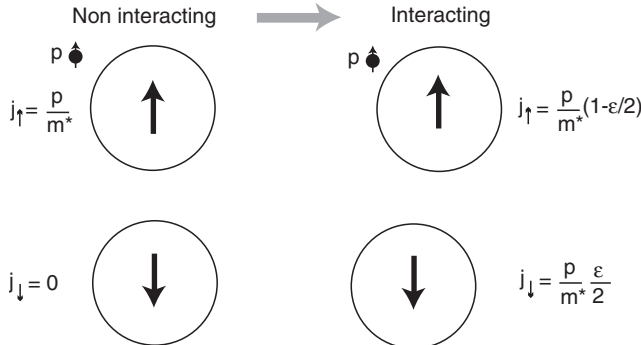


Figure 17. Conceptual description of the origin of the spin mass in a Fermi liquid

the expectation value of the current density operator  $\hat{\mathbf{J}}_\alpha$  in the state  $|\mathbf{p} \uparrow\rangle$  is equal to the total current density  $\frac{\mathbf{p}}{m_b}$  if  $\alpha = \uparrow$  or zero if  $\alpha = \downarrow$ . But in an interacting system this is no longer true. As the electron-electron interaction is slowly turned on some momentum can and will flow out of the  $\uparrow$  spin component into the  $\downarrow$  spin component (see Figure 17): both  $\mathbf{J}_\uparrow$  and  $\mathbf{J}_\downarrow$  will therefore have nonvanishing expectation values. The only thing we can say, in general, is that the expectation value of  $\mathbf{J}_\alpha$  in a quasiparticle state of momentum  $\mathbf{p}$  and spin  $\sigma$  is linear in  $\mathbf{p}$  (from symmetry) and can be written in the following form:

$$\langle \mathbf{p}\sigma | \hat{\mathbf{J}}_\alpha | \mathbf{p}\sigma \rangle \equiv c_{\alpha\sigma} \frac{\mathbf{p}}{m_b}, \quad (67)$$

where  $c_{\alpha\sigma}$  are real coefficients that add up to 1,

$$\sum_\alpha c_{\alpha\sigma} = 1 \quad (68)$$

for either value of  $\sigma$ . This condition follows from the fact that the *total* current operator  $\hat{\mathbf{J}} = \hat{\mathbf{J}}_\uparrow + \hat{\mathbf{J}}_\downarrow$  is equal to  $\frac{\mathbf{p}}{m_b}$ , of which  $|\mathbf{p}\sigma\rangle$  is an eigenstate.

Now the expectation value of the spin current is given by

$$\begin{aligned} \langle \mathbf{p} \uparrow | \hat{\mathbf{J}}_\uparrow - \hat{\mathbf{J}}_\downarrow | \mathbf{p} \uparrow \rangle &= (c_{\uparrow\uparrow} - c_{\downarrow\uparrow}) \frac{\mathbf{p}}{m_b} \\ \langle \mathbf{p} \downarrow | \hat{\mathbf{J}}_\uparrow - \hat{\mathbf{J}}_\downarrow | \mathbf{p} \downarrow \rangle &= (c_{\uparrow\downarrow} - c_{\downarrow\downarrow}) \frac{\mathbf{p}}{m_b}. \end{aligned} \quad (69)$$

In both cases, this will be less than  $\frac{\mathbf{p}}{m_b}$ . Say that we started with a noninteracting particle of momentum  $\mathbf{p}$  and spin  $\uparrow$ . As the electron-electron interaction is slowly turned on, momentum inevitably flows from the up-spin component (which initially has larger momentum) to the down spin component (which initially has none). At the end of the turning-on process the difference between the momenta of the two spin components is *less* than it would have been in the absence of the

Coulomb interaction. Therefore we expect:  $|c_{\uparrow\uparrow} - c_{\downarrow\downarrow}| < 1$  and  $|c_{\uparrow\downarrow} - c_{\downarrow\uparrow}| < 1$ . These constraints can be summarized by writing the  $2 \times 2$  matrix  $\hat{c} \equiv c_{\alpha\beta}$  in the following form:

$$\hat{c} = \begin{pmatrix} 1 - \frac{\epsilon_{\uparrow}}{2} & \frac{\epsilon_{\uparrow}}{2} \\ \frac{\epsilon_{\downarrow}}{2} & 1 - \frac{\epsilon_{\downarrow}}{2} \end{pmatrix}, \quad (70)$$

where  $\epsilon_{\uparrow}$  and  $\epsilon_{\downarrow}$  are two independent positive numbers, equal in the paramagnetic case. The eigenvalues of this matrix are 1 and  $1 - \frac{\epsilon_{\uparrow} + \epsilon_{\downarrow}}{2}$ . We define the *spin mass* (Qian et al., 2003) as

$$m_s = \frac{m_b}{1 - \frac{\epsilon_{\uparrow} + \epsilon_{\downarrow}}{2}}, \quad (71)$$

which, by definition, gives the correct relationship between the spin current and the spin momentum in the paramagnetic case.<sup>7</sup>

I emphasize that the spin mass is a collective property of the electron liquid, conceptually unrelated to the quasiparticle mass, which controls the quasiparticle dispersion relation. In particular, the spin mass differs from the bare mass  $m_b$  even in the paramagnetic state. There is no connection whatsoever between the spin mass and the spin-polarization dependence of the quasiparticle effective mass (the latter has been recently dubbed “the spintronic effective mass” (Zhang and Sarma, 2005)).

Before proceeding to a calculation of the spin mass one should probably ask how it could be measured. Figure 18 shows the concept of an experiment designed to do just this. We start with electrons in a parabolic quantum well and force a uniform oscillation in the spin channel: i.e., the up and down spin components of the electron liquid perform harmonic oscillations with opposite phases. This is the spin-channel analogue of the Kohn mode: it remain to be seen how efficiently current spectroscopic techniques, in particular cross-polarized Raman scattering,

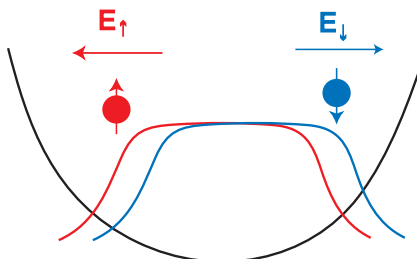


Figure 18. The Kohn mode in the spin channel as a probe for the spin mass of electrons

---

<sup>7</sup>In the general case, the eigenvector corresponding to the spin mass eigenvalue is a mixed channel, neither pure density nor pure spin. Nevertheless, we continue to refer to the eigenvalue  $m_s$  as the “spin mass”.

couple to this mode (D'Amico and Ullrich, 2006). The equation of motion for the macroscopic momentum in the spin channel  $\mathbf{P}_s \equiv \mathbf{P}_\uparrow - \mathbf{P}_\downarrow$  is

$$\dot{\mathbf{P}}_s = -e \frac{N}{2} \mathbf{E}_s - \gamma m \frac{N}{2} \mathbf{v}_s - \frac{N}{2} \mathbf{R}_s, \quad (72)$$

where  $\mathbf{E}_s \equiv \mathbf{E}_\uparrow - \mathbf{E}_\downarrow$  is the driving force in the spin channel,  $\mathbf{v}_s \equiv \mathbf{v}_\uparrow - \mathbf{v}_\downarrow$  and  $\mathbf{R}_s \equiv \mathbf{R}_\uparrow - \mathbf{R}_\downarrow$  are respectively the relative velocity and the relative separation of the centers of mass of the  $\uparrow$  and  $\downarrow$  electron distributions,  $k$  is the “elastic constant” related to the curvature of the potential, and  $\gamma$  is the spin drag coefficient. Taking into account the relation

$$\mathbf{P}_s = m_s \mathbf{v}_s = m_s \dot{\mathbf{R}}_s, \quad (73)$$

where  $m_s$  is the spin mass, we see that the frequency of the oscillations is down-shifted from  $\sqrt{\frac{k}{m}}$  (the frequency of the Kohn mode) to  $\sqrt{\frac{k}{m_s}}$ . In addition, the oscillations are damped. So both spin mass and spin drag coefficient could be obtained, in principle, from one measurement. We will see that this connection is far from being accidental.

The spin mass of a Fermi liquid can on one hand be related to the phenomenological parameters of the Landau theory of Fermi liquids (Nozières and Pines, 1966; Giuliani and Vignale, 2005), while on the other hand it can be directly calculated from an approximate microscopic theory (Qian et al., 2003). As for the first approach it suffices here to say that the ratio of the spin mass to the bare band mass  $m_b$  is given by (in 3 dimensions)

$$\frac{m_s}{m_b} = \frac{1 + F_1^s/3}{1 + F_1^a/3}, \quad (74)$$

where  $F_1^s = \sum_{\alpha\beta} F_1^{a\beta}$ ,  $F_1^a = \sum_{\alpha\beta} \alpha\beta F_1^{a\beta}$  (with  $\alpha, \beta = \pm 1$  for up and down spin) and

$$F_1^{a\beta} \equiv \frac{N_\alpha(0)}{2} \int_{-1}^{+1} d(\cos \theta) f_{\mathbf{p}\alpha, \mathbf{p}'\beta} \cos \theta, \quad (75)$$

where  $N_\alpha(0)$  is the density of states of quasiparticles of spin  $\alpha$  at the Fermi surface and  $f_{\mathbf{p}\alpha, \mathbf{p}'\beta}$  is the Landau quasiparticle interaction function. The second and the fourth column of Table 2 show the values of the spin mass obtained from the Landau parameters calculated by Yasuhara and Ousaka (1992) in both 3 and 2 dimensions for different values of the electron gas parameter  $r_s$ .

Let us now turn to the microscopic theory, which reveals a beautiful connection between the spin mass and the spin drag resistivity. To do this we return to the Kubo formula (57) for the frequency-dependent resistivity and recast it in the form of an equation of motion for the velocity field. For simplicity's sake, we work in the paramagnetic case,  $n_\uparrow = n_\downarrow = \frac{n}{2}$ , without impurities, and at zero temperature.

TABLE 2. Spin mass of an electron liquid calculated from Eq. (74) with the Landau parameters calculated by Yasuhara and Ousaka (1992) (second and fourth column) and from the mode-coupling theory of Qian et al. (2003) (third and fifth column)

$r_s$	$m_s/m_b$ (3D)	$m_s/m_b$ (3D)	$m_s/m_b$ (2D)	$m_s/m_b$ (2D)
1	1.02	1.01	1.15	1.18
2	1.06	1.03	1.46	1.77
3	1.11	1.03	1.83	2.78
4	1.17	1.04	2.21	4.11
5	1.23	1.04	2.59	5.36

Making use of the fact that  $\hat{\rho}(\omega) \cdot \hat{\mathbf{J}} = \hat{\mathbf{E}}$  and  $\mathbf{J}_\alpha = -en_\alpha \mathbf{v}_\alpha$  we arrive, after some straightforward manipulations, at the equation

$$-i\omega \sum_\beta \left[ \delta_{\alpha\beta} - \frac{1}{n_\alpha} \Re e \langle \langle \mathbf{P}_\alpha; \mathbf{P}_\beta \rangle \rangle_\omega \right] \mathbf{v}_\beta = -e\mathbf{E}_\alpha + \omega \frac{1}{n_\alpha} \sum_\beta \Im m \langle \langle \mathbf{P}_\alpha; \mathbf{P}_\beta \rangle \rangle_\omega \mathbf{v}_\beta. \quad (76)$$

Noting that in the absence of impurities

$$\langle \langle \mathbf{P}_\alpha; \mathbf{P}_\beta \rangle \rangle_\omega = -\alpha\beta \langle \langle \mathbf{P}_\uparrow; \mathbf{P}_\downarrow \rangle \rangle_\omega \quad (77)$$

(Newton's third law), and making use of Eq. (58) for the frequency-dependent spin drag coefficient, we see that the above equation (76) can be written in the physically transparent form

$$-i\omega m_s(\omega) \mathbf{v}_s = -e\mathbf{E}_s - \gamma(\omega) m \mathbf{v}_s, \quad (78)$$

where the frequency-dependent spin mass is given by

$$\begin{aligned} \frac{m_s(\omega)}{m} &= 1 + 4 \frac{\Re e \langle \langle \mathbf{P}_\uparrow; \mathbf{P}_\downarrow \rangle \rangle_\omega}{nm_b} \\ &= 1 + \frac{ne^2}{m_b} \frac{\Im m \rho_{\uparrow\downarrow}(\omega)}{\omega}. \end{aligned} \quad (79)$$

So we see that the spin mass is related to the imaginary part of the spin transresistivity  $\rho_{\uparrow\downarrow}(\omega)$ , while the spin drag coefficient is given by the real part of the same function. The real and the imaginary parts of the spin transresistivity are connected by the Kramers-Krönig dispersion relation

$$\Im m \rho_{\uparrow\downarrow}(\omega) = -\frac{2\omega}{\pi} \mathcal{P} \int_0^\infty \frac{\Re e \rho_{\uparrow\downarrow}(\omega')}{\omega'^2 - \omega^2} d\omega', \quad (80)$$

where  $\mathcal{P} \int$  denotes the Cauchy principal part integral. This leads us to the following relation between the spin mass and the spin drag coefficient (in a pure, translationally invariant electron liquid):

$$\frac{m_s(\omega)}{m} = 1 + \frac{2}{\pi} \mathcal{P} \int_0^\infty \frac{\gamma(\omega')}{\omega'^2 - \omega^2} d\omega' \\ \xrightarrow{\omega \rightarrow 0} 1 + \frac{2}{\pi} \int_0^\infty \frac{\gamma(\omega')}{\omega'^2} d\omega'. \quad (81)$$

The last integral on the right hand side exists because the spin drag coefficient of a translationally invariant electron liquid vanishes as  $\omega^2$  for  $\omega \rightarrow 0$  at  $T = 0$ , for about the same reason that the d.c. coefficient  $\gamma(0)$  vanishes as  $T^2$  as  $T$  tends to zero. Notice that the spin mass at zero frequency is always larger than the band mass, since the spin drag coefficient is positive.

The frequency-dependent spin drag coefficient  $\gamma(\omega)$  can be evaluated from the approximate microscopic expression (64), setting  $T = 0$ . Then this expression is put in Eq. (81) for the spin mass. In practice we find that it is necessary to account at least partially for exchange effects (not included in the RPA Eq. (64)), in order to avoid a severe overestimation of the spin mass (some details of the evaluation can be found in (Qian et al., 2003)).

Numerical results obtained in this manner are presented in the third and fifth column of Table 2. These numbers are substantially larger than the ones obtained from the Landau parameters. A 10% renormalization of the mass at  $r_s = 1$  in 2D is a significant effect: quite a bit larger than the corresponding renormalization of the quasiparticle effective mass. Perhaps this renormalization will be seen in experiments such as the one described earlier in this section.

## 9 Spin Hall Effect

As a final demonstration of the role played by SCD in spin-polarized transport I will say something about the intriguing phenomenon of the “spin Hall effect” (SHE)—an effect that has recently attracted much attention, motivated by prospects of using it as a source of spin polarized current (Engel et al., 2006). An experimental set up for the SHE is the “spin Hall bar” shown in Figure 19. An electric field is applied to a nonmagnetic two-dimensional electron liquid. As a result, a *spin current* begins to flow in a direction perpendicular to the electric field: that is, spin up and spin down electrons, with “up” and “down” defined with respect to the normal to the plane, drift in opposite directions perpendicular to the electric field (the transversal drift motion of course co-exists with the usual drift along the direction of the electric field). Eventually a steady state is established, in which the transverse spin current is suppressed by a transverse chemical potential gradient in the spin channel. The latter signals the appearance of a

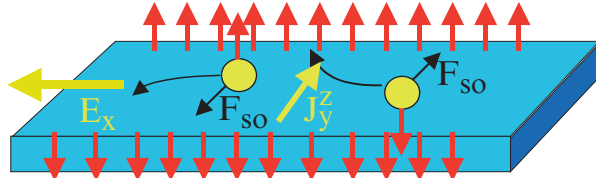


Figure 19. A “spin Hall bar” is used to measure the spin current  $J_y^z$  induced by an electric field  $E_x$  applied along the  $x$  axis

non-homogeneous spin density across the bar, with the largest spin accumulation occurring at the edges of the bar, where it can be detected by optical methods (e.g., Kerr rotation).

The SHE is related to the anomalous Hall effect (AHE) (Karplus and Luttinger, 1954; Nozières and Lewiner, 1973; Bergman, 1979) which occurs in ferromagnetic materials, but differs from that venerable ancestor in two crucial respects: (1) there is no magnetic field, nor a net magnetization, hence no broken time reversal symmetry; (2) the transversal current is not a charge current but a *spin* current.

The SHE (like the AHE) is a consequence of the spin-orbit interaction in a crystalline environment. To understand this somewhat subtle effect, recall that the Bloch states of a semiconductor have the standard form  $u_{nk}(\mathbf{r})e^{i\mathbf{k}\cdot\mathbf{r}}$ , where the functions  $u_{nk}(\mathbf{r})$  have the periodicity of the crystal lattice, and  $n$  is the band index. For finite but small wave vector  $\mathbf{k}$  the periodic functions  $u_{nk}$  of each band can be expressed as linear combinations of the  $\mathbf{k} = 0$  functions  $u_{n'0}$  of all the other bands. Although the carriers responsible for the SHE typically reside in just one band, say the lowest conduction band, their wave function contains an admixture of the  $k = 0$  valence band wavefunctions  $u_{v0}(\mathbf{r})e^{i\mathbf{k}\cdot\mathbf{r}}$ . One can eliminate this admixture by performing a unitary transformation (Winkler, 2003): the price paid for this simplification is that the dynamics of the decoupled conduction band is governed by a renormalized Hamiltonian, which includes a renormalized effective mass, a renormalized  $g$  factor, and—most important for our purposes—a spin-orbit coupling to any external slowly-varying potential  $V(r)$  which may be present in addition to the crystal potential. This spin-orbit coupling has the form

$$\hat{H}_{so} = \frac{\alpha}{\hbar} (\hat{\mathbf{p}} \times \nabla V) \cdot \sigma, \quad (82)$$

where

$$\alpha = \frac{\hbar^2 P^2}{3m^2} \left[ \frac{1}{E_g^2} - \frac{1}{(E_g + \Delta_{SO})^2} \right], \quad (83)$$

$E_g$  is the energy gap between the conduction band and the heavy/light holes bands;  $\Delta_{SO}$  is the gap between the heavy/light holes and the spin-orbit split hole band, and  $P$  is the matrix element of the momentum operator between the valence and the conduction band edges, and  $m$  is the bare electron mass (Winkler, 2003).

The coupling constant  $\alpha$  has the dimension of a squared length and for AlGaAs has a typical value  $\alpha = 4.4\text{\AA}^2$ . This is considerably smaller than the square of the effective Bohr radius ( $\sim 10^4 \text{\AA}^2$ ) and in this sense the spin-orbit coupling can be considered a small perturbation. However, notice that it is much larger than the spin-orbit coupling one would predict if one were to treat the conduction band electrons as free electrons of mass  $m_b$  in a vacuum: in that case the spin-orbit coupling constant would be  $\alpha_0 = -\frac{\hbar^2}{4m_b^2c^2} \simeq -10^{-3} \text{\AA}^2$ . Even the sign is wrong, let alone the magnitude! The physical reason for this difference is that the spin-orbit interaction (82) in a solid-state environment has its origin in the strong electric field experienced by the electrons in the vicinity of the nuclei: this affects more directly the valence band electrons (causing the valence bands to split) but also the conduction band electrons are affected, via interband mixing described above. Notice that the coupling constant  $\alpha$  of Eq. (83) would vanish if the spin-orbit splitting of the valence bands,  $\Delta_{SO}$ , were absent. Only the much smaller coupling  $\alpha_0$  would then be left.

After all these preliminaries we are ready to begin our discussion of the SHE. We assume that each electrons experiences in addition to the crystal potential (1) an electric field  $E_x\hat{x}$  directed along the  $x$  axis, (2) a random potential  $V_{ei}(\mathbf{r})$  due to impurities distributed in the plane, and (3) the electric field generated by all other electrons.

Under these conditions the  $z$ -component of the spin ( $z$  perpendicular to the plane) is conserved. As the up-spin electrons drift in the positive  $x$  direction under the action of the electric field  $E$  the spin-orbit interaction with the impurities causes them to be scattered in an asymmetric way, more in the  $+y$  direction than in the  $-y$  direction—an effect known as “skew scattering” (Smit, 1955, 1958).<sup>8</sup> At the same time, down-spin electrons are scattered more often in the  $-y$  direction than in the  $+y$  direction. This produces a net current  $J_y^z$  of the  $z$ -component of the spin along the  $y$  direction. Electron-electron interactions reduce the magnitude of this spin current through the spin Coulomb drag, which effectively enhances the spin-channel resistivity of the material. Finally, the spin current  $J_y^z$  has a universal contribution from the so-called “side-jump” mechanism (Berger, 1970, 1972; Nozières and Lewiner, 1973; Hankiewicz and Vignale, 2006)—a contribution that does not depend on the nature and the strength of the impurity potential, or the electron-electron interaction. This contribution can be traced back to the anomalous connection between the physical position operator and the usual canonical position operator (see discussion below), whereby the net force exerted by the electric field on spin-up or spin-down electrons translates into a systematic drift

---

<sup>8</sup>Also known as “Mott scattering”, skew scattering has long been used as a method to produce spin-polarized beams of particles. It should be noted that the asymmetric scattering is absent when the electron-impurity interaction is treated in the second order Born approximation. One needs to go at least to third order.

of these electrons in the  $-y$  or  $+y$  direction. The final result is (Hankiewicz and Vignale, 2006)

$$J_y^z = \frac{\rho_{ss}/2\rho_D}{1 + \rho_{SD}/\rho_D} J_x - \alpha n e^2 E_x, \quad (84)$$

where  $\rho_{ss} = \frac{m_b}{ne^2\tau_{ss}}$  is a resistivity related to the skew-scattering rate  $\frac{1}{\tau_{ss}}$ ,  $\rho_D$  is the usual Drude resistivity related to the usual elastic scattering rate  $\frac{1}{\tau}$ ,  $J_x = E_x/\rho_D$  is the electrical current in the  $x$  direction, and  $n$  is the electron density. Notice that the two terms on the right hand side of Eq. (84) have opposite signs for repulsive electron–impurity interaction, and that the skew-scattering term dominates at low impurity concentration, while the side-jump term takes over in high resistivity samples. The spin Coulomb drag affects only the skew scattering term.

A detailed derivation of the above result is presented in a recent paper by Hankiewicz and Vignale (2006). Here we merely touch on the main points. First of all, the result is obtained from a Hamiltonian of the form

$$H = H_0 + H_{so} + H_c + H_E, \quad (85)$$

where

$$H_0 = \sum_i \left[ \frac{\mathbf{p}_i^2}{2m_b} + V_{ei}(\mathbf{r}_i) \right] \quad (86)$$

is the noninteracting Hamiltonian,  $\mathbf{r}_i$  is the canonical position operator (not to be confused with the physical position operator—see discussion below),

$$H_c = \frac{1}{2} \sum_{i \neq j} \frac{e^2}{\epsilon_b |\mathbf{r}_i - \mathbf{r}_j|} \quad (87)$$

is the electron–electron interaction (screened by the background dielectric constant  $\epsilon_b$ ),

$$H_{so} = \frac{\alpha}{\hbar} \sum_i \left\{ \mathbf{p}_i \times \left[ \nabla_i V_{ei}(\mathbf{r}_i) + \nabla_i V_{ee}^i \right] \right\} \cdot \boldsymbol{\sigma}_i \quad (88)$$

is the spin–orbit interaction induced by the electric potential of the impurities and of the other electrons  $V_{ee}^i = \sum_{j \neq i} \frac{e^2}{\epsilon_b |\mathbf{r}_i - \mathbf{r}_j|}$ , and finally

$$H_E = \sum_i \left\{ e \mathbf{E} \cdot \mathbf{r}_i + e \frac{\alpha}{\hbar} (\mathbf{p}_i \times \mathbf{E}) \cdot \boldsymbol{\sigma}_i \right\} \quad (89)$$

is the interaction with the electric field. It should be noted that in this Hamiltonian we are not including any spin-dependent terms beyond the ones that arise from the interaction with the external field, the impurities, and the Coulomb field. Intrinsic spin splitting of the Bloch energy bands (which is present in general in non-centrosymmetric material such as GaAs) is therefore neglected.

The various spin-orbit terms appearing in the Hamiltonian can all be shown to arise from a single basic fact, namely, the change in form of the physical position operator under the transformation that eliminates the interband couplings. If we denote by  $\mathbf{r}_i$  the canonical position operator of the  $i$ -th electron, then the physical position operator is given by

$$\mathbf{r}_{phys,i} = \mathbf{r}_i - \frac{\alpha}{\hbar}(\mathbf{p}_i \times \sigma_i), \quad (90)$$

and the physical velocity operator (the time derivative of the physical position) is

$$\mathbf{v}_i = \frac{\mathbf{p}_i}{m_b} + \frac{\alpha}{\hbar} [\nabla_i V_{ei}(\mathbf{r}_i) + \nabla_i V_{ee}^i + e\mathbf{E}] \times \sigma_i - \frac{\alpha}{\hbar} (\mathbf{F}_i \times \sigma_i), \quad (91)$$

where the last term on the right hand side comes from the time derivative of the anomalous contribution to the position operator, Eq. (90), and  $\mathbf{F}_i \equiv \dot{\mathbf{p}}_i$  is the operator of the total force acting on the  $i$ -th electron. Notice that  $\mathbf{F}_i = -[\nabla_i V_{ei}(\mathbf{r}_i) + \nabla_i V_{ee}^i + e\mathbf{E}]$  is the negative of the expression in the square bracket of Eq. (91). Finally, the relevant spin-current operator is

$$\begin{aligned} \hat{\mathbf{J}}_y^z &= -\frac{e}{2\mathcal{V}} \sum_i \{v_{iy}\sigma_{iz} + \sigma_{iz}v_{iy}\} \\ &= -\frac{e}{\mathcal{V}} \sum_i \left\{ \frac{p_{iy}\sigma_{iz}}{m_b} + 2\frac{\alpha}{\hbar}F_{ix} \right\} \end{aligned} \quad (92)$$

$$\approx -\frac{e}{\mathcal{V}} \sum_i \frac{p_{iy}\sigma_{iz}}{m_b}, \quad (93)$$

where the last line follows from the fact that the net force  $\mathbf{F}_i$  acting on an electron vanishes when averaged in a steady-state ensemble.

The steady-state expectation value of  $\hat{\mathbf{J}}_y^z$  is efficiently calculated from the Boltzmann equation

$$-e\mathbf{E}_\sigma \cdot \frac{\mathbf{p}}{m_b} f'_{0\sigma}(\epsilon_p) = \dot{f}_{1\sigma}(\mathbf{p})_c, \quad (94)$$

where  $f_{1\sigma}(\mathbf{p}) = f_\sigma(\mathbf{p}) - f_{0\sigma}(\epsilon_p)$  is the deviation of the steady distribution function  $f_\sigma(\mathbf{p})$  from its equilibrium form  $f_{0\sigma}(\epsilon_p)$ ,  $\sigma$  is the  $z$ -component of the spin, and  $\dot{f}_{1\sigma}(\vec{p})_c$  is the collisional time derivative of the distribution function due to different scattering processes such as electron–impurity scattering and electron–electron scattering. As usual, the collisional time derivative is written as the difference of an in-scattering and an out-scattering term. For example, in the case of spin-conserving electron–impurity scattering one has:

$$\dot{f}_\sigma(\mathbf{p})_{c,imp} = - \sum_{\mathbf{p}'} [W_{\mathbf{p}\mathbf{p}'\sigma} f_\sigma(\mathbf{p}) - W_{\mathbf{p}'\mathbf{p}\sigma} f_\sigma(\mathbf{p}')] \delta(\tilde{\epsilon}_{p\sigma} - \tilde{\epsilon}_{p'\sigma}), \quad (95)$$

where  $W_{\mathbf{p}\mathbf{p}'\sigma}$  is the scattering rate for a spin- $\sigma$  electron to go from  $\mathbf{p}$  to  $\mathbf{p}'$ , and  $\tilde{\epsilon}_{p\sigma}$  is the particle energy, *including the energy of interaction with the electric field  $\mathbf{E}_\sigma$* . The last point is absolutely vital for a correct treatment of the “side-jump” contribution. We must use

$$\tilde{\epsilon}_{p\sigma} = \epsilon_p + 2e\alpha(\mathbf{E}_\sigma \times \sigma\hat{z}) \cdot \vec{k}, \quad (96)$$

where the last term on the right hand side is twice what one would surmise from the intuitive expression  $\tilde{\epsilon}_{p\sigma} = \epsilon_p + e\mathbf{E} \cdot \mathbf{r}_{phys}$ . Why? The reason is that the  $\delta$ -function in Eq. (95) expresses the conservation of energy in a scattering process. Scattering is a time-dependent process: therefore the correct expression for the change in position of the electron  $\Delta\mathbf{r}_{phys}$  must be calculated as the integral of the velocity over time:

$$\Delta\mathbf{r}_{phys} = \int_{-\infty}^{+\infty} \mathbf{v}_{phys} dt. \quad (97)$$

From Eq. (91) for  $\mathbf{v}_{phys}$  we see that the integral of the velocity gives  $\Delta\mathbf{r}_{phys} = -2\frac{\alpha}{\hbar}\Delta\mathbf{p} \times \sigma$ : hence the change in energy is correctly given by Eq. (96). Apparently, the change in momentum due to scattering affects the position in two ways: explicitly, via the second term on the right hand side of the expression (90) for the position operator, and implicitly, via the change in the canonical position operator, whose derivative contains a large term, proportional to the force that acts on the electron.

The electron-electron contribution to the collisional derivative has the form

$$\begin{aligned} \dot{f}_\sigma(\mathbf{p})_{c,e-e} = & - \sum_{\mathbf{p}'\mathbf{k}\mathbf{p}'} W_{\mathbf{p}\sigma,\mathbf{k}\bar{\sigma};\mathbf{p}'\sigma,\mathbf{k}'\bar{\sigma}}^C \{ f_\sigma(\mathbf{p})f_{\bar{\sigma}}(\mathbf{k})[1-f_\sigma(\mathbf{p}')][1-f_{\bar{\sigma}}(\mathbf{k}')] \\ & - f_\sigma(\mathbf{p}')f_{\bar{\sigma}}(\mathbf{k}')[1-f_\sigma(\mathbf{p})][1-f_{\bar{\sigma}}(\mathbf{k})] \} \delta_{\mathbf{p}+\mathbf{k},\mathbf{p}'+\mathbf{k}'} \delta(\tilde{\epsilon}_{p\sigma} + \tilde{\epsilon}_{k\bar{\sigma}} - \tilde{\epsilon}_{p'\sigma} - \tilde{\epsilon}_{k'\bar{\sigma}}), \end{aligned} \quad (98)$$

(D’Amico and Vignale, 2002), where  $W_{\mathbf{p}\sigma,\mathbf{k}-\sigma;\mathbf{p}'\sigma,\mathbf{k}'\sigma}^C$  is the electron-electron scattering rate from  $\mathbf{p}\sigma, \mathbf{k}-\sigma$  to  $\mathbf{p}'\sigma, \mathbf{k}'-\sigma$ , and the Pauli factors  $f_\sigma(\mathbf{p}), 1-f_\sigma(\mathbf{p}')$  etc. ensure that the initial states are occupied and the final states empty as required by Pauli’s exclusion principle. Notice that, for our purposes, only collisions between electrons of opposite spins are relevant, since collision between same-spin electrons conserve the total momentum of each spin component. Accordingly, only the former have been retained in Eq. (98).

The linearized Boltzmann equation is solved exactly under the assumption that the electron–impurity potential is rotationally invariant. The solution has the form

$$f_\sigma(\mathbf{p}) = f_{0\sigma}(\epsilon_k) - f'_{0\sigma}(\epsilon_k)\mathbf{p} \cdot \mathbf{V}_\sigma(p), \quad (99)$$

where  $\mathbf{V}_\sigma(p)$  is proportional to the electric field and depends only on the magnitude of  $\mathbf{p}$ . At low temperature we can ignore this dependence and replace  $\mathbf{V}_\sigma(p)$  by its value at the Fermi surface, which we denote simply by  $\mathbf{V}_\sigma$ . Thus, the

nonequilibrium distribution is simply the equilibrium distribution displaced in momentum space by a fixed amount  $\mathbf{V}_\sigma$ , and the spin current is simply

$$\mathbf{J}_y^z = -e(n_\uparrow \mathbf{V}_\uparrow - n_\downarrow \mathbf{V}_\downarrow). \quad (100)$$

Substituting Eq. (99) in the collision integrals we find (Hankiewicz and Vignale, 2006)

$$\begin{aligned} \dot{f}_{1\sigma}(\mathbf{p})_{c,imp} &= \sum_{\mathbf{p}'} W_{\mathbf{p}\mathbf{p}'}^s f'_{0\sigma}(\epsilon_p)(\mathbf{p} - \mathbf{p}') \cdot \mathbf{V}_\sigma \delta(\epsilon_p - \epsilon_{p'}) \\ &\quad + \sigma \sum_{\mathbf{p}'} W_{\mathbf{p}\mathbf{p}'}^a f'_{0\sigma}(\epsilon_p)(\hat{\mathbf{p}} \times \hat{\mathbf{p}}')_z (\mathbf{p} + \mathbf{p}') \cdot \mathbf{V}_\sigma \delta(\epsilon_p - \epsilon_{p'}) \\ &\quad + 2\sigma \frac{\alpha}{\hbar} \sum_{\mathbf{p}'} W_{\mathbf{p}\mathbf{p}'}^s f'_{0\sigma}(\epsilon_p) e(\vec{E}_\sigma \times \hat{\mathbf{z}}) \cdot (\mathbf{p} - \mathbf{p}') \delta(\epsilon_p - \epsilon_{p'}) , \end{aligned} \quad (101)$$

where  $W^s$  and  $W^a \sin \theta$  are the even and odd components of the scattering probability  $W$  with respect to the angle  $\theta$  between  $\mathbf{p}$  and  $\mathbf{p}'$ . The last term on the right hand side of this expression comes from the difference between  $\tilde{\epsilon}$  and  $\epsilon$ .

Similarly, for the Coulomb collision integral we get

$$\begin{aligned} \dot{f}_\sigma(\mathbf{p})_{c,e-e} &= -\frac{1}{k_B T} \sum_{\mathbf{p}\mathbf{p}'\mathbf{k}'} W_{\mathbf{p}\sigma,\mathbf{k}\bar{\sigma};\mathbf{p}'\sigma,\mathbf{k}'\bar{\sigma}}^C [\mathbf{V}_\sigma - \mathbf{V}_{\bar{\sigma}} + 2e \frac{\alpha}{\hbar} \sigma (\mathbf{E}_\sigma + \mathbf{E}_{\bar{\sigma}}) \times \hat{\mathbf{z}}] \cdot (\mathbf{p} - \mathbf{p}') \\ f_{0\sigma}(\epsilon_p) f_{0\bar{\sigma}}(\epsilon_k) f_{0\sigma}(-\epsilon_{p'}) f_{0\bar{\sigma}}(-\epsilon_{k'}) \delta_{\mathbf{p}+\mathbf{k},\mathbf{p}'+\mathbf{k}'} \delta(\epsilon_{p\sigma} + \epsilon_{k\bar{\sigma}} - \epsilon_{p'\sigma} - \epsilon_{k'\bar{\sigma}}) , \end{aligned} \quad (102)$$

where we have made use of the fact that the product  $f_{0\sigma}(\epsilon_p) f_{0\bar{\sigma}}(\epsilon_k) [1 - f_{0\sigma}(\epsilon_{p'})]$   $[1 - f_{0\bar{\sigma}}(\epsilon_{k'})]$  is equal to the product  $[1 - f_{0\sigma}(\epsilon_p)] [1 - f_{0\bar{\sigma}}(\epsilon_k)] f_{0\sigma}(\epsilon_{p'}) f_{0\bar{\sigma}}(\epsilon_{k'})$ , when  $\epsilon_{p\sigma} + \epsilon_{k\bar{\sigma}} - \epsilon_{p'\sigma} - \epsilon_{k'\bar{\sigma}} = 0$ .

The key quantity  $\mathbf{V}_\sigma$  is best determined from the consistency condition

$$-e \sum_{\mathbf{p}} \frac{\hbar \vec{k}}{m_b} \left[ \mathbf{E}_\sigma \cdot \frac{\mathbf{p}}{m_b} \right] f'_{0\sigma}(\epsilon_p) = \sum_{\mathbf{p}} \frac{\mathbf{p}}{m_b} \dot{f}_{1\sigma}(\mathbf{p})_c . \quad (103)$$

Inserting the expressions (101) and (102) in the right hand side of Eq. (103) and making use of  $\mathbf{J}_\sigma = -en_\sigma \mathbf{V}_\sigma$  we finally arrive at the desired linear equations for  $\mathbf{V}_\sigma$ :

$$\begin{aligned} -\frac{e}{m_b} \mathbf{E}_\sigma - 2 \frac{e\alpha\sigma(\mathbf{E}_\sigma \times \hat{\mathbf{z}})}{\hbar\tau_\sigma} &= \frac{\mathbf{V}_\sigma}{\tau_\sigma} + \sigma \frac{\mathbf{V}_\sigma \times \hat{\mathbf{z}}}{\tau_\sigma^{ss}} \\ &\quad + \frac{\gamma n_{\bar{\sigma}}}{n} \left[ \mathbf{V}_\sigma - \mathbf{V}_{\bar{\sigma}} + 2e \frac{\alpha}{\hbar} \sigma (\mathbf{E}_\sigma + \mathbf{E}_{\bar{\sigma}}) \times \hat{\mathbf{z}} \right] . \end{aligned} \quad (104)$$

Here  $\frac{1}{\tau_\sigma}$  is the usual Drude scattering rate,  $\frac{1}{\tau_\sigma^{ss}}$  is the scattering rate associated with the asymmetric component of the scattering probability, i.e., the skew scattering, and  $\gamma$  is the spin Coulomb drag coefficient.

Of particular interest are the equations for the paramagnetic case (Hankiewicz and Vignale, 2006) (the densities and the relaxation times are the same for the two spin components):

$$\mathbf{E}_c = \rho^D \mathbf{J}_c + 2(\rho^{ss} - \lambda\rho^D - \lambda\rho_{SD}) \mathbf{J}_s \times \hat{\mathbf{z}}, \quad (105)$$

$$\mathbf{E}_s = 4(\rho^{SD} + \rho^D) \mathbf{J}_s + 2(\rho^{ss} - \lambda\rho^D - \lambda\rho_{SD}) \mathbf{J}_c \times \hat{\mathbf{z}}, \quad (106)$$

where  $\lambda$  is a dimensionless parameter given by  $\lambda = 2\frac{\alpha m_b}{\hbar\tau}$ ,  $\rho^{ss} = \frac{m_b}{ne^2\tau^{ss}}$ ,  $\rho^D = \frac{m_b}{ne^2\tau}$ , and  $\mathbf{E}_c = \frac{\mathbf{E}_\uparrow + \mathbf{E}_\downarrow}{2}$ ,  $\mathbf{E}_s = \mathbf{E}_\uparrow - \mathbf{E}_\downarrow$ , and the charge and spin currents are  $\mathbf{J}_c = \mathbf{J}_\uparrow + \mathbf{J}_\downarrow$  and  $\mathbf{J}_s = \frac{\mathbf{J}_\uparrow - \mathbf{J}_\downarrow}{2}$ , respectively. The spin Coulomb drag renormalizes the longitudinal resistivity only in the spin channel. This is a consequence of the fact that the net force exerted by spin-up electrons on spin-down electrons is proportional to the difference of their drift velocities, i.e., to the spin current. Additionally, the electron-electron corrections to the spin-orbit interactions renormalize the transverse resistivity in the charge and spin channels, so the Onsager relations between spin and charge channels hold. Under the assumption that the electric field is in the  $x$  direction and has the same value for spin up and spin down, we see that Eqs. (105) and (106) yield the formula (84) for the spin current.

## 10 Conclusion

In this chapter we have shown that many-body correlations between electrons of opposite spin orientations have an important influence on virtually all aspects of spin-polarized transport. The concept of spin Coulomb drag plays a central role. This role has been illustrated in the examples of spin diffusion, spin injection, and the spin Hall effect. An intimately related concept is that of the spin mass, defined as the proportionality constant between spin current and spin momentum. We expect that this concept will prove useful not only in spin transport, but also in understanding the frequency differences between collective modes of similar spatial structure but different spin structure.

In a recent development (not reviewed here) it has been found that the spin drag coefficient is also involved in the microscopic calculation of the Gilbert damping coefficient – the so far phenomenological constant that controls the rate of relaxation of the transverse magnetization in a ferromagnet.

Many problems remain to be addressed, among which, outstanding, is the problem of introducing many-body correlations for nonclassical spins: i.e., in situations in which the direction of the spin can vary in space. Then the spin current becomes a  $3 \times 3$  tensor, and the drift diffusion equation must be generalized to include spin torques. This is a subtle and complex problem. Perhaps it will be solved by one of you.

## Appendix

In this Appendix we go through the steps in the derivation of Eq. (26). We start from Eq. (18) and immediately drop the time derivative (steady-state condition), and the  $\nabla \sigma_\alpha \cdot \mathbf{E}$  term (weak field assumption). (Notice that this is not allowed in spin-packet dynamics as the inhomogeneous spin distribution predates the application of the electric field.) We also assume that the equilibrium density is homogeneous, so the differential operators act only on the deviation from equilibrium. Finally, we assume that the net electric charge density is  $-e$  times the density deviation from equilibrium:  $\rho = -e(\delta n_\uparrow + \delta n_\downarrow)$ . Then we have

$$\nabla^2 \delta n_\alpha = \sum_\beta \left\{ (\hat{D}^{-1})_{\alpha\beta} \left( \frac{\delta n_\beta}{\tau_{\beta\bar{\beta}}} - \frac{\delta n_{\bar{\beta}}}{\tau_{\bar{\beta}\beta}} \right) + (\hat{D}^{-1})_{\alpha\beta} \sigma_\beta \frac{\delta n_\uparrow + \delta n_\downarrow}{\epsilon_0} \right\}. \quad (107)$$

We now switch from the densities  $\delta n_\alpha$  to the electrochemical potentials  $\delta \mu_\alpha$ , the connection between the two being given in Eq. (25). We make use of the Poisson equation

$$\nabla^2 \phi = -\frac{\rho}{\epsilon_0} \quad (108)$$

to write

$$\nabla^2 \delta n_\alpha = \sum_\beta \chi_{\alpha\beta} \left[ \nabla^2 \delta \mu_\beta + e^2 \frac{\delta n_\uparrow + \delta n_\downarrow}{\epsilon_0} \right]. \quad (109)$$

Making use of the Einstein relation (10) we see that the last term of Eq. (109) coincides with the last term in the curly brackets of Eq. (107), so Eq. (107) can be rewritten as

$$\sum_\beta \chi_{\alpha\beta} \nabla^2 \delta \mu_\beta = \sum_\beta (\hat{D}^{-1})_{\alpha\beta} \left( \frac{\delta n_\beta}{\tau_{\beta\bar{\beta}}} - \frac{\delta n_{\bar{\beta}}}{\tau_{\bar{\beta}\beta}} \right). \quad (110)$$

Now we recall the notation of Eq. (27):

$$\frac{1}{\tilde{D}_\alpha} \equiv \alpha [(\hat{D}^{-1})_{\alpha\uparrow} - (\hat{D}^{-1})_{\alpha\downarrow}]. \quad (111)$$

Then it is easy to see that Eq. (110) can be rewritten as

$$\nabla^2 \begin{pmatrix} \delta \mu_\uparrow \\ \delta \mu_\downarrow \end{pmatrix} = \hat{\chi}^{-1} \cdot \begin{pmatrix} \frac{1}{\tilde{D}_\uparrow \tau_{\uparrow\downarrow}} & -\frac{1}{\tilde{D}_\uparrow \tau_{\uparrow\downarrow}} \\ -\frac{1}{\tilde{D}_\downarrow \tau_{\uparrow\downarrow}} & \frac{1}{\tilde{D}_\downarrow \tau_{\uparrow\downarrow}} \end{pmatrix} \cdot \begin{pmatrix} \delta n_\uparrow \\ \delta n_\downarrow \end{pmatrix}. \quad (112)$$

Finally we substitute Eq. (25) for  $\delta n_\alpha$  on the right hand side of the above equation, and notice that the term containing  $\sum_\beta \chi_{\alpha\beta} e \delta \phi$  vanishes by virtue of the identity (12). And this takes us directly to Eq. (26), which we wanted to derive.

It is an interesting exercise to verify that, if the off-diagonal elements of  $\hat{\chi}$ ,  $\hat{D}$ , and  $\hat{\sigma}$  are absent or neglected, Eq. (26) reduces to

$$\nabla^2 \begin{pmatrix} \delta\mu_{\uparrow} \\ \delta\mu_{\downarrow} \end{pmatrix} = \begin{pmatrix} \frac{1}{D_{\uparrow}\tau_{\uparrow\uparrow}} & -\frac{1}{D_{\uparrow}\tau_{\uparrow\downarrow}} \\ -\frac{1}{D_{\downarrow}\tau_{\downarrow\uparrow}} & \frac{1}{D_{\downarrow}\tau_{\downarrow\downarrow}} \end{pmatrix} \cdot \begin{pmatrix} \delta\mu_{\uparrow} \\ \delta\mu_{\downarrow} \end{pmatrix}, \quad (113)$$

i.e., Eq. (2.8) of the paper by Hershfield and Zhao (1997). (Again, Eq. (12) plays a crucial role in the derivation).

## Acknowledgments

This work was supported by NSF Grant No. DMR-0313681.

## References

- Altschuler, B. L. and Aronov, A. G. (1985) Electron-electron interactions in disordered conductors, In A. L. Efros and M. Pollak (eds.), *Electron-Electron Interactions in Disordered Systems*, Modern Problems in Condensed Matter Sciences, Amsterdam, North Holland, p. 1.
- Baibich, M. N., Broto, J. M., Fert, A., Dau, F. N. V., Petroff, F., Etienne, P., Creuzet, G., Friederich, A., and Chazelas, J. (1988) Giant magnetoresistance of (001)Fe/(001)Cr magnetic superlattices, *Phys. Rev. Lett.* **61**, 2472.
- Berger, L. (1970) Side-jump mechanism for the Hall effect of ferromagnets, *Phys. Rev. B* **2**, 4559.
- Berger, L. (1972) Application of the side-jump model to the Hall effect and Nernst effect in ferromagnets, *Phys. Rev. B* **5**, 1862.
- Bergman, G. (1979) The anomalous Hall effect, *Phys. Today* **56**, 25.
- D'Amico, I. (2004) Spin injection and electric-field effect in degenerate semiconductors, *Phys. Rev. B* **69**, 165305.
- D'Amico, I. and Ullrich, C. A. (2006) Dissipation through spin Coulomb drag in electronic spin transport and optical excitations, *Phys. Rev. B* **74**, 121303.
- D'Amico, I. and Vignale, G. (2000) Theory of spin Coulomb drag in spin-polarized transport, *Phys. Rev. B* **62**, 4853.
- D'Amico, I. and Vignale, G. (2001) Spin diffusion in doped semiconductors: The role of Coulomb interactions, *Europhysics Letters* **55**, 566.
- D'Amico, I. and Vignale, G. (2002) Coulomb interaction effects in spin-polarized transport, *Phys. Rev. B* **65**, 85109.
- D'Amico, I. and Vignale, G. (2003) Spin Coulomb drag in the two-dimensional electron liquid, *Phys. Rev. B* **68**, 045307.
- Engel, H.-A., Rashba, E. I., and Halperin, B. I. (2006) Theory of Spin Hall Effects in Semiconductors, cond-mat/0603303.
- Flatté, M. E. and Byers, J. M. (2000) Spin diffusion in semiconductors, *Phys. Rev. Lett.* **84**, 4220.
- Flensberg, K., Jensen, T. S., and Mortensen, N. A. (2001) Diffusion equation and spin drag in spin-polarized transport, *Phys. Rev. B* **64**, 245308.
- Giuliani, G. F. and Vignale, G. (2005) *Quantum Theory of the Electron Liquid*, Cambridge University Press.
- Hankiewicz, E. and Vignale, G. (2006) Coulomb corrections to the extrinsic spin-Hall effect of a two-dimensional electron gas, *Phys. Rev. B* **73**, 115339.

- Hershfield, S. and Zhao, H. L. (1997) Charge and spin transport through a metallic ferromagnetic–paramagnetic–ferromagnetic junction, *Phys. Rev. B* **56**, 3296.
- Huang, K. (1963) *Statistical Mechanics*, New York, Wiley.
- I. V. Gornyi, A. G. Y. and Khveshchenko, D. V. (1999) Coulomb drag in double layers with correlated disorder, *Phys. Rev. Lett.* **83**, 152.
- Karplus, R. and Luttinger, J. M. (1954) Hall effect in ferromagnetics, *Phys. Rev.* **95**, 1154.
- Kikkawa, J. M., Smorchkova, I. P., Samarth, N., and Awschalom, D. D. (1997) Room temperature spin memory in two-dimensional electron gases, *Science* **277**, 1284.
- Kikkawa, J. M. and Awschalom, D. D. (1998) Resonant spin amplification in n-type GaAs, *Phys. Rev. Lett.* **80**, 4313.
- Kikkawa, J. M. and Awschalom, D. D. (1999) Lateral drag of spin coherence in gallium arsenide, *Nature* **397**, 139.
- Nozières, P. and Lewiner, C. (1973) A simple theory of the anomalous Hall effect in semiconductors, *J. Phys. (Paris)* **34**, 901.
- Nozières, P. and Pines, D. (1966) *Theory of Quantum Liquids I*, Benjamin.
- Qian, Z., Vignale, G., and Marinescu, D. C. (2003) Spin Mass of an Electron Liquid, *Phys. Rev. Lett.* **93**, 106601.
- Rojo, A. (1999) Electron-drag effects in coupled electron systems, *J. Phys.: Cond. Mat.* **11**, R31.
- Schmidt, G., Ferrand, D., Molenkamp, L. W., Filip, A. T., and van Wees, B. J. (2000) Fundamental obstacle for electrical spin injection from a ferromagnetic metal into a diffusive semiconductor, *Phys. Rev. B* **62**, R4790.
- Schmidt, G., Richter, G., Grabs, P., Gould, C., Ferrand, D., and Molenkamp, L. W. (2001) Large magnetoresistance effect due to spin injection into a nonmagnetic semiconductor, *Phys. Rev. Lett.* **87**, 227203.
- Smit, J. (1955) The spontaneous Hall effect in ferromagnetics I, *Physica* **21**, 877.
- Smit, J. (1958) The spontaneous Hall effect in ferromagnetics II, *Physica* **24**, 39.
- Smith, R. A. (1978) *Semiconductors*, New York, Cambridge.
- Streetman, B. G. and Banerjee, S. (1980) *Solid State Electronic Devices*, Prentice Hall.
- Valet, T. and Fert, A. (1993) Theory of the perpendicular magnetoresistance in magnetic multilayers, *Phys. Rev. B* **48**, 7099.
- Vignale, G. (2005) Observing the spin Coulomb drag in spin-valve devices, *Phys. Rev. B* **71**, 125103.
- Vignale, G. and D'Amico, I. (2003) Coulomb drag, magnetoresistance, and spin-current injection in magnetic multilayers, *Solid State Commun.* **127**, 829.
- Weber, C. P. and Awschalom, D. D. (2005) Observation of spin Coulomb drag in a two-dimensional electron gas, *Nature* **437**, 1330.
- Winkler, R. (2003) *Spin-Orbit Effects in Two-Dimensional Electron and Hole Systems*, Springer, New York.
- Yasuhara, H. and Ousaka, Y. (1992) Effective mass, Landau interactions function and self-energy of an electron liquid, *Int. J. Mod. Phys. B* **6**, 3089.
- Yu, Z. G. and Flatté, M. E. (2002) Electric-field dependent spin diffusion and spin injection into semiconductors, *Phys. Rev. B* **66**, 202202.
- Zhang, Y. and Sarma, D. (2005) Spin Polarization Dependence of Carrier Effective Mass in Semiconductor Structures: Spintronic Effective Mass, *Phys. Rev. Lett.* **95**, 256603.
- Zheng, L. and MacDonald, A. H. (1993) Coulomb drag between disordered two-dimensional electron-gas layers, *Phys. Rev. B* **48**, 8203.

# NUCLEAR SPIN DYNAMICS IN SEMICONDUCTOR NANOSTRUCTURES

IONEL TIFREA\*

*Department of Physics, California State University, Fullerton, CA 92834, USA*

*Department of Physics, “Babeş-Bolyai” University, Cluj-Napoca, Cluj 400084, Romania*

**Abstract:** In this chapter we present a theoretical analysis of the role played by nuclear spins in low dimensional semiconductor nanostructures. The hyperfine interaction between nuclear and electronic spins provides the basis for an efficient control of nuclear spin dynamics in systems with low dimensionality. We will address topics such as the nuclear spin relaxation time, dynamical nuclear polarization, induced hyperfine magnetic fields, and Overhauser shifts in the electronic spin resonance frequencies. Our example case is a parabolic quantum well, a structure which presents the advantage of simple analytical results.

**Keywords:** hyperfine interaction, dynamic nuclear polarization, semiconductor nanostructures

## 1 Introduction

Semiconductor nanostructures are the key ingredients of contemporary electronic devices. Such devices operate using the precise control of the electronic charge distribution using electric fields. Recent advances in the semiconductor industry lead to electronic devices whose dimensions are in the nanometer scale, making impossible to avoid quantum mechanical effects in these physical systems. One additional characteristic of particles subject to quantum mechanics is the particle's spin. Coherent control over the spin degree of freedom may lead to the development of new electronic devices with improved performance and functionality, even to the practical implementation of quantum information processing (Wolf et al., 2001; Awschalom et al., 2002). The electron spin number is 1/2 and the electronic spin coherence time can exceed 100 ns in GaAs semiconductor nanostructures at low temperatures (Kikkawa and Awschalom, 1998). However, these times are limited by electronic spin interactions with phonons, nuclear spins, other electron spins, and impurities. Another candidate for spin based electronics may be the nuclear spin. Usually, semiconductor nanostructures carry a variety of nuclear isotopes, however, not all of them are characterized by a nonzero value of

---

\*Email address: itifrea@fullerton.edu

the nuclear spin quantum number. For example, in GaAs semiconductor samples one finds three different nuclear isotopes ( $^{69}\text{Ga}$ ,  $^{71}\text{Ga}$ , and  $^{75}\text{As}$ ), all of them characterized by a nuclear spin number  $3/2$ . On the other hand, in Si semiconductor samples one finds three possible natural isotopes ( $^{28}\text{Si}$ ,  $^{29}\text{Si}$ , and  $^{30}\text{Si}$ ), however, just one of them,  $^{29}\text{Si}$ , has a nonzero nuclear spin. For a list of nuclear species in semiconductor nanostructures refer to the table of semiconductor isotopes in Appendix A (Table 1). Compared to electronic spin coherence times, nuclear spin coherence times are longer, of the order of 10 min in GaAs samples (Berg et al., 1990; Barrett et al., 1994; Smet et al., 2002). When carriers are present, the local electronic density of states at nuclei sites can be large enough to produce additional nuclear spin relaxation via the hyperfine interaction. Even under such conditions, nuclear spin coherence times are of the order of 1 s, making nuclei a reliable candidate for spin based devices and quantum computation. In the following we will focus our discussion mainly on the nuclear spin dynamics in semiconductor nanostructures.

The practical use of spin in device fabrication or quantum computing requires the preparation, manipulation, and measurements of pure quantum states, operations which have to be made in a timescale shorter than the particle's spin coherence time (Kane, 1998; Taylor et al., 2003). A natural way to control and manipulate particle spins will rely on magnetic fields. However, high magnetic fields are difficult to achieve and to change rapidly, making this method improper to use in spin based devices. Smet et al. (2002) and Desrat et al. (2002) used electric fields to change the spectrum of collective mode excitations tuning the electron density across a quantum Hall ferromagnet transition, and thereafter manipulate nuclear spins. In the case of nuclear spins, all the required operations can be achieved based on the hyperfine interaction between electronic and nuclear spins (Gershenfeld and Chuang, 1997; Taylor et al., 2003). The hyperfine interaction has a local character but still the single nuclear spin manipulation is hard to achieve. This inconvenience may be overcomed if instead of single spins we use nuclear spin clusters coupled antiferromagnetically (Meier et al., 2003). The standard technique used to extract information on nuclear spin dynamics is the nuclear magnetic resonance (NMR), a technique which is well known (Slichter, 2002) and extensively used in various applications. Additional techniques to address the nuclear spin dynamics in semiconductor nanostructures are the Faraday and Kerr rotation techniques.

In NMR experiments the nuclear spin polarization obtained in bulk samples is less than 1%, and to obtain a detectable signal the samples should have at least  $10^{17}$ – $10^{20}$  nuclei. On the other hand, in semiconductor nanostructured samples the number of available nuclei is  $10^{12}$ – $10^{15}$  nuclei in quantum wells, and  $10^5$ – $10^6$  nuclei in quantum dots. To overcome the lack of nuclear spins in these samples, and to obtain a detectable NMR signal, the nuclear spin polarization has to be greater than the one obtained in bulk materials. Different experimental methods

exploiting the hyperfine interaction were developed to control the nuclear spin dynamics in semiconductor nanostructures. Berg et al. (1990) and Barrett et al. (1994) used optically injected spin polarized electrons and the dynamical nuclear polarization effect (Overhauser, 1953b) to create a position dependent nuclear polarization in semiconductor quantum wells. The use of optical pumping, a method initially developed to investigate bulk semiconductors (Lampel, 1968), creates the required additional nuclear spin polarization for detectable NMR measurements. Barrett et al. (1994) reported a 3.3% nuclear spin polarization in a 300 Å GaAs quantum well and used NMR to measure the nuclear spin relaxation time and the Knight shift in the resonance frequency for  $^{71}\text{Ga}$  nuclei.

Nuclear spin dynamics can be extracted indirectly from Faraday and Kerr rotation experiments. These experimental techniques focus on the electron spin precession to provide information on the induced nuclear magnetic fields in semiconductor samples. Optical pumping and dynamical nuclear polarization is used to initialize the nuclear spin population. The electron spin Larmor precession frequency is a result of the electron spin interaction with two different magnetic fields, namely, the external applied magnetic field and the induced nuclear magnetic field due to the hyperfine interaction. The Faraday rotation technique was used by Malinowski and Harley (2000b) to extract information on the nuclear spin dynamics in a 9.6 nm GaAs quantum well. The induced nuclear magnetic fields were of the order of 1 T corresponding to a 6.5% nuclear spin polarization across the quantum well.

In semiconductor nanostructures, NMR, Faraday, and Kerr rotation rely on the optically induced nuclear spin polarization. Along with optical pumping, various additional methods were used to improve the results obtained using these techniques. Kawakami et al. (2001) used adjacent ferromagnetic layers to increase nuclear spin polarization in GaAs quantum wells. Depending on the type of the ferromagnetic layer the induced nuclear fields vary from 0.1 T to 0.7 T. However, such fields are not fringe fields and are generated by the dynamical nuclear polarization due to a nonequilibrium electronic spin population resulting from a spin selective electron scattering at the semiconductor–ferromagnet interface (Ciuti et al., 2002). Poggio et al. (2003) used gate voltages to prove the possibility of electrical control over a wide distribution of polarized nuclear spins in an AlGaAs parabolic quantum well (PQW). Experimental data proved that a 8 nm wide distribution of polarized nuclei can be manipulated electrically over a range of 20 nm with gates voltages up to 2 V.

Here we will present theoretical results for the nuclear spin dynamics in semiconductor nanostructures. We will focus mainly on quantum well systems, with a special emphasize on PQWs. We will derive general formulae for the nuclear and spin relaxation time from the hyperfine interaction (Tifrea and Flatté, 2003, 2004). Next, we will investigate the dynamical nuclear polarization (DNP) and derive formulae for the induced nuclear and electronic magnetic fields

in semiconductor nanostructures (Tifrea and Flatté, 2005a, b). The induced magnetic fields are responsible for resonance frequency shifts for both the electrons and the nuclei. Finally, we will estimate the Overhauser shifts (Tifrea and Flatté, 2005a; Tifrea et al., 2005). Our results are general and can be applied to any semiconductor nanostructure. For exemplification we will apply our results to the particular situation of a PQW, a semiconductor heterostructure for which analytical result are possible. We will also try to identify ways to control the spin relaxation times, induced magnetic fields, and resonance frequency shifts. To support our theoretical results, when possible, we will compare our results with experimental data.

## 2 Hyperfine Interaction and Spin Relaxation Times

When a nonzero spin particle is placed in a magnetic field the initial random orientation of particle's spins will change due to the spin–magnetic field interaction. Let consider the simple example of electrons. As we already mentioned, the electron spin quantum number is 1/2, meaning that as a result of the electronic spin–magnetic field interaction part of the electronic spins will end parallel to the applied magnetic field and the rest of them antiparallel to the applied magnetic field. However, such a process does not occur instantaneously, and its time dependence defines the characteristic spin relaxation times. How fast or how slow this process happens will depend on the particular mechanism which produces the spin alignment. For electrons some of the possible spin alignment mechanism are due to the interaction of electronic spins with phonons, other electron spins, and nuclei. All these mechanisms will be characterized by a spin relaxation time, however, the spin alignment will be finalized in a timescale of the order of the shorter spin relaxation time. In the following we will focus on the hyperfine interaction between electronic and nuclear spins to extract information on both the electronic and nuclear spin dynamics as they result from this mechanism. Our analysis is similar to the one proposed by Overhauser (1953a) for the case of bulk, three dimensional materials. However, the case of semiconductor nanostructures is slightly complicated by the low dimensionality of these physical systems.

The hyperfine interaction, which couples the electronic and nuclear spins is described by the Fermi contact term

$$H = \sum_n H(\mathbf{r}_n) = \sum_n \frac{8\pi}{3} \beta_e \beta_n (\vec{\sigma}_n \cdot \vec{\sigma}_e) \delta(\mathbf{r} - \mathbf{r}_n), \quad (1)$$

where  $\beta_n$  and  $\beta_e$  are the nuclear and electron magnetic moments,  $\vec{\sigma}_n$  and  $\vec{\sigma}_e$  the Pauli spin operators for the nucleus and electron, and  $\delta(x)$  is the usual delta function. The hyperfine interaction depends on the relative distance between the electronic and nuclear spins,  $\mathbf{r} - \mathbf{r}_n$ , via the argument of the delta function,

a signature of the local character of the hyperfine interaction. The main effect of the interaction is a spin-flip process involving both the electronic and nuclear spin. To identify this process we express the product of the two Pauli spin operators,  $(\vec{\sigma}_n \cdot \vec{\sigma}_e)$ , in terms of the creation and annihilation operators,  $\sigma_{n(e)}^\pm$ , as

$$\vec{\sigma}_n \cdot \vec{\sigma}_e = \sigma_n^z \sigma_e^z + 2(\sigma_n^+ \sigma_e^- + \sigma_n^- \sigma_e^+). \quad (2)$$

The first term in Eq. (2) does not contribute to the spin-flip process. The second term in Eq. (2) flips an electron spin from up to down along with a nuclear spin from down to up, whereas the last term in Eq. (2) describes the reverse process. Because the hyperfine interaction mechanism involves at the same time the flips of an electronic and a nuclear spin we expect to obtain a single time dependent equation which will determine both the electronic and nuclear spin relaxation times.

To obtain the general equation which describes the electronic and nuclear spin dynamics due to the hyperfine interaction we make the following approximations. We consider the electronic system in equilibrium with itself, so the electronic spin polarization is the same across the semiconductor nanostructure even if the local density of electronic state may differ from position to position. We consider the electronic spin system subject to an external magnetic field,  $\mathcal{H}$ , and that at any specific time we have  $N_+$  of the electrons with their spins oriented along the magnetic field (spin up) and  $N_-$  with their spins oriented antiparallel to the applied field (spin down). On the other hand, we assume the nuclear system will develop a spatially-dependent spin polarization. For simplicity we will consider for our calculation the case of nuclei with a total spin number 1/2; the generalization for higher nuclear spin numbers is straightforward (Overhauser, 1953a). In this case, we denote by  $M_+(\mathbf{r}_n)$  the probability of a nuclear spin to be oriented along the applied external field, and  $M_-(\mathbf{r}_n)$  the probability of a nuclear spin to be oriented antiparallel to the applied external field.

The spin relaxation process is time dependent and will be related to both the total electronic magnetization,  $D = N_+ - N_-$ , and the position-dependent nuclear magnetization,  $\Delta(\mathbf{r}_n) = M_+(\mathbf{r}_n) - M_-(\mathbf{r}_n)$ . We introduce  $W_{+-}(\mathbf{r}_n)$  and  $W_{-+}(\mathbf{r}_n)$  as the total numbers of electron spins which flip from down to up and from up to down per second from interaction with nucleus  $n$ . We can write the change in  $D$  as

$$\frac{dD}{dt} = 2 \sum_n [W_{+-}(\mathbf{r}_n) - W_{-+}(\mathbf{r}_n)] \quad (3)$$

and in  $\Delta(\mathbf{r}_n)$  as

$$\frac{d\Delta(\mathbf{r}_n)}{dt} = 2[W_{-+}(\mathbf{r}_n) - W_{+-}(\mathbf{r}_n)]. \quad (4)$$

The evaluation of  $W_{+-}(\mathbf{r}_n)$  and  $W_{-+}(\mathbf{r}_n)$  will be done based on Fermi's golden rule by treating the hyperfine interaction as a time dependent perturbation. According to Fermi's golden rule, the electronic transition probability from state  $\mathbf{k}_\downarrow$  to state  $\mathbf{k}'_\uparrow$  induced by nucleus  $n$  is given by

$$W_{\mathbf{kk}'}^{\downarrow\uparrow}(\mathbf{r}_n) = \frac{2\pi}{\hbar} |H_{\mathbf{kk}'}(\mathbf{r}_n)|^2 N_e(\mathbf{k}'_\uparrow) \delta(E_i - E_f), \quad (5)$$

where  $H_{\mathbf{kk}'}(\mathbf{r}_n) = \langle \psi_f(\mathbf{k}'_\uparrow) | H(\mathbf{r}_n) | \psi_i(\mathbf{k}_\downarrow) \rangle$  represents the matrix elements of the hyperfine interaction Hamiltonian for nucleus  $n$ ,  $N_e(\mathbf{k}'_\uparrow)$  is the electronic density of states for the final state, and  $E_i$  and  $E_f$  are the energies corresponding to the initial and final state. Accordingly, the total number of spin flips per second induced by nucleus  $n$ ,  $W_{+-}(\mathbf{r}_n)$ , is

$$W_{+-}(\mathbf{r}_n) = \sum_{\mathbf{k}} W_{\mathbf{kk}'}^{\downarrow\uparrow}(\mathbf{r}_n) M_+(\mathbf{r}_n) f_{FD}(\mathbf{k}_\downarrow, E_i) [1 - f_{FD}(\mathbf{k}'_\uparrow, E_f)], \quad (6)$$

where  $f_{FD}(\mathbf{k}_\sigma, E)$  is the usual Fermi–Dirac distribution function for an electron with momentum  $\mathbf{k}$  and spin  $\sigma$ . The spin-flip process conserves the total energy of the system

$$\frac{\mathbf{k}'_\uparrow^2}{2m} - \beta_e \mathcal{H} - \beta_n \mathcal{H} = \frac{\mathbf{k}_\downarrow^2}{2m} + \beta_e \mathcal{H} + \beta_n \mathcal{H}. \quad (7)$$

The energy conservation law allows us to eliminate  $\mathbf{k}'_\uparrow$  and gives us the possibility to estimate  $W_{+-}(\mathbf{r}_n)$  by replacing the sum over the momenta with an integration over the energy using the density of states. For small magnetic fields,  $\beta_{e(n)} \mathcal{H} \ll k_B T$  ( $T$  is the temperature), the integration can be performed simply as the Fermi–Dirac function can be expanded in a Taylor series.  $W_{+-}(\mathbf{r}_n)$  is calculated in a similar way using  $M_-(\mathbf{r}_n)$  instead of  $M_+(\mathbf{r}_n)$  and changing  $\mathcal{H}$  to  $-\mathcal{H}$ .

In the general case,  $I \neq 1/2$ ,  $\Delta(\mathbf{r}_n) = M_{m+1}(\mathbf{r}_n) - M_m(\mathbf{r}_n)$ , represents the difference in nuclear population between two adjacent nuclear spin levels and we will have to consider the possible nuclear spin flips accordingly. The nuclear magnetic quantum number,  $m$ , can take  $2I + 1$  different values,  $I$  being the nuclear spin number. The calculation is straightforward and the general time dependent electron magnetization can be obtained from the following equation:

$$\begin{aligned} \frac{dD}{dt} &= \frac{1}{V} \sum_n \frac{512\pi^3 \beta_n^2 \beta_e^2 \int d\varepsilon A_e^2(\mathbf{r}_n, \varepsilon) f'_{FD}(\varepsilon)}{9\hbar(2I+1) \int d\mathbf{r} d\varepsilon A_e(\mathbf{r}, \varepsilon) f'_{FD}(\varepsilon)} (D_0 - D) \\ &\quad + \sum_n \frac{512\pi^3 \beta_n^2 \beta_e^2 k_B T \int d\varepsilon A_e^2(\mathbf{r}_n, \varepsilon) f'_{FD}(\varepsilon)}{3\hbar I(I+1)(2I+1)} (\Delta_0(\mathbf{r}_n) - \Delta(\mathbf{r}_n)), \end{aligned} \quad (8)$$

where

$$A_e(\mathbf{r}_n, \varepsilon) = \sum_l |\psi_l(\mathbf{r}_n)|^2 \delta(\varepsilon - E_l), \quad (9)$$

$D_0$  and  $\Delta_0(\mathbf{r}_n)$  are the equilibrium values for  $D$  and  $\Delta(\mathbf{r}_n)$ , respectively, and  $f_{FD}$  is the Fermi–Dirac distribution function. Above,  $A_e(\mathbf{r}_n, \varepsilon)$  represents the electronic density of states,  $l$  labels the state, and  $\psi_l(\mathbf{r}_n)$  the electron wave function at the nucleus. Equation (8) defines the electron and nuclear spin relaxation times due to the hyperfine interaction. These definitions should be considered with some caution, as an exponential decay for the electronic magnetization is obtained only for the case when the nuclear population approaches equilibrium, or is kept at a fixed nonequilibrium value. To calculate the electron spin relaxation time we assume the nuclear polarization is fixed. On the other hand, to extract the nuclear spin relaxation time we use the total spin angular momentum conservation

$$\frac{dD}{dt} = -\frac{2I(I+1)(2I+1)}{3} \sum_n \frac{d\Delta(\mathbf{r}_n)}{dt}, \quad (10)$$

assume the electron spin polarization is refreshed, i.e., remains approximatively constant, and separate the resulting equation into  $n$  equations: one for each nucleus.

Equation (8) is a general equation valid for all semiconductor nanostructures. Let us consider in the following the particular case of a quantum well (QW) structure. Such structures are quasi-two-dimensional, respect to the growth direction the electronic motion being restricted to discrete energy levels through confinement in a potential well. The electron energy dispersion can be written as  $\varepsilon(\mathbf{k}) = \varepsilon_i + \mathbf{k}^2/2m_e$ , where  $\varepsilon_i$  is the minimum of the conduction subband  $i$  and  $\mathbf{k}$  is the electron momentum in the plane of the quantum well. When the Fermi energy of the electronic system is large compared to the distance between the possible electronic energy subbands, the electronic density of states can be written as

$$N(\varepsilon) = \begin{cases} m_e/2\pi, & \varepsilon_1 < E_F < \varepsilon_2, \\ 2m_e/2\pi, & \varepsilon_2 < E_F < \varepsilon_3, \\ \dots \\ jm_e/2\pi, & \varepsilon_j < E_F < \varepsilon_{j+1}, \end{cases} \quad (11)$$

where we consider that the  $j$ -th is the last subband of the system occupied by electrons. In the most general case, when multiple subbands are occupied by electrons, the electron wave function for different subbands will differ and the electronic spin-flip process can take place inside the same subband or between two different subbands. On the other hand, when the energy separation between the energy levels is large compared to the Fermi energy of the electronic system, the electrons will occupy only the first energy subband, similar to the case of a two dimensional electronic gas.

In the case of a QW the electron and nuclear spin relaxation times due to the hyperfine interaction can be written in terms of the electronic local density of states

$$T_{1e}^{-1} = \frac{1}{V} \sum_{\mathbf{r}_n} \frac{1024\pi^3 \beta_e^2 \beta_n^2 \int d\varepsilon A_e^2(\mathbf{r}_n, \varepsilon) f'_{FD}(\varepsilon)}{9\hbar(2I+1) \int d\mathbf{r} d\varepsilon A_e(\mathbf{r}, \varepsilon) f'_{FD}(\varepsilon)} \quad (12)$$

and

$$T_{1n}^{-1}(\mathbf{r}_n) = \frac{512\pi^3 \beta_e^2 \beta_n^2 k_B T \int d\varepsilon A_e^2(\mathbf{r}_n, \varepsilon) f'_{FD}(\varepsilon)}{3\hbar I(I+1)(2I+1)}. \quad (13)$$

For a QW structure the electronic wave function will be written as a product between an envelope function,  $\phi(z)$ , and a Bloch function,  $u_{n\mathbf{K}}(\mathbf{r})$ , such that  $\psi_{\mathbf{K},n}(\mathbf{r}_n) = \exp[i\mathbf{K} \cdot \mathbf{R}] \phi(z) u_{n\mathbf{K}}(\mathbf{r}_n)$ . Accordingly, the electronic local density of states at the nucleus position  $\mathbf{r}_n$  is

$$A_e(\mathbf{r}_n, \varepsilon) = \sum_{j\mathbf{k}} |\psi_{j\mathbf{K}}(\mathbf{r}_n)|^2 \delta(\varepsilon - E_{j\mathbf{K}}), \quad (14)$$

where  $j$  is the subband index,  $\mathbf{K}$  the momentum, and  $\psi_{j\mathbf{K}}(\mathbf{r}_n)$  the electron wave function at the nucleus. When multiple subbands are occupied,

$$\int d\varepsilon A_e^2(\mathbf{r}_n, \varepsilon) f'_{FD}(\varepsilon) = |u(\mathbf{r}_n)|^4 \sum_{j,k} |\phi_j(\mathbf{r}_n)|^2 |\phi_k(\mathbf{r}_n)|^2 \Theta(\varepsilon_{max\{j,k\}}), \quad (15)$$

with

$$\Theta(\varepsilon_j) = \frac{1}{\exp\left[\frac{\varepsilon_j - E_F}{k_B T}\right] + 1}, \quad (16)$$

a temperature dependent factor. In general, the temperature dependent factor becomes important when electrons start to occupy higher conduction subbands.

The electronic spin relaxation time (see Eq. (12)) is temperature independent, except for the case when the Fermi energy is closed to the bottom of a conduction subband. This suggests that the relaxation mechanism due to the hyperfine interaction can be the dominant one for electrons at low temperatures, as it is known that relaxation time due to other mechanisms increase when the temperature decreases (Overhauser, 1953a). The nuclear spin relaxation time (see Eq. (13)) follows the Korringa law (Korringa, 1950), i.e.,  $T_{1n} \sim T^{-1}$ . Similar to the electronic spin relaxation times, temperature corrections to the nuclear spin relaxation time become important when the Fermi energy approaches the bottom of an electronic conduction subband. According to Eq. (13) the nuclear spin relaxation time due to the hyperfine interaction will be position dependent. What is important, is the position dependence of the nuclear spin relaxation along the confinement direction. From the experimental point of view, a standard NMR experimental setup

will record signals from all nuclei in the sample, rather than nuclei from a specific position, i.e., the recorded nuclear spin relaxation time will be

$$\frac{1}{T_{1n}} = \frac{\int dz T_{1n}^{-1}(z) \mathcal{P}_n(z)}{\int dz \mathcal{P}_n(z)}, \quad (17)$$

where  $\mathcal{P}_n(z)$  is proportional to the initial position-dependence of the nuclear polarization. For the case of optical pumping, where the nuclear polarization is realized through the hyperfine interaction,  $\mathcal{P}_n(z) \propto |\phi(z)|^4$ .

Figure 1 presents the position dependence of the  $1/(T_{1n}T)$  ratio as function of the applied electric field for the case of an ideal PQW (see Appendix B for the exact parameters of the PQW). The plots assume single subband occupancy in the electronic conduction band. The electric field control over the nuclear spin relaxation times across the PQW suggests the growth of  $\delta$ -doped PQW, where an intentionally  $\delta$  doped layer is inserted in the original structure. The  $\delta$ -doped layer will consist on different nuclei respect to the host nuclei. For example, in an AlGaAs PQW, possible nuclei in the  $\delta$ -doped layer are In nuclei. This request is essential if nuclear spin relaxation times in the sample will be investigated via NMR.

Figure 2 presents the recorded nuclear spin relaxation time  $1/(T_{1n}T)$  as function of the Fermi energy for uniformly distributed nuclei in the PQW. Note that as the Fermi energy increases the electron density in the PQW increases, higher electronic subbands being occupied. Manipulation of the electronic density

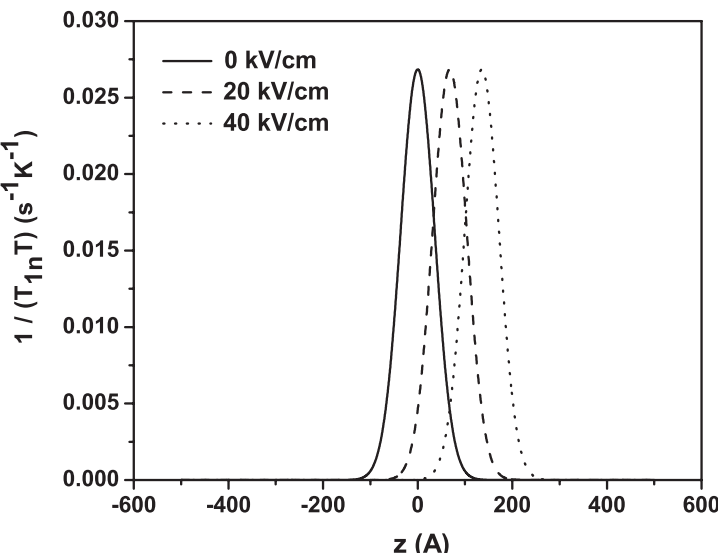


Figure 1. The position dependence of  $1/(T_{1n}T)$  in the ideal PQW for different values of the external electric field

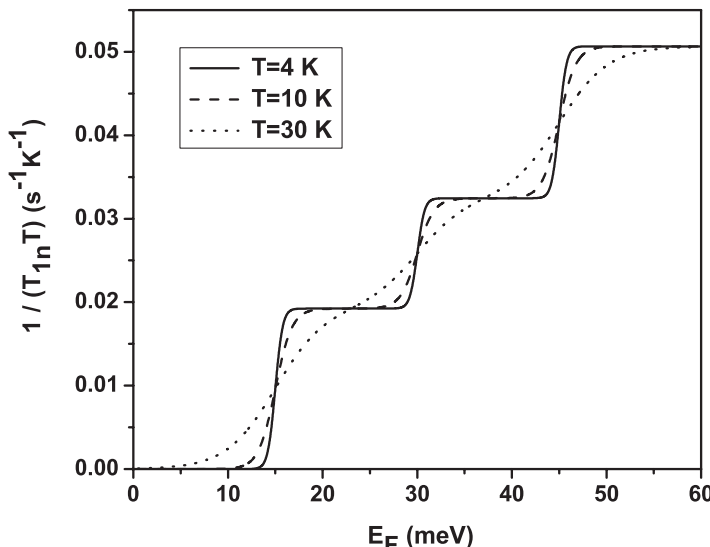


Figure 2. The recorded nuclear spin relaxation time  $1/(T_{1n}T)$  as function of Fermi energy in the ideal PQW for different temperatures (nuclear spin diffusion is neglected)

in the PQW, and implicitly of the corresponding Fermi energy, can be accomplished with a gate. The reference value of the energy is set at  $-\Delta E$  below the minimum of the first conduction band. The dependence of the recorded nuclear spin relaxation time is stepwise, decreasing every time when a new electronic subband becomes occupied. Corrections to Korringa law become important at high temperatures when new electronic subbands start to be occupied. For the particular case of our ideal PQW the temperature induced smearing completely removes the stepwise behavior of the recorded nuclear spin relaxation time around  $T = 30$  K. The results presented in Figure 2 are obtained in the absence of nuclear spin diffusion. Previous calculations show that the effects of nuclear spin diffusion on the recorded nuclear spin relaxation time are minimal (Tifrea and Flatté, 2004).

### 3 Dynamic Nuclear Polarization

The dynamical nuclear polarization (DNP) process was theoretically described by Overhauser (1953b) in bulk metallic samples and is a result of the hyperfine interaction between electronic and nuclear spins. In semiconductor systems, the effect was first used by Lampel (1968) to improve the NMR signal in bulk Si samples. Paget et al. (1977) demonstrated that DNP can be enhanced in GaAs sample using optical techniques. The same optical pumping technique was successfully used by Berg et al. (1990) and by Barrett et al. (1994) to polarized nuclei in quasi

two-dimensional semiconductor heterostructures. Recently, there is evidence that DNP along with optical pumping can lead to nuclear spin polarization in quantum dot samples (Gammon et al., 2001).

To understand the DNP theoretically we start from Eqs. (8) and (10). These two equations can be combined to obtain a general time dependent equation for the nuclear spin dynamics

$$\frac{d\Delta(\mathbf{r}_n)}{dt} = \frac{\Delta_0(\mathbf{r}_n) - \Delta(\mathbf{r}_n)}{T_{1n}(\mathbf{r}_n)} + \frac{1}{(2I+1)k_B T \tilde{N}} \frac{D_0 - D}{T_{1n}(\mathbf{r}_n)}, \quad (18)$$

where  $\tilde{N} = \int d\mathbf{r} d\varepsilon A_e(\mathbf{r}, \varepsilon) f'_{FD}(\varepsilon)$ . Equation (18) describes the nuclear spin dynamics as a result of the hyperfine interaction. Additionally, the nuclear spin dynamics will be influenced by other mechanism which involve the nuclear spin, i.e., interaction of nuclear spins with phonons, impurities, electron, and other nuclei. For a complete equation of the nuclear spin dynamics, such effects should be part of Eq. (18). To account for these additional interactions involving the nuclear spins we will have to adjust Eq. (18) by changing the first term in the right hand side

$$\frac{1}{T_{1n}(\mathbf{r}_n)} \rightarrow \frac{1}{T_{1n}(\mathbf{r}_n)} + \frac{1}{T'_n}, \quad (19)$$

where  $T'_n$  represents the nuclear spin relaxation time due to additional relaxation mechanisms. Note that such a change is not justified in the second term in the right hand side of Eq. (18) because this term is strictly related to the hyperfine interaction, i.e., is related to the electron spin-flip.

As it stands, Eq. (18) is a position and time dependent differential equation which under special conditions can be solved exactly. In optical DNP, spin polarized electrons created by absorption of polarized light or electron injection (Strand et al., 2003) will transfer their polarization to the nuclei via the hyperfine interaction. In most of the experimental setups the electron polarization,  $D$ , is kept constant as a result of continuous (or quasi-continuous) resupply of spin polarized electrons from optical pumping of the electron system. Translated in theory, we can consider the last term in Eq. (18) to be time independent, and accordingly we can solve the equation for  $\Delta(\mathbf{r}_n)$

$$\Delta(\mathbf{r}_n, t) = [\Delta_0 + \Delta_{ind}(\mathbf{r}_n)] \left\{ 1 - \exp \left[ -t \left( \frac{1}{T_{1n}(\mathbf{r}_n)} + \frac{1}{T'_n} \right) \right] \right\}, \quad (20)$$

where

$$\Delta_{ind}(\mathbf{r}_n) = \frac{1}{(2I+1)k_B T \tilde{N}} \frac{T'_n}{T_{1n}(\mathbf{r}_n) + T'_n} (D_0 - D) \quad (21)$$

represents the induced nuclear polarization due to the hyperfine interaction. In general, when subject to external magnetic fields, the nuclear polarization,  $\Delta_0$ , is less than 1%, meaning that the dominant nuclear polarization comes from DNP via the hyperfine interaction.

Two different time regimes can be identified in Eq. (20). First, in the initial stages of the DNP process ( $t \ll T_{min}$ ; with  $T_{min} = \min [T_{1n}, T'_n]$ ), the nonequilibrium nuclear system magnetization can be approximated as

$$\Delta(\mathbf{r}_n, t) \propto \Delta_{ind}(\mathbf{r}_n) \frac{t}{T_{min}} , \quad (22)$$

a linear dependence on time being predicted. This situation will lead to a nuclear polarization  $\Delta(\mathbf{r}_n, t) \propto |\psi_l(\mathbf{r}_n)|^4 t$  (Tifrea and Flatté, 2003), a dependence which was observed by Barrett et al. (1994) in GaAs semiconductor quantum wells. On the other hand, Eq. (20) predicts a saturated nuclear polarization

$$\Delta(\mathbf{r}_n, t) = \Delta_0 + \frac{1}{(2I+1)k_B T \tilde{N}} \frac{T'_n}{T_{1n}(\mathbf{r}_n) + T'_n} (D_0 - D) , \quad (23)$$

when  $t \gg T_{min}$ . This result should be regarded with some precaution. In real conditions, nuclei are also subject to nuclear spin–nuclear spin interactions which can be source of nuclear spin diffusion. Actually, nuclear spin diffusion is of main importance when we consider DNP in bulk semiconductor samples. As it was suggested by Paget (1982), due to the lack of electronic localization in bulk semiconductors, diffusion plays an important role for nuclear polarization of such samples. In bulk semiconductors the hyperfine interaction will be effective between donor nuclei and electrons, as shallow donors are the one responsible for electron localization. The nuclear polarization of the entire sample will be a result of nuclear spin diffusion, a process involving the donor nuclei and the rest of the nuclei in the system. To account for nuclear spin diffusion Eq. (18) should include an additional term on the right hand side of the equation. Such a term will include the diffusion constant which characterize the nuclear spin diffusion process. This constant was reported by Paget (1982) to be of the order of  $10^3 \text{ \AA}^2/\text{s}$  for GaAs bulk systems. Apparently, when nanostructured semiconductors are considered, nuclear spin diffusion can be neglected (Poggio et al., 2003; Strand et al., 2003). This conclusion is also sustained by more recent attempts to measure the nuclear spin diffusion constant (Malinowski and Harley, 2000b). In their experiment, Malinowski and Harley (2000b) used a double QW structure. One of the wells was subject of optical pumping. FR data were obtained for the second QW to extract information on the induced nuclear polarization. As the only source of nuclear polarization in this second well is nuclear spin diffusion from the first well, the experimental data lead to the conclusion that the diffusion process is characterized by a spin diffusion constant of the order of  $10^2 \text{ \AA}^2/\text{s}$ , one order of magnitude smaller than the one in bulk samples. However, additional theoretical and experimental efforts are needed to clarify the issue of nuclear spin diffusion in samples with reduced dimensionality such as quantum wells or quantum dots.

The result of DNP is a rearrangement of nuclear spins on the possible nuclear spin levels. In principle, the difference in occupation between adjacent level,  $\Delta(\mathbf{r}_n)$

could depend on the nuclear magnetic quantum number  $m$ . However, in the kinetic limit, when the dominant effect determining the occupation of a given level is DNP, then  $\Delta(\mathbf{r}_n)$  should not depend on  $m$ . The induced nuclear spin polarization can be calculated as

$$\mathcal{P} = \frac{\sum_m m M_m}{I \sum_m M_m}. \quad (24)$$

The nuclear spin polarization is an important parameter for NMR experiments, where the absorption signal is proportional to  $\mathcal{P}_1$ . For the case of nanostructured materials  $\mathcal{P}_1$  will be position dependent as nuclei in different regions of the sample will overlap differently with the electronic population. Also, due to the time evolution of DNP, nuclear spin polarization across the system will be time dependent.

Figure 3 presents the time and position dependence of the induced nuclear spin polarization for all active nuclear species in the AlGaAs PQW. The electron spin polarization was considered to be  $D = 50\%$  out of optical pumping, and the additional nuclear spin relaxation times of the order of 10 min,  $T'_n = 600$  s (McNeil and Clark, 1976). These times are obtained from interaction of nuclei with phonons in the system. We can clearly identify for all nuclear isotopes the

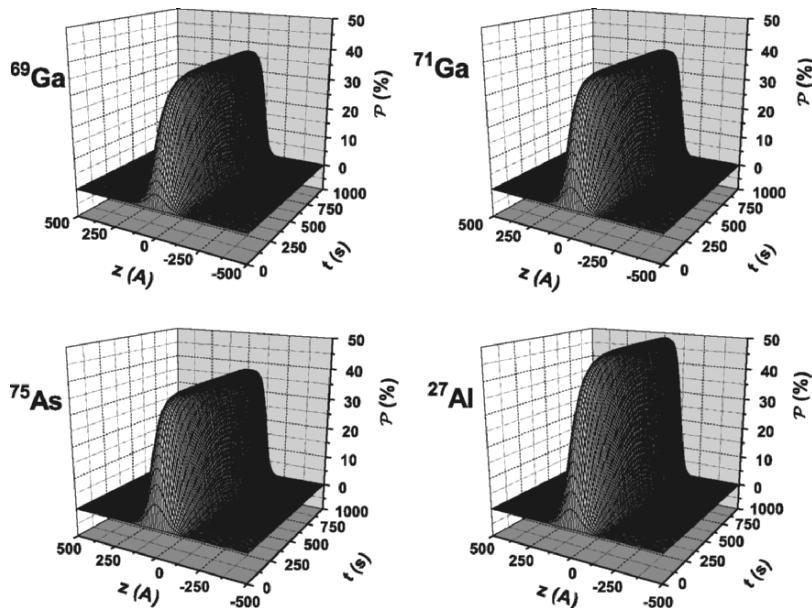


Figure 3. The position and time dependence of the induced nuclear spin polarization for all nuclear isotopes in the AlGaAs PQW ( $^{69}\text{Ga}$ ,  $^{71}\text{Ga}$ ,  $^{75}\text{As}$ ,  $^{27}\text{Al}$ ). As parameters we considered the optically pumped electron spin polarization to be  $D = 50\%$  and the additional nuclear spin relaxation time from other nuclear spin relaxation mechanisms  $T'_n = 600$  s (this value was considered for all active nuclear isotopes)

two regimes discussed previously, namely the linear dependence on time of the nuclear spin polarization in the initial stages of the DNP, and the saturation of the nuclear spin polarization in the late stages of the DNP. The maximum values for the induced nuclear spin polarization are in the center of the PQW where the probability to find electrons is higher, and implicitly the hyperfine interaction is more efficient. The nuclei in the vicinity of the PQW barriers are not polarized, as their overlap with the electronic system is very small. The acquired nuclear spin polarization depends on the nuclear isotope as different isotopes have different nuclear gyromagnetic numbers and different nuclear magnetic factors. The induced nuclear spin polarization is higher for the case of the  $^{27}\text{Al}$  isotope ( $I = 5/2$ ). The nuclear isotopes of Ga and As have the same nuclear magnetic number ( $I = 3/2$ ) and slightly different nuclear gyromagnetic factors, properties which account for their similar nuclear spin polarizations in the PQW (see Figure 3).

Three important parameters influence the value of the nuclear spin polarization in the PQW. Their role in the polarization of the  $^{71}\text{Ga}$  isotope is presented in Figure 4. These parameters play a similar role in the case of other nuclear isotopes in the sample. The first one is the additional nuclear spin relaxation time,  $T'_n$ . Its influence on the position dependence of the saturated nuclear spin polarization is presented in Figure 4a. The plot presents the nuclear spin polarization in the PQW as function of position for different values of  $T'_n$  and for a fixed temperature  $T = 5\text{ K}$  and a fixed initial spin polarization in the electronic system,  $D = 100\%$ . This parameter mainly affects the width of the polarized nuclear population across the

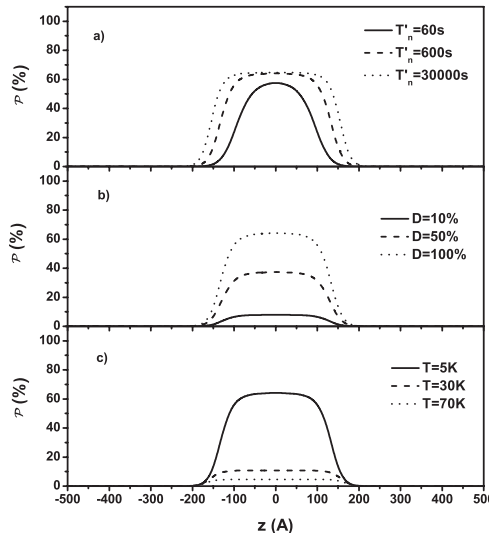


Figure 4. The position dependence of the saturated induced nuclear spin polarization for  $^{71}\text{Ga}$  nuclear isotope for different a) additional nuclear spin relaxation time, b) initial spin polarization in the electronic system, and c) values of the temperature

PQW, smaller the  $T'_n$ , narrower the polarized nuclear population. As one can see this parameter does not influence drastically the maximum value of the nuclear spin polarization in the system. Our estimation considered a constant value for  $T'_n$  across the nanostructure. This assumption should be valid when the additional nuclear spin relaxation mechanism is, for example, due to nuclear–phonon interaction. However, one may expect that some other types of interaction will induce a position dependent additional nuclear spin relaxation time. The second parameter is the initial spin polarization in the electronic system,  $D$ . The role of the initial spin polarization in the electronic system is considered in Figure 4b where we plotted the saturated nuclear spin polarization as function of position across the PQW for different values of the initial spin polarization in the electronic system and constant additional nuclear spin relaxation time,  $T'_n = 600$  s, and temperature,  $T = 5$  K. Our analytical estimations proved that higher the value of the spin polarization in the electronic system, greater the final spin polarization in the nuclear system. The spin polarization in the electronic system influences mainly the value of the maximum nuclear spin polarization and has little effect on its width across the PQW. The third parameter we considered is the temperature. We analyzed the effect of the temperature on the nuclear spin polarization keeping constant the additional nuclear spin relaxation time,  $T'_n = 600$  s and the initial spin polarization in the electronic system,  $D = 100\%$ . Our conclusions are summarized in Figure 4c where we plotted the value of the nuclear spin polarization for different temperature values. As we expected, as the temperature increases the maximum value of the nuclear spin polarization reduces. On the other hand, the temperature does not influence drastically the width of the polarized population on the restricted direction across the PQW. From the experimental point of view, based on our analysis, one can conclude that the DNP is more efficient at low temperatures and large initial spin polarization in the electronic system.

## 4 Induced Magnetic Fields

### 4.1 HYPERFINE MAGNETIC FIELDS

The effects of the hyperfine interaction on both nuclei and electrons can be understood if we consider the average over the orbital coordinates of the electron for the hyperfine interaction Hamiltonian:

$$\langle H_n \rangle = \frac{2}{3} \mu_0 g_0 \mu_B g_n \mu_n (\mathbf{I} \cdot \mathbf{S}) |\psi(\mathbf{r}_n)|^2 , \quad (25)$$

where  $\mathbf{S}$  and  $\mathbf{I}$  are the electronic and nuclear spin operators,  $\mu_0$  the vacuum magnetic permeability,  $g_0$  the free-electron  $g$ -factor,  $g_n$  the nuclear  $g$ -factor,  $\mu_B$  the electron Bohr magneton, and  $\mu_n$  the nuclear magneton. The matrix elements of the hyperfine interaction can be interpreted in terms of virtual magnetic fields acting on both electrons and nuclei.

The hyperfine interaction effects on electrons can be viewed as resulting from virtual magnetic fields,  $B_{hf}^n$ , created by nuclei. One can find the form of such fields if we rewrite the matrix elements of the hyperfine interaction Hamiltonian as  $g^* \mu_B B_{hf}^n$ , where  $g^*$  represents the effective electron  $g$ -factor. Simple calculations lead to

$$\mathbf{B}_{hf}^n(\mathbf{r}_n) = \frac{2\mu_0\mu_n}{3} \frac{g_0}{g^*} \phi^2(z) \sum_{\alpha} g_{n\alpha} |u_{\alpha}(\mathbf{r}_n)|^2 \langle \mathbf{I}_{\alpha}(z) \rangle, \quad (26)$$

where  $\alpha$  labels all nuclear species in the system,  $g_{n\alpha}$  represents the nuclear  $g$ -factor for the  $\alpha$  nucleus,  $\phi(z)$  the electronic envelope function,  $u_{\alpha}(\mathbf{r}_n)$  the electronic Bloch function at the  $\alpha$  nucleus, and  $\langle \mathbf{I}_{\alpha}(z) \rangle$  the average nuclear spin polarization corresponding to each of the nuclear species  $\alpha$ . In general, the value of the effective electronic  $g$ -factor will depend on the geometry of the semiconductor QW (Malinowski and Harley, 2000a). The virtual magnetic field created by nuclei is position dependent and will reflect both the position dependence of the electron distribution and of the nuclear spin polarization in the QW.

On the other hand, the effects of the hyperfine interaction on nuclei can be viewed as a virtual magnetic field created by the electrons,  $B_{hf}^e$ , whose form can be extracted if we rewrite the matrix elements of the hyperfine interaction as  $g_n \mu_n B_{hf}^e$ . One finds a position dependent virtual magnetic field acting on nuclei

$$\mathbf{B}_{hf}^e(\mathbf{r}_n) = -\frac{2\mu_0}{3} g_0 \mu_B \phi^2(z) |u(\mathbf{r}_n)|^2 \langle \mathbf{S} \rangle. \quad (27)$$

Different nuclear species are characterized by different values of the electronic Bloch functions at the nuclei sites, and accordingly the virtual electronic hyperfine magnetic fields will be species dependent. Also, the fields will be position dependent as a result of the electron distribution across the QW. On the other hand, there will be no position dependence of these fields due to the spin polarization in the electronic system, the average electronic spin polarization,  $\langle \mathbf{S} \rangle$ , being constant (position independent) as a result of optical pumping.

Figure 5 presents the position dependence of the virtual hyperfine field acting on the electrons. Each nuclear isotop in the PQW will contribute to the value of the virtual hyperfine field seen by the electrons. The position dependence of the hyperfine magnetic field acting on electrons is given by the position dependent concentration of different nuclear isotopes and also by the position dependence of the contact hyperfine interaction across the sample. The maximum values of the hyperfine fields acting on electrons are of the order of few hundreds gauss. The fields can be measured indirectly in FR experiments as Overhauser frequency shifts in the electronic spin resonance frequency. The divergences in the value of the magnetic field, observed at approximatively  $\pm 177.9$  Å, are due to a vanishing value of the effective electronic  $g$  factor at these points. Such divergencies will not

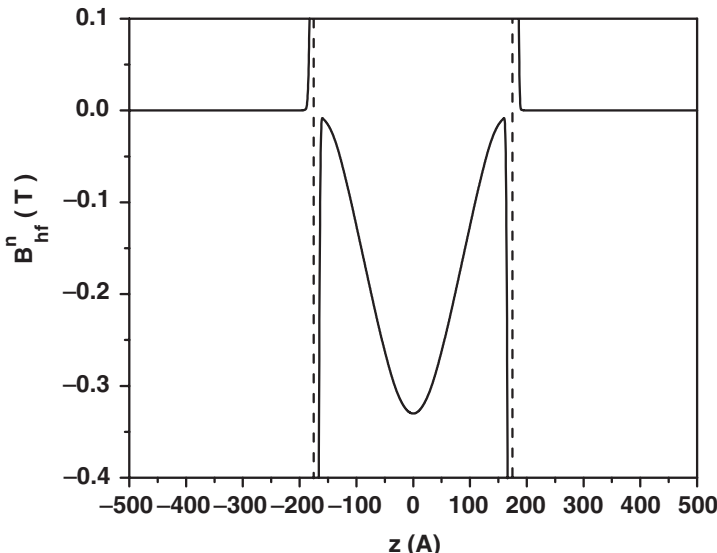


Figure 5. The position dependence of the virtual hyperfine magnetic field acting on electrons. The divergencies at  $\pm 177.9 \text{ \AA}$  are due to the zeros of the electronic effective  $g$  factor in the PQW

be visible in FR experiments, as the effective electronic  $g$  factor does not enter the expression of the Overhauser frequency shifts (for more details see section 5 of the chapter).

In Figure 6 we present the position dependence of the hyperfine magnetic field acting on different nuclear isotopes due to the polarized electrons in the system. The value of the initial spin polarization of the electronic system is considered to be  $D = 100\%$  constant across the PQW. According to Eq. (27) the magnetic fields will be different for each isotope in the sample depending on the value of the electronic Bloch function at the isotope site. For example the two Ga isotopes are characterized by the same value of the electronic Bloch function, and as a consequence they will be subject to similar hyperfine magnetic fields from the electrons (for the exact value of the electronic Bloch function at the Ga sites see Appendix B). On the other hand the Bloch function corresponding to As isotopes have a different value (Paget et al., 1977), resulting in higher hyperfine magnetic fields. For Al, as it substitutes Ga in the PQW, we consider the same value for the electronic Bloch function as the one for Ga isotopes, meaning that the hyperfine magnetic fields acting on Al nuclei will be identical to the ones acting on Ga nuclei. These fields should be detectable in NMR experiments as Knight shifts in the nuclear spin resonance frequency. As different nuclear isotopes have different nuclear gyromagnetic factors, the corresponding Knight shifts will be different even if the hyperfine magnetic fields acting on nuclei will be the same (the case of  $^{69}\text{Ga}$ ,  $^{71}\text{Ga}$ , and  $^{27}\text{Al}$  nuclei).

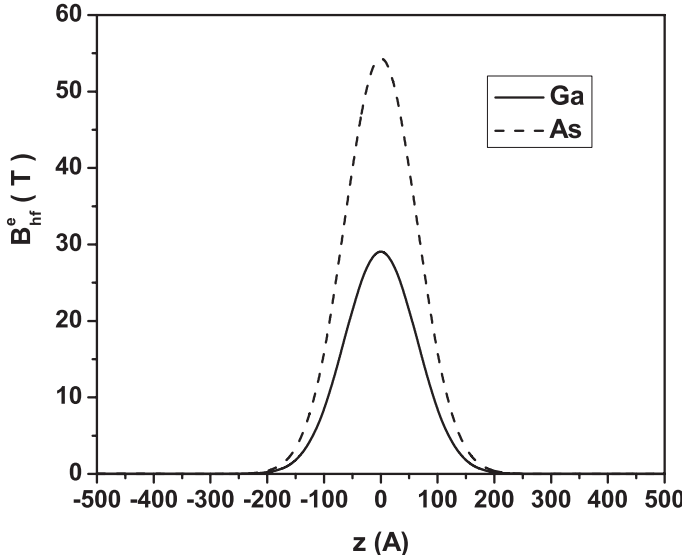


Figure 6. The position dependence of the virtual hyperfine magnetic field acting on Ga and As nuclei (the initial spin polarization in the electronic system is considered to be  $D = 100\%$ )

#### 4.2 DIPOLAR MAGNETIC FIELDS

Along with the virtual magnetic fields acting on both nuclei and electrons one can identify also the presence of an induced local dipolar nuclear magnetization,  $\mathcal{M}_{ind}$ . This additional magnetization is a result of nuclear spin–nuclear spin dipole interaction and is defined as

$$\mathcal{M}_{ind}^\alpha(\mathbf{r}_n) = \sum_m m M_m^\alpha(\mathbf{r}_n), \quad (28)$$

where  $\alpha$  labels the nuclear species. To calculate the induced field, we consider the dependence of the nuclear relaxation time on the growth direction (Tifrea and Flatté, 2003), and we assume that at each nuclear position  $z_n$  we have a uniformly magnetized plan at nuclei position. The dipolar field from the nuclei is

$$B_d(\mathbf{r}) = \mu_0 \mu_n \sum_\alpha \mathcal{M}_{ind}^\alpha(\mathbf{r}), \quad (29)$$

where  $\mathcal{M}_{ind}^\alpha(\mathbf{r})$  represents the total induced nuclear magnetization in the unit cell situated at position  $\mathbf{r}$ . This magnetic field will act both on the nuclei and the electrons. A simple calculation show that  $B_d(\mathbf{r}_n) \sim \Delta_{ind}(\mathbf{r}_n)$ , and as a result the time and the position dependence of the dipolar nuclear magnetic field can be extracted from Eqs. (20) and (21). The nuclear dipolar field profile across the QW

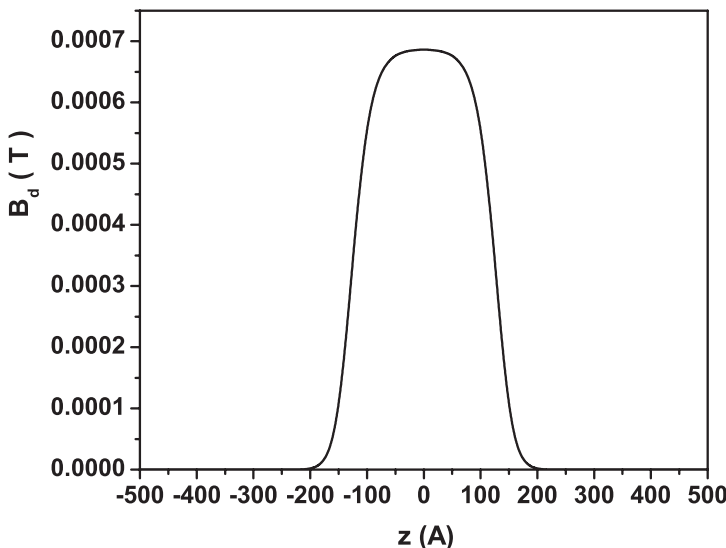


Figure 7. The position dependence of dipolar nuclear field acting on both electrons and nuclei in the sample

structure will depend on the position dependence of the nuclear spin relaxation time due to the hyperfine interaction and additional nuclear spin relaxation times due to other mechanisms. This is similar to the nuclear spin polarization case.

Figure 7 presents the position dependence of the dipolar nuclear field acting both on electrons and nuclei. The values of the field are obtained for an initial spin polarization in the electronic system  $D = 100\%$ , an additional nuclear spin relaxation time  $T'_n = 600$  s, and temperature  $T = 5$  K. As we expected, the dipolar field is much smaller than both the hyperfine magnetic fields acting on nuclei or electrons. This fact will make their detection difficult, especially if one considers the effects of this field on nuclei. However, if we use measurements of the electronic spin precession frequency, the effects of the dipolar magnetic fields may be possible to extract for samples with high electronic  $g$ -factors (for example InAs systems). In such systems, the differences between the hyperfine and dipolar fields acting on electrons can be as close as two orders of magnitude, depending on the value of the electronic  $g$ -factor.

## 5 Overhauser Frequency Shifts

The effects of DNP can be observed experimentally using NMR or FR experiments by measuring the Knight or Overhauser spin resonance frequencies shifts for nuclei or electrons. Such shifts are a result of the hyperfine interaction between the electronic and nuclear spins. In the following we will present a theoretical analysis of the spin precession frequency of electrons subject to an induced

position-dependent nuclear spin polarization in semiconductor nanostructures. Our results will be discussed in connection with FR experimental data obtained in the AlGaAs PQW (Poggio et al., 2003).

In the previous section of the chapter we presented a calculation of the hyperfine magnetic field acting on electrons due to the induced spin polarization in the nuclear system (see Eq. (26)). The effects of this *virtual* field can be measured in FR experiments, where the extracted Larmour frequency corresponding to the electron spin precession will depend both on the applied external magnetic field and the induced hyperfine magnetic field. The Overhauser shift corresponds to the change in the Larmour frequency due to DNP. The induced hyperfine magnetic field is position dependent, and accordingly the Overhauser shift will have a position dependence:

$$\Delta\nu_{hf}^e(\mathbf{r}) = -\frac{2\mu_0}{3h}g_0\mu_B\mu_n \sum_i g_n^i |\psi^i(\mathbf{r})|^2 c_i(\mathbf{r}) < \mathbf{I}_i(\mathbf{r}) >. \quad (30)$$

Different from the induced hyperfine magnetic fields, the Overhauser frequency shift depends only on the bare electronic *g* factor and is independent of the effective electronic *g* factor. Dipole nuclear spin interaction will induce an additional shift in the electronic spin precession frequency, however, such shifts are usually much smaller than the Overhauser shifts and will be neglected hereafter. Dipolar shifts are proportional to the effective electronic *g*-factor, and they may be important in systems with large values of the effective *g*-factor.

Figure 8 presents the position dependence of the calculated Overhauser frequency shift for the case of the PQW. Note that all nuclear isotopes in the PQW

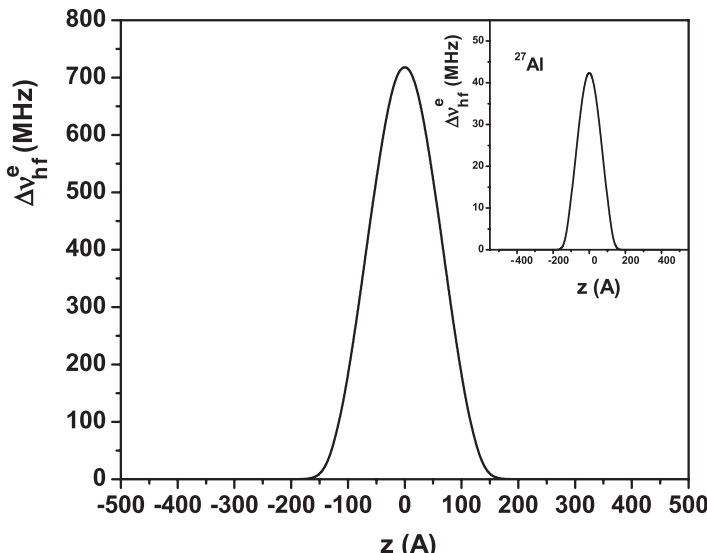


Figure 8. The position dependence of the Overhauser frequency shift in the PQW. Inset: the  $^{27}\text{Al}$  contribution to the total Overhauser shift

contribute to the total value of the Overhauser frequency shift. The inset of Figure 8 presents the contribution of the  $^{27}\text{Al}$  nuclear isotope. From the experimental point of view, the presence of the  $^{27}\text{Al}$  nuclear isotope was observed only in bulk AlGaAs samples (Ekimov and Safarov, 1972) despite a large effort in this direction.

In general, frequency shifts measured in FR experiments cannot trace a position dependence of the Overhauser shifts, the value of the measured Larmour precession frequency being a response of the entire sample. In other words, the experimental value of the Overhauser shift will be a convolution between a position dependent frequency shift and the probability to find electrons at various positions in the sample. Accordingly, when FR data are obtained for low dimensionality samples the recorded Overhauser shift should be obtained as

$$\Delta\nu_L = \frac{\int d\mathbf{r} \Delta\nu_{hf}^e(\mathbf{r}) |\psi(\mathbf{r})|^2}{\int d\mathbf{r} |\psi(\mathbf{r})|^2}. \quad (31)$$

Poggio et al. (2003) performed FR experiments to obtain Overhauser frequency shifts in an  $\text{Al}_x\text{Ga}_{1-x}\text{As}$  PQW, where the concentration of the  $^{27}\text{Al}$  nuclei is varied from 7% in the center of the well to 40% in the barriers. Directly below the PQW is a 450-nm  $\text{Al}_{0.4}\text{Ga}_{0.6}\text{As}$  barrier, then a 500-nm layer of low temperature-grown GaAs serving as a conduction barrier, and finally a 50-nm n-GaAs back gate contacted using annealed AuGe/Ni. Above the PQW is a 50-nm  $\text{Al}_{0.4}\text{Ga}_{0.6}\text{As}$  barrier followed by a transparent front gate consisting of 5 nm of titanium and 5 nm of gold which was evaporated on the sample surface. A voltage  $U_g$  applied across the front gate and the grounded back gate produces a constant electric field across the PQW and results in a negligible leakage current ( $<100 \mu\text{A}$ ). This sample has very similar properties with our example case (see Appendix B). Figure 9a presents the experimental data obtained by FR (Poggio et al., 2003).

The experiment considered different initial conditions. First, the nuclear spin polarization in the system is obtained in the absence of an applied external electric field. One expects in this situation that the nuclear spin polarization will be centered in the PQW. However, in reality due to the strong confinement in the PQW, even in the absence of applied gate voltages (gate voltages are equivalent of applied external fields), the electronic population is not centered, its position across the nanostructure being equivalent to the presence of a built in electrical potential  $U_0 = -1.1 \pm 0.1 \text{ V}$ . Overhauser frequency shifts are obtained thereafter for different applied gate voltages ( $\blacksquare - U_g = 0 \text{ V}$  in Figure 9a). Each point corresponds to a different gate voltage, and should be understood as a direct probe of the position dependent nuclear spin polarization in the sample. When external gate voltages are applied, the position of the electronic population across the PQW is changed, resulting in a different overlap of the electronic population

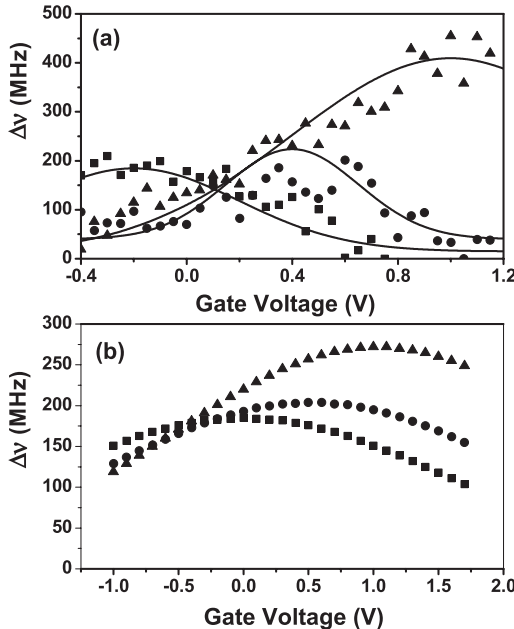


Figure 9. a) Overhauser frequency shifts for different initial nuclear spin polarizations ( $\blacksquare$  – 0 V,  $\bullet$  – 0.5 V,  $\blacktriangle$  – 1 V) – lines are included for eye guidance; b) The integrated Overhauser frequency shift calculated for an initial  $\sim 28\%$  electronic spin polarization ( $\blacksquare$  – 0 V,  $\bullet$  – 0.5 V,  $\blacktriangle$  – 1 V)

with the nuclear polarization in the system, and accordingly a different overall Overhauser shift. The timescale for the initial stage of the experiment is of the order of minutes (about 20 min), to allow for a saturated nuclear spin polarization in the system. On the other hand, the timescale for the final stage of the experiment is much shorter, so that the initial nuclear spin polarization in the system is not disturbed when FR data are collected. As expected, the maximum frequency shift is obtained when the gate voltage matches the value of the gate voltage used in the initial polarization of the nuclear spin system. Second, the initial stage of the experiment is repeated in the presence of an applied gate voltage, resulting in a different initial position dependence of the nuclear spin polarization across the PQW. The corresponding Overhauser shifts ( $\bullet$  –  $U_g = 0.5$  V,  $\blacktriangle$  –  $U_g = 1$  V) are then collected in the same way as for the  $U_g = 0$  V situation. By polarizing nuclei in the sample at different values of the gate voltage, a wide distribution of about 8 nm of polarized nuclei was controlled electrically over a distance of about 20 nm.

The experimental data should be interpreted as a probe of a position dependent nuclear spin polarization in the PQW. Figure 9b presents the calculated Overhauser frequency shifts based on Eq. (31). Several parameters were included in our calculation. We considered first the experimental data extracted when the initial nuclear spin polarization was obtained in the absence of a applied external

voltage. The analysis of the experimental data in this situation leads to the conclusion that the initial spin polarization in the electronic system is  $D \cong 28\%$  as a result of the optical pumping of the PQW. The value of the initial spin polarization in the electronic system was estimated such that the maximum of the theoretical Overhauser shift will match the maximum value of the experimental Overhauser shift. The obtained value is reasonable given the experimental conditions. With this value for the electronic spin polarization, the maximum nuclear spin polarization in the PQW as a result of DNP is about  $\sim 22\%$  for Ga and As nuclei, and about  $\sim 30\%$  for Al nuclei. If one averages the nuclear spin polarization across the PQW the obtained overall value is about 2.5%. Remember that only the nuclear population in the central regions of the PQW is polarized due to a very strong confinement in the electronic system, meaning that most of the nuclei in the PQW remain unpolarized (see for example Figure 3). When the initial nuclear spin polarization is obtained in the presence of an external electric potential, the maximum value of the Overhauser frequency shift is changed, mainly due to the fact that the electron population will overlap more  $^{27}\text{Al}$  nuclei than in the first situation when the nuclear polarization was obtained in the absence of an applied electric potential. This fact should be understood in connection with the position dependence of the Al and Ga nuclei across the PQW.

The calculated Overhauser frequency shifts match reasonable the experimental data. Some differences should be mentioned. The width of the polarized nuclear population is smaller in the theoretical estimations respect to the width proved experimentally. Also, as Figure 9 proves, the maximum value of the Overhauser shift calculated for the case when the initial nuclear spin polarization corresponds to an applied electric potential  $U_g = 1$  V, is slightly lower than the experimental value. In the first case, one explanation can be the nuclear spin diffusion, which in the theoretical calculations was completely ignored. Another possible explanation can be related to the value of the additional nuclear spin relaxation times due to other mechanisms than the hyperfine interaction mechanism; our calculation considered a constant value of 600 s for those times, which may be correct in bulk samples, but incorrect for the case of low dimensional nanostructures.

## 6 Summary

In summary, we presented a detailed analysis of the effects of the hyperfine interaction in low dimensional nanostructures systems. The results presented in this chapter are very general, and they should be applicable to any low dimensional system. The nuclear spin dynamics in semiconductor nanostructures is governed mainly by the hyperfine interaction between electronic and nuclear spins. We addressed topics such as the nuclear spin relaxation time, dynamical nuclear polarization, induced hyperfine magnetic fields, and Overhauser shifts in the electronic spin resonance frequencies. Our case example was an  $\text{Al}_x\text{Ga}_{1-x}\text{Al}$

PQW, a quasi-two-dimensional system where electrons are confined in a parabolic potential respect to one direction.

First, we discussed the hyperfine interaction and its implications on both the nuclear and electronic spin relaxation times. The calculated electron spin relaxation time as a result of hyperfine interaction for quantum well structures is of the order of  $10^{-5}$  s, much longer than electron spin relaxation times due to other interactions involving the electron spin. In other words, hyperfine interaction is not determinant for the electron spin relaxation time, as the dominant relaxation mechanism for the electron spin will be the one leading to the shorter relaxation time. On the other hand, hyperfine interaction is the main mechanism governing the nuclear spin dynamics. The resulting nuclear spin relaxation time depends on temperature and the local electronic density of states at the nuclear position. The temperature dependence of the relaxation time is given by Korringa law (Korringa, 1950), i.e.,  $T_{1n} \sim T^{-1}$ . For low dimensional nanostructures, the natural confinement of the electrons is responsible for the position dependence of the local electronic density of states, and implicitly for a position dependent nuclear spin relaxation time. Moreover, in quantum wells and quantum dots, the electronic envelope function can be manipulated with electric fields. Accordingly, electric fields may be used as an efficient way to manipulate the nuclear spin dynamics in the system.

An important effect of the electron spin–nuclear spin interaction is the dynamical nuclear polarization, also known as the Overhauser effect. When hyperfine interaction is efficient, due to the flip-flop process involving the electronic and nuclear spins, any spin polarization in the electronic system is efficiently transferred to the nuclear system, resulting in a nuclear spin polarization in the system. The reduced number of available nuclei in low dimensional nanostructures have to be balanced by large nuclear polarizations to increase the measured signals in NMR and FR experiments. Different from bulk materials where the nuclear spin polarization is less than 1%, in quantum wells or quantum dots, the nuclear spin polarization can be as big as 6.5% (Malinowski and Harley, 2000b), or 65% (Bracker et al., 2005). The second part of the chapter presented a detailed analysis of the dynamical nuclear polarization in low dimensional system, with an emphasize on the PQW. The induced nuclear spin polarization is both time and position dependent. As function of time, the induced nuclear spin polarization is characterized by two distinct regimes, i.e., a linear time dependence in the initial stages, and a saturation in the final stages of the DNP. As function of position, the induced nuclear spin polarization presents a maximum in the region with a maximum density of electrons. However, the position dependence of the induced nuclear spin polarization is complex, being influenced by factors such as additional nuclear spin relaxation mechanisms, temperature, and the initial spin polarization of the electronic system. A different visualization of DNP can be made in terms of induced hyperfine magnetic fields acting on nuclei and electrons.

Their effects can be observed in NMR or FR experiments as Knight shifts in the nuclear spin resonance frequency, or Overhauser shifts in the electron spin resonance frequency. DNP depends on the local electronic density of states, and it can be manipulated with electric fields in a similar way as nuclear spin relaxation times. Experimentally, this was proved by FR experiments in PQWs (Poggio et al., 2003). Our theoretical analysis of FR experiments leads to Overhauser frequency shifts close to the observed values for the PQW.

## Appendix

### A Table of Semiconductor Isotopes

Table 1 presents a list of semiconductor elements or isotopes as reported by Holden (1998). The first column gives the element symbol along with its atomic number. Second column reports the natural abundance of the isotope measured in atom percent—we limited the table only to elements with a nonzero natural abundance. The third column presents the nuclear spin number in units of  $\hbar$  and the parity of the isotope. The fourth column reports the nuclear magnetic moment in units of nuclear magneton units ( $\mu_n = 5.05078343 \times 10^{-27}$  J/T).

TABLE 1. Table of semiconductor isotopes (Holden, 1998)

Element or isotope	Natural abundance (%)	Nuclear spin number ( $\hbar$ )	Nuclear magnetic moment (nuclear magneton units)
$^{27}\text{Al}$	100	5/2+	+3.64151
$^{28}\text{Si}$	92.22 (2)	0+	
$^{29}\text{Si}$	4.69 (1)	1/2+	-0.5553
$^{30}\text{Si}$	3.09 (1)	0+	
$^{31}\text{P}$	100	1/2+	+1.13160
$^{64}\text{Zn}$	48.63 (60)	0+	
$^{66}\text{Zn}$	27.90 (27)	0+	
$^{67}\text{Zn}$	4.10 (13)	5/2-	+0.8755
$^{68}\text{Zn}$	18.75 (51)	0+	
$^{70}\text{Zn}$	0.62 (3)	0+	
$^{69}\text{Ga}$	60.108 (9)	3/2-	+2.01659
$^{71}\text{Ga}$	39.892 (9)	3/2-	+2.56227
$^{70}\text{Ge}$	20.84 (87)	0+	
$^{72}\text{Ge}$	27.54 (34)	0+	

TABLE 1 (*continued*)

Element or isotope	Natural abundance (%)	Nuclear spin number ( $\hbar$ )	Nuclear magnetic moment (nuclear magneton units)
<sup>73</sup> Ge	7.73 (5)	9/2+	-0.879467
<sup>74</sup> Ge	36.28 (73)	0+	
<sup>76</sup> Ge	7.61 (38)	0+	
<sup>75</sup> As	100	3/2-	+3.4687
<sup>74</sup> Se	0.89 (4)	0+	
<sup>76</sup> Se	9.37 (29)	0+	
<sup>77</sup> Se	7.63 (16)	1/2-	+0.53506
<sup>78</sup> Se	23.77 (28)	0+	
<sup>80</sup> Se	49.61 (41)	0+	
<sup>82</sup> Se	8.73 (22)	0+	
<sup>106</sup> Cd	1.25 (6)	0+	
<sup>108</sup> Cd	0.89 (3)	0+	
<sup>110</sup> Cd	12.49 (18)	0+	
<sup>111</sup> Cd	12.80 (12)	1/2+	-0.594886
<sup>112</sup> Cd	24.13 (21)	0+	
<sup>113</sup> Cd	12.22 (12)	1/2+	-0.622301
<sup>114</sup> Cd	28.73 (42)	0+	
<sup>116</sup> Cd	7.49 (18)	0+	
<sup>113</sup> In	4.29 (5)	9/2+	+5.529
<sup>115</sup> In	95.71 (5)	9/2+	+5.541
<sup>112</sup> Sn	0.97 (1)	0+	
<sup>114</sup> Sn	0.65 (1)	0+	
<sup>115</sup> Sn	0.34 (1)	1/2+	-0.9188
<sup>116</sup> Sn	14.54 (9)	0+	
<sup>117</sup> Sn	7.68 (7)	1/2+	-1.0010
<sup>118</sup> Sn	24.22 (9)	0+	
<sup>119</sup> Sn	8.59 (4)	1/2+	-1.0473
<sup>120</sup> Sn	32.59 (9)	0+	
<sup>122</sup> Sn	4.63 (3)	0+	
<sup>124</sup> Sn	5.79 (5)	0+	
<sup>121</sup> Sb	57.21 (5)	5/2+	+3.363
<sup>123</sup> Sb	42.79 (5)	7/2+	+2.550

## B Parabolic Quantum Wells

In this Appendix we present a brief overview of parabolic quantum wells. PQWs are semiconductor heterostructure where a parabolic confinement potential is realized by a precise control of the system composition. A standard example of a PQW is an  $\text{Al}_x\text{Ga}_{1-x}\text{As}$  heterostructure where the Al composition varies from low values in the center of the structure to higher values in its barriers. Such samples are grown by molecular beam epitaxy (Miller et al., 1984). Some of the most important properties of the PQW are the very good confinement of the electronic system in the centrum of the structure, an easy and effective electric field manipulation of the electron distribution across the system, and the equal energy spacing between adjacent conduction bands.

In general for any quantum well structure the dispersion relation is quasi-two-dimensional and the electronic wave function will be written as a product between an envelope function,  $\phi(z)$ , and a Bloch function,  $u_{n\mathbf{K}}(\mathbf{r})$ , such that  $\psi_{\mathbf{K},n}(\mathbf{r}_n) = \exp[i\mathbf{K} \cdot \mathbf{R}]\phi(z)u_{n\mathbf{K}}(\mathbf{r}_n)$ . For  $\mathbf{K} \sim 0$  the value of the Bloch function for the conduction band can be approximated as a constant. Its value at the  $^{71}\text{Ga}$  nucleus site was extracted by Tifrea and Flatté (2003) as  $|u(\mathbf{r}_n)|^2 = 5.2 \times 10^{25} \text{ cm}^{-3}$ . On the other hand, the electron's envelope function  $\phi(z)$ , and the characteristic subband energies,  $\varepsilon_n$ , can be calculated analytically using the time-independent Schrodinger equation:

$$\left(-\frac{\hbar^2}{2m_e} \frac{d^2}{dz^2} + V(z)\right)\phi(z) = \varepsilon_n\phi(z), \quad (32)$$

where the confining potential,  $V(z)$ , can be written as

$$V(z) = \frac{1}{2}m_e\omega_0^2z^2, \quad (33)$$

with  $m_e$  the electron mass and  $\omega_0$  the characteristic frequency. Equation (32) admits the following solution:

$$\phi_n(z) = N_n \exp\left[-\frac{m_e\omega_0}{2\hbar}z^2\right] H_{n-1}\left[\left(\frac{m_e\omega_0}{\hbar}\right)^{1/2} z\right] \quad (34)$$

and

$$\varepsilon_n = \left(n - \frac{1}{2}\right)\hbar\omega_0, \quad (35)$$

where the subband index  $n$  is a natural number,  $H_n(x)$  are the Hermite polynomials, and  $N_n$  is the normalization factor. In the presence of an external electric field,

$\mathcal{F}$ , the modified Schrodinger equation admits a similar solution

$$\begin{aligned}\phi_n(z, \mathcal{F}) = & N_n \exp\left[-\frac{m_e \omega_0}{2\hbar}(z - z_0)^2\right] \\ & \times H_{n-1} \left[\left(\frac{m_e \omega_0}{\hbar}\right)^{1/2} (z - z_0)\right]\end{aligned}\quad (36)$$

and

$$\varepsilon_n(\mathcal{F}) = \varepsilon_n - \frac{e^2 \mathcal{F}^2}{2m_e \omega_0^2}, \quad (37)$$

where  $z_0 = e\mathcal{F}/m_e \omega_0^2$ . The form of the envelope function is unchanged, simply its position across the quantum well is shifted with an amount proportional to the applied electric field, at the same time (see Figure 10), the minimum value of the electronic subbands being lowered. Note that for both situations the energy distance between adjacent conduction subbands,  $\Delta E = \varepsilon_n - \varepsilon_{n-1}$ , is a constant depending only on the confining potential's characteristic frequency  $\omega_0$ . We expect that these analytical result will represent a good starting point for the investigation of PQWs. However, for more accurate results we should rely on advance numerical methods (Lau et al., 2004).

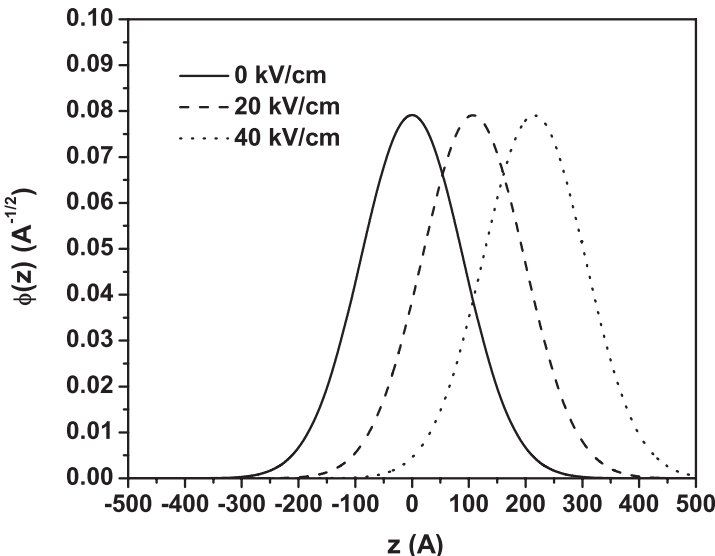


Figure 10. The position dependence of the electronic envelope function corresponding to the first conduction subband at different values of the applied electric field. The values correspond to the particular PQW we choose as an example ( $\omega_0 = 2.3 \times 10^{13} \text{ s}^{-1}$  and  $\Delta E = 15 \text{ meV}$ )

The effective electronic  $g$ -factor in bulk semiconductors is material dependent due to different values of the electron spin-orbit coupling. In  $\text{Al}_x\text{Ga}_{1-x}\text{As}$  bulk semiconductors, the value of the electronic  $g$ -factor will be composition dependent, i.e., will depend on the Al concentration,  $x$ . Experimental data obtained by Weisbuch and Hermann (1977) showed that the value of the effective electronic  $g$ -factor varies between  $g^* = -0.44$  for GaAs ( $x = 0$ ) to  $g^* = 0.6$  for  $\text{Al}_{0.36}\text{Ga}_{0.64}\text{As}$  ( $x = 0.36$ ) samples. The concentration dependence of the effective electronic  $g$ -factor is not linear, a good fit of the experimental data showing a logarithmic dependence:

$$g(x) = 0.8022 + 1.1832 \ln [0.3505 + 1.3509x], \quad (38)$$

where  $x$  represents the aluminum concentration. In the case of semiconductor nanostructures such as QWs or quantum dots, the effective electronic  $g$ -factor depends also on the sample's geometry (Malinowski and Harley, 2000a; Pryor and Flatté, 2006). In the case of  $\text{Al}_x\text{Ga}_{1-x}\text{As}$  PQWs grown by varying the Al concentration across the system, the effective electronic  $g$ -factor will be position dependent. To evaluate this dependence one has to rely on the exact knowledge of the Al concentration  $x$  as function of the position respect to the growth direction  $z$ .

For our example we considered  $\omega_0 = 2.3 \times 10^{13} \text{ s}^{-1}$  and  $\Delta E = 15 \text{ meV}$ . These parameters correspond to a  $1000 \text{ \AA}$   $\text{Al}_x\text{Ga}_{1-x}\text{As}$  PQW where the value of the aluminum concentration varies from 7% in the centrum of the structure to 40% in the barriers (Poggio et al., 2003). The system was also modeled numerically and the differences between analytical and numerical results are small. Figure 10 presents the position dependence of the electronic envelope function corresponding to the first conduction subband for different values of the applied electric field. The displacement of the electronic envelope function is  $53.75 \text{ \AA}$  when an electric field of  $10 \text{ kV/cm}$  is applied. We can conclude that the electric field control in the PQW is very effective, small applied electric fields leading to consistent changes in the electronic distribution across the system.

For the same sample the Al concentration as function of position respect to the growth direction,  $z$ , can be modeled using (Maranowski, 2000):

$$x_{\text{Al}} = \frac{-1.087 + \sqrt{1.3185 + 0.00023 \times z^2}}{0.876}. \quad (39)$$

Equation (39) is related to the growth process for the  $\text{Al}_x\text{Ga}_{1-x}\text{As}$  PQW. Accordingly one can calculate the position dependence of the effective electronic  $g$ -factor in the PQW. The value of the effective electronic  $g$ -factor will change from negative values in the center to positive values in the barriers of the well (see Figure 11). This fact is supported experimentally by FR data (Salis et al., 2001).

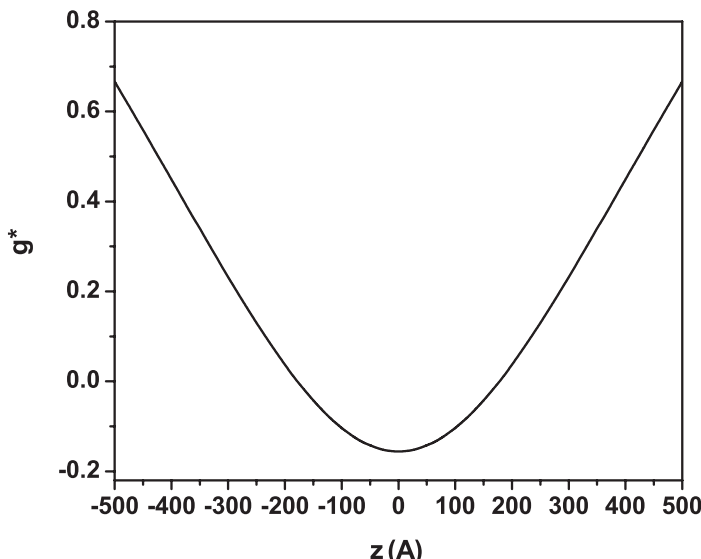


Figure 11. The position dependence of the effective electronic  $g$ -factor in the PQW. The values correspond to the particular PQW we choose as an example ( $\omega_0 = 2.3 \times 10^{13} \text{ s}^{-1}$  and  $\Delta E = 15 \text{ meV}$ )

## Acknowledgments

I would like to thank Michael E. Flatté (University of Iowa, USA) for his contributions to this project. Special thanks to D. D. Awschalom and M. Poggio (University of California, Santa Barbara, USA) for sharing their experimental results on nuclear spin dynamics in parabolic quantum wells. This contribution was financially supported by DARPA/ARO DAAD19-01-1-0490 and by the Romanian Department of Education and Research under the ANCS-CEEX 2974/2005 grant.

## References

- Awschalom, D. D., Samarth, N., and Loss, D. (eds.) (2002) *Semiconductor Spintronics and Quantum Computation*, Springer Verlag.
- Barrett, S. E., Tycko, R., Pfeiffer, L. N., and West, K. W. (1994) Directly detected nuclear magnetic resonance of optically pumped GaAs quantum wells, *Phys. Rev. Lett.* **72**, 1368.
- Berg, A., Dobers, M., Gerhardts, R. R., and von Klitzing, K. (1990) Magnetoquantum oscillations of the nuclear-spin-lattice relaxation near a two-dimensional electron gas, *Phys. Rev. Lett.* **64**, 2563.
- Bracker, A. S., E. A. Stinnett, a. D. G., Ware, M. E., Tischler, J. G., Shabaev, A., Efros, A. L., Park, D., Gershoni, D., Korenev, V. L., and Merkulov, I. A. (2005) Optical pumping of the electronic and nuclear spin of single charge-tunable quantum dots, *Phys. Rev. Lett.* **94**, 047402.
- Ciuti, C., McGuire, J. P., and Sham, L. J. (2002) Spin polarization of semiconductor carriers by reflection off a ferromagnet, *Phys. Rev. Lett.* **89**, 156601.

- Desrat, W., Maude, D. K., Potemski, M., and Portal, J. C. (2002) Resistively detected nuclear magnetic resonance in the quantum hall regime: Possible evidence for a skyrme crystal, *Phys. Rev. Lett.* **88**, 256807.
- Ekimov, A. and Safarov, V. (1972) Optical detection of dynamical polarization of nuclei in semiconductors, *JETP Lett.* **15**, 179.
- Gammon, D., Efros, A. L., Kennedy, T. A., Rosen, M., Katzer, D. S., Park, D., Brown, S. W., Korenev, V. L., and Merkulov, I. A. (2001) Electron and nuclear spin interactions in the optical spectra of single GaAs quantum dots, *Phys. Rev. Lett.* **86**, 5176.
- Gershenfeld, N. A. and Chuang, I. L. (1997) Bulk spin-resonance quantum computation, *Science* **275**, 350.
- Holden, N. E. (1998) Table of the Isotopes, Technical report, Brookhaven National Laboratory, Upton, New York 11973, USA.
- Kane, B. E. (1998) A silicon-based nuclear spin quantum computer, *Nature (London)* **393**, 133.
- Kawakami, R. K., Kato, Y., Hanson, M., Malajovich, I., Stephens, J. M., Johnson-Halperin, E., Salis, G., Gossard, A. C., and Awschalom, D. D. (2001) Ferromagnetic imprinting of nuclear spins in semiconductors, *Science* **294**, 131.
- Kikkawa, J. M. and Awschalom, D. D. (1998) Resonant Spin amplification in n-type GaAs, *Phys. Rev. Lett.* **80**, 4313.
- Korringa, J. (1950) Nuclear magnetic relaxation and resonance line shift in metals, *Physica* **16**, 601.
- Lampel, G. (1968) Nuclear dynamic polarization by optical electronic saturation and optical pumping in semiconductors, *Phys. Rev. Lett.* **20**, 491.
- Lau, W. H., Olesberg, J. T., and Flatté, M. E. (2004) Electronic structures and electron spin decoherence in (001)-grown layered zincblende semiconductors, cond-mat/0406201.
- Malinowski, A. and Harley, R. T. (2000a) Anisotropy of the electron g factor in lattice-matched and strained-layer III-V quantum wells, *Phys. Rev. B* **62**, 2051.
- Malinowski, A. and Harley, R. T. (2000b) Dynamic nuclear Overhauser shifts in Larmor beats from a quantum well, *Solid State Commun.* **114**, 419.
- Maranowski, K. D. (2000) Parabolically graded semiconductor quantum wells for emission of far-infrared radiation, Ph.D. thesis, University of California, Santa Barbara, USA.
- McNeil, J. A. and Clark, W. G. (1976) Nuclear quadrupolar spin-lattice relaxation in some III-V compounds, *Phys. Rev. B* **13**, 4705.
- Meier, F., Levy, J., and Loss, D. (2003) Quantum computing with antiferromagnetic spin clusters, *Phys. Rev. B* **68**, 134417.
- Miller, R. C., Gossard, A. C., Kleinman, D. A., and Munteanu, O. (1984) Parabolic quantum wells with the  $\text{GaAs}-\text{Al}_x\text{Ga}_{1-x}\text{As}$  system, *Phys. Rev. B* **29**, 3740.
- Overhauser, A. W. (1953a) Paramagnetic relaxation in metals, *Phys. Rev.* **89**, 689.
- Overhauser, A. W. (1953b) Polarization of nuclei in metals, *Phys. Rev.* **92**, 411.
- Paget, D. (1982) Optical detection of NMR in high-purity GaAs: Direct study of the relaxation of nuclei close to shallow donors, *Phys. Rev. B* **25**, 4444.
- Paget, D., Lampel, G., Sapoval, B., and Safarov, V. I. (1977) Low field electron-nuclear spin coupling in gallium arsenide under optical pumping conditions, *Phys. Rev. B* **15**, 5780.
- Poggio, M., Steeves, G. M., Myers, R. C., Kato, Y., Gossard, A. C., and Awschalom, D. D. (2003) Local manipulation of nuclear spins in a semiconductor quantum well, *Phys. Rev. Lett.* **91**, 207602.
- Pryor, C. E. and Flatté, M. E. (2006) Landé g factors and orbital momentum quenching in semiconductor quantum dots, *Phys. Rev. Lett.* **96**, 026804.
- Salis, G., Kato, Y., Ensslin, K., Driscoll, D. C., Gossard, A. C., and Awschalom, D. D. (2001) Electrical control of spin coherence in semiconductor nanostructures, *Nature (London)* **414**, 619.

- Slichter, C. P. (2002) *Principles of Magnetic Resonance*, Springer Verlag.
- Smet, J. H., Deutschmann, R. A., Ertl, F., Wegscheider, W., Abstreiter, G., and von Klitzing, K. (2002) Gate–voltage control of spin interactions between electrons and nuclei in a semiconductor, *Nature (London)* **415**, 281.
- Strand, J., Schultz, B. D., Isakovic, A. F., Palmstrom, C. J., and Crowell, P. A. (2003) Dynamic Nuclear Polarization by Electrical Spin Injection in Ferromagnet–Semiconductor Heterostructures, *Phys. Rev. Lett.* **91**, 036602.
- Taylor, J. M., Marcus, C. M., and Lukin, M. D. (2003) Long-lived memory for mesoscopic quantum bits, *Phys. Rev. Lett.* **90**, 206803.
- Tifrea, I. and Flatté, M. E. (2003) Electric field tunability of nuclear and electronic spin dynamics due to the hyperfine interaction in semiconductor nanostructures, *Phys. Rev. Lett.* **90**, 237601.
- Tifrea, I. and Flatté, M. E. (2004) Nuclear spin dynamics in parabolic quantum wells, *Phys. Rev. B* **69**, 115305.
- Tifrea, I. and Flatté, M. E. (2005a) Dynamical nuclear polarization and nuclear magnetic fields in semiconductor nanostructures (unpublished).
- Tifrea, I. and Flatté, M. E. (2005b) Magnetic fields from nuclear polarization in parabolic quantum wells, *J. Supercond.: Incorporating Novel Mag.* **18**, 207.
- Tifrea, I., Poggio, M., Flatté, M. E., and Awschalom, D. D. (2005) Overhauser frequency shifts in semiconductor nanostructures (unpublished).
- Weisbuch, C. and Hermann, C. (1977) Optical detection of conduction–electron spin resonance in GaAs,  $\text{Ga}_{1-x}\text{In}_x\text{As}$ , and  $\text{Ga}_{1-x}\text{Al}_x\text{As}$ , *Phys. Rev. B* **15**, 816.
- Wolf, S. A., Awschalom, D. D., Buhrman, R. A., Daughton, J. M., von Molnár, S., Roukes, M. L., Chtchelkanova, A. Y., and Treger, D. M. (2001) Spintronics: a spin-based electronics vision for the future, *Science* **294**, 1488.

# SPIN COHERENCE IN SEMICONDUCTORS

J. BEREZOVSKY, W. H. LAU, S. GHOSH, J. STEPHENS, N. P. STERN,  
and D. D. AWSCHALOM

*Center for Spintronics and Quantum Computation, University of California,  
Santa Barbara, CA 93106 USA*

**Abstract:** The potential for spin-based information processing in spintronic devices has spurred significant research on spin coherence in semiconductors. We review some recent advances in the physics of semiconductor spin coherence, focusing on phenomena in both bulk and heterostructure systems. Coherent spin ensembles can be generated and manipulated optical, electrical, and magnetic interactions. Optical measurement techniques enable both temporal and spatial resolution of spin dynamics, allowing observation of electrical control and generation of spin polarization, including the recent discovery of the spin Hall effect. Spin dynamics are also studied for spins confined in quantum dots.

**Keywords:** spintronics, quantum dots, nuclear spin, spin Hall effect, magnetic semiconductors

## 1 Introduction

The physics of spins in semiconductors was first seriously explored in seminal theoretical and experimental work in the 1960s (Meier and Zakharchenya, 1984). From this fertile ground has sprouted a keen interest in the potential applications of semiconductor spins (referred to as spintronics (Wolf et al., 2001)). Existing semiconductor devices typically rely only on the charge of the electron and the orbital part of the electron wavefunction. However, the quantum mechanical electron spin can also be both manipulated and detected in semiconductors. Recent research has led to an increased understanding of the rich behavior of spins in semiconductors, leading to new possibilities for utilizing electron spin as a new degree of freedom for solid state information processing in semiconductor spintronics.

A significant barrier to the practical use of spins in semiconductors is the ephemeral nature of the spin state—unlike charge, spin is not a conserved quantity. The average time for the loss of spin information is described by two quantities, the longitudinal spin lifetime,  $T_1$  (also known as the spin-flip time), and the transverse spin lifetime  $T_2$  (also known as the coherence time). In general,  $T_1$  refers to the time for the relative amplitudes of the spin eigenstates (e.g., spin-up and spin-down) to become scrambled and  $T_2$  refers to the time for the relative

phase of the eigenstates to be lost. In the case where many spins are measured simultaneously, inhomogeneities in the spin dynamics over the ensemble result in a reduced effective transverse spin lifetime, referred to as  $T_2^*$ .

There are several mechanisms that contribute to the decay and decoherence of spins in semiconductors. Through spin–orbit coupling in a noncentrosymmetric crystal (e.g., zinc-blende, wurtzite), an electron’s momentum acts as a magnetic field seen by the electron spin (Yu and Cardona, 1996). In the D'yakonov–Perel mechanism (D'yakonov and Perel, 1971), as the electron momentum is repeatedly scattered, the electron spin state is randomized as it precesses about this randomly fluctuating effective field. Furthermore, the spin–orbit interaction mixes the spin and momentum eigenstates, directly linking momentum scattering with spin scattering. This path to spin decoherence is known as the Elliot–Yafet mechanism (Elliot, 1954). These two spin–orbit mediated mechanisms show opposite dependence on the momentum scattering rate. In the Elliot–Yafet mechanism, more momentum scattering leads to more spin scattering. In contrast, as momentum scattering increases, the fluctuating effective field of the D'yakonov–Perel mechanism tends to “cancel out”, in an effect akin to motional narrowing seen in nuclear magnetic resonance (Abragam, 1961).

Electron spins can also be flipped through interactions with other spin systems, such as through the electron–hole exchange interaction (Bir–Aronov–Pikus mechanism (Bir et al., 1976)), or through the hyperfine interaction with nuclear spins (Lampel, 1968). These mechanisms become significant when the electron wavefunction has significant overlap with the holes or with nuclei, respectively.

Despite the inevitability of spin decoherence, relatively long spin lifetimes have been measured in some semiconductor systems. In bulk n-type GaAs,  $T_2^*$  has been found to exceed 100 ns at low temperature (Kikkawa and Awschalom, 1998). Some II–VI semiconductors, such as ZnSe show robust spin coherence up to room temperature (Kikkawa et al., 1997). Furthermore, by confining electrons within a quantum dot, momentum scattering is suppressed, leading to longer spin lifetimes.

The selection rules governing optical transitions from the valence band to the conduction band of noncentrosymmetric crystals provide a useful means for initializing and detecting spin polarization in these materials (Meier and Zakharchenya, 1984) (see Figure 1).

The conduction band minimum (the  $\Gamma$ -point) is twofold degenerate, corresponding to the two spin states ( $S = 1/2, S_z = \pm 1/2$ ). The six states at the valence band maximum are split into the fourfold degenerate heavy holes ( $J = 3/2, J_z = \pm 3/2$ ) and light holes ( $J = 3/2, J_z = \pm 1/2$ ), and the doubly degenerate split-off holes ( $J = 1/2, J_z = \pm 1/2$ ). The split-off band is typically sufficiently far from the heavy and light holes that split-off hole transitions can be ignored for excitation near the band edge.

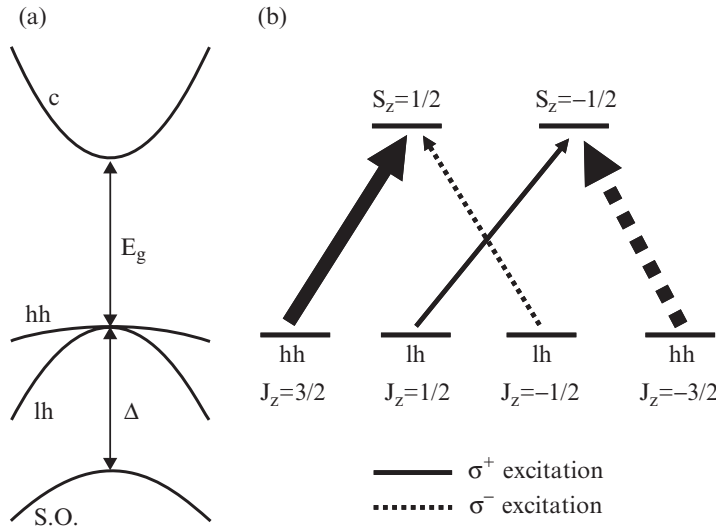
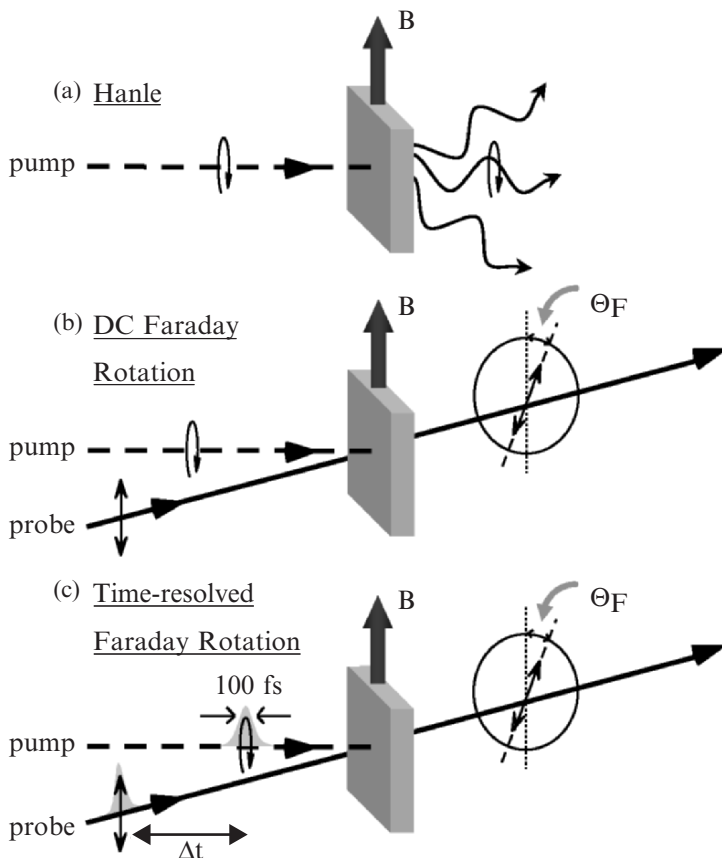


Figure 1. (a) Schematic of the band structure of a zinc-blende semiconductor, showing the conduction band (c), heavy hole band (hh), light hole band (lh), and split-off hole band (s.o.). Also indicated are the energy gap,  $E_g$ , and the spin-orbit splitting  $\Delta$ . (b) Diagram of the four band-edge transitions and selection rules for circularly polarized light. The width of the lines indicates the strength of the transition

A circularly polarized photon carries angular momentum of  $1 \hbar$ , and thus can only drive transitions with  $\Delta L_z = \pm 1$ . For example, absorption of a photon with  $l = 1$  can drive the transition from the heavy hole with  $J_z = -3/2$  to the electron with  $S_z = -1/2$ , or the transition from the light hole with  $J_z = -1/2$  to the electron with  $S_z = 1/2$ . Calculating the dipole transition matrix elements for these two transitions, one finds that the heavy hole transition is more likely than the light hole transition by a factor of 3. In this way, circularly polarized optical excitation near the band edge results in the pumping of a net electron spin polarization in the conduction band.

The situation is improved further in strained crystals or with quantum confinement which can lift the degeneracy between the heavy and light holes. In this case, transitions from only one hole band can be driven resulting in nearly 100% spin polarization. These spin-dependent selection rules not only allow for the initialization of spin-polarized electrons and holes, but also the measurement of spin polarization. In the opposite process of optical spin pumping, when spin-polarized electrons and holes recombine radiatively, the resulting luminescence is circularly polarized. By measuring this polarization, the spin polarization at the time of the recombination can be inferred.

In a Hanle measurement (Figure 2a), spins are optically initialized using circularly polarized light perpendicular to an applied magnetic field. As the



*Figure 2.* (a) Schematic of a Hanle measurement. Spins are injected with circularly polarized excitation, and the degree of circular polarization of the photoluminescence is measured. (b) Schematic of a DC Faraday rotation measurement. Spin polarization is measured through the rotation of a linearly polarized probe beam. (c) Schematic of a time-resolved Faraday rotation measurement. A circularly polarized pump pulse excites spins, which are probed a time  $\Delta t$  later through the rotation of a linearly polarized probe pulse

injected spins precess about this field, the steady-state spin polarization becomes randomized. The resulting curve of polarization versus magnetic fields typically shows a Lorentzian lineshape, with width proportional to the transverse spin lifetime.

A more direct measurement of spin polarization can be obtained through the Faraday effect (Faraday, 1846). Here, a net spin polarization in a material results in a different index of refraction for left and right circularly polarized light. Thus when linearly polarized light is transmitted through the material, the two circularly polarized components acquire a relative phase shift, yielding a rotation of the polarization of the transmitted light. The angle through which the polarization is

rotated is proportional to the spin polarization along the axis of the light propagation. The same effect occurs upon reflection off of the sample, in this case known as Kerr rotation.

Faraday rotation (or Kerr rotation) can be used to probe the steady-state spin polarization, similar to the Hanle measurement discussed above (Stephens et al., 2004) (Figure 2b). By using Faraday rotation instead of a traditional Hanle measurement, one gains the ability to measure spins that do not undergo radiative recombination. Additionally, Faraday rotation provides spectroscopic information about the energy levels occupied by the spins through the energy-dependence of the Faraday effect (Meier and Awschalom, 2005).

The Faraday and Kerr effects can be used in conjunction with ultrafast optical techniques for time-resolved measurements of spin coherence in semiconductors (Awschalom et al., 1985; Baumberg et al., 1994; Ostreich et al., 1995; Crooker et al., 1997) (Figure 2c). In such measurements, a mode-locked Ti:Sapphire laser provides a train of pump and probe pulses with sub-picosecond duration, which are both focused to a spot on the sample. The pump pulse is circularly polarized, and serves to optically inject spin-polarized electrons into the conduction band. The arrival of the probe pulse is delayed from the pump by changing the optical path length of the probe. The probe is linearly polarized, and the resulting Faraday (or Kerr) rotation of the probe serves as an instantaneous measurement of the spin polarization at the moment of incidence on the sample. If the spins are initialized into a coherent superposition of spin eigenstates, the projection of the resulting dynamics along the probe direction can be observed as a function of time. For example, Figure 3 shows the coherent quantum beating between electron spin

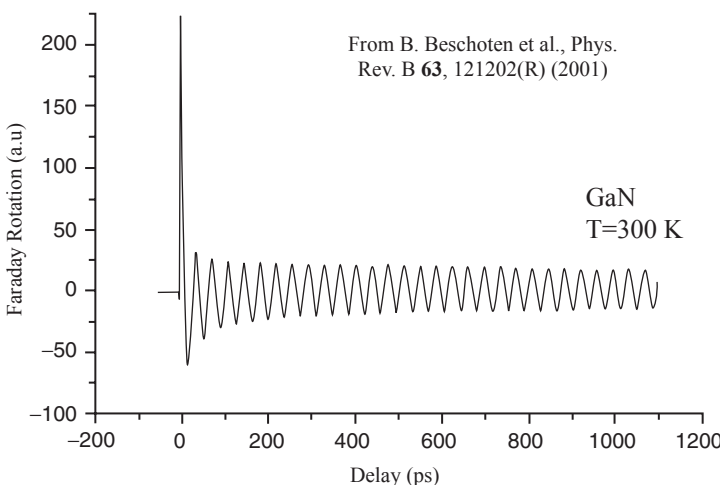


*Figure 3.* Coherent spin precession in GaN measured by time-resolved Faraday rotation

levels Zeeman-split by a transverse magnetic field in GaN at room temperature. By fitting such a curve, the transverse spin lifetime and the electron  $g$ -factor can be extracted.

## 2 Electrical Generation and Manipulation of Spin Polarization

The behavior of spins in a magnetic field is governed by the Zeeman interaction

$$H_Z = (\mu_B/\hbar)\vec{S} \cdot \overleftrightarrow{g} \cdot \vec{B}, \quad (1)$$

where  $\mu_B$  is the Bohr magneton,  $\hbar$  is Planck's constant,  $\vec{S}$  is the spin angular momentum operator,  $\overleftrightarrow{g}$  is the Landé  $g$  tensor, and  $\vec{B}$  is the externally applied and controlled magnetic field. The capability of manipulating electron spins in nonmagnetic semiconductors in the absence of such an external magnetic field has vital implications for spin-based quantum information processing (Loss and DiVincenzo, 1998) and spin-based electronics (Wolf et al., 2001; Awschalom et al., 2002). Single qubit operations require a local Hamiltonian which is tunable and controllable within coherence times that generally do not exceed a few nanoseconds. The scaling down of devices for on-chip integration requires precise control of magnetic fields at micron-scale dimensions or even smaller. External magnetic fields are limited on both accounts—it is both difficult to create large fields in a short timescale, as well as to spatially localize a field without complicated architectures. While recent experiments (Kato et al., 2003) have achieved electron spin manipulation by electrically controlling the  $g$  tensor  $\overleftrightarrow{g}$  of the Zeeman Hamiltonian, this type of approach still requires a static externally applied magnetic field.

The spin-orbit (SO) interaction provides a unique pathway for spin manipulation through electric fields without magnetic fields or magnetic materials (Aronov et al., 1991). The SO Hamiltonian, given by

$$H_{SO} = \frac{\hbar}{4m_0^2c^2} [\vec{\nabla}V(\vec{r}) \times \vec{p}] \cdot \vec{\sigma} \quad (2)$$

is a consequence of relativity arising from the transformation of an electric field into an effective magnetic field in the frame of a moving electron. This electric field need not be a real field, but a “quasi electric field”, arising from asymmetries in the crystal field, the band gap, or strain-induced spin-splitting, each acting like an internal magnetic field  $B_{int}$  due to the SO coupling. In this section, we describe experiments investigating the existence of strain-induced  $B_{int}$  in n-GaAs and n-ZnSe and show electrical generation of spin polarization in these semiconductors through SO coupling, performed at low temperatures in GaAs (Kato et al., 2004a) and up to room temperature in ZnSe (Stern et al., 2006).

The GaAs samples are grown by molecular beam epitaxy (MBE) and consist of a 2  $\mu\text{m}$  n-GaAs layer ( $n = 3 \times 10^{16} \text{ cm}^{-3}$ ) acting as a spin probe layer at the surface and a 2  $\mu\text{m}$  film of Al<sub>0.4</sub>Ga<sub>0.6</sub>As underneath serving as a stressor/etch layer. The semi-insulating GaAs (001) substrate is removed by chemical etching in order to form a rectangular membrane  $\sim 100 \mu\text{m}$  by  $\sim 300 \mu\text{m}$ . The processed membrane has curvature, possibly due to the larger lattice constant or the oxidation of the Al<sub>0.4</sub>Ga<sub>0.6</sub>As layer, thereby straining the n-GaAs film. Ni\Ge\Au\Ni\Au Ohmic contacts are evaporated on the surface in order to apply an in-plane electric field  $\vec{E}$  along [1̄10]. The in-plane strain, estimated using optical interference fringes at room temperature, is  $\sim 10^{-5}$ .

Electron spin dynamics is probed using time- and spatially-resolved Faraday rotation (FR) spectroscopy (Kikkawa and Awschalom, 1999). Figures 4a and 4b show the spatiotemporal evolution of a coherent electron spin packet with zero external field, under various applied  $E$ . The spin packet drifts under the electric field, as expected, but the polarization also precesses as it travels down the channel. This precession is in excess of  $3\pi$  over 60  $\mu\text{m}$  in 13 ns and confirms the existence of  $B_{int}$ . To accurately characterize this internal magnetic field, FR is measured as a function of an external magnetic field  $B_{ext}$ . As in the case of time-resolved FR, the signal is oscillatory and described by  $\theta_0 \exp(-\Delta t/\tau) \cos(g\mu_B B \Delta t/\hbar)$ , where  $\theta_0$  is the initial amplitude,  $\Delta t$  is the pump-probe delay (in these set of measurements, fixed at 13.1 ns),  $\tau$  is the transverse spin lifetime,  $g$  is the electron  $g$ -factor, and  $B$  is the magnitude of the total magnetic

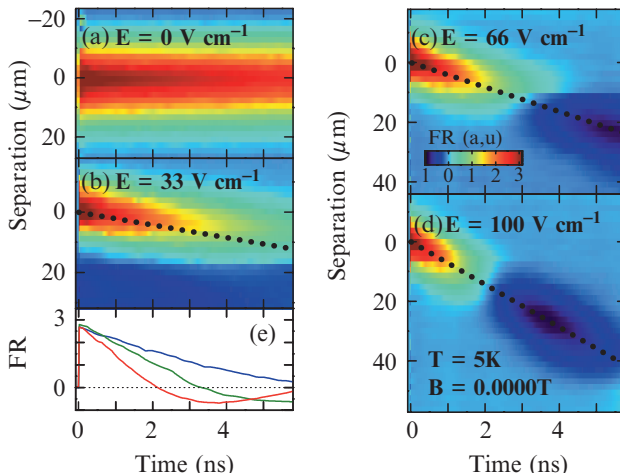


*Figure 4.* Spatiotemporal evolution of the photoexcited spin packet at zero magnetic field. (a)–(d) FR as a function of pump–probe separation and time delay for  $E = 0, 33, 67, 100 \text{ V cm}^{-1}$ , respectively. The dotted lines are determined by the drift velocity of the spin packet. (e) Linecuts along the dotted lines in (b)–(d). Data originally presented in Kato et al. (2004a)

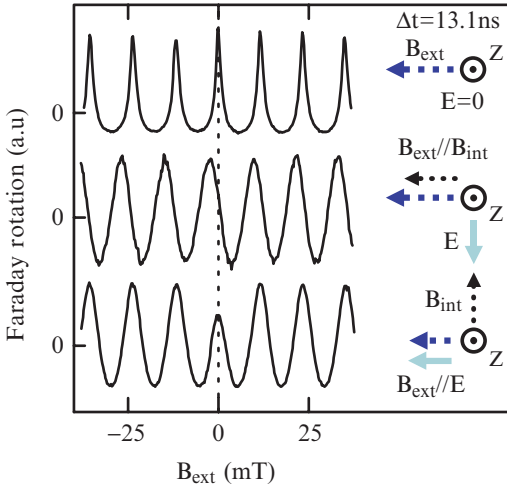


Figure 5. Characterization of the internal magnetic field showing the dependence of FR on the external magnetic field in three different geometries, with  $E = 0$ ,  $E \parallel B_{ext}$ , and  $E \perp B_{ext}$ . The curves are offset and scaled for clarity. Data originally presented in Kato et al. (2004a)

field experienced by the electrons. In the absence of an applied electric field (Figure 5, top trace), the average  $k = 0$  and therefore  $B_{int} = 0$  and the oscillations are centered at  $B = B_{ext} = 0$ . With an applied  $E$  perpendicular to  $B_{ext}$  (center trace), both the external and internal magnetic fields are along the same direction and add directly so that  $B = B_{ext} + B_{int}$  and the oscillatory signal is centered at  $-B_{int}$ . For  $E$  parallel to  $B_{ext}$ , the center peak is suppressed (bottom trace). In this geometry,  $B_{int}$  is perpendicular to  $B_{ext}$  (Kato et al., 2004a; Sih et al., 2006a) resulting in a total field magnitude of  $B = \sqrt{B_{ext}^2 + B_{int}^2}$  which is always greater than zero for a nonzero  $B_{int}$ .

In both cases above, the amplitude of the signal decreases with increasing voltage, which is further investigated by spatially separating the pump and the probe by a distance  $d$  along the direction of  $E$  (Figure 3). Due to the laser profile of the pump beam, the optically injected spins have a Gaussian spatial profile which is centered at  $d = 0$  when  $E = 0$ . An applied voltage ( $E \neq 0$ ) imparts a nonzero average momentum  $k$  to the injected spin packet, causing it to drift with an average velocity  $v_d$ . Spins at the leading edge of the packet experience a larger  $B_{int}$  than the trailing edge. This variation is due to the spread in the drift velocities of the spin packet arising from spin diffusion. The reported value of  $B_{int}$  for each  $E$  are obtained from a linear fit at the center of the spin packet, and is observed to be more than 20 mT. The spin-splitting arising from this  $B_{int}$ ,  $\Delta_0 = g\mu_B B_{int}$ , is plotted as a function of  $v_d$ . Figure 6 (inset) shows a phenomenological linear relation  $\Delta_0 = \beta v_d$ . In the data presented,  $\beta = 99 \text{ neV ns } \mu\text{m}^{-1}$ , while in an unstrained sample (without substrate removal)  $\beta$  is almost an order of magnitude smaller, tying the internal magnetic field to the strain decisively.

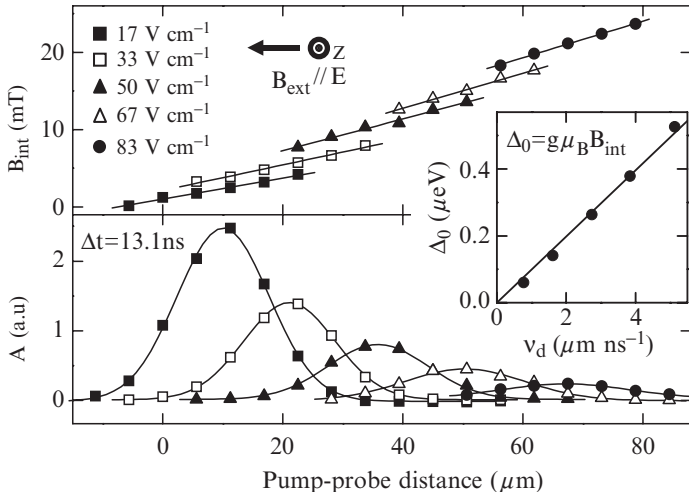


Figure 6.  $B_{int}$  (top) and  $A$  (bottom) as a function of the pump–probe separation  $d$  in the  $E \parallel B_{ext}$  geometry for  $E = 17$  (solid squares), 33 (open squares), 50 (solid triangles), 67 (open triangles), and 83 (solid circles)  $\text{V cm}^{-1}$ . Symbols are data and the lines are fits. The inset shows the spin-splitting  $\Delta_0$  as a function of  $v_d$ . Data originally presented in Kato et al. (2004a)

$B_{int}$  arising from strain is also measured in n-InGaAs and n-ZnSe samples, where the strain is a result of lattice mismatch (Jain et al., 1996) between the epilayers and the GaAs substrates. In case of n-ZnSe, the in-plane compressive strain is estimated to be  $\sim 10^{-3}$  for epilayers between 100 and 300 nm in thickness. Interestingly, the  $\beta$  values obtained in n-ZnSe samples are almost the same as those mentioned above in the n-GaAs sample, (Ghosh, 2006) even though the bulk SO coupling parameter in ZnSe is about half that of GaAs (Winkler, 2003).

The electrical control of spin states discussed so far still requires the creation of spin coherence by optical injection. Encoding of spin information by electrical means, without a polarized optical pulse or magnetic materials would provide a further step towards developing an all-electrical protocol for spintronic devices. An early theoretical work pointed out the possibility of using a current flow to obtain magnetization in materials lacking inversion symmetry (Levitov et al., 1985) (such as n-GaAs and n-ZnSe). Prior experiments for detection of current induced spin polarization (CISP) in other systems (Vorobev et al., 1979; Hammar et al., 1999) have had added complications.

Figure 7a shows the measurement geometry for studying CISP in an n-In<sub>0.07</sub>Ga<sub>0.93</sub>As channel used for the strain related studies above. A square-wave voltage with peak-to-peak value  $V_{pp}$  at frequency  $f = 51.2$  kHz is applied to one of the contacts while the other is grounded. An alternating electric field with amplitude  $E = V_{pp}/(2l)$  is established along the InGaAs channel of width  $w$  and length  $l$ . The current-induced FR is lock-in detected at  $f$  and is measured as a function

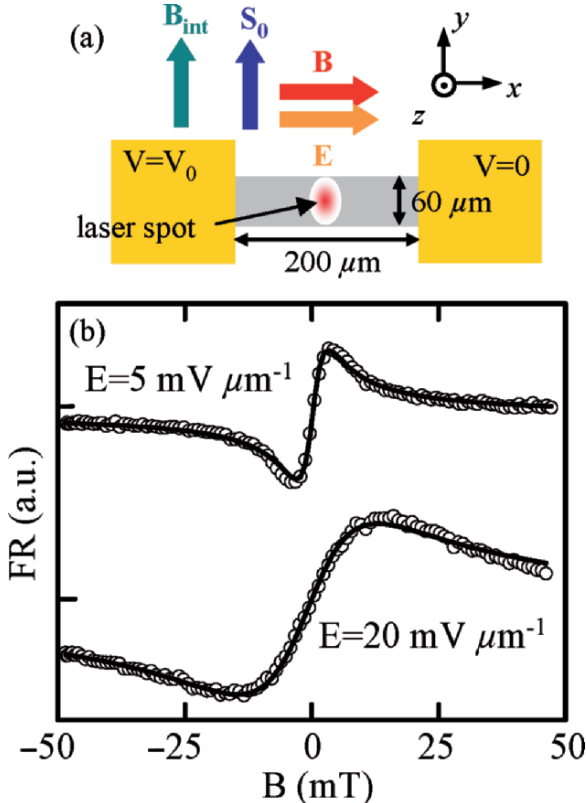


Figure 7. (a) Schematic of the device and geometry in measuring current induced spin polarization. Squares are the metal contacts at the ends of the channel. (b) Voltage-induced FR as a function of  $B_{ext}$  for  $E = 5$  and  $20 \text{ mV } \mu\text{m}^{-1}$  with  $\vec{E} \parallel [1\bar{1}0]$ . Open circles are data and the solid lines are the fits to Eq. (3). Data originally presented in Kato et al. (2004b)

of magnetic field  $B_{ext}$  applied parallel to the alternating  $E$ , along the  $x$  axis. The curves in Figure 7b can be explained by assuming a constant orientation rate for spins polarized along the  $y$  axis. In a similar process to the Hanle measurement (Figure 2a), the  $z$  component of spin per unit volume  $\rho_z$  can be written as

$$\rho_z = \int_0^\infty dt [\gamma \exp(-t/\tau) \sin(\Omega t)] = \rho_{el} \frac{\Omega t}{(\Omega t)^2 + 1}, \quad (3)$$

where  $\gamma$  is the number of spins oriented along the  $y$  axis per unit time per unit volume,  $\tau$  is the transverse spin lifetime,  $\Omega = g\mu_B B/\hbar$  is the electron Larmor frequency, and  $\rho_{el} \equiv \gamma\tau$  is the steady-state spin density due to electrical excitation. The upper limit for the integration is taken as  $\infty$  because the modulation period

is much longer than  $\tau$ . Assuming Gaussian beam profiles and a spatially uniform  $\rho_{el}$ , we find the FR to be

$$\theta_F = \theta_{el} \frac{\Omega t}{(\Omega t)^2 + 1}. \quad (4)$$

This odd-Lorentzian shape is indicative of spins generated in-plane and perpendicular to  $E$ . Temperature dependence of this effect shows  $\rho_{el}$  ( $\sim 10 \mu\text{m}^{-3}$ ) not varying significantly up to  $T = 60$  K. At higher  $T$ ,  $\rho_{el}$  becomes smaller due to the decline of  $\tau$ , and is below the noise level for  $T > 150$  K.

Similar measurements in 1.5  $\mu\text{m}$  thick  $n$ -ZnSe samples yield a  $\rho_{el} \sim 12 \mu\text{m}^{-3}$  at  $T = 20$  K, with the CISPR persisting up to room temperature.

The microscopic origin of CISPR is not well understood. Strain-enhanced inversion asymmetry terms in the Hamiltonian manifest as  $B_{int}$  and could generate the spin polarization. In general, the internal magnetic field strength shows a close correlation to the amount of strain in n-GaAs structures, but the CISPR shows little correlation to the strength of  $B_{int}$ . In the experiment with n-ZnSe epilayers, the CISPR is comparable in magnitude to that observed in GaAs, which is most surprising, since no  $B_{int}$  is measured in these thick n-ZnSe samples.

### 3 The Spin Hall Effect

The spin Hall effect refers to the generation of a spin current transverse to a charge current in nonmagnetic systems in the absence of an applied magnetic field. A pure spin current can be interpreted as a current generated by an equal number of spin-up and spin-down electrons moving in opposite directions, resulting in a flow of a spin angular momentum with no net charge current. This spin current is generated by spin-dependent scattering (D'yakonov and Perel, 1971; Hirsch, 1999) or the effect of the spin-orbit interaction on the band structure (Murakami et al., 2003; Sinova et al., 2004). The former is associated with the extrinsic spin Hall effect, whereas the latter is associated with the intrinsic spin Hall effect. While the extrinsic mechanism is mediated by spin-dependent scattering, where spin-orbit coupling mixes the spin and momentum eigenstates, the intrinsic spin Hall mechanism is mediated by an effect of the momentum-dependent internal magnetic field  $B_{int}$ . This internal effective magnetic field arises from spin-orbit coupling, which generates spin-splitting for electrons with finite momentum  $\mathbf{k}$  in semiconductors without a inversion center. For example, bulk inversion asymmetry in zincblende crystal structures such as GaAs introduces the momentum-dependent internal effective magnetic field known as the Dresselhaus effect, whereas structural inversion asymmetry in semiconductor heterostructures with asymmetry along the growth direction leads to the momentum-dependent internal effective magnetic field known as the Bychkov-Rashba effect.

### 3.1 THE SPIN HALL EFFECT IN BULK GALLIUM ARSENIDE

Experiments on optical detection of the spin Hall effect (Kato et al., 2004c) are performed on a series of thin-film samples fabricated from a 2  $\mu\text{m}$ -thick epilayer of unstrained n-doped GaAs, with a Si doping density  $n = 3 \times 10^{16} \text{ cm}^{-3}$ . The n-GaAs epilayer and the underlying 2  $\mu\text{m}$  of undoped Al<sub>0.4</sub>Ga<sub>0.6</sub>As were grown on a (001) semi-insulating GaAs substrate using molecular beam epitaxy. Mesas were patterned using standard photolithography and a chemical etch, and the n-type layers are contacted with annealed Ni/Ge/Au/Ni/Au. To minimize unintentional strain from sample mounting, all the samples are left attached to the 500  $\mu\text{m}$ -thick substrate.

Static Kerr rotation is used to probe the electron spin polarization in the samples. The samples are measured in a scanning Kerr microscope (Stephens et al., 2003) and mounted such that the main channels are perpendicular to the externally applied in-plane magnetic field. To measure the spin polarization,  $\sim 150$  fs pulses from a mode-locked Ti:sapphire laser with repetition rate of 76 MHz is tuned to the absorption edge of the sample at a wavelength of  $\lambda = 825$  nm. A linearly polarized beam is incident upon the sample through an objective lens with numerical aperture of 0.73, which provides approximately 1  $\mu\text{m}$  lateral spatial resolution. The rotation of the polarization axis of the reflected beam is proportional to the net magnetization of the electron spins along the beam ( $z$ ) propagation direction (Crooker et al., 1997). A square wave voltage with amplitude  $\pm V/2$  and frequency 1169 Hz is applied to two Ohmic contacts of the device for lock-in detection measurements. The measurements are performed at a temperature  $T = 30$  K, and the center of the channel is taken to be the origin.

Figure 8a shows an unstrained GaAs sample with a channel parallel to the [110] crystallographic direction with a width  $w = 77 \mu\text{m}$ , a length  $l = 300 \mu\text{m}$ , and a mesa height  $h = 2.3 \mu\text{m}$ . Kerr rotation is measured as a function of external applied magnetic field  $B_{\text{ext}}$ , and data for typical scans are shown in Figure 8b. The data shown are taken at positions  $x = -35 \mu\text{m}$  and  $x = +35 \mu\text{m}$ , respectively, which correspond to the two edges of the channel. These curves correspond to a measurements of the Hanle effect (D'yakonov and Perel, 1971; Meier and Zakharchenya, 1984) in which the projection of the spin polarization along the  $z$ -axis diminishes with an applied transverse magnetic field due to spin precession. The data are well fit to a Lorentzian function given by

$$\theta_K = \theta_0 / [(\omega_L \tau_s)^2 + 1], \quad (5)$$

where  $\theta_0$  is the amplitude of Kerr rotation,  $\omega_L = g \mu_B B / \hbar$ , where  $g$  is the electron  $g$ -factor ( $g = -0.44$  for this sample as measured using time-resolved Kerr rotation (Crooker et al., 1997)),  $\mu_B$  is the Bohr magneton, and  $\hbar$  is Planck's constant divided by  $2\pi$ . The amplitude of Kerr rotation is of opposite sign for the two edges of the sample, indicating an accumulation of electron spins polarized

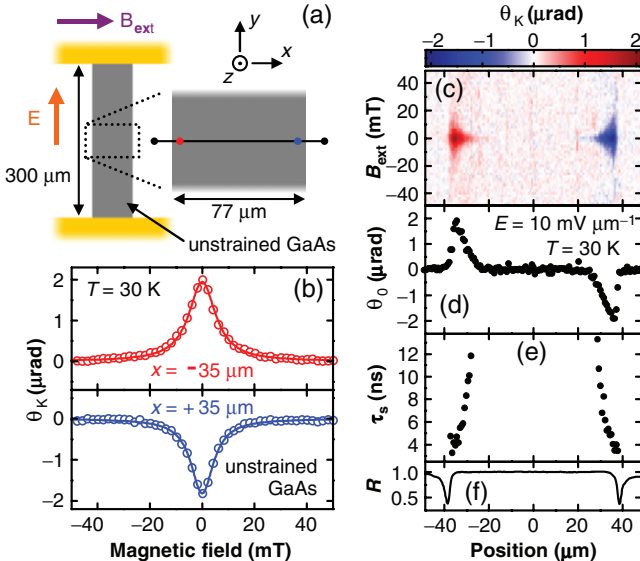


*Figure 8.* The spin Hall effect in unstrained GaAs. Data are taken at  $T = 30$  K and a linear background has been subtracted from each  $B_{ext}$  scan. (a) Schematic of the unstrained GaAs sample and the experimental geometry. (b) Typical measurement of KR as a function of  $B_{ext}$  for  $x = -35$   $\mu\text{m}$  (top) and  $x = +35$   $\mu\text{m}$  (bottom) for  $E = 10$  mV/ $\mu\text{m}$ . Solid lines are fits as explained in text. (c) KR as a function of  $x$  and  $B_{ext}$  for  $E = 10$  mV/ $\mu\text{m}$ . The dark region on the left (right) corresponds to the spin polarization in the  $z$  ( $-z$ ) direction (see the original figure in color in Kato et al. (2004c)). (d) and (e) Spatial dependence of peak KR  $\theta_0$  and spin lifetime  $\tau_s$  across the channel, respectively, obtained from fits to data in (c). (f) Reflectivity  $R$  as a function of  $x$ .  $R$  is normalized to the value on the GaAs channel. The two dips indicate the position of the edges and the width of the dips gives an approximate spatial resolution. Data originally presented in Kato et al. (2004c)

in the  $+z$  direction at  $x = -35$   $\mu\text{m}$  and in the  $-z$  direction at  $x = +35$   $\mu\text{m}$ . This is a signature of the spin Hall effect, as the spin polarization is expected to be out-of-plane and change sign for opposing edges (D'yakonov and Perel, 1971; Hirsch, 1999; Zhang, 2000; Murakami et al., 2003; Sinova et al., 2004). Shown in Figure 8c is a one-dimensional spatial profile of the spin accumulation across the channel which is mapped out by repeating  $B_{ext}$  scans at each position. The amplitude of Kerr rotation, which is proportional to the spin density, is at a maximum at the two edges and falls off rapidly with distance away from the edge, disappearing at the center of the channel (Figure 8d) as expected for the spin Hall effect (Zhang, 2000; Murakami et al., 2003).

Equilibrium spin polarization due to current-induced magnetic fields cannot explain this spatial profile, and moreover, such polarization is estimated to be less than  $10^{-6}$ , which is below our detection capability. Figure 8e shows the width of the Lorentzian becomes narrower as the distance from the edge increases, corresponding to an increase in the spin lifetime. A two-dimensional spatial image

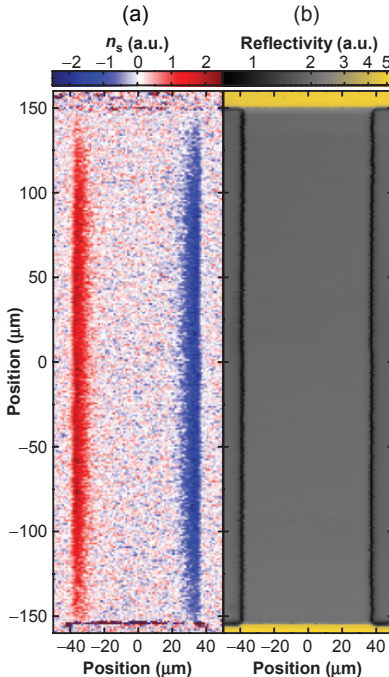


*Figure 9.* Two-dimensional images of spin density  $n_s$  (a) and  $R$  (b) for the unstrained GaAs sample measured at  $T = 30$  K and  $E = 10$  mV/ $\mu$ m. In (a), the dark region on the left (right) corresponds to the spin polarization in the  $z$  ( $-z$ ) direction (see the original figure in color in Kato et al. (2004c)). Data originally presented in Kato et al. (2004c)

of the entire sample is displayed in Figures 9a and 9b. The image shows the electrically polarized spins accumulated along the two edges of the sample with opposite net spin polarization. The spin polarization at the two edges is uniform over a length of 150  $\mu$ m but decreases near the contacts. The latter is expected as unpolarized electrons are injected at the contacts.

The origin of the observed spin Hall effect in these samples is likely to be extrinsic, as the intrinsic effect is only expected in systems with large spin-splitting that depends on electron wavevector  $k$ . While  $k^3$  spin-splitting in bulk GaAs (Dresselhaus, 1955) may give rise to the intrinsic spin Hall effect, this is unlikely as negligible spin-splitting has been observed in unstrained n-GaAs (Kato et al., 2004a). Measurements are also performed on another sample with channel parallel to the [110] crystallographic direction, and essentially the same behavior is reproduced. In addition, similar behavior is found in strained InGaAs samples which consist of a 500 nm n-In<sub>0.07</sub>Ga<sub>0.93</sub>As epilayer capped with 100 nm of undoped GaAs (Kato et al., 2004c). Furthermore, no marked crystallographic direction dependence is observed in these strained InGaAs samples, which suggests that the observed spin Hall effect is extrinsic.

### 3.2 THE SPIN HALL EFFECT AT ROOM TEMPERATURE IN ZINC SELENIDE

Despite weaker spin-orbit coupling, II-VI semiconductors also exhibit the spin Hall effect. A series of  $1.5\text{ }\mu\text{m}$  thick n-type Cl-doped ZnSe epilayer samples with room temperature carrier concentrations  $n = 5 \times 10^{16}\text{ cm}^{-3}$ ,  $9 \times 10^{17}\text{ cm}^{-3}$ , and  $9 \times 10^{18}\text{ cm}^{-3}$  are grown by molecular beam epitaxy on semi-insulating (001) GaAs substrates (Stern et al., 2006). The channel of the ZnSe samples is patterned either along [110] or [1 $\bar{1}$ 0] crystallographic direction with width  $w = 100\text{ }\mu\text{m}$  and length  $l = 235\text{ }\mu\text{m}$ . The absorption edge of these samples occurs approximately at 440 nm, and measured  $g$ -factor is 1.1.

Figure 10a shows the geometry of the spin Hall effect measurements for ZnSe epilayers. Typical Kerr rotation data for scans of  $B_{ext}$  near the edges of the channel at  $x = \pm 48\text{ }\mu\text{m}$  on the  $n = 9 \times 10^{18}\text{ cm}^{-3}$  sample are displayed in Figure 10b, and the data are fit to Eq. (5). Observation of the spin Hall effect is highly dependent on n-doping, as no spin Hall signature is measured in samples with lower  $n$ . The growth of higher doped samples is restricted by molecular beam epitaxy

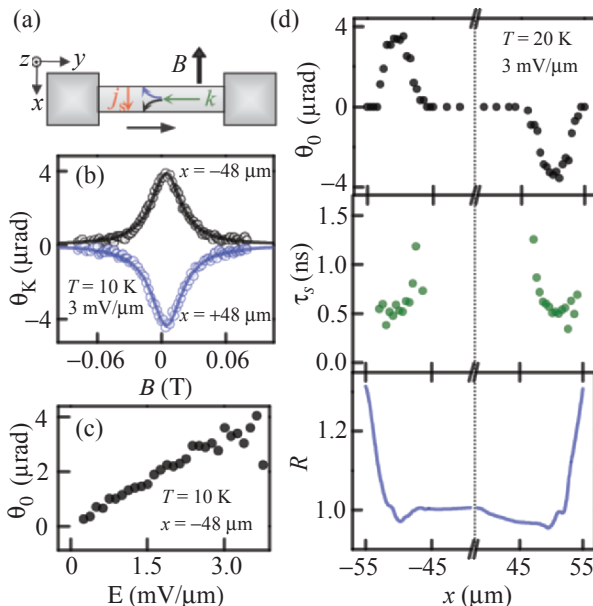


**Figure 10.** (a) Schematic showing the measurement geometry for the spin Hall effect, with  $B_{ext} \parallel x$ . For  $E > 0$ ,  $j_x^s < 0$ . (b)  $\theta_K$  (open circles) and fits (lines) at  $y = 0\text{ }\mu\text{m}$  as a function of  $B_{ext}$  for  $x = -48\text{ }\mu\text{m}$  (top) and  $x = +48\text{ }\mu\text{m}$  (bottom) at  $T = 20\text{ K}$ . (c) Electric field dependence of the spin accumulation amplitude  $\theta_0$ . Above  $E = 3\text{ mV}/\mu\text{m}$  the signal deteriorates due to heating. (d) Spatial dependence of the fit parameters  $\theta_{el}$  and  $\tau_s$ , as well as the reflectivity  $R$  of the beam (normalized to 1 at  $x = 0$ ), which is used to monitor the position. Data originally presented in Stern et al. (2006)

conditions. The spin Hall signal is also observed in ZnSe epilayer with  $n = 8.9 \times 10^{18} \text{ cm}^{-3}$ . No differences in spin accumulation between the [110] and [1\bar{1}\bar{0}] channel are observed.

The amplitude of the spin accumulation  $\theta_0$  is linear in  $E$  (Figure 10c), while no appreciable change in  $\tau_s$  is observed with increasing  $E$ . As observed for the spin Hall effect in the unstrained GaAs samples discussed earlier,  $\tau_s$  increases away from the channel edge (Figure 10d). The magnitude and sign of the spin polarization localized along the edges of the channel are found by direct comparison to the current-induced spin polarization (Stern et al., 2006) in a geometry with  $E \parallel B$ , which is calibrated by comparison to time-resolved Kerr rotation. At 20 K, the estimated peak spin density ( $n_0$ ) is approximately  $\approx 16 \text{ spins}/\mu\text{m}^3$  on the  $x = -50 \mu\text{m}$  ( $x = +50 \mu\text{m}$ ) edge along  $y$ , with spin polarization along  $+z$  ( $-z$ ).

Using a spin drift-diffusion model for the spin accumulation generated by a spin current source (Zhang, 2000; Kato et al., 2004c; Tse et al., 2005), the spin profile can be fit by  $\theta_0 = -n_0 \operatorname{sech}(w/2L_s) \sinh(y/L_s)$ , where  $L_s$  is the spin diffusion length (Figure 10d). These fits give  $L_s = 1.9 \pm 0.2 \mu\text{m}$  at  $T = 20 \text{ K}$ . Ignoring complications arising from boundary conditions, the spin current density along  $x$  can be written as  $|j_x^s| = L_s n_0 / \tau_s$  (Kato et al., 2004c). It follows that the spin Hall conductivity,  $\sigma_{SH} = -j_x^s/E_y = 3 \pm 1.5 \Omega^{-1}\text{m}^{-1}/|e|$  at  $T = 20 \text{ K}$ . Uncertainties in the overall optical calibration make this only an order-of-magnitude estimate. The spin Hall conductivity for ZnSe is of comparable magnitude and of the same sign as that predicted by theory (Engel et al., 2005; Tse and Sarma, 2006) for GaAs with a dominant extrinsic spin Hall effect (Stern et al., 2006).

Measurements of current-induced spin polarization and the spin Hall effect on the ZnSe samples at higher temperatures are displayed in Figures 11a and 11b, respectively. Shown in Figure 11c is temperature dependence of the various parameters discussed above. The spin polarization is an order of magnitude weaker at room temperature and  $L_s$  decreases from  $1.9 \mu\text{m}$  at  $20 \text{ K}$  to  $1.2 \mu\text{m}$  at  $295 \text{ K}$ . The estimated spin Hall conductivity decreases to  $\sigma_{SH} \approx 0.5 \Omega^{-1}\text{m}^{-1}/|e|$  at room temperature.

### 3.3 THE SPIN HALL EFFECT IN TWO-DIMENSIONAL ELECTRON GASES

We investigate the spin Hall effect in a two-dimensional electron gas laterally confined in (110) AlGaAs quantum wells. Optical measurements in (110)-oriented quantum wells may provide insights into the two proposed spin Hall mechanisms by allowing one to isolate the contributions of the Dresselhaus and Bychkov-Rashba internal effective magnetic fields. In two-dimensional systems, quantum confinement alters the Dresselhaus field. For example, the Dresselhaus field is oriented along the growth direction in (110) quantum wells, whereas this field is in-plane in (001) quantum wells. Since the Dresselhaus and Bychkov-Rashba fields are mutually perpendicular, one can independently tune the in-plane  $B_{int}$

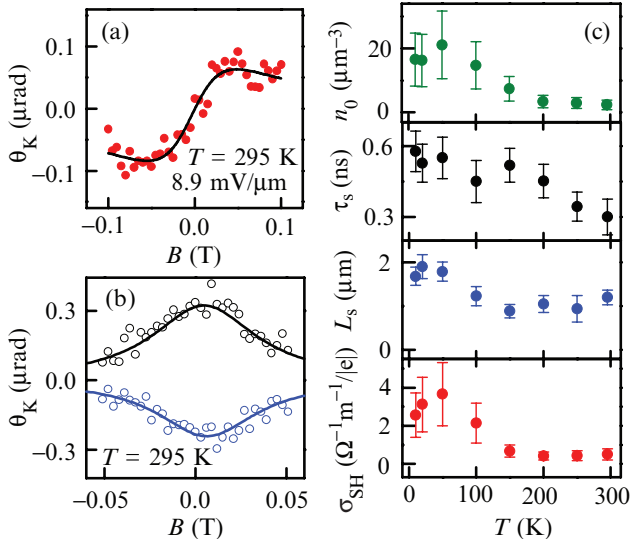


Figure 11. (a) KR (circles) and fit (line) of CISPR at room temperature. Adjacent-point averaging was done to improve signal-to-noise. (b) KR (circles) and fits (lines) of spin Hall polarization at  $x = -48 \mu\text{m}$  (top) and  $x = +48 \mu\text{m}$  (bottom) for  $T = 295 \text{ K}$ . (c) Temperature dependence of density  $n_0$ , coherence time  $\tau$ , spin diffusion length  $L_s$ , and spin Hall conductivity  $\sigma_{SH}$ . Data originally presented in Stern et al. (2006)

with the Bychkov–Rashba effect and the out-of-plane  $B_{int}$  with the Dresselhaus field using engineered (110) heterostructures.

The modulation-doped (110) oriented single quantum wells are digitally grown by molecular beam epitaxy on (110) semi-insulating GaAs substrates. The quantum well structure behaves like a single 7.5 nm  $\text{Al}_{0.1}\text{Ga}_{0.9}\text{As}/\text{Al}_{0.4}\text{Ga}_{0.6}\text{As}$  quantum well. The absorption edge of the these quantum wells occurs approximately at a wavelength of 719 nm, and the measured  $g$ -factor is  $-0.33$ . The devices for the optical spin Hall measurements were fabricated using standard photolithography and a chemical etch (Sih et al., 2005), and Ohmic contacts are made using annealed AuGe/Ni (Figure 12a).

The spin polarization in the two-dimensional electron gas is spatially resolved using low temperature scanning Kerr rotation microscopy in the Voigt geometry as described earlier. All of measurements are performed at  $T = 30 \text{ K}$ , and the center of the channel is taken to be the origin  $O$ . Figure 12b shows typical Kerr rotation data of scans as a function of the applied in-plane magnetic field  $B_{ext}$  for positions near the two opposite edges of a channel parallel to the [001] crystallographic direction. The data is fit to a Lorentzian given by Eq. (5).

In Figure 12c, a one-dimensional spatial profile of the spin accumulation near the edges of the channel is mapped out by repeating  $B_{ext}$  scans as a function of position. The reflectivity  $R$  shows the position of the edges of the channel,

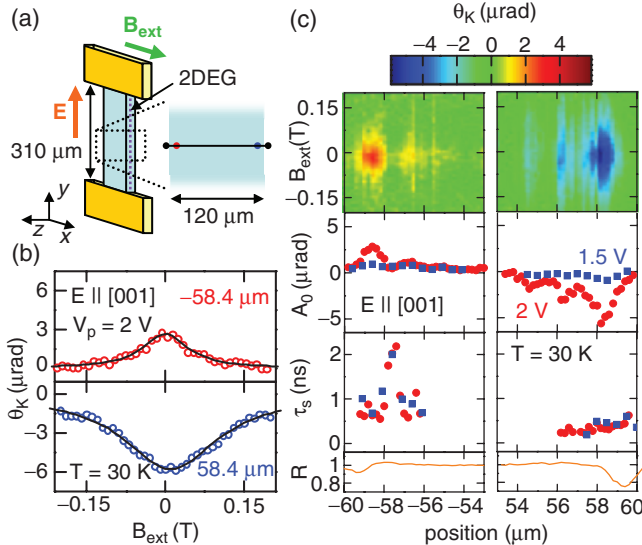


**Figure 12.** Spin Hall effect in a two-dimensional electron gas (a) Device schematic and measurement geometry. (b) Kerr rotation (hollow symbols) and fits (lines) as a function of applied in-plane magnetic field  $B_{ext}$  for  $x = -58.4 \mu\text{m}$  (top) and  $x = +58.4 \mu\text{m}$  (bottom). The channel has width  $w = 120 \mu\text{m}$ , length  $l = 310 \mu\text{m}$ , and mesa height  $h = 0.1 \mu\text{m}$ . A linear background is subtracted for clarity. (c)  $B_{ext}$  scans as a function of position near the edges of the channel of a device fabricated along for  $V_p = 2 \text{ V}$ . Amplitude  $A_0$ , spin coherence time  $\tau_s$ , and reflectivity  $R$  are plotted for  $V_p = 1.5 \text{ V}$  (squares) and 2 V (circles). The dark region on the left (right) panel corresponds to the spin polarization in the  $z$  ( $-z$ ) direction (see the original figure in color in Sih et al. (2005)). Data originally presented in Sih et al. (2005)

at  $x = \pm 59.4 \mu\text{m}$ . There are two spin Hall peaks at each edge of the channel, one around  $x = \pm 58.6 \mu\text{m}$  and one of smaller amplitude around  $x = \pm 56.4 \mu\text{m}$ . This structure was not observed in previous measurements on bulk epilayers (Kato et al., 2004c) as we discussed earlier, and could be due to an additional contribution from spin-polarized carriers undergoing spin precession about the in-plane Bychkov–Rashba field as they diffuse towards the center of the channel. As in the previous measurements (Kato et al., 2004c) for bulk semiconductors, the asymmetry in  $|\theta_0|$  for the right and left edges and a spatial dependence of  $\tau_s$  were also observed in a two-dimensional electron gas.

In the  $[001]$  oriented device, electrically induced spin polarization is observed only at the edges of the channel. In contrast, devices fabricated along the  $[1\bar{1}0]$ ,  $[1\bar{1}\bar{1}]$ , and  $[\bar{1}\bar{1}2]$  crystallographic directions also exhibit spin polarization at the center of the channel. Data taken at  $x = 0 \mu\text{m}$  for  $\mathbf{E}$  along  $[1\bar{1}0]$ ,  $[1\bar{1}\bar{1}]$ , and  $[\bar{1}\bar{1}2]$  are displayed in Figure 13b. Since the net spin polarization is oriented along the growth direction and depends on the direction of  $\mathbf{E}$  relative to the crystallographic axes, this effect is attributed to the Dresselhaus field. The application

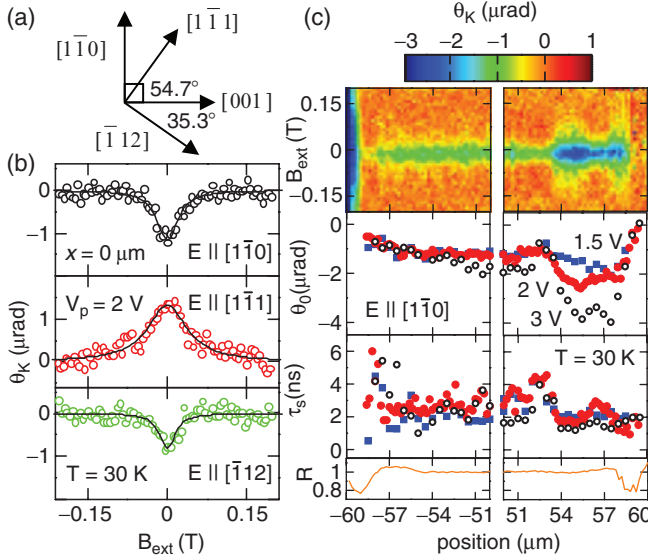


**Figure 13.** Current-induced spin polarization in a two-dimensional electron gas (a) Relative orientations of crystal directions in the (110) plane. (b) Kerr rotation (hollow symbols) and fits (lines) as a function of  $B_{ext}$  for  $E \parallel [1\bar{1}0]$  (top),  $E \parallel [1\bar{1}1]$  (middle), and  $E \parallel [\bar{1}12]$  (bottom) at the center of the channel. (c)  $B_{ext}$  scans as a function of position near the edges of the channel of a device fabricated along  $w = 118 \mu\text{m}$  and  $l = 310 \mu\text{m}$  for  $V_p = 2 \text{ V}$ . Amplitude  $A_0$ , spin coherence time  $\tau_s$ , and reflectivity  $R$  are plotted for  $V_p = 1.5 \text{ V}$  (squares),  $2 \text{ V}$  (filled circles) and  $3 \text{ V}$  (open circles). The dark regions correspond to the spin polarization in the  $z$  direction, whereas the light colored regions in the middle correspond to the spin polarization in the  $-z$  direction. (see the original figure in color in Sih et al. (2005)). Data originally presented in Sih et al. (2005)

of an electric field results in a nonzero average drift velocity of the electrons (i.e.,  $\mathbf{k} \neq 0$ ), which produces a nonzero effective magnetic field that orients spins (Aronov and Lyanda-Geller, 1989; Edelstein, 1990). The opposite sign of  $\theta_0$  for  $E \parallel [1\bar{1}0]$  and  $E \parallel [1\bar{1}1]$  may seem surprising since these crystallographic directions are only separated by 35.3° in the (110) plane (Figure 13a), but it is consistent with the calculated  $B_{int}$  due to the cubic Dresselhaus field in a (110) quantum well (Winkler, 2003). In addition, it also predicts that  $B_{int}$  should be zero for  $E \parallel [001]$  as observed. We note that the measured current-induced spin polarization in (110) AlGaAs quantum wells is out-of-plane instead of in-plane as in the case of bulk semiconductors (Kato et al., 2004b; Sih et al., 2005; Stern et al., 2006).

A spatial profile of the spin polarization near the edges of a channel for a device oriented along [1-10] crystallographic direction is shown in Figure 13c. The amplitude of the Kerr rotation is negative across the entire channel, and  $|\theta_0|$  increases with increasing  $V_p$ .  $|\theta_0|$  is nearly constant across the channel for  $-52 \mu\text{m} < x < +52 \mu\text{m}$ . However,  $|\theta_0|$  becomes smaller near the left edge of the channel, and a negative peak in  $\theta_0$  is seen near the right edge, which is due to the spin Hall

effect. The scan for  $V_p = 3$  V suggests that there may be two spin Hall peaks, at  $x = 55.5 \mu\text{m}$  and  $x = 57.5 \mu\text{m}$ , which is similar to the two peaks with  $\sim 2 \mu\text{m}$  spacing observed in the [001] oriented device. In contrast to the spin Hall measurements for bulk n-GaAs, n-InGaAs, and n-ZnSe semiconductors (Kato et al., 2004b; Kato et al., 2004c; Stern et al., 2006), the spin Hall profile in two-dimensional electron gases shows complex structure.

### 3.4 GENERATING SPIN CURRENT IN SEMICONDUCTORS WITH THE SPIN HALL EFFECT

Now we investigate electrically induced spin currents generated by the spin Hall effect in GaAs structures that distinguish edge effects from spin transport. Spin current is generally difficult to measure directly, but it can be calculated from the measured spin accumulation created by the spin Hall effect at the edges of a channel (Zhang, 2000). Because spin is not a conserved quantity in the presence of the spin-orbit interaction (Rashba, 2004; Shi et al., 2006), it is complicated to determine the spin current through analysis of the spin accumulation, which is strongly affected by the choice of boundary conditions (Tse et al., 2005; Galitski et al., 2006). In addition, the spin accumulation observed at the edges of the channel could be due to an edge effect, such as depletion near the edge producing a local effective magnetic field from the Bychkov–Rashba effect (Bychkov and Rashba, 1984) and not due to a bulk spin current. This local effective magnetic field could result in an electrically induced spin polarization, similar to the spatially homogeneous polarization that has been measured in strained semiconductors (Kato et al., 2004b) and semiconductor heterostructures (Silov et al., 2004; Shi et al., 2006).

In order to clarify the origin of the electrically induced spin polarization, devices are designed to separate the effects of the boundary of the electric field from edge effects (Sih et al., 2006b). Using the techniques described in the previous sections, these devices were fabricated from a  $2 \mu\text{m}$ -thick epilayer of n-doped GaAs, similar to the samples described in the previous sections. Each mesa consists of a main channel and two smaller transverse channels extending from the main channel. The main channels, fabricated along the  $[1\bar{1}0]$  crystallographic direction, have length  $l = 316 \mu\text{m}$  and width  $w = 60 \mu\text{m}$ , and the transverse channels are  $40 \mu\text{m}$  wide. One mesa has two side arms that are  $10$  and  $20 \mu\text{m}$  long, whereas the other mesa has two side arms that are  $30$  and  $40 \mu\text{m}$  long (Figure 14a). Measurements are performed at a temperature  $T = 30$  K, and the absorption edge of the sample occurs at  $825 \text{ nm}$ .

In Figure 14b we show representative Kerr scans for a position near the edge of the channel and away from either side arm ( $x = 26 \mu\text{m}$ ,  $y = 0 \mu\text{m}$ ). The curve is fit to a Lorentzian function given by Eq. (5). This measurement is repeated for positions across the channel and the side arms.

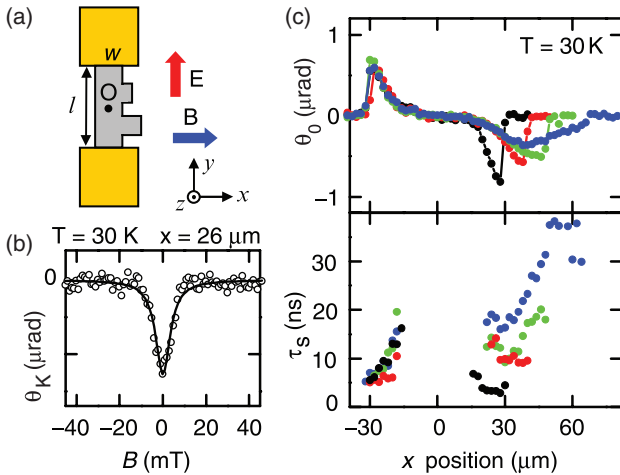


*Figure 14.* (a) Measurement schematic and experimental geometry. We take the center of the channel to be the origin  $O$ . (b) Kerr rotation as a function of magnetic field at  $(x,y) = (26 \mu\text{m}, 0 \mu\text{m})$ . Line is a Lorentzian fit from which the amplitude and spin lifetime can be determined. (c) (top) Spin polarization amplitude as a function of position measured for the channel (circles) and with 10  $\mu\text{m}$  (down triangles), 20  $\mu\text{m}$  (up triangles) and 40  $\mu\text{m}$  (squares) side arms. (bottom) Spin coherence time as a function of position. Data are taken at  $T = 30 \text{ K}$  and  $V = 6 \text{ V}$ . Data originally presented in Sih et al. (2006b)

The spin polarization amplitude and spin coherence times for the 60  $\mu\text{m}$  wide channel and for the channel with 10  $\mu\text{m}$ , 20  $\mu\text{m}$ , and 40  $\mu\text{m}$  side arms are displayed in Figure 7c. It is seen that the spin polarization amplitude near the left edge at  $x = -30 \mu\text{m}$  is unaltered in the presence of the side arms. In contrast, the spin polarization amplitude near the right edge  $x = 30 \mu\text{m}$  is modified by the addition of the side arms. The dependence of spatial profile of the spin accumulation on the side arm is apparent. We observe that the spin polarization amplitude is not always largest near the edge of the mesa. This indicates that the spin accumulation is not a local effect caused by the boundary of the sample boundary. In addition, the amplitude of the spin polarization is smaller for longer side arms at any position  $x$ . This suggests that the spins are drifting from the main channel towards the end of the side arms.

We observe that the magnetic field dependence of the spin polarization is also different in the side arms. The spin coherence time is inversely proportional to the width of the field scans in the Hanle model (i.e., Eq. (5)). The spin coherence time appears to increase near the edge at  $x = -30 \mu\text{m}$ , as reported in Kato et al. (2004c). The spin coherence time appears to increase even more as the distance increases farther from the edge of the channel. As noted in Kato et al. (2004c), it is possible the line shape could be influenced by an actual change in the spin coherence time for the spins that have diffused or the time that it takes for the spins to drift from the edge of the channel. The change in the line shape in the

transverse channels can be explained using a model that incorporates spin drift (Crooker et al., 2005; Lou et al., 2006), and it is not due to an actual change in spin coherence time.

The Hanle model assumes a constant rate of spin generation, which does not accurately reflect what occurs in the side arms, where there should be minimal electric current. In order to explain the change in the line shape of the field scans and spatial dependence of spin accumulation in the side arm, we employ a model that takes into account the fact that the spins are generated in the main channel and subsequently drift into the side arm (Crooker et al., 2005; Lou et al., 2006). This spin signal is calculated by averaging the spin orientations of the precessing electrons over the Gaussian distribution of their arrival times. For spins injected with an initial spin polarization  $S_0$  along the  $z$  direction at  $x_1$  and then flow with a spin drift velocity  $v_{sd}$  before they are measured at a position  $x_2$ ,

$$S_z(x_1, x_2, B) = \int_0^{\infty} \frac{S_0}{\sqrt{4\pi D t}} e^{-(x_2 - x_1 - v_{sd}t)^2 / 4Dt} e^{-t/\tau_s} \cos(\omega_L t) dt, \quad (6)$$

where  $D$  is the spin diffusion constant.  $S_z(x_2, B)$  is calculated by integrating  $x_1$  over the width of the main channel, from  $-30 \mu\text{m}$  to  $+30 \mu\text{m}$ . We apply this model to measurements taken on the  $40 \mu\text{m}$  side arm, which is schematically shown in Figure 15a. The spin coherence time  $\tau_s = 11.4 \text{ ns}$  is determined using resonant spin amplification (Kikkawa and Awschalom, 1998). The same set of parameters is used to compute  $S_z(x, B)$  for three positions in the side arm as indicated in Figure 15a. It can be seen from Figure 15b that the model reproduces the line shape and the spatial dependence of amplitude using  $D = 10 \text{ cm}^2/\text{s}$  and  $v_{sd} = 1.6 \times 10^5 \text{ cm/s}$  and without assuming a spatially dependent spin coherence time. The value obtained for  $v_{sd}$  may have a contribution from both the spin Hall effect and the electric field gradients in the transverse channel.

To address the homogeneity of the spin polarization along the longitudinal ( $y$ ) direction, spatial scans along the channel and across the side arms are performed. The amplitude determined from Lorentzian fits is shown in Figure 15c. We observe the amplitude of the spin polarization builds up from zero at the contact ( $y = -158 \mu\text{m}$ ) to a maximum value over  $50 \mu\text{m}$  from the scans taken at  $x = -26 \mu\text{m}$  and  $x = 26 \mu\text{m}$ . The scans taken at  $x = 26 \mu\text{m}$  show that the amplitude drops near the side arm due to spin drift into the side arm, which has edges at  $y = -70 \mu\text{m}$  and  $y = -30 \mu\text{m}$ , whereas the amplitude of the scans taken at  $x = -26 \mu\text{m}$  are insensitive to the position of the side arm. Scans taken across the side arm, at  $x = 36 \mu\text{m}$  and  $x = 56 \mu\text{m}$ , show that the amplitude is largest near the edges of the side arm, which may also be due to spin drift.

These measurements demonstrate that the spin Hall effect can drive transport of spins over length scales that are many times the spin diffusion length  $L_s = 9 \mu\text{m}$

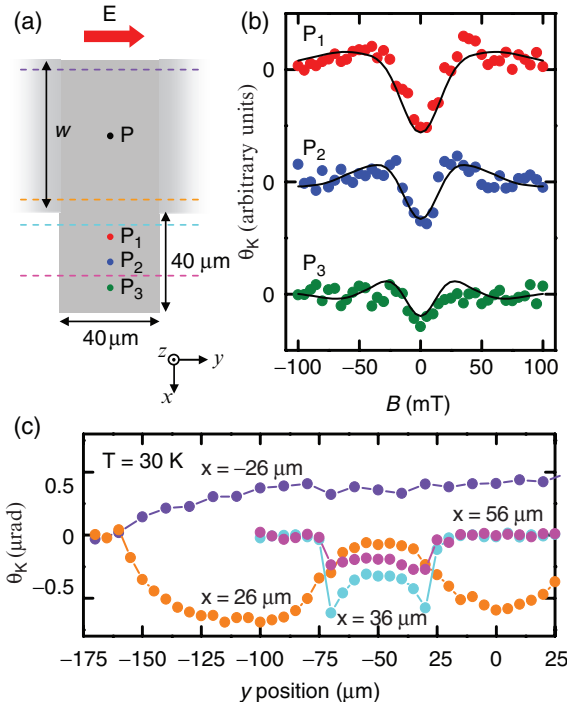


*Figure 15.* (a) Measurement schematic showing sample dimensions.  $P$  indicates the position  $(x,y) = (0 \mu\text{m}, -50 \mu\text{m})$ . (b) Kerr rotation as a function of magnetic field for three different  $x$  positions at  $y = -50 \mu\text{m}$  on the  $40 \mu\text{m}$  side arm. Taking  $x = 0 \mu\text{m}$  to be the center of the channel, the edges of the main channel are at  $x = -30 \mu\text{m}$  and  $x = +30 \mu\text{m}$  ( $w = 60 \mu\text{m}$ ). Measurements are shown for  $x = 40 \mu\text{m}$  ( $P_1$ , top),  $x = 50 \mu\text{m}$  ( $P_2$ , middle) and  $x = 60 \mu\text{m}$  ( $P_3$ , bottom). Solid lines are calculated from a model that accounts for spin drift, as described in the text. The same values for  $S_0$ ,  $\tau_s$ ,  $v_{sd}$ , and  $D$  are used for all three curves. (c) Amplitude of Kerr rotation measured as a function of longitudinal position  $y$  for  $x = -26 \mu\text{m}$ ,  $x = 26 \mu\text{m}$ ,  $x = 36 \mu\text{m}$  and  $x = 56 \mu\text{m}$ . These positions are shown as dashed lines in part (a) of this figure. One contact edge is located at  $y = -158 \mu\text{m}$ , and the edges of the side arm are at  $y = -70 \mu\text{m}$  and  $y = -30 \mu\text{m}$ . Data originally presented in Sih et al. (2006b)

(from fits of the spatial spin Hall profile to the model in Zhang (2000)) and with a transverse spin drift velocity  $v_{sd} = 1.6 \times 10^5 \text{ cm/s}$  that is comparable to the longitudinal charge drift velocity  $v_{cd} = 4.8 \times 10^5 \text{ cm/s}$  at  $V = 6 \text{ V}$ .

#### 4 Spin Accumulation in Forward-Biased MnAs/GaAs Schottky Diodes

This section describes a series of experiments in which silicon-doped n-type GaAs epilayers are mated with epitaxial layers of ferromagnetic (FM) metals which are grown by molecular beam epitaxy (MBE). These hybrid materials are excited optically and electrically and it is shown that under appropriate conditions they

can be used to generate both electron and nuclear spin polarizations in the GaAs semiconductor.

Previous experiments have shown how electron and nuclear spin polarizations can be created in n-type GaAs epilayers covered with thin metallic ferromagnets under optical excitation, a process dubbed ferromagnetic imprinting of nuclear spins (Kawakami et al., 2001). Subsequent work showed that optically-excited electrons interact with the ferromagnet, and coherently rotate to become polarized either parallel or antiparallel to the FM magnetization, an effect known as ferromagnetic proximity polarization (FPP) (Epstein et al., 2002). These spin-polarized electrons then polarize the nuclear spin system via the well-known dynamic nuclear polarization (DNP) process. These effects were further shown to be tunable using a modest applied voltage and to be largest under forward bias conditions (Epstein et al., 2003). In these conditions electrons are swept from the semiconductor into the ferromagnet. In the case of the nuclear spin polarization low temperatures (below  $\sim 60$  K) are required but the FPP mechanism for electron spin polarization was shown to be robust up to at least 110 K (Epstein et al., 2002) and presumably works up to the Curie temperature of the ferromagnet. The FPP effect therefore could potentially be useful in future spin-based devices which operate at room temperature and higher. These effects are illustrated in Figure 16. One limitation of these experiments, however, is that above band-gap optical-excitation of the semiconductor was required. It would be more convenient for many devices if the spin polarization could be generated using purely electrical means.

Similar reasoning has resulted in much effort being devoted to the injection of electrons from ferromagnetic metals into semiconductors since these systems

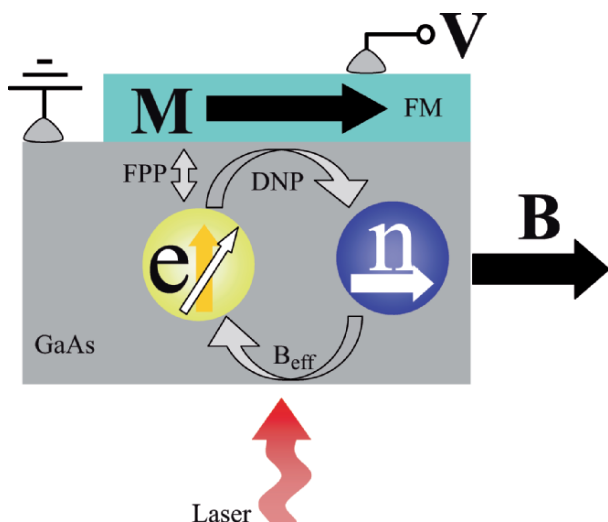


Figure 16. Cartoon picture of the rich environment that exists for electron spins in semiconductor/ferromagnet heterostructures under illumination

have the potential to serve as room-temperature sources of spin polarization (Wolf et al., 2001). To date, most research in this vein has focused on electron currents flowing through a tunnel barrier from the ferromagnet to the semiconductor. For example, spin injection has been observed for tunneling through Schottky (Zhu et al., 2001; Ramsteiner et al., 2002) and aluminum oxide (Motsnyi et al., 2002) tunneling barriers, as well as in more complicated structures such as magnetic tunnel transistors (Jiang et al., 2003). All of these schemes share the common feature that spin-polarized electrons are injected from the FM into the semiconductor (SC). In this section a new means of electrically generating such spin polarizations in a lateral device that requires neither optical excitation nor that the sample be reverse biased is described (Stephens et al., 2004). Specifically, spin accumulation in ferromagnetic MnAs/GaAs Schottky-diode structures biased in the forward direction is demonstrated. In these experiments an electron current flows from the GaAs into the MnAs, and a net electron spin polarization arises in the GaAs as illustrated in Figure 17. Spatiotemporal Kerr microscopy was used to laterally image the electron spin and the resulting dynamic nuclear polarization that arises from the nonequilibrium electron polarization.

Samples grown by molecular beam epitaxy consist of 25 nm type-A MnAs, 500 nm n-GaAs, and 400 nm Al<sub>0.75</sub>Ga<sub>0.25</sub>As, grown on a semi-insulating GaAs (100) substrate. Using photolithography and wet etching, a 50 × 100 μm<sup>2</sup> MnAs mesa was defined at the center of a channel etched into the n-GaAs layer, as shown in Figure 18a. A metal contact (100 nm Ni:Ge:Au:Ni:Au stack) was deposited in an electron-beam evaporator on the n-GaAs across the channel from the MnAs mesa, patterned using wet lithography and lift-off techniques, and annealed in a rapid thermal annealer (1 min at  $T = 400^\circ\text{C}$  in nitrogen) to form an Ohmic contact. A second similarly-patterned contact was then deposited on the MnAs mesa, thus forming a Schottky diode in series with a resistor, which shows typical rectifying I–V characteristics. Hysteresis loops measured in a superconducting quantum interference device magnetometer showed that the MnAs is ferromagnetic with a Curie temperature of 320 K. While the data presented below are from a single sample with the n-GaAs layer Si doped at 8e16 cm<sup>-3</sup>, a number

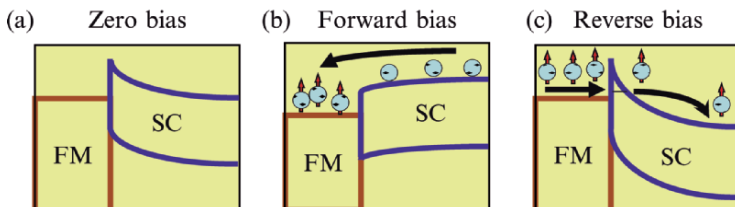


Figure 17. Schematic energy-band diagrams for metal-semiconductor Schottky barrier under (a) zero bias, (b) positive (forward) bias, and (c) negative (reverse) bias

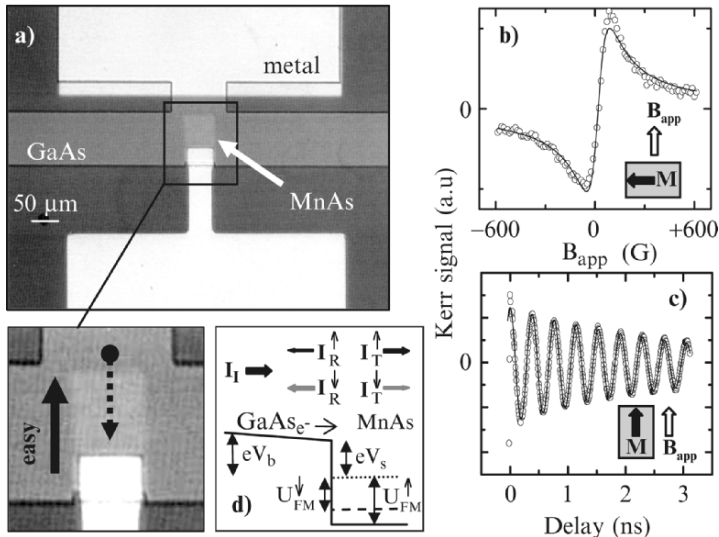


Figure 18. (a) Charge-coupled device micrographs of spin accumulation device. Close-up depicts the MnAs magnetic easy axis direction as well as the linecut measurement path (see text). (b) TRKR and (c) Hanle-MOKE data (symbols) and fits (lines) at  $T = 7.5$  K. Insets show the two measurement geometries. (d) Schematic conduction band diagram of Schottky interface for magnetization parallel to spin-up electrons. Also depicted is a cartoon of the spin-dependent incident ( $I_I$ ), reflected ( $I_R$ ), and transmitted ( $I_T$ ) electron currents. Data originally presented in Stephens, et al. (2004).

of samples with doping ranging from  $6\text{e}16$  to  $1\text{e}18 \text{ cm}^{-3}$  showed similar effects.<sup>1</sup> A control sample with a nonmagnetic Schottky diode showed none of the spin effects discussed below.

Measurements of electron spin polarization were performed using the Hanle-MOKE technique described in more detail elsewhere (Stephens et al., 2003). The Hanle-MOKE signal  $\langle S \rangle$  versus field scans can be fit to:

$$\langle S \rangle = \frac{A\omega_L}{((1/T_2^*)^2 + \omega_L^2)}, \quad (7)$$

where  $A$  is proportional to the spin polarization rate,  $T_2^*$  is the transverse spin lifetime, and  $\omega_L$  is the precession frequency. The quantity  $AT_2^*$  is then proportional to the time-averaged spin polarization in zero applied field. These measurements are possible when the electron spins we wish to measure precess (those oriented

<sup>1</sup>For similar current density, temperature, and applied field conditions, samples with doping  $6\text{e}16$ ,  $8\text{e}16$ , and  $1\text{e}17 \text{ cm}^{-3}$  all showed maximum effective nuclear fields of 0.35–0.45 T. The magnitude of electron spin accumulation that occurs over this doping range does not vary widely. A sample with doping  $1\text{e}18 \text{ cm}^{-3}$  showed greatly reduced transverse spin lifetime and negligible nuclear spin polarization.

by FPP) about the applied magnetic field. Thus samples were mounted such that their magnetization is perpendicular to  $B_{app}$ .

Nuclear polarization was measured using time-resolved Kerr rotation (TRKR). When the sample magnetization and applied magnetic field have suitable geometry the Larmor frequency of the coherently-precessing electron spins acts as a magnetometer of the effective nuclear field present in the semiconductor as described by the relation  $S(\Delta t) = S_0 \exp(-\Delta t/T_2^*) \cos(\omega_L \Delta t)$ . Here  $\omega_L = g\mu_B(B_{app} + B_n)/\hbar$ , with  $g$  the electron  $g$ -factor (-0.44),  $\mu_B$  the Bohr magneton,  $B_{app}$  the applied magnetic field,  $B_n$  the effective nuclear field, and  $\hbar$  Planck's constant. Nuclear polarization is generated below  $T = 60$  K and when  $B_{app}$  and the sample magnetization  $\mathbf{M}$  are parallel.

The samples were mounted in a custom-built liquid helium cryostat which can reach temperatures down to  $T = 5$  K and the pump and probe beams were focused through a long-focal-length, large numerical aperture microscope objective. The spatial resolution of the TRKR microscope was set 2  $\mu\text{m}$  spot size of the optical beams and the objective can be scanned with 20 nm resolution. Repeating TRKR and Hanle-MOKE measurements as a function of lateral position on the sample yields spatial maps of both the electron and nuclear spin polarization present in the GaAs. More information on the microscope apparatus can be found in the following section and in Stephens et al. (2003). For the Hanle-MOKE measurements the probe power was 550  $\mu\text{W}$  and for the TRKR measurements the pump power was 450  $\mu\text{W}$  and probe power was 350  $\mu\text{W}$ . It was determined from lab-time dependent measurements in the TRKR geometry that compared to the electrically-generated nuclear polarization the pump and probe beams acted only as negligible perturbation on the nuclear spin system.

Characteristic Hanle-MOKE and TRKR curves, along with schematics of each measurement geometry, are shown in Figures 18b and 18c. For the Hanle-MOKE measurement, the sample was mounted with the magneto-crystalline easy axis of the MnAs perpendicular to the applied field. Because of the strong uniaxial anisotropy present in MnAs, the magnetization deviates only slightly from the easy axis in the magnetic fields used in these experiments. A 6 kHz square wave was applied to the Schottky diode, oscillating between  $V_b = 0$  and +1.5 V, which allowed the use of lock-in detection of the electrically induced MOKE signal. For these bias voltages the resulting current was found to be  $I_b = 0.0$  and 1.65 mA, respectively.

#### 4.1 SPATIAL MAPS OF ELECTRON AND NUCLEAR SPIN POLARIZATION

Fitting the curves obtained through the Hanle-MOKE technique yields the spatial map of the time-averaged spin polarization  $AT_2^*$  shown in Figure 19a. As expected, switching the magnetization of the FM yielded a sign change in the Hanle-MOKE signal (not shown). For the nuclear polarization measurements, the sample was

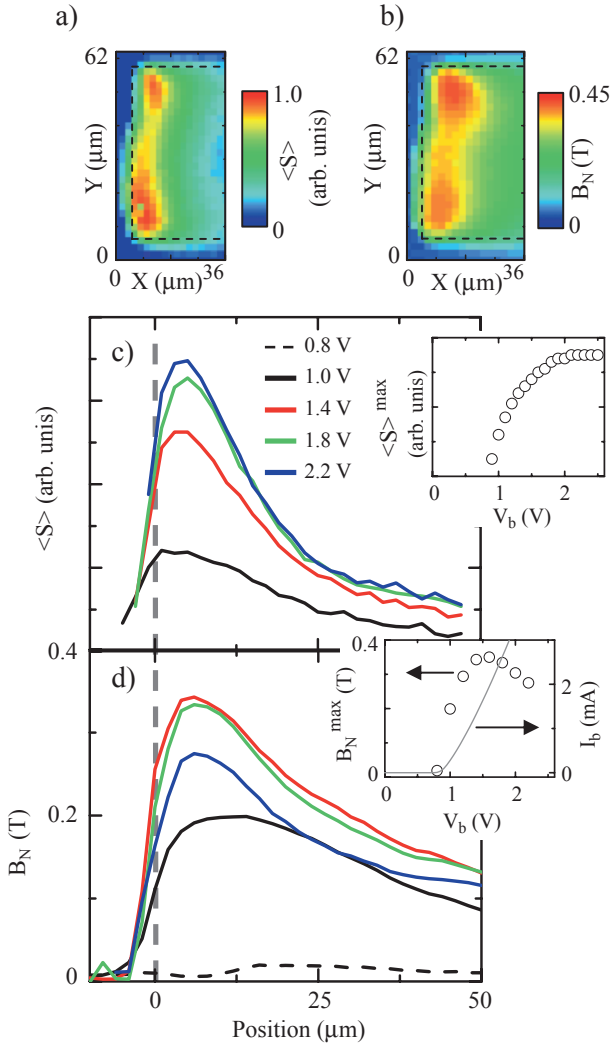


*Figure 19.* (a) 2D image of time-averaged electron spin ( $AT_2^*$ ) taken at  $T = 7.5$  K with a square-wave between 0 and 1.5 V applied at 6 kHz. Dotted lines show outline of MnAs mesa. (b) 2D image of effective nuclear field  $B_N$  taken at  $T = 7.5$  K with forward bias of 1.5 V and applied field of 2 kG. Linecuts of (c)  $AT_2^*$  for various forward biases between 0.8 and 2.2 V, and (d)  $B_N$  along the path indicated in Figure 18a. Insets show the peak value of each as a function of bias. Data originally presented in Stephens, et al. (2004).

mounted with the MnAs easy axis parallel to  $B_{app}$ . With  $B_{app} = 2$  kG, and a forward bias of +1.5 V ( $I_b = 1.65$  mA), nuclear polarization was observed to build up under the MnAs mesa over the course of approximately 20 min, with a maximum effective nuclear field  $B_n = 0.45$  T and a maximum effective field gradient of  $8e10^4$  T/m. The sign of the effective nuclear field indicates that the

electron spin is polarized antiparallel to the MnAs magnetization, in agreement with previous measurements (Epstein et al., 2002). Figure 19b shows an image of the resulting nuclear polarization which is in qualitative agreement with the electron polarization. Discrepancies between the images of electron and nuclear polarization may be due in part to the fact that electron spins decay with the transverse lifetime in the case of the Hanle-MOKE measurement, but the longitudinal lifetime is the relevant timescale in the DNP measurement. Sweeping the field and measuring the nuclear polarization yielded a hysteresis loop similar to those previously measured (Kawakami et al., 2001), with a switching event occurring at the MnAs coercive field, thus confirming the role of the FM in this phenomenon.

TRKR and Hanle-MOKE measurements were also used to investigate the dependence of nuclear and electron spin polarizations on the forward-bias current. Figure 19c shows line cuts of the electron spin polarization taken along the path indicated by the dashed line in the inset of Figure 18a. No measurable electron polarization for  $V_b < 0.8$  V (which corresponds to the turn-on of the Schottky diode) was observed. At higher voltages, current begins flowing and the electron polarization increases. The maxima of these curves as a function of applied bias are shown in the inset of Figure 19c.

The same line cuts were measured using the TRKR technique, and the extracted nuclear spin polarization is shown in Figure 19d. The results closely match the electron polarization profiles. Again, the maxima of these curves are shown in the inset. One difference between the two measured spin profiles is that the nuclear polarization reaches a maximum at about  $V_b = 1.6$  V and subsequently decreases at higher bias, possibly a result of resistive heating.

Temperature dependence measurements of both the nuclear and electron spin were also performed, the results of which are shown in Figure 20. A TRKR measurement with optically injected spins at zero applied field was used to normalize the Hanle-MOKE results as a function of temperature since the magnitude of the Kerr effect was observed to decrease by 30% from  $T = 7.5$  to 50 K. It was found that the magnitude of the nuclear polarization and the time-average electron spin polarization both decrease monotonically with increasing temperature, but that the nuclear polarization decreases more quickly. This is expected since the nuclear polarization depends not only on the average electron spin polarization but also on the nuclear relaxation time, which decreases with increasing temperature (Abragam, 1961). Figures 21a and 21b show the same current dependence measurements as Figure 19d, but with the spin accumulation rate  $A$  and spin depolarization rate  $1/T_2^*$  plotted separately. We see that the spin accumulation rate is sharply peaked near the leading edge of the MnAs, and is quite small elsewhere under the mesa. Similarly, the spin depolarization rate has a peak at the leading edge, but then decreases to a constant value farther away. The shape of  $A$  as a function of position is similar to what one would expect for the lateral current

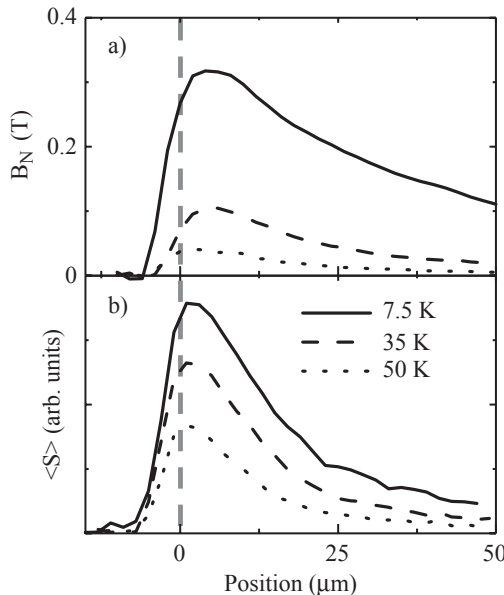


Figure 20. Linecuts at various temperatures taken along the path shown in Figure 18a of (a) effective nuclear field and (b) time-averaged electron spin from  $T = 7.5$  K to  $T = 50$  K. Dashed vertical line indicates the position of the front edge of the MnAs mesa. For the nuclear field measurement the forward bias was 1.5 V while for the electron spin measurement a 6 kHz square wave between 0 and 1.5 V was applied. Data originally presented in Stephens, et al. (2004).

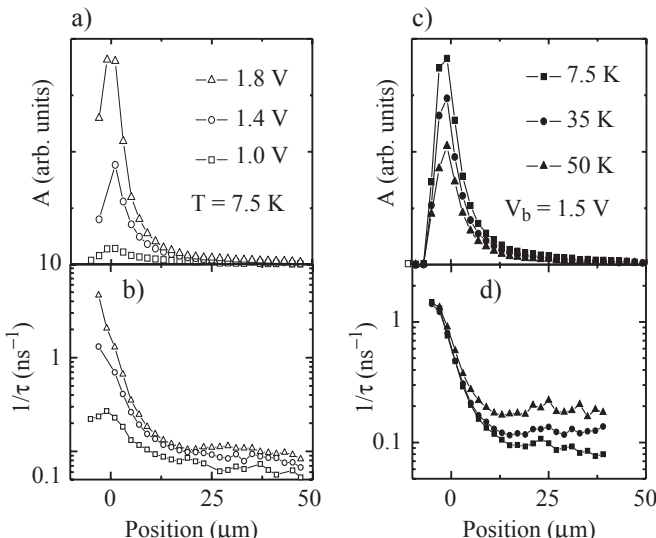


Figure 21. Linecuts showing the bias dependence of (a) the electron spin accumulation rate  $A$  and (b) the electron spin depolarization rate  $1/T_2^*$  taken at  $T = 7.5$  K. Linecuts of  $A$  and  $1/T_2^*$  for  $T = 7.5$  K to  $T = 50$  K are shown in (c) and (d), respectively. Data originally presented in Stephens, et al. (2004).

density across the SC–FM interface, since the conductivity of the GaAs is much lower than that of the metallic MnAs. The strongly enhanced spin depolarization rate in the vicinity of the MnAs leading edge is likely due to transport of spin into the FM or away from the probe spot within the SC, an effect that will be greatest near the front of the magnetic mesa where the current density is largest. The temperature dependences of  $A$  and  $1/T_2^*$  are shown in Figures 21c and 21d. Here, the spin lifetime appears to be dominated by a temperature independent contribution near the edge of the MnAs mesa, which again is consistent with the picture of spin being transported away from the probe spot in the area of high current density.

The observed effect may be qualitatively described by a simple model of spin-dependent reflection off the FM–SC interface (Ciuti et al., 2002; McGuire et al., 2003). The ferromagnet is modeled as exchange-split parabolic bands, resulting in different wave vectors in the ferromagnet for the two spin channels at a given energy. In this picture one can think of the FM acting as a filter for the higher energy spins such that electrons of one spin type are preferentially removed, leaving behind more of the other spins. The wave function matching conditions at the interface result in spin-dependent reflection and transmission coefficients for electrons incident at the interface.

We consider transport across the interface under forward bias (see schematic shown in Figure 18d), ignoring the spatial dependence of the current density and assuming the spin-flip time is sufficiently long such that the two spin channels are independent. Using the Drude relation, the spin polarization due to reflection can be calculated from the spin-dependent currents flowing through the interface:

$$\frac{n_\uparrow - n_\downarrow}{n_\uparrow + n_\downarrow} = \frac{\int_0^k dk_z k_z \int_0^{\sqrt{k_f^2 - k_z^2}} dk_{\parallel} k_{\parallel} (T_\uparrow - T_\downarrow)}{\int_0^k dk_z k_z \int_0^{\sqrt{k_f^2 - k_z^2}} dk_{\parallel} k_{\parallel} (T_\uparrow + T_\downarrow)} \quad (8)$$

where  $k_f$  is the Fermi wave vector in the semiconductor,  $k_z$  is its component in the growth direction,  $k_{\parallel}$  is the component parallel to the interface,  $n$  is the doping density, and  $T_\uparrow$  and  $T_\downarrow$  are the transmission coefficients for the two spin channels. Using reasonable material parameters<sup>2</sup> and assuming the SC spin lifetime is dominated by current flow into the FM, the theory estimates the spin polarization to be a few percent and is consistent with the observed nuclear polarization (Strand et al., 2003). Another theory (Bauer et al., 2005) points out that the conductivity mismatch between FM and SC enhances the FPP effect, similarly to the case of spin injection via reverse-bias tunneling.

---

<sup>2</sup>GaAs: effective mass  $m^* = 0.07$ , mobility  $\mu = 3000 \text{ cm}^2/\text{V}\cdot\text{s}$ , doping  $n = 8e16 \text{ cm}^{-3}$ ; MnAs:  $m^* = 1$ , spin-up potential = 3.0 eV, spin-down potential = 1.5 eV; Schottky barrier height:  $U_b = 0.8 \text{ eV}$ .

## 5 Spin Coherence in Quantum Dots

The physics of electron and hole spins in semiconductors changes drastically when the carriers are spatially confined on length scales smaller than the extent of the bulk wavefunction. This is the case in semiconductor quantum dots (QDs), where quantum confinement splits the continuum of states in the conduction and valence band into discrete energy levels. Thus for sufficiently large splitting, momentum scattering is effectively suppressed. Without momentum scattering, spin decoherence caused by spin-orbit related mechanisms (such as the D'yakonov-Perel and Elliot-Yafet mechanisms) is not significant.

Because of this enhanced spin coherence, a spin-1/2 electron in a QD is an attractive candidate for use as a quantum bit for quantum computing. Loss and DiVincenzo proposed a quantum computer based on electron spin qubits, shown in Figure 22, in which QDs are defined by gates above a two-dimensional electron gas (2DEG), gates are used to control the coupling between QDs, and the spins are operated on through electron spin resonance (Loss and DiVincenzo, 1998). Many other proposals for spin-based quantum computers have followed (Kane, 1998; Barnes et al., 2000; Vrijen et al., 2000; Levy, 2001).

The QDs in the Loss and DiVincenzo proposal are an example of top-down fabrication. A planar 2DEG is carved up into puddles of electrons using submicron gates deposited on the surface of the sample (Figure 23a). QDs can also be created in a top-down manner by etching narrow pillars out of a 2DEG (Austing et al., 1998) (Figure 23b). In contrast, bottom-up fabrication is also possible. When InAs is deposited on GaAs by molecular beam epitaxy, nanometer-scale InAs islands can form spontaneously due to the mismatch of lattice constants (Leonard et al., 1993) (Figure 23c). These islands of low-bandgap InAs serve as a layer of naturally forming QDs embedded within a semiconductor structure. Here, we will focus on QDs synthesized through chemical processes (Figure 23d).

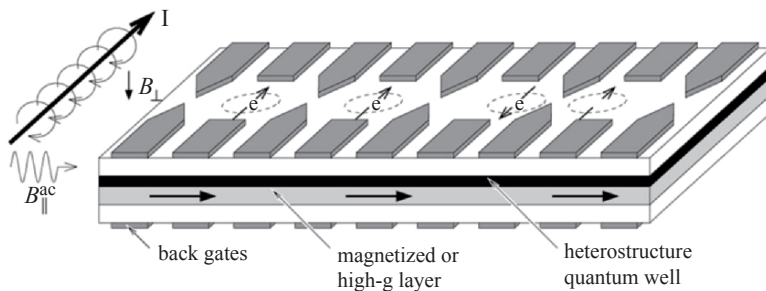


*Figure 22.* Proposed spin-based quantum computer from Loss and DiVincenzo (Loss and DiVincenzo, 1998). Electrodes form QDs in the 2DEG layer, and control coupling between qubits. The spins are manipulated by bringing them into resonance with an ESR field

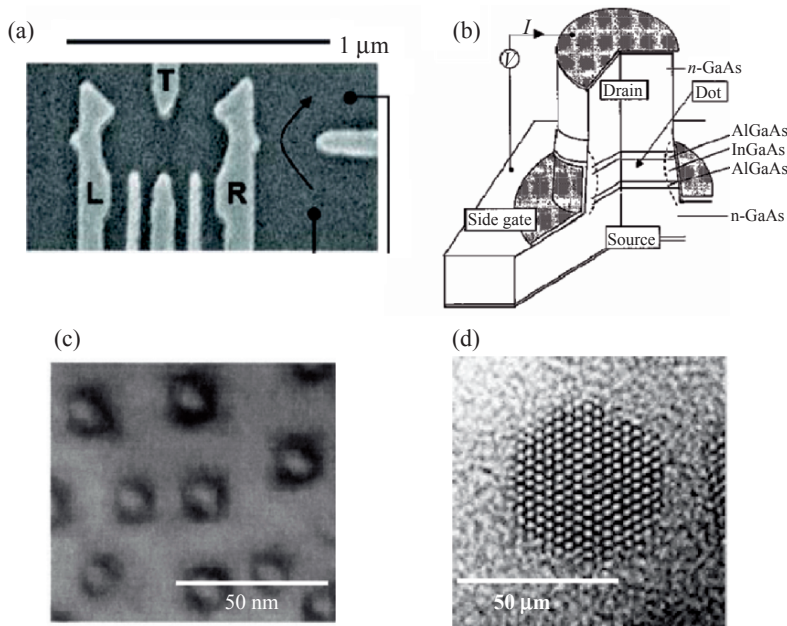


**Figure 23.** (a) Scanning electron microscope (SEM) image of a gate-defined 2DEG QD. (From J. Petta et al., *Science* **309**, 2180 (2005).) (b) Schematic of an etched pillar QD. (From L. P. Kouwenhoven et al., *Science* **278**, 1788 (1997).) (c) Transmission electron microscope (TEM) image of MBE-grown, strain-induced, InAs QDs on GaAs. (From M. Grundmann et al., *Physica E* **5**, 167 (2000).) (d) High-resolution TEM image of a chemically-synthesized CdSe nanocrystal QD (From Manna et al. (2000))

Using standard, table-top colloidal chemistry, nanocrystals of many different semiconducting materials can be nucleated and grown (Murray et al., 1993). These nanocrystal QDs have a number of attractive characteristics. The diameter of the QDs can be varied from smaller than 1 nm to larger than 10 nm, allowing the energy of the quantum confinement to be tuned over a large range. For this reason, such colloidal QDs have found great practical use as luminescent markers for biological tagging. The variety of materials that can be used for these nanocrystals offers another dimension of flexibility, even allowing different materials to be layered concentrically. By varying the growth conditions, nanocrystals can be grown in a number of shapes ranging from nearly spherical, to rods, or branching structures (Manna et al., 2000). Furthermore, the chemistry-based synthesis allows the surface of the QDs to be functionalized with a large variety of molecules, modifying the behavior of the QDs, or linking them together.

Spins can be optically injected into colloidal quantum dots using circularly polarized light, just as in bulk semiconductors. Time-resolved Faraday rotation (TRFR) proves to be a very useful probe of the resulting spin dynamics

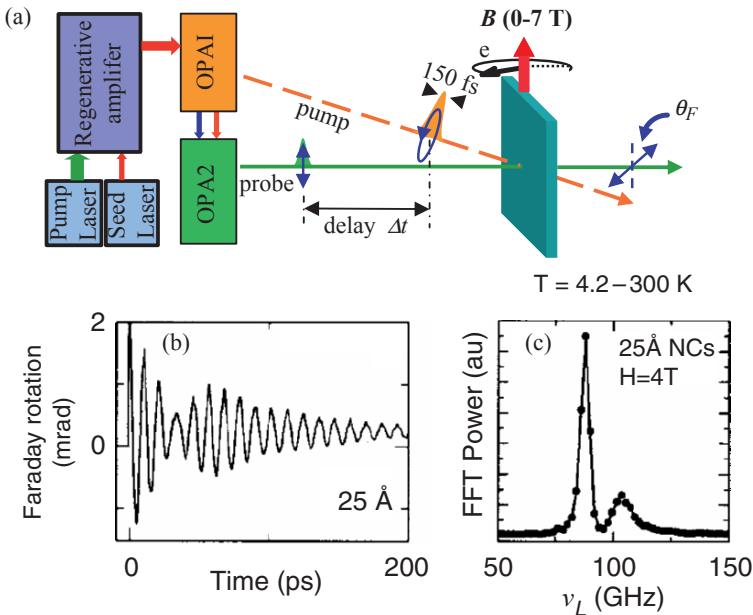


Figure 24. (a) Schematic of the experimental setup for two-color TRFR on CdSe colloidal QDs. The QDs are dispersed in a polymer matrix, and mounted in a magneto-optical cryostat. (b) Typical TRFR on 2.5 nm diameter CdSe QDs at  $T = 5$  K and  $B = 4.0$  T. (c) The Fourier transform of the data in (b). Data originally presented in Berezovsky, et al. (2005).

(Gupta et al., 1999). For these measurements, a regeneratively amplified Ti:Sapphire laser is used to seed and pump two optical parametric amplifiers (OPAs), which output synchronized, ultrafast optical pulses tunable over the entire visible spectrum. These pulses then serve as the pump and probe in nondegenerate time-resolved measurements (see Figure 24a).

TRFR in an ensemble of 2.5 nm diameter CdSe colloidal QDs as a function of pump–probe delay is shown in Figure 24b. Here, a magnetic field is applied perpendicular to the direction of the pump and probe beams. The measured rotation is proportional to the net spin polarization along the measurement axis. The oscillatory behavior is due to the precession of the spins about the applied field. The oscillations decay within a few nanoseconds due to spin decoherence and dephasing. Though decoherence mechanisms that depend on momentum scattering are suppressed in this case, the overlap of the electron wavefunction with nuclear spins is enhanced due to the confinement. Thus dephasing due to the fluctuating hyperfine interaction may be the dominant mechanism in these QDs (Khaetskii et al., 2002; Merkulov et al., 2002). This is consistent with the temperature dependence of the spin lifetime, which is seen to be nearly constant from room temperature down to 5 K.

The Fourier transform of the TRFR is shown in Figure 24c. There are two distinct precession frequencies (or  $g$ -factors), which can also be seen in the beating in the time-domain data. The presence of two precession frequencies is a general feature of the spin dynamics in this type of QD, and they have been attributed to precession of electron spins and precession of exciton (electron plus hole) spins (Gupta et al., 2002). This assignment is further supported by measurements of spin dynamics in CdSe QDs electrochemically charged with excess electrons (Stern et al., 2005).

Both of the observed  $g$ -factors are seen to vary monotonically with the size of the QD. This is a reflection of the general dependence of the effective  $g$ -factor in a semiconductor on the band-gap: as the band-gap decreases, the  $g$ -factor becomes increasingly less than the bare electron  $g$ -factor of 2.

Further control over the energy level structure and the spin dynamics in colloidal QDs can be gained by layering different materials within a single nanocrystal. By embedding layers with a small bandgap between layers with larger bandgap, one creates a potential well for electrons and holes in the shape of a spherical shell. Such structures are known as quantum dot quantum wells (QDQWs) (Eychmuller et al., 1993; Mews et al., 1994; Battaglia et al., 2003; Battaglia et al., 2005). Spin dynamics have been investigated in a series of QDQWs consisting of a high bandgap CdS core, surrounded by a low bandgap CdSe shell, and a CdS cap, shown schematically in Figure 25a.

In the radial direction, the conduction and valence band profile of the QDQW (Figure 25b) consists of a potential well in the CdSe shell region. As the width of the shell is varied, the quantum confinement changes accordingly. This is seen in the photoluminescence from a series of QDQWs with different CdSe shell widths, shown in Figure 25c. The spin dynamics are measured using TRFR and show typical coherent spin precession. The  $g$ -factors extracted from the TRFR measurements (Figure 25d) show the same dependence on shell width (Berezovsky et al., 2005) as expected for the change in quantum confinement in the shell. This sort of band-structure engineering allows for control over the energy level spectrum of a QD, and also allows for the possibility of coupling multiple shells within a single nanocrystal heterostructure.

The properties of colloidal QDs can be varied in a number of ways through molecular functionalization of the surface of the nanocrystals. For example, the nanocrystals can be bound to specific sites (e.g., onto a DNA scaffold (Warner and Hutchinson, 2003)), the luminescence can be quenched or shifted in energy (Leatherdale and Bawendi, 2004; Wuister et al., 2004), or charge transport between nanocrystals can be enhanced or suppressed (Morgan et al., 2002). In the realm of spin physics, it has been found that electron spins can be coherently transferred between QDs via molecular bridges (Ouyang and Awschalom, 2003).

In these measurements, samples were prepared by alternately dipping a substrate into a solution containing CdSe QDs, and another containing the linking

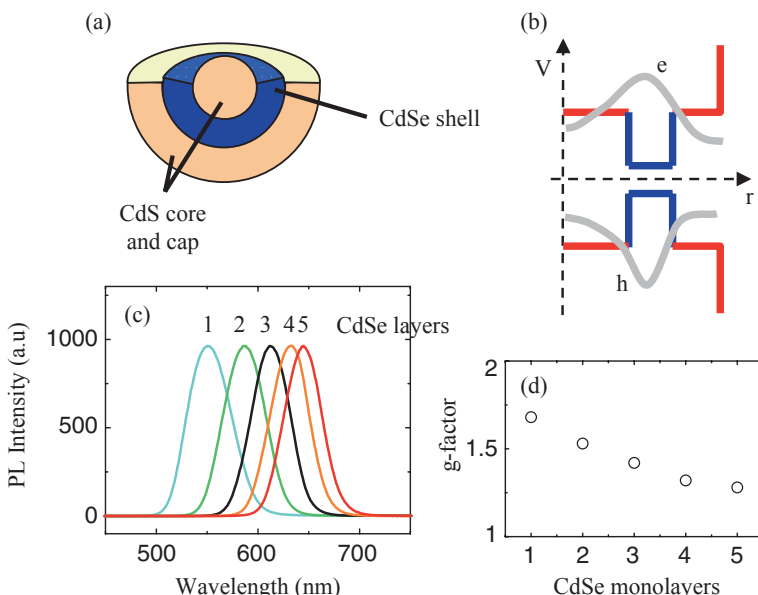


Figure 25. (a) Cut-away schematic of a QDQW with a single CdSe shell. (b) Illustration of the radial conduction and valence band profiles with electron and hole wavefunctions confined in the shell. (c) Photoluminescence (normalized) of QDQWs for various shell thicknesses. (d)  $g$ -factor of QDQWs as a function of shell thickness. Data originally presented in Berezovsky, et al. (2005).

molecules (1,4-benzenedimethanethiol). Two sizes of QDs were used, referred to as A (3.4 nm diameter) and B (7.0 nm diameter). Samples were fabricated with all A-type QDs, all B-type QDs, or a mixture of the two, and were measured using nondegenerate TRFR.

In samples containing all A or all B QDs, typical spin precession is observed in an applied magnetic field, with distinct  $g$ -factors for A and B due to the difference in size (Figures 26a and 26b). If either the pump or probe is tuned to an energy below the absorption edge of the QDs, no signal is observed. When the pump is below the absorption edge, the light is not absorbed, and no carriers are injected. When the probe is at an energy below the absorption edge, the Faraday effect is not present.

The situation is different in a sample with molecularly linked A and B QDs. In this case, the pump can be placed at an energy above the absorption edge of the larger, B QDs, but below the absorption edge of the smaller, A QDs. In the absence of the molecular linkers, one would not expect to see spin precession due to the A-type QDs, since spin injection cannot occur. However, with the molecular linker connecting A and B QDs, spin precession from both A and B  $g$ -factors is observed when probing above the absorption edge of both QD sizes (Figure 26c). This implies that spins are pumped into the larger QDs, and then are transferred to the smaller dots.

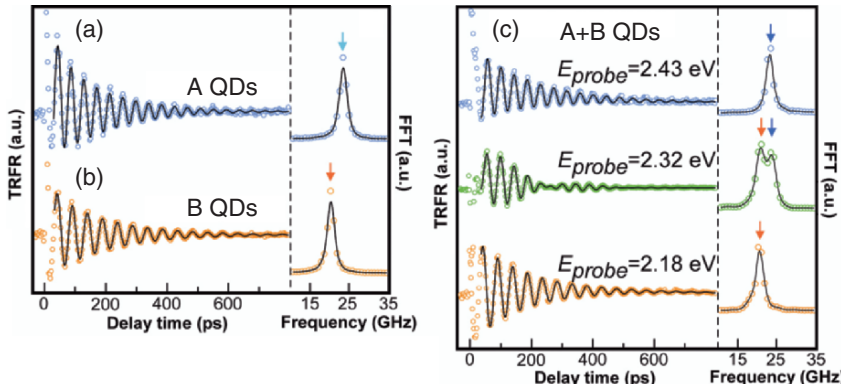


Figure 26. (a) Spin precession in 3.4 nm (A) QDs. (b) Spin precession in 7.0 nm (B) QDs. (c) Spin precession in molecularly linked A and B QDs, with spin injection only into the B QDs. At low (high) probe energy, only the B (A) precession frequency is observed. At intermediate probe energy, precession is observed in both QD sizes. Data originally presented in Berezovsky, et al. (2005).

These results can be understood in terms of tunneling between two asymmetric coupled potential wells (Meier et al., 2004). The molecules used as the linkers contain an extended pi-orbital that may facilitate the tunnel coupling of the two QDs. The efficiency of the spin transfer is seen to increase substantially with increasing temperature, which may be explained by the thermal motion of the linker molecules (Chen and Reed, 2002).

### Acknowledgments

We would like to thank DARPA, NSF, ONR, and AFOSR for financial support. N. P. S. thanks the Fannie and John Hertz Foundation.

### References

- Abragam, A. (1961) *The Principles of Magnetic Resonance*, Clarendon.
- Aronov, A. G. and Lyanda-Geller, Y. B. (1989) Nuclear electric resonance and orientation of carrier spins by an electric field, *JETP Lett.* **50**, 431.
- Aronov, A. G., Lander-Geller, Y. B., and Pikus, G. E. (1991) The spin polarization of electrons due to the electric current, *Sov. Phys. JETP* **73**, 537.
- Austing, D. G., Honda, T., Muraki, K., Tokura, Y., and Tarucha, S. (1998) Quantum dot molecules, *Physica B* **249–251**, 206.
- Awschalom, D. D., Halbout, J.-M., von Molnar, S., Siegrist, T., and Holtzberg, F. (1985) Dynamic spin organization in dilute magnetic systems, *Phys. Rev. Lett.* **55**, 1128.
- Awschalom, D. D., Loss, D., and Samarth, N. (eds.) (2002) *Semiconductor Spintronics and Quantum Computation*, Springer.
- Barnes, C. H. W., Shilton, J. M., and Robinson, A. M. (2000) Quantum computation using electrons trapped by surface acoustic waves, *Phys. Rev. B* **62**, 8410.

- Battaglia, D., Li, J. J., Wang, Y., and Peng, X. (2003) Colloidal two-dimensional systems: CdSeq quantum shells and wells, *Angew. Chem. Int. Ed.* **42**, 5035.
- Battaglia, D., Blackman, B., and Peng, X. (2005) Coupled and decoupled dual quantum systems in one semiconductor nanocrystal, *J. Am. Chem. Soc.* **127**, 10889.
- Bauer, G., Tserkovnyak, Y., Brataas, A., Ren, J., Xiz, K., Zwierzycki, M., and Kelly, P. (2005) Spin accumulation and decay in magnetic Schottky barriers, *Phys. Rev. B* **72**, 155304.
- Baumberg, J. J., Awschalom, D. D., Samarth, N., Luo, H., and Furdyna, J. K. (1994) Spin beats and dynamical magnetization in quantum structures, *Phys. Rev. Lett.* **72**, 717.
- Berezovsky, J., Ouyang, M., Meier, F., Awschalom, D. D., Battaglia, D., and Peng, X. (2005) Spin dynamics and level structure of quantum-dot quantum wells, *Phys. Rev. B* **71**, 081309(R).
- Bir, G. L., Aronov, A. G., and Pikus, G. E. (1976) Spin relaxation of electrons due to scattering by holes, *Sov. Phys. JETP* **42**, 705.
- Bychkov, Y. A. and Rashba, E. I. (1984) Oscillatory effects and the magnetic susceptibility of carriers in inversion layers, *J. Phys. C* **17**, 6039.
- Chen, J. M. and Reed, M. A. (2002) Electronic transport of molecular systems, *Chem. Phys.* **281**, 127.
- Ciuti, C., McGuire, J. P., and Sham, L. J. (2002) Spin polarization of semiconductor carriers by reflection off a ferromagnet, *Phys. Rev. Lett.* **89**, 156601.
- Crooker, S. A., Awschalom, D. D., Baumberg, J. J., Flack, F., and Samarth, N. (1997) Optical spin resonance and transverse spin relaxation in magnetic semiconductor quantum wells, *Phys. Rev. B* **56**, 7574.
- Crooker, S. A., Furis, M., Lou, X., Adelmann, C., Smith, D. L., Palmstrom, C. J., and Crowell, P. A. (2005) Imaging spin transport in lateral ferromagnet/semiconductor structures, *Science* **309**, 2191.
- Dresselhaus, G. (1955) Spin-orbit coupling effects in zinc blende structures, *Phys. Rev.* **100**, 580.
- D'yakonov, M. I. and Perel, V. I. (1971) Spin orientation of electrons associated with interband absorption of light in semiconductors, *Sov. Phys. JETP* **33**, 1053.
- Edelstein, V. M. (1990) Spin polarization of conduction electrons induced by electric current in two-dimensional asymmetric electron systems, *Solid State Commun.* **73**, 233.
- Elliot, R. J. (1954) Theory of the effect of spin-orbit coupling on magnetic resonance in some semiconductors, *Phys. Rev.* **96**, 266.
- Engel, H.-A., Halperin, B. I., and Rashba, E. I. (2005) Theory of spin Hall conductivity in n-doped GaAs, *Phys. Rev. Lett.* **95**, 166605.
- Epstein, R. J., Malajovich, I., Kawakami, R. K., Chye, Y., Hanson, M., Petroff, P. M., Gossard, A. C., and Awschalom, D. D. (2002) Spontaneous spin coherence in n-GaAs produced by ferromagnetic proximity polarization, *Phys. Rev. B* **65**, 121202(R).
- Epstein, R. J., Stephens, J., Hanson, M., Chye, Y., Gossard, A. C., Petroff, P. M., and Awschalom, D. D. (2003) Voltage control of nuclear spin in ferromagnetic Schottky diodes, *Phys. Rev. B* **68**, 041305.
- Eychmuller, A., Mews, A., and Weller, H. (1993) A quantum dot quantum well: CdS/HgS/CdS, *Chem. Phys. Lett.* **208**, 59.
- Faraday, M. (1846) Experimental researches in electricity, *Philosophical Transactions R. Soc. London* **136**, 1.
- Galitski, V. M., Burkov, A. A., and Sarma, S. D. (2006) Boundary conditions for spin diffusion, cond-mat/0601677 (unpublished).
- Ghosh, S., Stern, N. P., Maertz, B., Awschalom, D. D., Xiang, G., Zhu, M. and Samarth, N. (2006) Internal magnetic field in thin ZnSe epilayers, *Appl. Phys. Lett.* **89**, 242116.
- Gupta, J. A., Peng, X., Alivisatos, A. P., and Awschalom, D. D. (1999) Spin coherence in semiconductor quantum dots, *Phys. Rev. B* **59**, R10421.

- Gupta, J. A., Awschalom, D. D., Efros, A. L., and Rodina, A. V. (2002) Spin dynamics in semiconductor nanocrystals, *Phys. Rev. B* **66**, 125307.
- Hammar, P. R., Bennet, B. R., Yang, M. J., and Johnson, M. (1999) Observation of spin injection at a ferromagnet-semiconductor interface, *Phys. Rev. Lett.* **83**, 203.
- Hirsch, J. E. (1999) Spin Hall effect, *Phys. Rev. Lett.* **83**, 1834.
- Jain, S. C., Willander, M., and Maes, H. (1996) Stresses and strains in epilayers, stripes and quantum structures of III-V compound semiconductors, *Semicond. Sci. Technol.* **11**, 641.
- Jiang, X., Wang, R., van Dijken, S., Shelby, R., Macfarlane, R., Solomon, G. S., Harris, J., and Parkin, S. S. P. (2003) Optical detection of hot-electron spin injection into GaAs from a magnetic tunnel transistor source, *Phys. Rev. Lett.* **90**, 256603.
- Kane, B. E. (1998) A silicon-based nuclear spin quantum computer, *Nature* **393**, 133.
- Kato, Y. K., Myers, R. C., Gossard, A. C., and Aschwalom, D. D. (2003) Gigahertz electron spin manipulation using voltage-controlled g-tensor modulation, *Science* **299**, 1201.
- Kato, Y. K., Myers, R. C., Gossard, A. C., and Aschwalom, D. D. (2004a) Coherent spin manipulation without magnetic fields in strained semiconductors, *Nature* **427**, 50.
- Kato, Y. K., Myers, R. C., Gossard, A. C., and Awschalom, D. D. (2004b) Current-induced spin polarization in strained semiconductors, *Phys. Rev. Lett.* **93**, 176601.
- Kato, Y. K., Myers, R. C., Gossard, A. C., and Awschalom, D. D. (2004c) Observation of the spin Hall effect in semiconductors, *Science* **306**, 1910.
- Kawakami, R. K., Kato, Y., Hanson, M., Malajovich, I., Stephens, J. M., Johnston-Halperin, E., Salis, G., Gossard, A. C., and Awschalom, D. D. (2001) Ferromagnetic imprinting of nuclear spins in semiconductors, *Science* **294**, 131.
- Khaetskii, A. V., Loss, D., and Glazman, L. (2002) Electron spin decoherence in quantum dots due to interaction with nuclei, *Phys. Rev. Lett.* **88**, 186802.
- Kikkawa, J. M. and Awschalom, D. D. (1998) Resonant spin amplification in n-type GaAs, *Phys. Rev. Lett.* **80**, 4313.
- Kikkawa, J. M. and Awschalom, D. D. (1999) Lateral drag of spin coherence in gallium arsenide, *Nature* **397**, 139.
- Kikkawa, J. M., Smorchkova, I. P., Samarth, N., and Awschalom, D. D. (1997) Room-temperature spin memory in two-dimensional electron gases, *Science* **277**, 1284.
- Lampel, G. (1968) Nuclear dynamic polarization by optical electronic saturation and optical pumping in semiconductors, *Phys. Rev. Lett.* **20**, 491.
- Leatherdale, C. A. and Bawendi, M. G. (2004) Observation of solvatochromism in CdSe colloidal quantum dots, *Phys. Rev. B* **63**, 165315.
- Leonard, D., Krishnamurthy, K., Reeves, C. M., Denbaars, S. P., and Petroff, P. M. (1993) Direct formation of quantum-sized dots from uniform coherent islands of InGaAs on GaAs surfaces, *Appl. Phys. Lett.* **63**, 3203.
- Levitov, L. S., Nazarov, Y. V., and Eliashberg, G. M. (1985) Magnetoelectric effects in conductors with mirror isomer symmetry, *Sov. Phys. JETP* **61**, 133.
- Levy, J. (2001) Quantum-information processing with ferroelectrically coupled quantum dots, *Phys. Rev. A* **64**, 052306.
- Loss, D. and DiVincenzo, D. P. (1998) Quantum computation with quantum dots, *Phys. Rev. A* **57**, 120.
- Lou, X., Adelmann, C., Furis, M., Crooker, S. A., Palmstrom, C. J., and Crowell, P. A. (2006) Electrical detection of spin accumulation at a ferromagnet–semiconductor interface, *Phys. Rev. Lett.* **96**, 176603.
- Manna, L., Scher, E. F., and Alivisatos, A. P. (2000) Synthesis of soluble and processable rod-, arrow-, teardrop-, and tetrapod-shaped CdSe nanocrystals, *J. Am. Chem. Soc.* **122**, 12700.

- McGuire, J. P., Ciuti, C., and Sham, L. J. (2003) Theory of spin orientation of semiconductor carriers at a ferromagnetic interface, cond-mat/0302088 v1 (unpublished).
- Meier, F. and Awschalom, D. D. (2005) Faraday rotation spectroscopy of quantum-dot quantum wells, *Phys. Rev. B* **71**, 205315.
- Meier, F. and Zakharchenya, B. P. (eds.) (1984) *Optical Orientation*, Elsevier.
- Meier, F., Cerletti, V., Gywata, O., Loss, D., and Awschalom, D. D. (2004) Electronic transport in films of colloidal CdSe nanocrystals, *Phys. Rev. B* **69**, 195315.
- Merkulov, I. A., Efros, A. L., and Rosen, M. (2002) Electron spin relaxation by nuclei in semiconductor quantum dots, *Phys. Rev. B* **65**, 205309.
- Mews, A., Eychmuller, A., Giersig, M., Schoos, D., and Weller, H. (1994) Preparation, characterization, and photophysics of the quantum dot quantum well system cadmium sulfide/mercury sulfide/cadmium sulfide, *J. Phys. Chem.* **98**, 934.
- Morgan, N. Y., Leatherdale, C. A., Drndić, M., Jarosz, M. V., Kastner, M. A., and Bawendi, M. (2002) Electronic transport in films of colloidal CdSe nanocrystals, *Phys. Rev. B* **66**, 075339.
- Motsnyi, V. F., Boeck, J. D., Das, J., Roy, W. V., Borghs, G., Goovaerts, E., and Safarov, V. I. (2002) Electrical spin injection in a ferromagnet/tunnel barrier/semiconductor heterostructure, *Appl. Phys. Lett.* **81**, 265.
- Murakami, S., Nagaosa, N., and Zhang, S. C. (2003) Dissipationless quantum spin current at room temperature, *Science* **301**, 1348.
- Murray, C. B., Norris, D. J., and Bawendi, M. G. (1993) Synthesis and characterization of nearly monodisperse CdE (E = sulfur, selenium, tellurium) semiconductor nanocrystallites, *J. Am. Chem. Soc.* **115**, 8706.
- Ostreich, T., Schonhammer, K., and Sham, L. J. (1995) Theory of spin beatings in the Faraday rotation of semiconductors, *Phys. Rev. Lett.* **75**, 2554.
- Ouyang, M. and Awschalom, D. D. (2003) Coherent spin transfer between molecularly bridged quantum dots, *Science* **301**, 1074.
- Ramsteiner, M., Hao, H. Y., Kawaharazuka, A., Zhu, H. J., Kastner, M., Hey, R., Daueritz, L., Grahn, H. T., and Ploog, K. H. (2002) Electrical spin injection from ferromagnetic MnAs metal layers into GaAs, *Phys. Rev. B* **66**, 081304(R).
- Rashba, E. I. (2004) Spin currents, spin populations, and dielectric function of noncentrosymmetric semiconductors, *Phys. Rev. B* **70**, 161201(R).
- Shi, J., Zhang, P., Xiao, D., and Niu, Q. (2006) Proper definition of spin current in spin-orbit coupled systems, *Phys. Rev. Lett.* **96**, 076604.
- Sih, V., Myers, R. C., Kato, Y. K., Lau, W. H., Gossard, A. C., and Awschalom, D. D. (2005) Spatial imaging of the spin Hall effect and current-induced polarization in two-dimensional electron gases, *Nature Phys.* **1**, 31.
- Sih, V., Knotz, H., Stephens, J., Horowitz, V. R., Gossard, A. C., and Awschalom, D. D. (2006a) Mechanical control of spin-orbit splitting in GaAs and In<sub>0.04</sub>Ga<sub>0.96</sub>As epilayers, *Phys. Rev. B* **73**, 241316(R).
- Sih, V., Lau, W., Myers, R. C., Horowitz, V. R., Gossard, A. C., and Awschalom, D. D. (2006b) Generating spin currents in semiconductors with the spin Hall effect, *Phys. Rev. Lett.* **97**, 096605.
- Silov, A. Y., Blajnov, P. A., Wolter, J. H., Hey, R., Ploog, K. H., and Averkiev, N. S. (2004) Current-induced spin polarization at a single heterojunction, *Appl. Phys. Lett.* **85**, 5929.
- Sinova, J., Culcer, D., Niu, Q., Sinitsyn, N. A., Jungwirth, T., and MacDonald, A. H. (2004) Universal intrinsic spin Hall effect, *Phys. Rev. Lett.* **92**, 126603.
- Stephens, J., Kawakami, R. K., Berezovsky, J., Hanson, M., Shepherd, D. P., Gossard, A. C., and Awschalom, D. D. (2003) Spatial imaging of magnetically patterned nuclear spins in GaAs, *Phys. Rev. B* **68**, 041307(R).

- Stephens, J., Berezovsky, J., McGuire, J. P., Sham, L. J., Gossard, A. C., and Awschalom, D. D. (2004) Spin accumulation in forward-biased MnAs/GaAs schottky diodes, *Phys. Rev. Lett.* **93**, 097602.
- Stern, N. P., Poggio, M., Bartl, M. H., Hu, E. L., Stucky, G. D., and Awschalom, D. D. (2005) Spin dynamics in electrochemically charged CdSe quantum dots, *Phys. Rev. B* **72**, 161303.
- Stern, N. P., Ghosh, S., Xiang, G., Zhu, M., Samarth, N., and Awschalom, D. D. (2006) Current-induced polarization and the spin Hall effect at room temperature, *Phys. Rev. Lett.* **97**, 126603.
- Strand, J., Schultz, B. D., Isakovic, A. F., Palmstrom, C. J., and Crowell, P. A. (2003) Dynamic nuclear polarization by electrical spin injection in ferromagnet–semiconductor heterostructures, *Phys. Rev. Lett.* **91**, 036602.
- Tse, W.-K. and Sarma, S. D. (2006) Spin Hall effect in doped semiconductor structures, *Phys. Rev. Lett.* **96**, 056601.
- Tse, W.-K., Fabian, J., Zutic, I., and Sarma, S. D. (2005) Spin accumulation in the extrinsic spin Hall effect, *Phys. Rev. B* **72**, 241303(R).
- Vorobev, L. E., Ivchenko, E. L., Pikus, G. E., Farbshtain, I. I., Shalygin, V. A., and Shturbin, A. V. (1979) Optical activity in tellurium induced by a current, *JETP Lett.* **29**, 441.
- Vrijen, R., Yablonovitch, E., Wang, K., Jiang, H. W., Balandin, A., Roychowdhury, V., Mor, T., and DiVincenzo, D. (2000) Electron-spin-resonance transistors for quantum computing in silicon-germanium heterostructures, *Phys. Rev. A* **62**, 012306.
- Warner, M. G. and Hutchinson, J. E. (2003) Linear assemblies of nanoparticles electrostatically organized on DNA scaffolds, *Nature Mat.* **2**, 272.
- Winkler, R. (ed.) (2003) *Spin-orbit Coupling Effects in Two-Dimensional Electron and Hole Systems*, Springer.
- Wolf, S. A., Awschalom, D. D., Buhrman, R. A., Daughton, J. M., von Molnár, S., Roukes, M. L., Chtchelkanova, A. Y., and Treger, D. M. (2001) Spintronics: a spin-based electronics vision for the future, *Science* **294**, 1488.
- Wuister, S. F., Donega, C., and Meijerink, A. (2004) Influence of thiol capping on the exciton luminescence and decay kinetics of CdTe and CdSe quantum dots, *J. Phys. Chem. B* **108**, 17393.
- Yu, P. and Cardona, M. (1996) *Fundamentals of Semiconductors*, Springer.
- Zhang, S. (2000) Spin Hall effect in the presence of spin diffusion, *Phys. Rev. Lett.* **85**, 393.
- Zhu, H. J., Ramsteiner, M., Kostial, H., Wassermeier, M., Schnherr, H.-P., and Ploog, K. H. (2001) Room-temperature spin injection from Fe into GaAs, *Phys. Rev. Lett.* **87**, 016601.

# QUANTUM COMPUTING WITH SUPERCONDUCTORS I: ARCHITECTURES

MICHAEL R. GELLER\* and EMILY J. PRITCHETT†

*Department of Physics, University of Georgia, Athens, Georgia 30602, USA*

ANDREW T. SORNBORGER‡

*Department of Mathematics, University of Georgia, Athens, Georgia 30602, USA*

F. K. WILHELM§

*Department Physik, Center for Nanoscience, and Arnold Sommerfeld Center for theoretical physics, Ludwig-Maximilians-Universität, 80333 München, Germany*

**Abstract:** Josephson junctions have demonstrated enormous potential as qubits for scalable quantum computing architectures. Here we discuss the current approaches for making multi-qubit circuits and performing quantum information processing with them.

**Keywords:** spintronics, quantum dots, nuclear spin, spin Hall effect, magnetic semiconductors

## 1 Introduction

Macroscopic quantum behavior in a Josephson junction (JJ) was first demonstrated in the mid-1980s by John Clarke's group at UC Berkeley (Devoret et al., 1985; Martinis et al., 1985, 1987; Clarke et al., 1988). These experiments used a superconducting device referred to as a large area, current-biased JJ, which would later become the phase qubit. Beginning in the mid-1990s the group of James Lukens at SUNY Stony Brook (Rouse et al., 1995; Friedman et al., 2000) and a collaboration between the Delft University group of Hans Mooij and the MIT group of Terry Orlando (Mooij et al., 1999; van der Wal et al., 2000) demonstrated macroscopic quantum behavior in superconducting loops interrupted by one or more JJs (called superconducting quantum interference devices, or SQUIDS), what would later become flux qubits. And in the late 1990s the group of Yasunobu Nakamura at NEC in Tsukuba (Nakamura et al., 1997, 1999) developed the first

---

\*mgeller@uga.edu

†epritchett@hal.physast.uga.edu

‡ats@math.uga.edu

§Present address: Physics Department and Institute for Quantum Computing, University of Waterloo, Waterloo, Ontario N2L 3G1, Canada; fwilhelm@iqc.ca

Cooper-pair box or charge qubit. Many of the earlier experiments were motivated by seminal theoretical work of Caldeira and Leggett (1981, 1983).

The modern era of superconducting quantum computation began in 2002. That year, the group of Siyuan Han at the University of Kansas and the group of John Martinis, then at NIST Boulder and currently at UC Santa Barbara, independently showed that long-lived quantum states in a current-biased JJ can be controllably prepared, manipulated, and subsequently measured (Martinis et al., 2002; Yu et al., 2002). This same year, the group of Michel Devoret, then at the CEA in Saclay and currently at Yale University, demonstrated similar quantum control using a Cooper-pair box (Vion et al., 2002). These experiments suggest that JJ-based qubits can be used as the building blocks of a solid-state quantum computer, creating a tremendous interest in this intrinsically scalable approach. An impressive list of additional experimental achievements soon followed, including the demonstration of two-qubit quantum logic (Yamamoto et al., 2003).

In this chapter we will review the current approaches for making multi-qubit systems. For a more detailed discussion of single qubits we refer to the excellent review by Makhlin et al., (2001). Also, a recent introductory account of the field has been given by You and Nori (2005). The approach we follow here is to construct circuit models for the basic qubits and coupled-qubit architectures. Many designs have been proposed, but only the simplest have been implemented experimentally to date.

After reviewing in section 2 the basic phase, flux, and charge qubits, we discuss three broad classes of coupling schemes. The simplest class uses fixed linear coupling elements, such as capacitors or inductors, and is discussed in section 3. The principal effect of fixed, weak couplings is to lift degeneracies of the uncoupled qubit pair. However, because such interactions are always present (always turned on), the uncoupled qubit states, which are often used as computational basis states, are not stationary. A variety of approaches have been proposed to overcome this shortcoming. In section 4 we discuss tunable couplings that allow the interactions of section 3 to be tuned, ideally between “on” and “off” values. A related class of *dynamic* couplings is discussed in section 5, which make use of coupling elements that themselves have active internal degrees of freedom. They act like tunable coupling elements, but also have additional functionality coming from the ability to excite the internal degrees of freedom. Examples of this are resonator-based couplings, which we discuss in some detail.

## 2 The Basic Qubits: Phase, Flux, and Charge

The primitive building block for all the qubits is the JJ shown in Figure 1. The low-energy dynamics of this system is governed by the phase difference  $\varphi$  between the condensate wave functions or order parameters on the two sides of the insulating

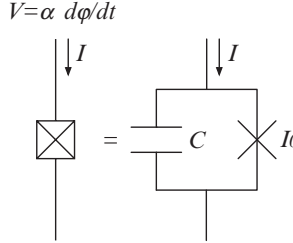


Figure 1. Circuit model for a current-biased JJ, neglecting dissipation. Here  $\alpha \equiv \hbar/2e$

barrier. The phase difference is an operator canonically conjugate to the Cooper-pair number difference  $N$ , according to<sup>1</sup>

$$[\varphi, N] = i. \quad (1)$$

The low-energy eigenstates  $\psi_m(\varphi)$  of the JJ can be regarded as probability-amplitude distributions in  $\varphi$ . As will be explained below, the potential energy  $U(\varphi)$  of the JJ is manipulated by applying a bias current  $I$  to the junction, providing an external control of the quantum states  $\psi_m(\varphi)$ , including the qubit energy-level spacing  $\Delta\epsilon$ . The crossed box in Figure 1 represents a “real” JJ. The cross alone represents a nonlinear element that satisfies the Josephson equations<sup>2</sup>

$$I = I_0 \sin \varphi \quad \text{and} \quad V = \alpha \dot{\varphi}, \quad (2)$$

with critical current  $I_0$ . The capacitor accounts for junction charging.<sup>3</sup> A single JJ is characterized by two energy scales, the Josephson coupling energy

$$E_J \equiv \frac{\hbar I_0}{2e}, \quad (3)$$

where  $e$  is the magnitude of the electron charge, and the Cooper-pair charging energy

$$E_c \equiv \frac{(2e)^2}{2C}, \quad (4)$$

with  $C$  the junction capacitance. For example,

$$E_J = 2.05 \text{ meV} \times I_0 [\mu\text{A}] \quad \text{and} \quad E_c = \frac{320 \text{ neV}}{C [\text{pF}]}, \quad (5)$$

---

<sup>1</sup>We define the momentum  $P$  to be canonically conjugate to  $\varphi$ , and  $N \equiv P/\hbar$ . In the phase representation,  $N = -i \frac{\partial}{\partial \varphi}$ .

<sup>2</sup> $\alpha \equiv \hbar/2e$ .

<sup>3</sup>This provides a simple mean-field treatment of the *inter*-condensate electron-electron interaction neglected in the standard tunneling Hamiltonian formalism on which the Josephson equations are based.

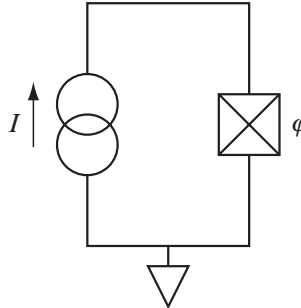


Figure 2. Basic phase qubit circuit

where  $I_0[\mu\text{A}]$  and  $C[\text{pF}]$  are the critical current and junction capacitance in microamperes and picofarads, respectively. In the regimes of interest to quantum computation,  $E_J$  and  $E_c$  are assumed to be larger than the thermal energy  $k_B T$  but smaller than the superconducting energy gap  $\Delta_{\text{sc}}$ , which is about  $180 \mu\text{eV}$  in Al. The relative size of  $E_J$  and  $E_c$  vary, depending on the specific qubit implementation.

## 2.1 PHASE QUBIT

The basic phase qubit consists of a JJ with an external current bias, and is shown in Figure 2. The classical Lagrangian for this circuit is

$$L_{\text{JJ}} = \frac{1}{2} M \dot{\varphi}^2 - U, \quad M \equiv \frac{\hbar^2}{2E_c}. \quad (6)$$

Here

$$U \equiv -E_J(\cos \varphi + s \varphi), \quad \text{with} \quad s \equiv \frac{I}{I_0} \quad (7)$$

is the effective potential energy of the JJ, shown in Figure 3. Note that the “mass”  $M$  in (6) actually has dimensions of mass  $\times$  length<sup>2</sup>. The form (6) results from equating the sum of the currents flowing through the capacitor and ideal Josephson element to  $I$ . The phase qubit implementation uses  $E_J \gg E_c$ .

According to the Josephson equations, the classical canonical momentum  $P = \frac{\partial L}{\partial \dot{\varphi}}$  is proportional to the charge  $Q$  or to the number of Cooper pairs  $Q/2e$  on the capacitor according to  $P = \hbar Q/2e$ . The quantum Hamiltonian can then be written as

$$H_{\text{JJ}} = E_c N^2 + U, \quad (8)$$

where  $\varphi$  and  $N$  are operators satisfying (1). Because  $U$  depends on  $s$ , which itself depends on time,  $H_{\text{JJ}}$  is generally time-dependent. The low lying stationary states when  $s \lesssim 1$  are shown in Figure 4. The two lowest eigenstates  $|0\rangle$  and  $|1\rangle$  are used to make a qubit.  $\Delta\epsilon$  is the level spacing and  $\Delta U$  is the height of the barrier.

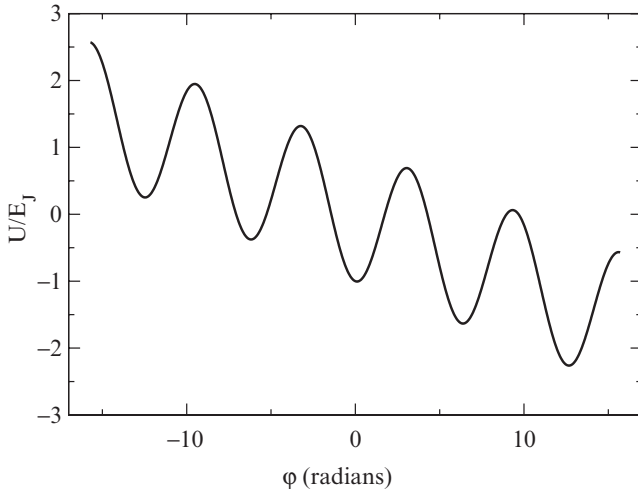


Figure 3. Effective potential for a current-biased JJ. The slope of the cosine potential is  $s$ . The potential is harmonic for the qubit states unless  $s$  is very close to 1

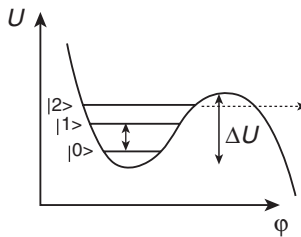


Figure 4. Effective potential in the anharmonic regime, with  $s$  very close to 1. State preparation and readout are carried out in this regime

A useful “spin  $\frac{1}{2}$ ” form of the phase qubit Hamiltonian follows by projecting (8) to the qubit subspace. There are two natural ways of doing this. The first is to use the basis of the  $s$ -dependent eigenstates, in which case

$$H = -\frac{\hbar\omega_p}{2} \sigma^z, \quad (9)$$

where

$$\omega_p \equiv \omega_{p0}(1-s^2)^{\frac{1}{4}} \quad \text{and} \quad \omega_{p0} \equiv \sqrt{2E_c E_J}/\hbar. \quad (10)$$

The  $s$ -dependent eigenstates are called instantaneous eigenstates, because  $s$  is usually changing with time. The time-dependent Schrödinger equation in this basis contains additional terms coming from the time-dependence of the basis states themselves, which can be calculated in closed form in the harmonic limit (Geller and Cleland, 2005). These additional terms account for all nonadiabatic effects.

The second spin form uses a basis of eigenstates with a fixed value of bias,  $s_0$ . In this case

$$H = -\frac{\hbar\omega_p(s_0)}{2}\sigma^z - \frac{E_J\ell}{\sqrt{2}}(s - s_0)\sigma^x, \quad (11)$$

where

$$\ell \equiv \ell_0(1 - s_0)^{-\frac{1}{8}} \quad \text{and} \quad \ell_0 \equiv \left(\frac{2E_c}{E_J}\right)^{\frac{1}{4}}. \quad (12)$$

This form is restricted to  $|s - s_0| \ll 1$ , but it is very useful for describing rf pulses.

The angle  $\ell$  characterizes the width of the eigenstates in  $\varphi$ . For example, in the  $s_0$ -eigenstate basis (and with  $s_0$  in the harmonic regime), we have<sup>4</sup>

$$\varphi = x_{01}\sigma^x + \arcsin(s_0)\sigma^0, \quad \text{with} \quad x_{mm'} \equiv \langle m|\varphi|m'\rangle. \quad (13)$$

Here  $x_{mm'}$  is an effective dipole moment (with dimensions of angle, not length), and  $x_{01} = \ell/\sqrt{2}$ .

## 2.2 CHARGE QUBIT

In the charge qubit, the JJ current is provided capacitively, by changing the voltage  $V_g$  on a gate, as in Figure 5. In this case  $E_J \ll E_c$ , and the small capacitance is achieved by using a Cooper-pair box, which is a nanoscale superconducting island or quantum dot.

The Lagrangian and Hamiltonian for this system are

$$L = \frac{1}{2}\alpha^2(C + C_g)\dot{\varphi}^2 + E_J \cos \varphi - \alpha C_g V_g \dot{\varphi} \quad (14)$$

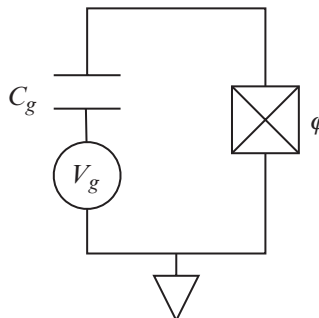


Figure 5. Basic charge qubit circuit. The upper wire constitutes the superconducting box or island

---

<sup>4</sup> $\sigma^0$  is the identity matrix.

and

$$H = E_c(N - N_g)^2 - E_J \cos \varphi, \quad \text{with} \quad E_c = \frac{(2e)^2}{2(C+C_g)}. \quad (15)$$

Here

$$N_g \equiv -\frac{C_g V_g}{2e} \quad (16)$$

is the gate charge, the charge qubit's control variable.

It is most convenient to use the charge representation here, defined by the Cooper-pair number eigenstates  $|n\rangle$  satisfying

$$N|n\rangle = n|n\rangle. \quad (17)$$

Because  $e^{i\varphi}|n\rangle = |n+1\rangle$ , the  $\cos \varphi$  term in (15) acts as a Cooper-pair tunneling operator. In the qubit subspace,

$$N - N_g = -(N_g - \frac{1}{2})\sigma^0 - \frac{1}{2}\sigma^z, \quad (18)$$

$$(N - N_g)^2 = (N_g - \frac{1}{2})\sigma^z + \text{const}, \quad (19)$$

$$\cos \varphi = \frac{1}{2}\sigma^z. \quad (20)$$

The charge qubit Hamiltonian can then be written in spin form in the  $\{|0\rangle, |1\rangle\}$  charge basis as

$$H = E_c(N_g - \frac{1}{2})\sigma^z - \frac{E_J}{2}\sigma^x, \quad (21)$$

or in the  $\{|+\rangle, |-\rangle\}$  basis of  $N_g = \frac{1}{2}$  eigenstates

$$|\pm\rangle \equiv \frac{|0\rangle \pm |1\rangle}{\sqrt{2}} \quad (22)$$

as

$$H = E_c \left( N_g - \frac{1}{2} \right) \sigma^x - \frac{E_J}{2} \sigma^z. \quad (23)$$

## 2.3 FLUX QUBIT

The flux qubit uses states of quantized circulation, or magnetic flux, in a SQUID ring. The geometry is illustrated in Figure 6. The current bias in this case is supplied by the circulating supercurrent. The total magnetic flux  $\Phi$  can be written as

$$\Phi = \Phi_x - cLI, \quad (24)$$

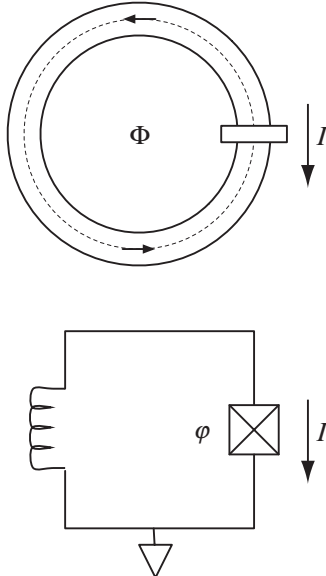


Figure 6. Basic rf-SQUID flux qubit and circuit model.  $\Phi$  is the total flux threading the ring. The dashed curve in the upper figure indicates the integration contour  $\Gamma$  used to derive condition (26). The coil in the lower figure has self-inductance  $L$

where  $\Phi_x$  is the external contribution and  $cLI$  is the self-induced component, with

$$I = \alpha C \dot{\varphi} + I_0 \sin \varphi \quad (25)$$

the circulating current and  $L$  the self-inductance.<sup>5</sup> The relations (24) and (25) determine  $\Phi$  given  $\varphi$ , but there is a second condition relating these quantities, namely

$$\frac{\Phi}{\Phi_{sc}} = \frac{\varphi}{2\pi} \bmod 1, \quad \text{with} \quad \Phi_{sc} \equiv \frac{hc}{2e}. \quad (26)$$

This second condition follows from the Meissner effect, which says that the current density in the interior of the ring vanishes, requiring the total vector potential  $\mathbf{A}$  to be proportional to the gradient of the phase of the local order parameter. It is obtained by integrating  $\mathbf{A}$  around the contour  $\Gamma$  in Figure 6.

The relation (24) then becomes

$$\alpha^2 C \ddot{\varphi} + E_J \sin \varphi + \frac{\hbar^2 \omega_{LC}^2}{2E_c} \left( \varphi - \frac{2\pi\Phi_x}{\Phi_{sc}} \right) = 0, \quad (27)$$

where

$$\omega_{LC} \equiv \frac{1}{\sqrt{LC}}. \quad (28)$$

---

<sup>5</sup> $L$  here is not to be confused with the Lagrangian.

This leads to the Lagrangian and Hamiltonian

$$L = \frac{1}{2} \alpha^2 C \dot{\varphi}^2 + E_J \cos \varphi - \frac{\hbar^2 \omega_{LC}^2}{4E_c} \left( \varphi - \frac{2\pi\Phi_x}{\Phi_{sc}} \right)^2 \quad (29)$$

and

$$H = E_c N^2 - E_J \cos \varphi + \frac{\hbar^2 \omega_{LC}^2}{4E_c} \left( \varphi - \frac{2\pi\Phi_x}{\Phi_{sc}} \right)^2. \quad (30)$$

The ring's self-inductance has added a quadratic contribution to the potential energy, centered at  $2\pi\Phi_x/\Phi_{sc}$ .

The control variable in the flux qubit is  $\Phi_x$ . By choosing

$$\frac{\Phi_x}{\Phi_{sc}} = \frac{1}{2} \bmod 1, \quad (31)$$

one produces the double-well potential shown in Figure 7. The condition (31) corresponds to the point of maximum frustration between the two directions of circulating supercurrent. By deviating slightly from the point (31), the energies of the  $|0\rangle$  and  $|1\rangle$  change, without changing the barrier height that controls the tunneling between the wells.

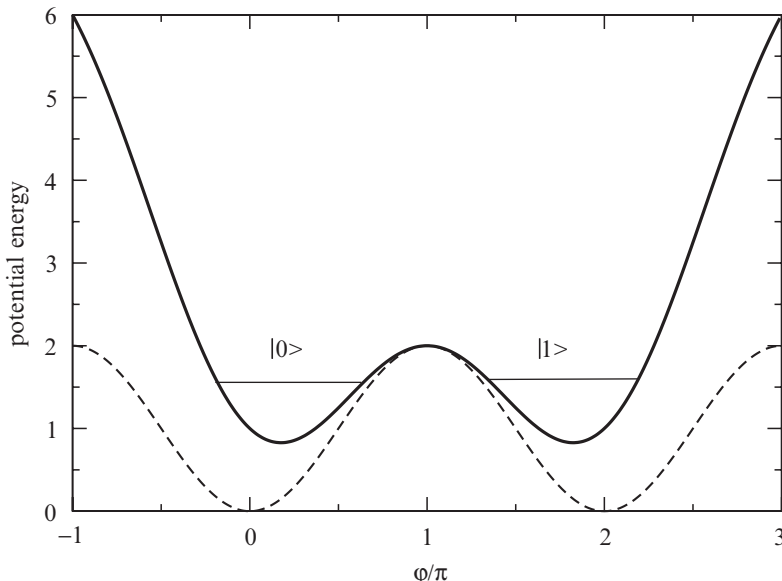


*Figure 7.* Double-well potential of the flux qubit. The dashed curve is the cosine potential of the JJ alone; the solid curve shows the modification caused by the self-inductance of the ring. The states  $|0\rangle$  and  $|1\rangle$  are that of circulating and counter-circulating supercurrent, which become degenerate at the maximal frustration point (31)

We can write the flux qubit Hamiltonian in spin form as

$$H = B_z \sigma^z + B_x \sigma^x, \quad (32)$$

where  $B_z$  and  $B_x$  are parameters that depend on the SQUID geometry and  $\Phi_x$ . In the simplest rf SQUID flux qubit discussed here,  $B_z$  characterizes the well asymmetry, and is tunable (via  $\Phi_x$ ), whereas  $B_x$  depends on the barrier height and is fixed by the value of  $E_J$ . However, below we will describe a modification that allows the barrier height to be tuned as well.

Hybrid charge-flux qubits have also been demonstrated, and have shown to be successful in reducing decoherence caused by interactions with the environment (Vion et al., 2002).

### 3 Fixed Linear Couplings

By fixed linear couplings we refer to coupling produced by electrically linear elements such as capacitors or inductors that lead to interaction Hamiltonians with fixed coupling strengths. In the cases usually considered, the coupling strengths are also weak, much smaller than the qubit level spacing, and we will assume that here as well. We discuss two prominent examples, capacitively coupled phase and charge qubits. For discussions of the third prominent example, inductively coupled flux qubits, we refer the reader to the literature (Mooij et al., 1999; Orlando et al., 1999; Makhlin et al., 2001; Massen van den Brink, 2005).

#### 3.1 CAPACITIVELY COUPLED PHASE QUBITS

Capacitively coupled phase qubits have been demonstrated by the University of Maryland group of Fred Wellstood (Berkley et al., 2003) and by the UC Santa Barbara group of John Martinis (McDermott et al., 2005). The architecture was discussed theoretically by Johnson et al. (2003), Blais et al. (2003) and Strauch et al. (2003).

Referring to Figure 8, the equations of motion for the two phase variables are<sup>6</sup>

$$\alpha^2(C_1 + C_{\text{int}})\ddot{\varphi}_1 + E_{J1}(\sin \varphi_1 - s_1) - \alpha^2 C_{\text{int}}\ddot{\varphi}_2 = 0, \quad (33)$$

$$\alpha^2(C_2 + C_{\text{int}})\ddot{\varphi}_2 + E_{J2}(\sin \varphi_1 - s_1) - \alpha^2 C_{\text{int}}\ddot{\varphi}_1 = 0, \quad (34)$$

and the Lagrangian is

$$L = \sum_i \left[ \frac{\alpha^2}{2}(C_i + C_{\text{int}})\dot{\varphi}_i^2 + E_{Ji}(\cos \varphi_i + s_i \varphi_i) \right] - \alpha^2 C_{\text{int}}\dot{\varphi}_1\dot{\varphi}_2. \quad (35)$$

---

<sup>6</sup> $\alpha \equiv \hbar/2e$ .

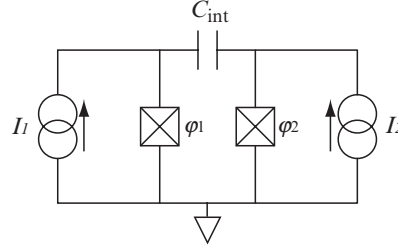


Figure 8. Capacitively coupled phase qubit circuit

To find the Hamiltonian, invert the capacitance matrix in

$$\begin{pmatrix} p_1 \\ p_2 \end{pmatrix} = \alpha^2 \begin{pmatrix} C_1 + C_{\text{int}} & -C_{\text{int}} \\ -C_{\text{int}} & C_2 + C_{\text{int}} \end{pmatrix} \begin{pmatrix} \dot{\varphi}_1 \\ \dot{\varphi}_2 \end{pmatrix}, \quad (36)$$

where the  $p_i$  are the canonical momenta. This leads to

$$H = \sum_i \left[ \frac{p_i^2}{2\alpha^2 \tilde{C}_i} - E_{Ji}(\cos \varphi_i + s_i \varphi_i) \right] + \frac{p_1 p_2}{\alpha^2 \tilde{C}_{\text{int}}}, \quad (37)$$

where

$$\tilde{C}_1 \equiv C_1 + (C_{\text{int}}^{-1} + C_2^{-1})^{-1}, \quad (38)$$

$$\tilde{C}_2 \equiv C_2 + (C_{\text{int}}^{-1} + C_1^{-1})^{-1}, \quad (39)$$

$$\tilde{C}_{\text{int}} \equiv C_1 C_2 (C_1^{-1} + C_2^{-1} + C_{\text{int}}^{-1})^{-1}. \quad (40)$$

This can be written as

$$H = \sum_i H_i + \delta H, \quad \delta H \equiv g' N_1 N_2, \quad (41)$$

where

$$g' \equiv \frac{(2e)^2}{\tilde{C}_{\text{int}}} \rightarrow 2 \left( \frac{C_{\text{int}}}{C} \right) E_c. \quad (42)$$

The arrow in (42) applies to the further simplified case of identical qubits and weak coupling.

The coupling constant  $g'$  defined in (42) is inconvenient, however, because the energy scale  $E_c$  appearing in (42) is too small. A better definition is

$$g \equiv \frac{g'}{2\ell_1 \ell_2} \rightarrow \left( \frac{C_{\text{int}}}{C} \right) \hbar \omega_p, \quad (43)$$

where  $\ell$  is the scale introduced in (12).

In the instantaneous basis, the spin form of the momentum operator is

$$N = p_{01} \begin{pmatrix} 0 & 1 \\ -1 & 0 \end{pmatrix}, \quad (44)$$

where

$$p_{01} \equiv \langle 0 | p | 1 \rangle = -\frac{i}{\sqrt{2}\ell}. \quad (45)$$

Then

$$H = \sum_i H_i + \delta H, \quad H_i = -\frac{\hbar\omega_p}{2} \sigma_i^z, \quad \delta H \equiv g \sigma_i^y \sigma_i^y. \quad (46)$$

In the uncoupled qubit basis  $\{|00\rangle, |01\rangle, |10\rangle, |11\rangle\}$ , the qubit–qubit interaction in terms of (43) is simply

$$\delta H = g \begin{pmatrix} 0 & 0 & 0 & -1 \\ 0 & 0 & 1 & 0 \\ 0 & 1 & 0 & 0 \\ -1 & 0 & 0 & 0 \end{pmatrix}. \quad (47)$$

Two-qubit quantum logic has not yet been demonstrated with this architecture. Methods for performing a controlled-Z and a modified swap gate have been proposed by Strauch et al. (2003), and four controlled-NOT implementations have also been proposed recently (Geller et al., 2006).

### 3.2 CAPACITIVELY COUPLED CHARGE QUBITS

A circuit for capacitively coupled charge qubits is given in Figure 9. This architecture has been demonstrated by Pashkin et al. (2003), and used to perform a CNOT by Yamamoto et al. (2003). This work is currently the most advanced in the field

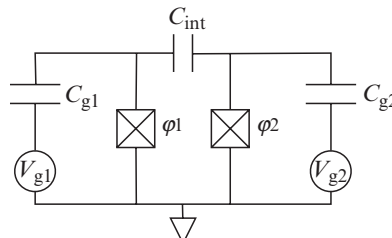


Figure 9. Capacitively coupled charge qubit circuit

of solid-state quantum information processing. The equations of motion for the two phases are<sup>7</sup>

$$\alpha^2(C_1 + C_{g1} + C_{\text{int}})\ddot{\varphi}_1 + E_{J1} \sin \varphi_1 - \alpha C_{g1} \dot{V}_{g1} - \alpha^2 C_{\text{int}} \dot{\varphi}_2 = 0, \quad (48)$$

$$\alpha^2(C_2 + C_{g2} + C_{\text{int}})\ddot{\varphi}_2 + E_{J2} \sin \varphi_2 - \alpha C_{g2} \dot{V}_{g2} - \alpha^2 C_{\text{int}} \dot{\varphi}_1 = 0, \quad (49)$$

and the Lagrangian is

$$L = \sum_i \left[ \frac{\alpha^2}{2} (C_i + C_{gi} + C_{\text{int}}) \dot{\varphi}_i^2 + E_{Ji} \cos \varphi_i - \alpha C_{gi} V_{gi} \dot{\varphi}_i \right] - \alpha^2 C_{\text{int}} \dot{\varphi}_1 \dot{\varphi}_2. \quad (50)$$

Then the Hamiltonian is

$$\begin{aligned} H = & \sum_i \left[ \frac{(p_i + \alpha C_{gi} V_{gi})^2}{2\alpha^2 \tilde{C}_i} - E_{Ji} \cos \varphi_i \right] \\ & + \frac{(p_1 + \alpha C_{g1} V_{g1})(p_2 + \alpha C_{g2} V_{g2})}{\alpha^2 \tilde{C}_{\text{int}}}, \end{aligned} \quad (51)$$

where

$$\tilde{C}_1 \equiv C_1 + C_{g1} + [C_{\text{int}}^{-1} + (C_2 + C_{g2})^{-1}]^{-1}, \quad (52)$$

$$\tilde{C}_2 \equiv C_2 + C_{g2} + [C_{\text{int}}^{-1} + (C_1 + C_{g1})^{-1}]^{-1}, \quad (53)$$

$$\tilde{C}_{\text{int}} \equiv C_1 + C_{g1} + C_2 + C_{g2} + (C_1 + C_{g1})(C_2 + C_{g2})C_{\text{int}}^{-1}. \quad (54)$$

This can be written as

$$H = \sum_i [E_{ci}(N_i - N_{gi})^2 - E_{Ji} \cos \varphi_i] + \delta H, \quad (55)$$

where

$$\delta H = g(N_1 - N_{g1})(N_2 - N_{g2}), \quad E_{ci} \equiv \frac{(e2)^2}{2\tilde{C}_i}, \quad g \equiv \frac{(e2)^2}{2\tilde{C}_{\text{int}}}. \quad (56)$$

The spin form in the charge basis is

$$H = \sum_i \left[ E_{ci}(N_{gi} - \frac{1}{2})\sigma_i^z - \frac{E_{Ji}}{2}\sigma_i^x \right] + \delta H, \quad (57)$$

with

$$\delta H = \frac{g}{2} \left[ \left( N_{g1} - \frac{1}{2} \right) \sigma_2^z + \left( N_{g2} - \frac{1}{2} \right) \sigma_1^z \right] + \frac{g}{4} \sigma_1^z \sigma_2^z. \quad (58)$$

When  $N_{g1} = N_{g2} = \frac{1}{2}$ , this is a pure Ising interaction.

---

<sup>7</sup> $\alpha \equiv \hbar/2e$ .

## 4 Tunable Couplings

By introducing more complicated coupling elements, we can introduce some degree of tunability into the architectures discussed above.

### 4.1 TUNABLE $E_J$

A simple way to make the Josephson energy  $E_J$  effectively tunable in a circuit is to use a well known quantum interference effect that occurs in a dc SQUID; see Figure 10. The tunability of  $E_J$  can be understood from two different viewpoints.

The first is to imagine introducing a hole in a current-biased JJ as in the “physical” model of Figure 10. Tunneling occurs in the up and down direction in each of the left and right arms of the interferometer. Recalling our interpretation of  $\cos \varphi$  as a Cooper-pair tunneling operator, the two arms of the interferometer result in

$$\cos \varphi \rightarrow \frac{e^{i(\varphi+\pi\frac{\Phi_x}{\Phi_{sc}})} + e^{-i(\varphi+\pi\frac{\Phi_x}{\Phi_{sc}})}}{2} + \frac{e^{i(\varphi-\pi\frac{\Phi_x}{\Phi_{sc}})} + e^{-i(\varphi-\pi\frac{\Phi_x}{\Phi_{sc}})}}{2}. \quad (59)$$

Here we have assumed a symmetric interferometer. The first pair of terms corresponds to tunneling (in both the up and down directions) in the left arm, which acquires half of the total Aharonov–Bohm phase  $2\pi\Phi_x/\Phi_{sc}$ ; the right arm has the opposite Aharonov–Bohm phase shift. Then the  $\cos \varphi$  term in the potential energy of (8) becomes

$$E_J^0 \cos \varphi \rightarrow E_J(\Phi_x) \cos \varphi, \quad \text{with} \quad E_J(\Phi_x) \equiv E_J^0 \cos\left(\frac{\pi\Phi_x}{\Phi_{sc}}\right). \quad (60)$$

The effective Josephson energy in (60) can be tuned by varying  $\Phi_x$ .

The second way to obtain (60) is to consider the circuit model in Figure 10, and again assume symmetry (identical JJs). This leads to the coupled equations of motion

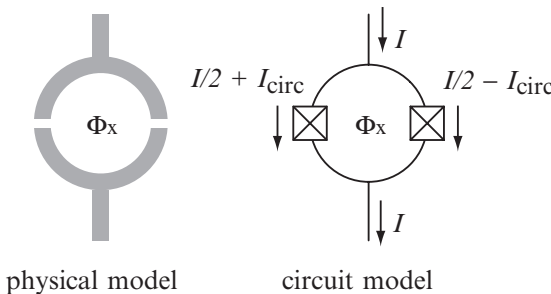


Figure 10. Tuning  $E_J$  with a dc SQUID

$$\alpha C \ddot{\varphi}_1 + I_0 \sin \varphi_1 = \frac{I}{2} + I_{\text{circ}}, \quad (61)$$

$$\alpha C \varphi_2 + I_0 \sin \varphi_2 = \frac{I}{2} - I_{\text{circ}}. \quad (62)$$

Defining

$$\bar{\varphi} \equiv \frac{\varphi_1 + \varphi_2}{2} \quad (63)$$

and using

$$\varphi_1 - \varphi_2 = \frac{2\pi\Phi_x}{\Phi_{\text{sc}}} \quad (64)$$

then leads to

$$\alpha^2(2C)\ddot{\bar{\varphi}} + E_J(\Phi_x) \sin \bar{\varphi} - \alpha I = 0, \quad (65)$$

in agreement with (60).

The ability to tune  $E_J$  is especially useful for inductively coupled flux qubits (Makhlin et al., 2001).

## 4.2 CHARGE QUBIT REGISTER OF MAKHLIN, SCHÖN, AND SHNIRMAN

Makhlin et al. (1999) have proposed coupling charge qubits by placing them in parallel with an inductor, such that the resulting  $LC$  oscillator (the capacitance provided by the JJs) has a frequency much higher than the qubit frequency. The case of two qubits is illustrated in Figure 11, but the method applies to more than two qubits as well.

The derivation of the circuit Hamiltonian follows methods similar to that used above, and is

$$H = \sum_i \left[ E_{ci} \left( N_{gi} - \frac{1}{2} \right) \sigma_i^z - \frac{E_{Ji}}{2} \sigma_i^x \right] + \frac{LC_{\text{qb}}^2 E_{J1} E_{J2}}{4\alpha^2 C^2} \sigma_1^y \sigma_2^y. \quad (66)$$

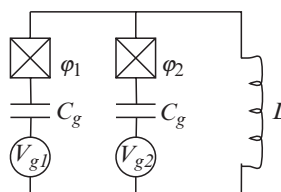


Figure 11. Circuit of Makhlin, Schön, and Shnirman

The significant feature of the interaction in (66), compared to (58), is that the  $E_{\text{Js}}$  here can be tuned by using dc SQUIDs. This gives, in principle, a fully tunable interaction between any pair of qubits attached to the same inductor.

#### 4.3 ELECTROSTATIC TRANSFORMER OF AVERIN AND BRUDER

Averin and Bruder (2003) considered a related coupled charge qubit circuit, shown in Figure 12, which we have reorganized to emphasize the similarity to Figure 11. The Hamiltonian in this case is

$$H = \sum_i \left[ E_{ci}(N_i - N_{gi})^2 - E_{Ji} \cos \varphi_i \right] + H_{\text{trans}} \quad (67)$$

and

$$H_{\text{trans}} = E_c \left( N - N_g - q \right)^2 - E_J \cos \varphi, \quad (68)$$

where

$$q \equiv q_g - \left( N_1 - N_{g1} + N_2 - N_{g2} \right) \frac{C_m}{C_{\Sigma i}}, \quad (69)$$

$$q_g \equiv 2N_g \left( 1 - \frac{C_m}{C_{\Sigma i}} \right). \quad (70)$$

The operator  $q$  here is a function of the charge qubit variables, but commutes with the transformer degrees of freedom.

As in the register of Makhlin, Schön, and Shnirman, we assume the transformer degrees of freedom are fast compared with the qubit variables, so that the transformer remains in its instantaneous ground state manifold. Then

$$H_{\text{trans}} \rightarrow \epsilon_0(q). \quad (71)$$

This finally leads to an effective Hamiltonian

$$H = \sum_i \left[ E_{ci} \left( N_{gi} - \frac{1}{2} \right) \sigma_i^z - \frac{E_{Ji}}{2} \sigma_i^x \right] + \sum_i a \sigma_i^z + b \sigma_1^z \sigma_2^z, \quad (72)$$

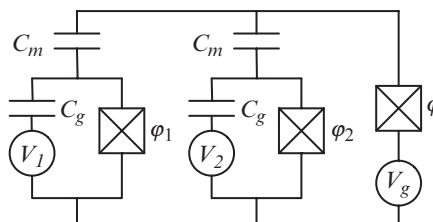


Figure 12. Electrostatic transformer

involving charge qubit variables only, where

$$a \equiv \frac{\epsilon_0 \left( q_0 + \frac{C_m}{C_{\Sigma i}} \right) - \epsilon_0 \left( q_0 - \frac{C_m}{C_{\Sigma i}} \right)}{4}, \quad (73)$$

$$b \equiv \frac{\epsilon_0 \left( q_0 + \frac{C_m}{C_{\Sigma i}} \right) + \epsilon_0 \left( q_0 - \frac{C_m}{C_{\Sigma i}} \right) - 2\epsilon_0(q_0)}{4}. \quad (74)$$

The discrete second-order derivative  $b$ , which can be interpreted as a capacitance, can be tuned to zero by varying  $q_0$ , providing the desired tunability.

#### 4.4 RF COUPLING

Finally, we briefly mention an interesting proposal by Rigetti et al. (2005) to use rf pulses to effectively bring permanently detuned qubits into resonance. This is a very promising approach, but has not yet been demonstrated experimentally.

### 5 Dynamic Couplings: Resonator Coupled Qubits

Several investigators have proposed the use of  $LC$  resonators (Shnirman et al., 1997; Makhlin et al., 1999; Mooij et al., 1999; You et al., 2002; Yukon, 2002; Blais et al., 2003; Plastina and Falci, 2003; Zhou et al., 2004), superconducting cavities (Blais et al., 2004; Wallraff et al., 2004), or other types of oscillators (Marquardt and Bruder, 2001; Zhu et al., 2003) to couple JJs together. Although harmonic oscillators are ineffective as computational qubits, because the lowest pair of levels cannot be frequency selected by an external driving field, they are quite desirable as bus qubits or coupling elements. Resonators provide for additional functionality in the coupling, and can be made to have very high  $Q$  factor. Here we will focus on phase qubits coupled by nanomechanical resonators (Cleland and Geller, 2004; Sornborger et al., 2004; Geller and Cleland, 2005; Pritchett and Geller, 2005).

#### 5.1 QUBIT-RESONATOR HAMILTONIAN

The Hamiltonian that describes the low-energy dynamics of a single large-area, current-biased JJ, coupled to a piezoelectric nanoelectromechanical disk resonator, can be written as (Cleland and Geller, 2004; Geller and Cleland, 2005)

$$H = \sum_m \epsilon_m c_m^\dagger c_m + \hbar\omega_0 a^\dagger a - ig \sum_{mm'} x_{mm'} c_m^\dagger c_{m'} (a - a^\dagger), \quad (75)$$

where the  $\{c_m^\dagger\}$  and  $\{c_m\}$  denote particle creation and annihilation operators for the Josephson junction states ( $m = 0, 1, 2, \dots$ ),  $a$  and  $a^\dagger$  denote ladder operators

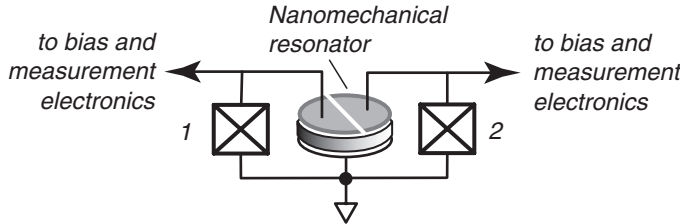


Figure 13. Two current-biased Josephson junctions (crossed boxes) coupled to a piezoelectric disk resonator

for the phonon states of the resonator's dilatational (thickness oscillation) mode of frequency  $\omega_0$ ,  $g$  is a coupling constant with dimensions of energy, and  $x_{mm'} \equiv \langle m|\varphi|m'\rangle$ . The value of  $g$  depends on material properties and size of the resonator, and can be designed to achieve a wide range of values. An illustration showing two phase qubits coupled to the same resonator is given in Figure 13. Interactions between the JJ and resonator may be controlled by changing the JJ current, giving rise to changes in the JJ energy spacing,  $\Delta\epsilon$ . For instance, a state can be transferred from the JJ to the resonator by bringing the JJ and resonator in resonance,  $\Delta\epsilon = \hbar\omega_0$ , and waiting for a specified period.

## 5.2 STRONG COUPLING AND THE RWA

For small couplings  $g \ll \Delta\epsilon$ , the JJ-resonator system may be approximated by the Jaynes–Cummings model; this is usually referred to as the rotating wave approximation (RWA). However, once the coupling becomes comparable to the level spacing,  $g \approx \Delta\epsilon$ , the RWA breaks down. When the JJ is weakly coupled to the resonator, with  $g/\Delta\epsilon$  below a few percent, gates such as a memory operation (state transfer to and from the resonator) work well, and qubits are stored and retrieved with high fidelity. *However, such gates are intrinsically slow.* As  $g/\Delta\epsilon$  is increased, making the gate faster, the fidelity becomes very poor, and it becomes necessary to deviate from the RWA protocol. Below, we first discuss an analytical approach to capture the leading corrections to the RWA at intermediate coupling strengths (Sornborger et al., 2004). We then discuss a strong coupling information processing example: a quantum memory register (Pritchett and Geller, 2005).

## 5.3 BEYOND THE RWA

For simplicity we will consider only two levels in a single junction. However, all possible phonon-number states are included. The Hamiltonian may then be written as the sum of two terms,  $H = H_{JC} + V$ . The first term,

$$H_{JC} \equiv \epsilon_0 c_0^\dagger c_0 + \epsilon_1 c_1^\dagger c_1 + \hbar\omega_0 a^\dagger a - igx_{01} [c_1^\dagger c_0 a - c_0^\dagger c_1 a^\dagger] \quad (76)$$

is the exactly solvable Jaynes–Cummings Hamiltonian, the eigenfunctions of which are known as dressed states. We will consider the second term,

$$V \equiv -ig \left[ x_{00} c_0^\dagger c_0 (a - a^\dagger) + x_{01} c_0^\dagger c_1 a - x_{01} c_1^\dagger c_0 a^\dagger + x_{11} c_1^\dagger c_1 (a - a^\dagger) \right], \quad (77)$$

as a perturbation. The RWA applied to the Hamiltonian  $H$  amounts to neglecting  $V$ . Therefore, perturbatively including  $V$  is equivalent to perturbatively going beyond the RWA.

### 5.3.1 Dressed states

The eigenstates of  $H_{\text{JC}}$ , or the dressed states, are labeled by the nonnegative integers  $j = 0, 1, 2, \dots$  and a sign  $\sigma = \pm 1$ . On resonance, these are

$$|\psi_j^\sigma\rangle \equiv \frac{|0, j+1\rangle - i\sigma|1, j\rangle}{\sqrt{2}}, \quad (\omega_d = 0) \quad (78)$$

and

$$W_j^\sigma \equiv \epsilon_0 + (j+1)\hbar\omega_0 + \sigma \sqrt{j+1} \frac{\hbar\Omega_0(0)}{2}, \quad (\omega_d = 0). \quad (79)$$

Here, the vacuum ( $j = 0$ ) Rabi frequency on resonance is  $\Omega_0(0) = 2g|x_{01}|/\hbar$ .

### 5.3.2 Dressed-state propagator

In quantum computing applications one will often be interested in calculating transition amplitudes of the form

$$\langle f | e^{-iHt/\hbar} | i \rangle, \quad (80)$$

where  $|i\rangle$  and  $|f\rangle$  are arbitrary initial and final states of the uncoupled qubit-resonator system. Expanding  $|i\rangle$  and  $|f\rangle$  in the dressed-state basis reduces the time-evolution problem to that of calculating the quantity

$$G_{jj'}^{\sigma\sigma'}(t) \equiv \langle \psi_j^\sigma | e^{-iHt/\hbar} | \psi_{j'}^{\sigma'} \rangle, \quad (81)$$

as well as  $\langle \psi_j^\sigma | e^{-iHt/\hbar} | 00 \rangle$  and  $\langle 00 | e^{-iHt/\hbar} | 00 \rangle$ .  $G_{jj'}^{\sigma\sigma'}(t)$  is a propagator in the dressed-state basis, and would be equal to  $\delta_{\sigma\sigma'}\delta_{jj'}e^{-iW_j^\sigma t/\hbar}$  if  $V$  were absent, that is, in the RWA.

To be specific, we imagine preparing the system at  $t = 0$  in the state  $|10\rangle$ , which corresponds to the qubit in the excited state  $m = 1$  and the resonator in the ground state  $n = 0$ . We then calculate the interaction-representation probability amplitude

$$c_{mn}(t) \equiv e^{iE_{mn}t/\hbar} \langle mn | e^{-iHt/\hbar} | 10 \rangle \quad (82)$$

for the system at a later time  $t$  to be in the state  $|mn\rangle$ . Here  $E_{mn} \equiv \epsilon_m + n\hbar\omega_0$ . Inserting complete sets of the dressed states leads to

$$c_{00}(t) = \sum_{\sigma j} \langle \psi_j^\sigma | 10 \rangle \langle 00 | e^{-iHt/\hbar} | \psi_j^\sigma \rangle, \quad (83)$$

and, for  $mn \neq 00$ ,

$$c_{mn}(t) = e^{iE_{mn}t/\hbar} \sum_{j=0}^{\infty} \begin{pmatrix} \langle \psi_j^+ | mn \rangle \\ \langle \psi_j^- | mn \rangle \end{pmatrix}^\dagger \begin{pmatrix} G_{j0}^{++} & G_{j0}^{+-} \\ G_{j0}^{-+} & G_{j0}^{--} \end{pmatrix} \begin{pmatrix} \langle \psi_0^+ | 10 \rangle \\ \langle \psi_0^- | 10 \rangle \end{pmatrix}. \quad (84)$$

So far everything is exact within the model defined in Eq. (75).

To proceed, we expand the dressed-state propagator in a basis of *exact* eigenstates  $|\Psi_\alpha\rangle$  of  $H$ , leading to

$$G_{jj'}^{\sigma\sigma'}(t) = \sum_{\alpha} \langle \psi_j^{\sigma} | \Psi_\alpha \rangle \langle \psi_{j'}^{\sigma'} | \Psi_\alpha \rangle^* e^{-i\mathcal{E}_\alpha t/\hbar}. \quad (85)$$

Here  $\mathcal{E}_\alpha$  is the energy of stationary state  $|\Psi_\alpha\rangle$ . The propagator is an infinite sum of periodic functions of time. We approximate this quantity by evaluating the  $|\Psi_\alpha\rangle$  and  $\mathcal{E}_\alpha$  perturbatively in the dressed-state basis.

We test our perturbed dressed-state method for the case of a finite-dimensional single-qubit, five-phonon system. The bias current is chosen to make the system exactly in resonance. The Hamiltonian for this system is diagonalized numerically, and the probability amplitudes  $c_{mn}(t)$  are calculated exactly, providing a test of the accuracy of the analytic perturbative solutions. Setting the initial state to be  $c_{mn}(0) = \delta_{m1}\delta_{n0}$ , as assumed previously, we simulate the transfer of a qubit from the Josephson junction to the resonator, by leaving the systems in resonance for half a vacuum Rabi period  $\pi\hbar/g|x_{01}|$ .

In Figure 14, we plot the probabilities for a relatively strong coupling,  $g/\Delta\epsilon = 0.30$ . For this coupling strength, the RWA is observed to fail. For example,

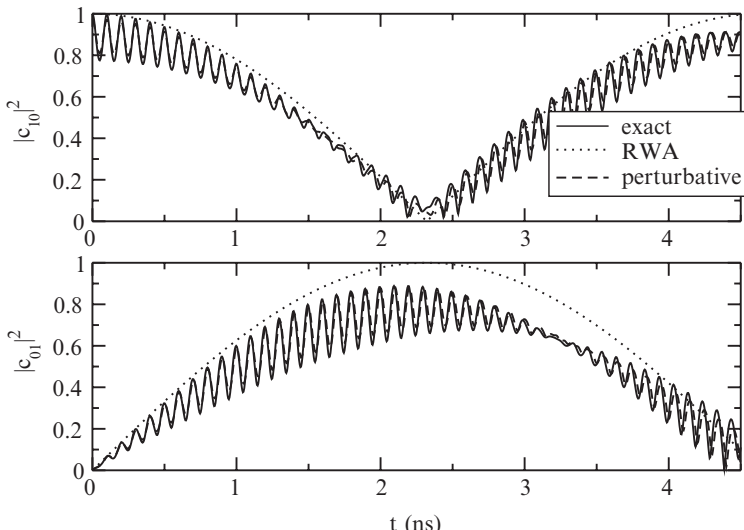


*Figure 14.* Probabilities  $|c_{10}|^2$  and  $|c_{01}|^2$  for the intermediate case of  $g/\Delta\epsilon = 0.30$ . Here there are large deviations from the RWA behavior, which are correctly accounted for by the dressed-state perturbative method

the RWA predicts a perfect state transfer between the junction and the resonator, and does not exhibit the oscillations present in the exact solution. The dressed-state perturbation theory does correctly capture these oscillations.

#### 5.4 MEMORY OPERATION WITH STRONG COUPLING

Here we study a complete memory operation, where the qubit is stored in the resonator and then transferred back to the JJ, for a large range of JJ-resonator coupling strengths (Pritchett and Geller, 2005). Also, we show that a dramatic improvement in memory performance can be obtained by a numerical optimization procedure where the resonant interaction times and off-resonant detunings are varied to maximize the overall gate fidelity. This allows larger JJ-resonator couplings to be used, leading to faster gates and therefore more operations carried out within the available coherence time. The results suggest that it should be possible to demonstrate a fast quantum memory using existing superconducting circuits, which would be a significant accomplishment in solid-state quantum computation.

In the upper panel of Figure 15 we plot the memory fidelity for the qubit state  $2^{-\frac{1}{2}}(|0\rangle + |1\rangle)$  as a function of  $g/\Delta\epsilon$ . We actually report the fidelity squared,

$$F^2 = |\alpha^* c_{00}(t_f) + \beta^* c_{10}(t_f)|^2, \quad (86)$$

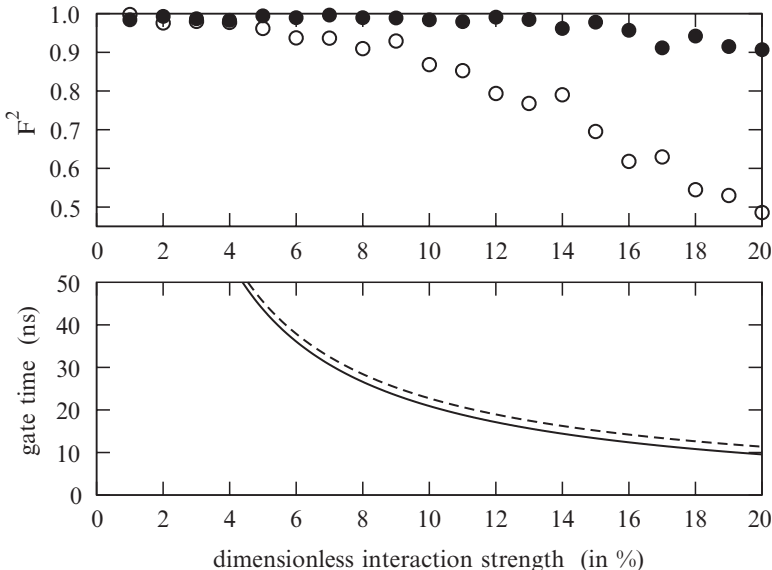


*Figure 15.* Upper panel: Memory fidelity for equator state  $2^{-\frac{1}{2}}(|0\rangle + |1\rangle)$  as a function of  $g/\Delta\epsilon$ , using both the RWA (unfilled circles) and optimized (solid circles) pulse times. Lower panel: Time needed to store and retrieve state, using both the RWA (dashed curve) and optimized (solid curve) pulse times

which is the probability that the memory device operates correctly. As expected, the fidelity gradually decreases with increasing  $g$ . The lower panel of Figure 15 gives the gate time as a function of  $g/\Delta\epsilon$ . These results suggest that memory fidelities better than 90% can be achieved using phase qubits and resonators with coherence times longer than a few tens of ns.

### Acknowledgments

This work was supported by the NSF under grants DMR-0093217 and CMS-040403.

### References

- Averin, D. V. and C. Bruder: 2003, Variable electrostatic transformer: Controllable coupling of two charge qubits. *Phys. Rev. Lett.* **91**, 57003.
- Berkley, A. J., H. Xu, R. C. Ramos, M. A. Gubrud, F. W. Strauch, P. R. Johnson, J. R. Anderson, A. J. Dragt, C. J. Lobb, and F. C. Wellstood: 2003, Entangled macroscopic quantum states in two superconducting qubits. *Science* **300**, 1548–50.
- Blais, A., A. Massen van den Brink, and A. M. Zagoskin: 2003, Tunable coupling of superconducting qubits. *Phys. Rev. Lett.* **90**, 127901.
- Blais, A., R.-S. Huang, A. Wallraff, S. M. Girvin, and R. J. Schoelkopf: 2004, Cavity quantum electrodynamics for superconducting electrical circuits: An architecture for quantum computation. *Phys. Rev. A* **69**, 62320.
- Caldeira, A. O. and A. J. Leggett: 1981, Influence of dissipation on quantum tunneling in macroscopic systems. *Phys. Rev. Lett.* **46**, 211–4.
- Caldeira, A. O. and A. J. Leggett: 1983, Quantum tunneling in a dissipative system. *Ann. Phys. (N.Y.)* **149**, 374–456.
- Clarke, J., A. N. Cleland, M. H. Devoret, D. Esteve, and J. M. Martinis: 1988, Quantum mechanics of a macroscopic variable: The phase difference of a Josephson junction. *Science* **239**, 992–7.
- Cleland, A. N. and M. R. Geller: 2004, Superconducting qubit storage and entanglement with nanomechanical resonators. *Phys. Rev. Lett.* **93**, 70501.
- Devoret, M. H., J. M. Martinis, and J. Clarke: 1985, Measurements of macroscopic quantum tunneling out of the zero-voltage state of a current-biased Josephson junction. *Phys. Rev. Lett.* **55**, 1908–11.
- Friedman, J. R., V. Patel, W. Chen, S. K. Tolpygo, and J. E. Lukens: 2000, Quantum superpositions of distinct macroscopic states. *Nature (London)* **406**, 43–6.
- Geller, M. R. and A. N. Cleland: 2005, Superconducting qubits coupled to nanoelectromechanical resonators: An architecture for solid-state quantum information processing. *Phys. Rev. A* **71**, 32311.
- Geller, M. R., E. J. Pritchett, A. T. Sornborger, M. Steffen, and J. M. Martinis: 2006, Controlled-NOT logic for Josephson phase qubits. e-print cond-mat/0000000.
- Johnson, P. R., F. W. Strauch, A. J. Dragt, R. C. Ramos, C. J. Lobb, J. R. Anderson, and F. C. Wellstood: 2003, Spectroscopy of capacitively coupled Josephson-junction qubits. *Phys. Rev. B* **67**, 20509.
- Makhlin, Y., G. Schön, and A. Shnirman: 1999, Josephson-junction qubits with controlled couplings. *Nature (London)* **398**, 305–7.

- Makhlin, Y., G. Schön, and A. Shnirman: 2001, Quantum-state engineering with Josephson-junction devices. *Rev. Mod. Phys.* **73**, 357–400.
- Marquardt, F. and C. Bruder: 2001, Superposition of two mesoscopically distinct quantum states: Coupling a Cooper-pair box to a large superconducting island. *Phys. Rev. B* **63**, 54514.
- Martinis, J. M., M. H. Devoret, and J. Clarke: 1985, Energy-level quantization in the zero-voltage state of a current-biased Josephson junction. *Phys. Rev. Lett.* **55**, 1543–6.
- Martinis, J. M., M. H. Devoret, and J. Clarke: 1987, Experimental tests for the quantum behavior of a macroscopic degree of freedom: The phase difference across a Josephson junction. *Phys. Rev. B* **35**, 4682–98.
- Martinis, J. M., S. Nam, J. Aumentado, and C. Urbina: 2002, Rabi oscillations in a large Josephson-junction qubit. *Phys. Rev. Lett.* **89**, 117901.
- Massen van den Brink, A.: 2005, Hamiltonian for coupled flux qubits. *Phys. Rev. B* **71**, 64503.
- McDermott, R., R. W. Simmonds, M. Steffen, K. B. Cooper, K. Cicak, K. D. Osborn, D. P. Oh, S. Pappas, and J. M. Martinis: 2005, Simultaneous state measurement of coupled Josephson phase qubits. *Science* **307**, 1299–302.
- Mooij, J. E., T. P. Orlando, L. S. Levitov, L. Tian, C. H. van der Wal, and S. Lloyd: 1999, Josephson persistent-current qubit. *Science* **285**, 1036–9.
- Nakamura, Y., C. D. Chen, and J. S. Tsai: 1997, Spectroscopy of energy-level splitting between two macroscopic quantum states of charge coherently superposed by Josephson coupling. *Phys. Rev. Lett.* **79**, 2328–31.
- Nakamura, Y., Y. A. Pashkin, and J. S. Tsai: 1999, Coherent control of macroscopic quantum states in a single-Cooper-pair box. *Nature (London)* **398**, 786–8.
- Orlando, T. P., J. E. Mooij, L. Tian, C. H. van der Wal, L. S. Levitov, S. Lloyd, and J. J. Mazo: 1999, Superconducting persistent-current qubit. *Phys. Rev. B* **60**, 15398–413.
- Pashkin, Y. A., T. Yamamoto, O. Astafiev, Y. Nakamura, D. V. Averin, and J. S. Tsai: 2003, Quantum oscillations in two coupled charge qubits. *Nature (London)* **421**, 823–6.
- Plastina, F. and G. Falci: 2003, Communicating Josephson qubits. *Phys. Rev. B* **67**, 224514.
- Pritchett, E. J. and M. R. Geller: 2005, Quantum memory for superconducting qubits. *Phys. Rev. A* **72**, 10301.
- Rigetti, C., A. Blais, and M. H. Devoret: 2005, Protocol for universal gates in optimally biased superconducting qubits. *Phys. Rev. Lett.* **94**, 240502.
- Rouse, R., S. Han, and J. E. Lukens: 1995, Observation of resonant tunneling between macroscopically distinct quantum levels. *Phys. Rev. Lett.* **75**, 1614–7.
- Shnirman, A., G. Schön, and Z. Hermon: 1997, Quantum manipulations of small Josephson junctions. *Phys. Rev. Lett.* **79**, 2371–4.
- Sornborger, A. T., A. N. Cleland, and M. R. Geller: 2004, Superconducting phase qubit coupled to a nanomechanical resonator: Beyond the rotating-wave approximation. *Phys. Rev. A* **70**, 52315.
- Strauch, F. W., P. R. Johnson, A. J. Dragt, C. J. Lobb, J. R. Anderson, and F. C. Wellstood: 2003, Quantum logic gates for coupled superconducting phase qubits. *Phys. Rev. Lett.* **91**, 167005.
- van der Wal, C. H., A. C. J. ter Haar, F. K. Wilhelm, R. N. Schouten, C. J. P. M. Harmans, T. P. Orlando, S. Lloyd, and J. E. Mooij: 2000, Quantum superpositions of macroscopic persistent current. *Science* **290**, 773–7.
- Vion, V., A. Aassime, A. Cottet, P. Joyez, H. Pothier, C. Urbina, D. Esteve, and M. H. Devoret: 2002, Manipulating the quantum state of an electrical circuit. *Science* **296**, 886–9.
- Wallraff, A., D. I. Schuster, A. Blais, L. Frunzio, R.-S. Huang, J. Majer, S. Kumar, S. M. Girvin, and R. J. Schoelkopf: 2004, Strong coupling of a single photon to a superconducting qubit using circuit quantum electrodynamics. *Nature (London)* **431**, 162–7.
- Yamamoto, T., Y. A. Pashkin, O. Astafiev, Y. Nakamura, and J. S. Tsai: 2003, Demonstration of conditional gate operations using superconducting charge qubits. *Nature (London)* **425**, 941–4.

- You, J. Q. and F. Nori: 2005, Superconducting circuits and quantum information. *Phys. Today*, November 2005, 42.
- You, J. Q., J. S. Tsai, and F. Nori: 2002, Scalable quantum computing with Josephson charge qubits. *Phys. Rev. Lett.* **89**, 197902.
- Yu, Y., S. Han, X. Chu, S.-I. Chu, and Z. Wang: 2002, Coherent temporal oscillations of macroscopic quantum states in a Josephson junction. *Science* **296**, 889–92.
- Yukon, S. P.: 2002, A multi-Josephson junction qubit. *Physica C* **368**, 320–3.
- Zhou, X., M. Wulf, Z. Zhou, G. Guo, and M. J. Feldman: 2004, Dispersive manipulation of paired superconducting qubits. *Phys. Rev. A* **69**, 30301.
- Zhu, S.-L., Z. D. Wang, and K. Yang: 2003, Quantum-information processing using Josephson junctions coupled through cavities. *Phys. Rev. A* **68**, 34303.

## SUPERCONDUCTING QUBITS II: DECOHERENCE

F. K. WILHELM<sup>†</sup>, M. J. STORCZ, and U. HARTMANN

*Department Physik, Center for Nanoscience, and Arnold Sommerfeld Center for theoretical physics, Ludwig-Maximilians-Universität, 80333 München, Germany*

MICHAEL R. GELLER<sup>‡</sup>

*Department of Physics and Astronomy, University of Georgia, Athens, Georgia 30602, USA*

**Abstract:** This is an introduction to elementary decoherence theory as it is typically applied to superconducting qubits.

**Keywords:** spintronics, quantum dots, nuclear spin, spin Hall effect, magnetic semiconductors

**Abbreviations:** SQUID – superconducting quantum interference device; qubit – quantum bit; TSS – two state system

### 1 Introduction

The transition from quantum to classical physics, now known as decoherence, has intrigued physicists since the formulation of quantum mechanics (Feynman and Vernon, 1963; Peres, 1993; Zurek, 1993; Giulini et al., 1996; Leggett, 2002). It has been put into the poignant Schrödinger cat paradox (Schrödinger, 1935) and was considered an open fundamental question for a long time.

In this chapter, we study the theory of decoherence as it is applied to superconducting qubits. The foundations of the methodology used are rather general results of quantum statistical physics and resemble those applied to chemical physics, nuclear magnetic resonance, optics, and other condensed matter systems (Weiss, 1999). All these realizations introduce their subtleties—typical couplings, temperatures, properties of the correlation functions. We will in the following largely stick to effective spin notation in order to emphasize this universality, still taking most of the examples from superconducting decoherence. This paper is based on lectures 2 and 3 of the NATO-ASI on “Manipulating quantum coherence in superconductors and semiconductors” in Cluj-Napoca, Romania, 2005. It is *not*

---

<sup>†</sup>Present address: Department of Physics and Astronomy and Institute for Quantum Computing, University of Waterloo, Waterloo, Ontario N2L 3G1, Canada; fwilhelm@iqc.ca

<sup>‡</sup>mgeller@uga.edu

intended to be a review summarizing the main papers in the field. Rather, it is an (almost) self-contained introduction to some of the relevant techniques, aimed to be accessible to researchers and graduate students with a knowledge of quantum mechanics (Cohen-Tannoudji et al., 1992) and statistical physics (Landau and Lifshitz, 1984) on the level of a first graduate course. So much of the material here is not new and most certainly known to more experienced researchers, however, we felt a lack of a single reference which allows newcomers to get started without excessive overhead. References have largely been chosen for the aid they provide in learning and teaching the subject, rather than importance and achievement.

### 1.1 BASIC NOTIONS OF DECOHERENCE

The mechanisms of decoherence are usually related to those of energy dissipation. In particular, decoherence is irreversible. If we take as an example a pure superposition state

$$|\psi\rangle = (|0\rangle + |1\rangle)/\sqrt{2} \quad \rho_{\text{pure}} = |\psi\rangle\langle\psi| = \frac{1}{2} \begin{pmatrix} 1 & 1 \\ 1 & 1 \end{pmatrix} \quad (1)$$

and compare it to the corresponding classical mixture leading to the same expectation value of  $\sigma_z$

$$\rho_{\text{mix}} = \frac{1}{2} \begin{pmatrix} 1 & 0 \\ 0 & 1 \end{pmatrix} \quad (2)$$

we can see that the von-Neumann entropy  $\rho = -k_B \text{Tr}[\rho \log \rho]$  rises from  $S_{\text{pure}} = 0$  to  $S_{\text{mix}} = k_B \ln 2$ . Hence, decoherence taking  $\rho_{\text{pure}}$  to  $\rho_{\text{mix}}$  creates entropy and is irreversible.

Quantum mechanics, on the other hand, is always reversible. It can be shown, that any *isolated* quantum system is described by the Liouville von-Neumann equation

$$i\hbar\dot{\rho} = [H, \rho], \quad (3)$$

which conserves entropy. Indeed, also the CPT theorem of relativistic quantum mechanics (Sakurai, 1967) states, that for each quantum system it is possible to find a counterpart (with inverted parity and charge) whose time arrow runs backwards. The apparent contradiction between microreversibility—reversibility of the laws of quantum physics described by Schrödinger's equation—and macroirreversibility is a problem at the foundation of statistical thermodynamics. We also remark that the Lagrangian formalism (Landau and Lifshitz, 1982) which was used as the starting point in the previous chapter of this book (Geller et al., 2006) does not even accomodate friction on a classical level without artificial and in general non-quantizable additions.

## 1.2 HEAT BATHS AND QUANTUM BROWNIAN MOTION

The standard way out of this dilemma is to introduce a continuum of additional degrees of freedom acting as a heat bath for the quantum system under consideration (Feynman and Vernon, 1963; Caldeira and Leggett, 1981, 1983). The complete system is fully quantum-coherent and can be described by Eq. (3). However, the heat bath contains unobserved degrees of freedom which have to be integrated out to obtain the *reduced system*; the reduced system is the original quantum system which does not contain the bath explicitly, but whose dynamics are influenced by the bath. The dynamics of the reduced system now show both *dissipation* (energy exchange with the heat bath) and *decoherence* (loss of quantum information to the heat bath). Another view on this is that any finite combined quantum system shows dynamics which are periodic in time. The typical periods are given by the inverse level splittings of the system. Thus, a continuous heat bath shows periodicity and reversibility only on an infinite, physically unobservable timescale.

A standard example, taken from Ingold (1998), of irreversibility in both classical and quantum mechanics is (quantum) Brownian motion (QBM), which we will now describe in the one-dimensional case. The underlying Hamiltonian of a single particle in an oscillator bath has the general structure

$$H = H_s + H_{sb} + H_b + H_c. \quad (4)$$

Here, the system Hamiltonian  $H_s$  describes an undamped particle of mass  $M$  in a scalar potential,  $H_s = \frac{P^2}{2M} + V(q)$ .  $H_b$  describes a bath of harmonic oscillators,  $H_b = \sum_i \left( \frac{p_i^2}{2m_i} + \frac{1}{2}m_i\omega_i^2 x_i^2 \right)$ . The coupling between these two components is bilinear,  $H_{sb} = -q \sum_i c_i x_i$ . If this were all, the effective potential seen by the particle would be altered even on the classical level, as will become more obvious later on. Thus, we have to add a counter term which does not act on the bath,  $H_c = q^2 \sum_i \frac{c_i^2}{2m_i\omega_i^2}$ . Adding this counterterm gives the Hamiltonian the following intuitive form:

$$H = \frac{P^2}{2M} + V(q) + \sum_i \left( \frac{p_i^2}{2m_i} + \frac{1}{2}m_i\omega_i^2 \left( x_i - \frac{c_i}{m_i\omega_i^2} q \right)^2 \right) \quad (5)$$

indicating that the bath oscillators can be viewed as attached to the particle by springs. Here, we have introduced sets of new parameters,  $c_i$ ,  $\omega_i$ , and  $m_i$  which need to be adjusted to the system of interest. This aspect will be discussed later on. We treat this system now using the Heisenberg equation of motion

$$i\hbar \dot{O}(t) = [O(t), H] \quad (6)$$

for the operators  $q$ ,  $P$ ,  $x_i$ , and  $p_i$ , which (as a mathematical consequence of the correspondence principle) coincide with the classical equations of motion. The bath oscillators see the qubit acting as an external force

$$\ddot{x}_i + \omega_i^2 x_i = \frac{c_i}{m_i} q(t). \quad (7)$$

This equation of motion can be solved by variation of constants, which can be found in textbooks on differential equations such as (Zill, 2000)

$$x_i(t) = x_i(0) \cos \omega_i t + \frac{p_i(0)}{m_i \omega_i} \sin \omega_i t + \frac{c_i^2}{m_i \omega_i^2} \int_0^t dt' \sin \omega_i(t-t') q(t'). \quad (8)$$

Analogously, we find the equation of motion for the particle

$$\ddot{q} = -\frac{\partial V}{\partial q} - \sum_i \frac{c_i}{m_i} x_i - q \sum_i \frac{c_i^2}{m_i \omega_i^2}. \quad (9)$$

Substituting Eq. (8) into Eq. (9) eliminates the bath coordinates up to the initial condition

$$\begin{aligned} M\ddot{q} &= -\frac{\partial V}{\partial q} - \sum_i \frac{c_i^2}{m_i \omega_i} \int_0^t dt' \sin \omega_i(t-t') q(t') \\ &\quad + \sum_i c_i \left( x_i(0) \cos \omega_i t + \frac{p_i(0)}{m_i \omega_i} \sin \omega_i t \right) - q \sum_i \frac{c_i^2}{m_i \omega_i^2}. \end{aligned} \quad (10)$$

We now integrate by parts and get a convolution of the velocity plus boundary terms, one of which shifts the origin of the initial position, the other cancels the counterterm (indicating, that without the counterterm we would obtain a potential renormalization). The result has the compact form

$$M\ddot{q} + \frac{\partial V}{\partial q} + \int_0^t dt' \gamma(t-t') \dot{q}(t') = \xi(t). \quad (11)$$

This structure is identified as a Langevin equation with memory friction. If interpreted classically, this is the equation of motion of a Brownian particle—a light particle in a fluctuating medium. In the quantum limit, we have to read  $q$ ,  $x_i$  and the derived quantity  $\xi$  as operators. We see both sides of open system dynamics—dissipation encoded in the damping kernel  $\gamma$  and decoherence encoded in the noise term  $\xi$ . We can express  $\gamma$  as

$$\gamma(t) = \sum_i \frac{c_i^2}{m_i \omega_i^2} \cos \omega_i t = \int_0^\infty \frac{d\omega}{\omega} J(\omega) \cos \omega t \quad (12)$$

where we have introduced the spectral density of bath modes

$$J(\omega) = \sum_i \frac{c_i^2}{m_i \omega_i} \delta(\omega - \omega_i), \quad (13)$$

which is the only quantifier necessary to describe the information encoded in the distribution of the  $m_i$ ,  $\omega_i$ , and  $c_i$ . The right hand side of Eq. (11) is a noise term and reads

$$\xi(t) = \sum_i c_i \left[ \left( x_i(0) - \frac{c_i}{m_i \omega_i^2} q(0) \right) \cos \omega_i t + \frac{p_i(0)}{m_i \omega_i} \sin \omega_i t \right]. \quad (14)$$

This crucially depends on the initial condition of the bath. If we assume that the bath is initially equilibrated around the initial position  $q(0)$  of the particle, we can show, using the standard quantum-statistics of the simple harmonic oscillator, that the noise is unbiased,  $\langle \xi(t) \rangle = 0$ , and its correlation function is given by

$$K(t) = \langle \xi(t) \xi(0) \rangle = \int d\omega J(\omega) [\cos \omega t (2n(\hbar\omega) + 1) - i \sin \omega t], \quad (15)$$

where  $n$  is the Bose function,  $n(\hbar\omega) = (e^{\hbar\omega/kT} - 1)^{-1}$ , and  $2n(\hbar\omega) + 1 = \coth\left(\frac{\hbar\omega}{2k_B T}\right)$ . Here and henceforth, angular brackets around an operator indicate the quantum-statistical average,  $\langle O \rangle = \text{Tr}(\rho O)$  with  $\rho$  being the appropriate density matrix. We will get back to the topic of the initial condition in section 3.1.2 of this chapter.

The noise described by  $\xi(t)$  is the *quantum* noise of the bath. In particular, the correlation function is time-translation invariant,

$$K(t) = \langle \xi(t + \tau) \xi(\tau) \rangle \quad (16)$$

but not symmetric

$$K(-t) = \langle \xi(0) \xi(t) \rangle = K^*(t) \neq K(t), \quad (17)$$

which reflects the fact that  $\xi$  as defined in Eq. (14) is a time-dependent operator which does generally not commute at two different times. Explicitly, the imaginary part of  $K(t)$  changes its sign under time reversal. Indeed, if the derivation of Eq. (15) is done explicitly, one directly sees that it originates from the finite commutator. Moreover, we can observe that at  $T \gg \omega$  we have  $2n + 1 \rightarrow 2k_B T / \hbar\omega \gg 1$ , thus the integral in Eq. (15) is dominated by the symmetric real part now describing purely thermal noise. At any temperature, the symmetrized semiclassical spectral noise power in frequency space reads

$$S(\omega) = \frac{1}{2} \langle \xi(t) \xi(0) + \xi(0) \xi(t) \rangle_\omega = S(-\omega), \quad (18)$$

where  $\langle \dots \rangle_\omega$  means averaging and Fourier transforming. This quantity contains a sign of the quantum nature of noise. Unlike classical noise, it does not disappear at low temperatures  $T \ll \hbar\omega/k_B$ , but saturates to a finite value set by the zero-point fluctuations, whereas at high temperature we recover thermal noise. Note, that the same crossover temperature dictates the asymmetry in Eq. (17). Both observations

together can be identified with the fact, that zero-point fluctuations only allow for emission of energy, not absorption, as will be detailed in a later section of this chapter.

Our approach in this chapter is phenomenological. The main parameter of our model is the spectral density  $J(\omega)$ . We will show in sections 1.3, 2.1.1, and 2.1.2 how  $J(\omega)$  can be derived explicitly for Josephson junction circuits. Oscillator baths accurately model numerous other situations. Decoherence induced by phonons in quantum dot systems allows to directly identify the phonons as the bath oscillators (Brandes and Kramer, 1999; Storcz et al., 2005a), whereas in the case of electric noise from resistors or cotunneling in dots (Hartmann and Wilhelm, 2004) it is less obvious—the Bosons are electron–hole excitations, which turn out to have the commutation relation of hard-core Bosons (von Delft and Schoeller, 1998) with the hard-core term being of little effect in the limits of interest (Weiss, 1999).

Going back to our phenomenology, we introduce the most important case of an Ohmic bath

$$J(\omega) = \gamma\omega f(\omega/\omega_c). \quad (19)$$

Here,  $\gamma$  is a constant of dimension frequency and  $f$  is a high-frequency cutoff function providing  $f(x) \simeq 1$  at  $x < 1$  and  $f \rightarrow 0$  at  $x > 1$ . Popular choices include the hard cutoff,  $f(x) = \theta(1 - x)$ , exponential cutoff,  $f(x) = e^{-x}$ , and the Drude cutoff  $f(x) = \frac{1}{1+x^2}$ . We will see in section 1.3 that the Drude cutoff plays a significant role in finite electrical circuits, so we chose it here for illustration purposes. In this case, the damping kernel reduces to

$$\gamma(\tau) = \gamma\omega_c e^{-\omega_c\tau}. \quad (20)$$

For  $\omega_c \rightarrow \infty$ ,  $\gamma$  becomes a delta function and we recover the classical damping with damping constant  $\gamma$ ,  $\gamma(\tau) = \gamma\delta(\tau)$ . Here, “classical damping” alludes to the damping of particle motion in fluid or of charge transport in a resistor (thus the name Ohmic, see also section 1.3). With finite  $\omega_c$ , the Ohmic models leads to classical, linear friction proportional to the velocity, smeared out over a memory time set by the inverse cutoff frequency defining a correlation time  $t_c = \omega_c^{-1}$ . On the other hand, as it turns out in the analysis of the model, e.g. in section 2.3.1, an infinite cutoff always leads to unphysical divergencies. Examples will be given later on. All examples from the class of superconducting qubits have a natural ultraviolet cutoff set by an appropriate  $1/RC$  or  $R/L$  with  $R$ ,  $L$ , and  $C$  being characteristic resistances, inductances, and capacitances of the circuit, respectively. Note, that parts of the open quantum systems literature do not make this last observation.

We will not dwell on methods of solution of the quantum Langevin equation, as the focus of this work is the decoherence of qubit systems. Methods include the associated Fokker–Planck equation, path integrals, and quantum trajectory

simulations. The quantum Langevin equation finds application in the theory of quantum decay in chemical reactions, the dissipative harmonic oscillator, and the decoherence of double-slit experiments.

### 1.2.1 How general are oscillator baths?

Even though the model introduced looks quite artificial and specific, it applies to a broad range of systems. The model essentially applies as long as the heat bath can be treated within linear response theory, meaning that it is essentially infinite (i.e. cannot be exhausted), has a regular spectrum, and is in thermal equilibrium. We outline the requirement of only weakly perturbing the system, i.e. of linear response theory (Kubo et al., 1991). The derivation is rather sketchy and just states the main results because this methodology will not be directly used later on. Introductions can be found, e.g. in Kubo et al. (1991), Ingold (1998), and Callen and Welton (1951).

In linear response theory, we start from a Hamiltonian  $H_0$  of the oscillator bath which is perturbed by an external force  $F$  coupling to a bath operator  $Q$ ,

$$H = H_0 - FQ, \quad (21)$$

where the perturbation must be weak enough to be treated to lowest order. It is a result of linear response theory that the system responds by a shift of  $Q$  (taken in the Heisenberg picture) according to

$$\langle \delta Q(t) \rangle_\omega = \chi(\omega)F(\omega), \quad (22)$$

where the susceptibility  $\chi$  can be computed to lowest order as the correlation function

$$\chi = \langle Q(0)Q(0)\theta(t) \rangle_\omega \quad (23)$$

computed in thermal equilibrium. We can split the correlation function into real and imaginary parts  $\chi = \chi' + i\chi''$ . The real part determines the fluctuations, i.e.

$$\frac{1}{2} \langle \delta Q(t)\delta Q(0) + \delta Q(0)\delta Q(t) \rangle_\omega = \chi', \quad (24)$$

whereas the imaginary part determines the energy dissipation

$$\langle E(t) \rangle_\omega = \omega\chi''|F|^2. \quad (25)$$

Together with the Eqs. (12) and (18) tracing both damping and noise back to a single function  $\chi$  constitute the famous fluctuation–dissipation theorem (Callen and Welton, 1951), a generalization of the Einstein relation in diffusion.

In this very successful approach we have characterized the distribution of the observable  $Q$  close to thermal equilibrium by its two-point correlation function

alone. This is a manifestation of the fact that its distribution, following the central limit theorem is Gaussian, i.e. can be characterized by two numbers only: mean and standard deviation. Oscillator baths provide exactly these ingredients: by properly choosing  $J(\omega)$  they can be fully adjusted to any  $\chi(\omega)$ , and all higher correlation functions—correlation functions involving more than two operators—can also be expressed through  $J$  hence do not contain any independent piece of information.

This underpins the initial statement that oscillator baths can describe a broad range of environments, including those composed of Fermions and not Bosons, such as a resistor. As explained in section 1.2, the oscillators are introduced artificially—on purely statistical grounds as a tool to describe fluctuations and response—and can only sometimes be directly identified with a physical entity.

There are still a number of environments where the mapping on an oscillator bath is in general not correct. These include: i) baths of uncoupled spins (e.g. nuclear spins), which are not too big and can easily saturate, i.e. explore the full finite capacity of their bounded energy spectrum; ii) shot noise, which is not in thermal equilibrium; iii) nonlinear electrical circuits such as many Josephson circuits; and iv) in most cases  $1/f$  noise, whose microscopic explanation either hints at non-Gaussian (spin-like) or nonequilibrium sources as discussed in section 3.2.

### 1.3 OSCILLATOR BATH MODELS FOR JOSEPHSON JUNCTION DEVICES

We have now learned two approaches to characterize the oscillator bath: through noise, and through friction. We will now apply the characterization by friction to a simple Josephson circuit with Josephson energy  $E_J$ , junction capacitance  $C_J$ , and arbitrary shunt admittance in parallel, all biased by an external current  $I_B$ . We are extending the method presented in the previous chapter (Geller et al., 2006) to include the admittance. We start with the elementary case of a constant conductance,  $Y(\omega) = G$ . The total current splits up into the three elements as

$$I_B = I_c \sin \phi + C \frac{\Phi_0}{2\pi} \ddot{\phi} + G \frac{\Phi_0}{2\pi} \dot{\phi}. \quad (26)$$

Reordering terms, we can cast this into the shape of Newton's equation for a particle with coordinate  $\phi$ .

$$C \left( \frac{\Phi_0}{2\pi} \right)^2 \ddot{\phi} + G \left( \frac{\Phi_0}{2\pi} \right)^2 \dot{\phi} + \frac{\partial V}{\partial \phi} = 0. \quad (27)$$

Here, we have multiplied the equation by another  $\Phi_0/2\pi$  to ensure proper dimensions of the potential energy

$$V(\phi) = -I_B \frac{\Phi_0}{2\pi} \phi + E_J (1 - \cos \phi), \quad (28)$$

where we have introduced the Josephson energy  $E_J = I_0\Phi_0/2\pi$ . This expression can be readily compared to Eq. (11). We see that the friction term has no memory, i.e.  $\gamma(t) \propto \delta(t)$ , and using the results of section 1.2 we can infer that  $J(\omega) = G(\Phi_0/2\pi)\omega$ , i.e. an Ohmic resistor leads naturally to an Ohmic spectral density as mentioned before. Note that this has no cutoff, but any model of an Ohmic resistor leads to reactive behavior at high frequencies.

We see that we missed the noise term on the right, which would represent current noise originating in  $G$  and which would have to be included in a more sophisticated circuit analysis which careful engineers would do. By applying the fluctuation dissipation theorem to  $\gamma$  we can add on the proper noise term, whose correlation function is given by Eq. (15)—or we can simply use this equation with the  $J(\omega)$  obtained.

We want to generalize this system now to an arbitrary shunt admittance  $Y(\omega)$ . For that, it comes in handy to work in Fourier space and we denote the Fourier transform by  $\mathcal{F}$ . Analogous to Eq. (27), we can find the following expression:

$$-\omega^2 C \left( \frac{\Phi_0}{2\pi} \right)^2 \phi + i\omega Y(\omega) \left( \frac{\Phi_0}{2\pi} \right)^2 \phi + \mathcal{F} \left( \frac{\partial V}{\partial \phi} \right) = 0. \quad (29)$$

We have to remember that the damping Kernel  $\gamma$  is the Fourier cosine transform of  $J(\omega)/\omega$ , which also implies that it is a real valued function. We can split  $Y$  into real (dissipative) and imaginary (reactive) parts  $Y = Y_d + iY_r$ . For any finite electrical circuit,  $Y_d$  is always an even and  $Y_r$  always an odd function of frequency. All this allows us to rewrite Eq. (29)

$$-\omega^2 C \left( \frac{\Phi_0}{2\pi} \right)^2 \phi - \omega Y_r(\omega) \left( \frac{\Phi_0}{2\pi} \right)^2 \phi + i\omega Y_d(\omega) \left( \frac{\Phi_0}{2\pi} \right)^2 \phi + \mathcal{F} \left( \frac{\partial V}{\partial \phi} \right) = 0. \quad (30)$$

Thus, the general expression for the spectral density reads  $J(\omega) = \omega Y_d = \omega \text{Re}Y(\omega)$ , i.e. it is controlled by the *dissipative* component of  $Y(\omega)$  alone. There is a new term containing the reactive component  $Y_r$  which modifies the non-dissipative part of the dynamics and can lead, e.g. to mass or potential renormalization, or something more complicated. Comparing this result to the structure of the susceptibility  $\chi$  in the discussion of section 1.2.1 it looks like the real and imaginary part have changed their role and there is an extra factor of  $\omega$ . This is due to the fact that  $Y$  links  $I$  and  $V$ , whereas the energy-valued perturbation term in the sense of section 1.2.1 is  $QV$ . This aspect adds a time-derivative  $Y = \dot{\chi}$  which leads to a factor  $i\omega$  in Fourier space.

This last result can be illustrated by a few examples. If  $Y(\omega) = G\Phi_0/2\pi$ , we recover the previous Eq. (27). If the shunt is a capacitor  $C_s$ , we have  $Y(\omega) = i\omega C_s$  and we get from Eq. (30) the equation of motion of a particle with larger mass, parameterized by a total capacitance  $C_{\text{tot}} = C_J + C_s$ . On the other hand, if the shunt is an inductance  $L_s$ , we obtain  $Y(\omega) = (i\omega L_s)^{-1}$ , leading to a new contribution to the potential originating from the inductive energy

$$V_{tot}(\phi) = V(\phi) + \frac{(\Phi_0)^2}{8\pi^2 L} \phi^2 \quad (31)$$

and no damping term. Finally, let us consider the elementary mixed case of a shunt consisting of a resistor  $R_s$  and a capacitor  $C_s$  in series. We find  $Y(\omega) = \frac{i\omega C_s}{1+i\omega R_s C_s}$  which can be broken into a damping part which is suppressed below a rolloff frequency  $\omega_r = (RC)^{-1}$ ,  $Y_d \frac{1}{R} \frac{1}{1+\omega^2/\omega_r^2}$  and a reactive part which responds capacitively below that rolloff,  $Y_r = i\omega C \frac{1}{1+\omega^2/\omega_r^2}$ . As the rollofs are very soft, there is no straightforward mapping onto a very simple model and we have to accept that the dynamics get more complicated and contain a frequency-dependent mass and friction as well as time-correlated noise, all of which gives rise to rich physics (Robertson et al., 2005).

## 2 Single Qubit Decoherence

### 2.1 TWO-STATE OSCILLATOR BATH MODELS

In the previous section, we introduced the notion of an oscillator bath environment for continuous systems including biased Josephson junctions. We derived quantum Langevin equation demonstrating the analogy to classical dissipative motion, but did not describe how to solve them. In fact, solving these equations in all generality is extremely hard in the quantum limit, thus a restriction of generality is sought. For our two-state systems (TSS) of interest, qubits, we are specifically interested in the case where the potential in the Hamiltonian of Eq. (5) forms a double well with exactly one bound state per minimum, tunnel-coupled to each other and well separated from the higher excited levels, (Geller et al., 2006). When we also concentrate on the low-energy dynamics, we can replace the particle coordinate  $q$  by  $q_0 \sigma_z$  and the Hamiltonian reads

$$H = \frac{\epsilon}{2} \sigma_z + \frac{\Delta}{2} \sigma_x + \frac{\sigma_z}{2} \sum_i \lambda_i (a_i + a_i^\dagger) + \sum_i \omega_i (a_i^\dagger a_i + 1/2), \quad (32)$$

where  $\epsilon$  is the energy bias and  $\Delta$  is the tunnel splitting. This is the famous Spin-Boson Hamiltonian (Leggett et al., 1987; Weiss, 1999). We have dropped the counterterm, which is  $\propto q^2$  in the continuous limit and, due to  $q = \pm q_0$  is constant in the two-state case. The spectral density is constructed out of the  $J(\omega)$  in the continuous limit

$$J_{TSS} = \sum_i \lambda_i^2 \delta(\omega - \omega_i) = \frac{q_0^2}{2\pi\hbar} J(\omega). \quad (33)$$

The Spin-Boson Hamiltonian, Eq. (33) is more general than the truncation of the energy spectrum in a double-well potential may suggest. In fact, it can be

derived by an alternative procedure which performs the two-state approximation first (or departs from a two-state Hamiltonian without asking for its origin) and then characterizes the bath. The oscillator bath approximation holds under the same conditions explained in section 1.2.1. The Spin-Boson model makes the assumption, that each oscillator couples to the same observable of the TSS which can always be labelled  $\sigma_z$ . This is a restrictive assumption which is not necessarily true for all realizations of a dissipative two-state system.

As the two-state counterpart to classical friction used in the continuous case is not straightforward to determine, the environmental spectrum is computed from the semiclassical noise of the environment, following the prescription that, if we rewrite Eq. (32) in the interaction picture with respect to the bath as

$$H_I = \frac{\epsilon + \delta\epsilon(t)}{2}\sigma_z + \frac{\Delta}{2}\sigma_x + \sum_i \omega_i(a_i^\dagger a_i + 1/2) \quad (34)$$

we can identify  $\delta\epsilon$  for any physical model mapping on the Spin-Boson model as

$$\frac{1}{2} \langle \delta\epsilon(t)\delta\epsilon(0) + \delta\epsilon(0)\delta\epsilon(t) \rangle_\omega = J_{\text{TSS}}(\omega) \coth\left(\frac{\hbar\omega}{2k_B T}\right). \quad (35)$$

An application of this procedure will be presented in the next subsection.

### 2.1.1 Characterization of qubit environments through noise

A standard application of the characterization of the environment is the description of control electronics of relatively modest complexity, attached to a flux qubit. We look at the definite example shown in Figure 1. It shows a simplified model of the microwave leads providing the control of a flux qubits. The microwaves inductively couple to the sample by a mutual inductance  $M$  between the qubit and a coil with self-inductance  $L$ . These leads are mounted in the cold part of the cryostat, usually on the qubit chip, and are connected to the outside world by a coaxial line which almost inevitably has an impedance of  $Z = 50 \Omega$ . That impedance provides—in light of the discussion in the previous section—a significant source of damping and decoherence. As a design element, one can put two resistors of size  $R$  close to the coil.

The environmental noise is easily described by the Nyquist noise (Callen and Welton, 1951) of the voltage  $V$  between the arms of the circuit, see Figure 1. The Johnson–Nyquist formula gives the voltage noise

$$S_V = \frac{1}{2} \langle V(t)V(0) + V(0)V(t) \rangle = \hbar\omega \text{Re}Z_{\text{eff}} \coth\left(\frac{\hbar\omega}{2k_B T}\right), \quad (36)$$

where  $Z_{\text{eff}}$  is the effective impedance between the arms, here of a parallel setup of a resistor and an inductor

$$Z_{\text{eff}} = \frac{i\omega L_{\text{eff}}R}{R + i\omega L_{\text{eff}}}, \quad (37)$$

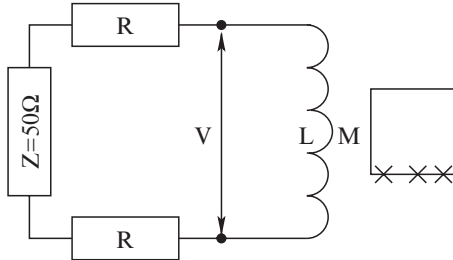


Figure 1. Typical on-chip electromagnetic environment of a superconducting flux qubit, consisting of the flux control coil with self-inductance  $L$ , mutual inductance  $M$  to the qubit, shunt impedance  $Z$ , and on-chip decoupling resistors  $R$

and  $L_{\text{eff}}$  is the total impedance of the coupled set of conductors as seen from the circuit. For microwave leads, the total inductance is dominated by the self-inductance of the coil, hence  $L_{\text{eff}} \approx L$ .

We need to convert the voltage noise into energy level noise of the qubit. A voltage fluctuation  $\delta V$  leads to a current fluctuation in the coil following

$$\delta I = \delta V / i\omega L. \quad (38)$$

The current noise produces flux noise through the qubit loop

$$\delta\Phi = M\delta I = \frac{M}{i\omega L}\delta V, \quad (39)$$

which converts into energy bias noise following

$$\delta\epsilon = I_s\delta\Phi = \frac{MI_s}{i\omega L}\delta V, \quad (40)$$

with  $I_s$  being the circulating current in the potential minima of the qubit. Thus, the energy level correlation function reads

$$S_\epsilon = \left( \frac{MI_s}{i\omega L} \right)^2 S_V, \quad (41)$$

which allows us to express the spectral density through the impedance as

$$J(\omega) = \hbar\omega \left( \frac{MI_s}{i\omega L} \right)^2 \text{Re}Z_{\text{eff}}(\omega). \quad (42)$$

With the specific circuit shown in Figure 1, we find that the environment is Ohmic with a Drude cutoff

$$J(\omega) = \frac{\alpha\omega}{1 + \omega^2/\omega_c^2}, \quad (43)$$

with  $\omega_c = L/R$  and  $\alpha = \frac{4M^2I_s^2}{\hbar(Z+2R)}$ . Thus, we find a simple method to engineer the decoherence properties of the circuit with our goal being to reduce  $J(\omega)$  by

decoupling the device from the shunt  $Z$ . The method of choice is to put large resistors  $R$  on chip. Their size will ultimately be limited by the necessity of cooling them to cryogenic temperatures. The friction method introduced earlier, section 1.3, leads to the same result.

### 2.1.2 Linearization of nonlinear environments

In general, nonlinear environments important for qubit devices can also be identified. In superconducting devices, these include electronic environments which in addition to the linear circuit elements discussed in the previous section, also contain Josephson junctions. In general, such environments cannot be described by oscillator bath models, whose response would be strictly linear. Here, we want to concentrate on the case of a nonlinear environment—a SQUID detector—in the regime of small signal response, i.e. in a regime where it can be linearized. This linearization can be illustrated by the concept of Josephson inductance. Let us remind ourselves, that a linear inductor is defined through the following current–flux relation

$$I(\Phi) = \Phi/L, \quad (44)$$

whereas the small flux-signal response of a Josephson junction can be approximated as

$$I = \sin\left(2\pi\frac{\Phi}{\Phi_0}\right) \approx I_c \sin\left(2\pi\frac{\bar{\Phi}}{\Phi_0}\right) + \frac{\delta\Phi}{L_J}, \quad (45)$$

where we have split the flux into its average  $\bar{\Phi}$  and small deviations  $\delta\Phi$  and have introduced the Josephson inductance  $L_J = \Phi_0/2\pi I_c \cos \bar{\phi}$ . Thus, the small-signal response is inductive.

We would now like to demonstrate this idea on the example of a DC-SQUID detector inductively coupled to the qubit, see Figure 2.

In the first stage, we again need to find the voltage noise between the branches of the circuit. This is given by Eq. (36) with the appropriate inductance calculated from the circuit shown in the lower panel of Figure 2,  $Z_{\text{eff}}^{-1} = R^{-1} + i\omega C + (i\omega L_J)^{-1}$ . This is the impedance of an  $LC$  resonator with damping. The conversion into energy level noise goes along similar lines as before, incorporating the SQUID equations as described here and in standard literature (Tinkham, 1996; Clarke and Braginski, 2004).

The DC-SQUID is a parallel setup of two Josephson junctions 1 and 2, which for simplicity are assumed to be identical. The total current flowing through the device is

$$I_B = I_c(\sin \phi_1 + \sin \phi_2) = 2I_c \cos(\delta\phi/2) \sin \bar{\phi}, \quad (46)$$

where we have introduced  $\bar{\phi} = (\phi_1 + \phi_2)/2$  and  $\delta\phi = \phi_1 - \phi_2$ . Now we need to remember that the phases  $\phi_i$  are connected to the Schrödinger equation for the

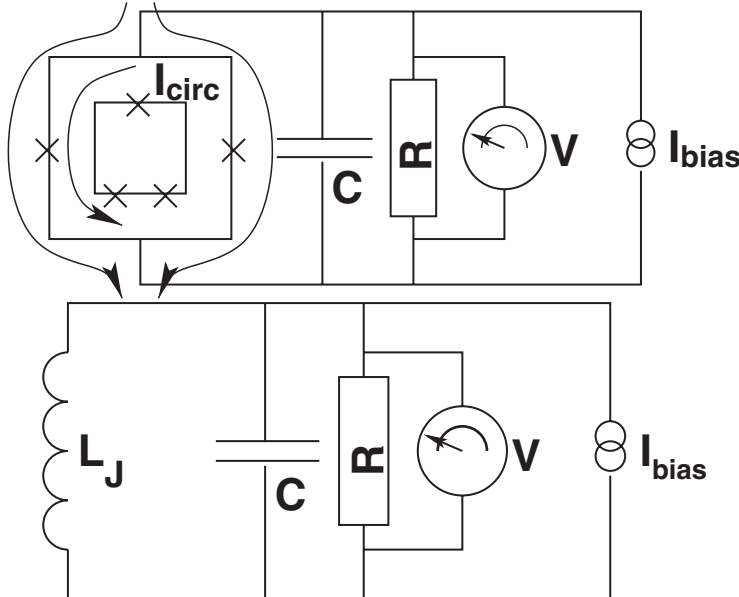


Figure 2. Upper panel: DC-SQUID readout circuit consisting of the actual SQUID, a shunt capacitor, and a voltmeter with an unavoidable resistor. Lower panel: Linearized circuit used for the noise calculation

superconducting condensate. Thus, an elementary calculation (Tinkham, 1996; Clarke and Braginski, 2004) leads to

$$\delta\phi = 2\pi \frac{\Phi}{\Phi_0} \text{mod}2\pi, \quad (47)$$

where  $\Phi$  is the total magnetic flux through the loop. This is identical to the flux applied externally using a biasing coil plus the qubit flux as we neglect self-inductance. Thus, for the bias current  $I_B$  the DC-SQUID acts like a tunable Josephson junction with a critical current  $I_{c,\text{eff}}(\Phi) = 2I_c|\cos(\pi\Phi/\Phi_0)|$ . Thus, we can translate voltage fluctuations into phase fluctuations as

$$\delta\bar{\phi} = \left( \frac{2\pi}{\Phi_0} \right) \frac{\delta V}{i\omega}. \quad (48)$$

The qubit is coupling to the magnetic flux which—assuming a symmetric SQUID geometry—is coupled only to the circulating current

$$I_{\text{circ}} = I_c(\sin\phi_1 - \sin\phi_2)/2 = I_c \cos(\bar{\phi}) \sin \frac{\pi\Phi}{\Phi_0}. \quad (49)$$

We can now express its fluctuations through the fluctuations of  $\bar{\phi}$

$$\delta I_{\text{circ}} = -I_c \sin \frac{\pi\Phi}{\Phi_0} \sin(\bar{\phi}) \delta\bar{\phi} = \frac{I_B}{2} \tan \frac{\pi\Phi}{\Phi_0} \delta\phi, \quad (50)$$

where in the last step we have used Eq. (46). With the remaining steps analogous to the previous section, we obtain

$$J(\omega) = \hbar\omega \left( M I_s \frac{I_B}{2} \frac{2\pi}{\Phi_0} \tan \frac{\pi\Phi}{\Phi_0} \right)^2 \text{Re}Z_{\text{eff}}. \quad (51)$$

Here,  $Z_{\text{eff}}$  is the impedance of the linearized circuit shown in the bottom panel of Figure 2. This result reveals a few remarkable features. Most prominently, it shows that  $J(\omega)$  can be tuned by shifting the working point of the linearization through changing the bias current  $I_B$ . In particular,  $J(\omega)$  can be set to zero by choosing  $I_B = 0$ . The origin of this decoupling can be seen in Eq. (50), which connects the bias current noise to the circulating current noise. The physical reason for this is, that in the absence of a bias current the setup is fully symmetric—any noise from the external circuitry splits into equal amounts on the branches of the loop and thus does not lead to flux noise. For a detector, this is a highly desired property. It allows to switch the detector off completely. When we do not bias, we have (for the traditional switching current measurement) no sensitivity and with it no backaction. This means, that if the device is really highly symmetric, one can push this device to the strong measurement regime while still being able to operate in the “off” state of the detector. This effect has been predicted in van der Wal et al. (2003) and Wilhelm et al. (2003). Experimentally, it was first observed that the decoupled point was far from zero bias due to a fabrication issue (Burkard et al., 2005), which was later solved such that our prediction has indeed been verified (Bertet et al., 2005a).

## 2.2 THE BLOCH EQUATION

So far, we have discussed the characterization of the environment at length. We did not specify how to describe the qubit dynamics under its influence. For a continuous system, we have derived the quantum Langevin equation (11). Even though this equation looks straightforward, solving it for potentials other than the harmonic oscillator is difficult without further approximations. We will now show first how to describe decoherence in a phenomenological way and then discuss how to reconcile microscopic modelling with the Bloch equation.

For describing the decoherence of a qubit we have to use the density matrix formalism, which can describe pure as well as mixed states. In the case of a qubit with a two-dimensional Hilbert space, we can fully parameterize the density matrix by its three spin projections  $S_i = \text{Tr}(\rho\sigma_i)$ ,  $i = x, y, z$  as

$$\rho = \frac{1}{2} \left( 1 + \sum_i S_i \sigma_i \right), \quad (52)$$

where the  $\sigma_i$  are Pauli matrices. This notation is inspired by spin resonance and is applicable to any two-state system including those realized in superconducting qubits. We can take the analogy further and use the typical NMR notation with a strong static magnetic field  $B_z(t)$  applied in one direction identified as the  $z$ -direction and a small AC field,  $B_x(t)$  and  $B_y(t)$  in the  $xy$ -plane. In that case, there is clearly a preferred-axis symmetry and two distinct relaxation rates, the longitudinal rate  $1/T_1$  and the transversal rate  $1/T_2$  can be introduced phenomenologically to yield

$$\dot{S}_z = \gamma(\vec{B} \times \vec{S})_z - \frac{S_z - S_{z,eq}}{T_1}, \quad (53)$$

$$\dot{S}_{x/y} = \gamma(\vec{B} \times \vec{S})_{x/y} - \frac{S_{x/y}}{T_2}, \quad (54)$$

where we have introduced the equilibrium spin projection  $S_{z,eq}$  and the spin vector  $\vec{S} = (S_x, S_y, S_z)^T$ . Note that the coherent part of the time evolution is still present. It enters the Bloch equation via the Hamiltonian, decomposed into Pauli matrices as  $H = -\gamma\vec{B} \cdot \vec{S}$ . This spin notation is also useful for superconducting qubits, even though the three components usually depend very distinct observables such as charge, flux, and current. This parameterization leads to the practical visualization of the state and the Hamiltonian as a point and an axis in three-dimensional space, respectively. The free evolution of the qubit then corresponds to Larmor precession around the magnetic field. The pure states of the spin have  $\vec{S}^2 = 1$  and are hence on a unit sphere, the Bloch sphere, whereas the mixed states are inside the sphere—in the Bloch ball.

The rates are also readily interpreted in physical terms. As the large static field points in the  $z$ -direction in our setting, the energy dissipation is given as

$$\frac{d\langle E \rangle}{dt} = -\gamma B_z \dot{S}_z \quad (55)$$

and hence its irreversible part is given through  $1/T_1$ . On the other hand, the purity (or linearized entropy)  $P = \text{Tr}\rho^2 = 1/4 + \sum_i S_i^2$  decays as

$$\dot{P} = 2 \sum_i \dot{S}_i S_i = -\frac{S_x^2 + S_y^2}{T_2} - \frac{S_z(S_z - S_{z,eq})}{T_1}, \quad (56)$$

thus all rates contribute to decoherence. Note, that at low temperatures  $S_{z,eq} \rightarrow 1$  so the  $T_1$ -term in general augments the purity and reestablishes coherence. This can be understood as the system approaches the ground state, which is a pure state. In this light, it needs to be imposed that  $P \leq 1$  as otherwise the density matrix has negative eigenvalues. This enforces  $T_2 \leq 2T_1$ .

### 2.2.1 Solutions of the Bloch equation and spectroscopy

The rates shown in the Bloch equation are also related to typical spectroscopic parameters (Abragam, 1983; Goorden and Wilhelm, 2003). We chose a rotating driving field

$$B_x = (\omega_R/\gamma) \cos \omega t, \quad (57)$$

$$B_y = (\omega_R/\gamma) \sin \omega t. \quad (58)$$

In spectroscopy, we are asking for the steady state population, i.e. for the long-time limit of  $S_z$ . Transforming the Bloch equation into the frame co-rotating with the driving field and computing the steady-state solution, we obtain

$$S_z(\omega) = \frac{\omega_R^2}{(\omega - \gamma B)^2 + \gamma^2} \quad (59)$$

with a linewidth  $\gamma^2 = 1/T_2^2 + \omega_R^2 T_2/T_1$ . This simple result allows spectroscopic determination of all the parameters of the Bloch equation: At weak driving,  $\omega_R \sqrt{T_1 T_2} \ll 1$ , the line width is  $1/T_2$ . This regime can be easily identified as the spectral line not being saturated, i.e. the height grows with increasing drive. In fact, the height of the resonance is  $S_z(\gamma B) = \omega_R^2 T_2^2$ , which (knowing  $1/T_2$ ) allows to determine  $\omega_R$ . Due to the heavy filtering between the room-temperature driving and the cryogenic environment, this is not known a priori. To determine  $T_1$ , one goes to the high driving regime with a saturated line, i.e. a line which does not grow any more with higher power,  $\omega_R \sqrt{T_1 T_2} \gg 1$  and finds a line width of  $\omega_R \sqrt{T_1/T_2}$ . With all other parameters known already, this allows to find  $T_1$ . Alternatively, real-time measurements of  $T_1$  are possible under a wide range of conditions.

## 2.3 HOW TO DERIVE THE BLOCH EQUATION: THE BLOCH–REDFIELD TECHNIQUE

We now show how to derive Bloch-like equations from the system-bath models we studied before using a sequence of approximations. The *Born approximation* works if the coupling between system and bath is weak. The *Markov approximation* works if the coupling between system and bath is the slowest process in the system, in particular if it happens on a timescale longer than the correlation time of the environment. Quantitatively, we can put this into the *motional narrowing condition*

$$\frac{\lambda \tau_c}{\hbar} \ll 1, \quad (60)$$

where  $\lambda$  is the coupling strength between the system and its environment and  $\tau_c$  the correlation time of the environment. In the case treated in Eq. (19) we

would have  $\tau_c = 1/\omega_c$ . If this is satisfied, an averaging process over a time scale longer than  $\tau_c$  but shorter than  $\lambda^{-1}$  can lead to simple evolution equations, the so-called Bloch–Redfield equations (Argyres and Kelley, 1964). The derivation in Cohen-Tannoudji et al. (1992) follows this inspiration. We will follow the very elegant and rigorous derivation using projection operators as given in (Argyres and Kelley, 1964; Weiss, 1999). We are going to look at a quantum subsystem with an arbitrary finite dimensional Hilbert space, accomodating also qubit and multiple-qubit systems.

As a starting point for the derivation of the Bloch–Redfield equations (70), one usually (Weiss, 1999) takes the Liouville equation of motion for the density matrix of the whole system  $W(t)$  (describing the time evolution of the system)

$$\dot{W}(t) = -\frac{i}{\hbar} [H_{\text{total}}, W(t)] = \mathcal{L}_{\text{total}} W(t), \quad (61)$$

where  $H_{\text{total}}$  is the total Hamiltonian and  $\mathcal{L}_{\text{total}}$  the total Liouvillian of the whole system. This notation of the Liouvillian uses the concept of a *superoperator*. Superoperator space treats density matrices as vectors. Simply arrange the matrix elements in a column, and each linear operation on the density matrix can be written as a (super)matrix multiplication. Thus, the right hand side of the Liouville equation can be written as a single matrix products, not a commutator, where a matrix acts from the left and the right at the same time. Hamiltonian and Liouvillian consist of parts for the relevant subsystem, the reservoir and the interaction between these

$$H_{\text{total}} = H_{\text{sys}} + H_{\text{res}} + H_I, \quad (62)$$

$$\mathcal{L}_{\text{total}} = \mathcal{L}_{\text{sys}} + \mathcal{L}_{\text{res}} + \mathcal{L}_I. \quad (63)$$

$H_{\text{sys}}$  is the Hamiltonian which describes the quantum system (in our case: the qubit setup),  $H_{\text{res}}$  represents for the environment and  $H_I$  is the interaction Hamiltonian between system and bath.

Projecting the density matrix of the whole system  $W(t)$  on the relevant part of the system (in our case the qubit), one finally gets the reduced density matrix  $\rho$  acting on the quantum system alone

$$\rho(t) = \text{Tr}_B W(t) = P W(t), \quad (64)$$

so  $P$  projects out onto the quantum subsystem. As in the previous derivation in section 1.2, we need to formally solve the irrelevant part of the Liouville equation first. Applying  $(1 - P)$ , the projector on the irrelevant part, to Eq. (61) and the obvious  $W = PW + (1 - P)W$  we get

$$(1 - P)\dot{W} = (1 - P)\mathcal{L}_{\text{total}}(1 - P)W + (1 - P)\mathcal{L}_{\text{total}}\rho. \quad (65)$$

This is an inhomogenous linear equation of motion which can be solved with variation of constants, yielding

$$(1 - P)\rho(t) = \int_0^t dt' e^{(1-P)\mathcal{L}_{\text{total}}(t-t')'} (1 - P)\mathcal{L}_{\text{total}}\rho(t') + e^{(1-P)\mathcal{L}_{\text{total}}t} (1 - P)W(0). \quad (66)$$

Putting this result into Eq. (61) one gets the Nakajima–Zwanzig equation (Nakajima, 1958; Zwanzig, 1960)

$$\begin{aligned} \dot{\rho}(t) = & P\mathcal{L}_{\text{total}}\rho(t) + \int_0^t dt' P\mathcal{L}_{\text{total}}e^{(1-P)\mathcal{L}_{\text{total}}(t-t')} (1 - P)\mathcal{L}_{\text{total}}\rho(t') \\ & + P\mathcal{L}_{\text{total}}e^{(1-P)\mathcal{L}_{\text{total}}t} (1 - P)W(0). \end{aligned} \quad (67)$$

So far, all we did was fully exact. The dependence on the initial value of the irrelevant part of the density operator  $(1 - P)W(0)$  is dropped, if the projection operator is chosen appropriately—using factorizing initial conditions, i.e.  $W = \rho \otimes (1 - P)W$ . A critical assessment of this assumption will be given in section 3.1.2. As  $P$  commutes with  $\mathcal{L}_{\text{sys}}$ , one finds

$$\dot{\rho} = P(\mathcal{L}_{\text{sys}} + \mathcal{L}_I)\rho(t) + \int_0^t dt' P\mathcal{L}_Ie^{(1-P)\mathcal{L}_{\text{total}}(t-t')'} (1 - P)\mathcal{L}_I\rho(t'). \quad (68)$$

The reversible motion of the relevant system is described by the first (instantaneous) term of Eq. (68), which contains the system Hamiltonian in  $\mathcal{L}_{\text{sys}}$  and a possible global energy shift originating from the environment in  $R\mathcal{L}_I$ . The latter term can be taken into account by the redefinition  $H'_S = H_S + PH_I$  and  $H'_I = (1 - P)H_I$ . The irreversibility is given by the second (time-retarded) term. The integral kernel in Eq. (68) still consists of all powers in  $\mathcal{L}_I$  and the dynamics of the reduced density operator  $\rho$  of the relevant system depends on its own whole history. To overcome these difficulties in practically solving Eq. (68), one has to make approximations. We begin by assuming that the system bath interaction is weak and restrict ourselves to the Born approximation, second order in  $\mathcal{L}_I$ . This allows us to replace  $\mathcal{L}_{\text{total}}$  by  $\mathcal{L}_{\text{sys}} + \mathcal{L}_{\text{res}}$  in the exponent. The resulting equation is still nonlocal in time. As it is convolutive, it can in principle be solved without further approximations (Loss and DiVincenzo, 2003). To proceed to the more convenient Bloch–Redfield limit, we remove the memory firstly by propagating  $\rho(t')$  forward to  $\rho(t)$ . In principle, this would require solving the whole equation first and not be helpful. In our case, however, we can observe that the other term in

the integral—the kernel of the equation—is essentially a bath correlation function which only contributes at  $t - t' < \tau_c$ . Using the motional narrowing condition Eq. (60), we see that the system is unlikely to interact with the environment in that period and we can replace the evolution of  $\rho$  with the free evolution,  $\rho(t') = e^{\mathcal{L}_{\text{sys}}(t-t')} \rho(t)$ . After this step, the equation is local in time, but the coefficients are still time-dependent. Now we flip the integration variable  $t' \rightarrow t - t'$  and then use the motional narrowing condition again to send the upper limit of the integral to infinity, realizing that at such large time differences the kernel will hardly contribute anyway. We end up with the Bloch–Redfield equation

$$\dot{\rho}(t) = P(\mathcal{L}_{\text{sys}} + \mathcal{L}_I)\rho(t) + \int_0^\infty dt' P\mathcal{L}_I e^{(1-P)(\mathcal{L}_{\text{sys}}+\mathcal{L}_{\text{res}})t'} (1-P)\mathcal{L}_I \rho(t). \quad (69)$$

The Bloch–Redfield equation is of Markovian form, however, by properly using the free time evolution of the system (back-propagation), they take into account all bath correlations which are relevant within the Born approximation (Hartmann et al., 2000). In Hartmann et al. (2000), it has also been shown that in the bosonic case the Bloch–Redfield theory is numerically equivalent to the path-integral method.

The resulting Bloch–Redfield equations for the reduced density matrix  $\rho$  in the eigenstate basis of  $H_{\text{sys}}$  then read (Weiss, 1999)

$$\dot{\rho}_{nm}(t) = -i\omega_{nm}\rho_{nm}(t) - \sum_{k,\ell} R_{nmk\ell}\rho_{k\ell}(t), \quad (70)$$

where  $R_{nmk\ell}$  are the elements of the Redfield tensor and the  $\rho_{nm}$  are the elements of the reduced density matrix.

The Redfield tensor has the form (Blum, 1996; Weiss, 1999)

$$R_{nmk\ell} = \delta_{\ell m} \sum_r \Gamma_{nrrk}^{(+)} + \delta_{nk} \sum_r \Gamma_{\ell rrm}^{(-)} - \Gamma_{\ell mnk}^{(+)} - \Gamma_{\ell mnk}^{(-)}. \quad (71)$$

The rates entering the Redfield tensor elements are given by the following Golden-Rule expressions (Blum, 1996; Weiss, 1999)

$$\Gamma_{\ell mnk}^{(+)} = \hbar^{-2} \int_0^\infty dt e^{-i\omega_{nk}t} \langle \tilde{H}_{I,\ell m}(t) \tilde{H}_{I,nk}(0) \rangle, \quad (72)$$

$$\Gamma_{\ell mnk}^{(-)} = \hbar^{-2} \int_0^\infty dt e^{-i\omega_{\ell m}t} \langle \tilde{H}_{I,\ell m}(0) \tilde{H}_{I,nk}(t) \rangle, \quad (73)$$

where  $H_I$  appears in the interaction representation

$$\tilde{H}_I(t) = \exp(iH_{\text{res}}t/\hbar) H_I \exp(-iH_{\text{res}}t/\hbar). \quad (74)$$

$\omega_{nk}$  is defined as  $\omega_{nk} = (E_n - E_k)/\hbar$ . In a two-state system, the coefficients  $\ell$ ,  $m$ ,  $n$ , and  $k$  stand for either + or – representing the upper and lower eigenstates. The possible values of  $\omega_{nk}$  in a TSS are  $\omega_{++} = \omega_{--} = 0$ ,  $\omega_{+-} = \frac{2\delta}{\hbar}$ , and  $\omega_{-+} = -\frac{E}{\hbar}$ , where  $E$  is the energy splitting between the two charge eigenstates with  $E = \sqrt{\epsilon^2 + \Delta^2}$ . Now we apply the secular approximation, which again refers to weak damping, to discard many rates in the Redfield tensor as irrelevant. The details of this approximation are most transparent in the multi-level case and will be discussed in more detail in section 4.1. In the TSS case, the secular approximation holds whenever the Born approximation holds. After the secular approximation, the Bloch–Redfield equation coincides with the Bloch equation with

$$1/T_1 = \sum_n R_{nnn} = R_{++++} + R_{----} = \Gamma_{+---} + \Gamma_{-+++}, \quad (75)$$

$$\begin{aligned} 1/T_2 &= \text{Re}(R_{nnnm}) = \text{Re}(R_{+---}) = \text{Re}(R_{-+++}) \\ &= \text{Re}(\Gamma_{+---} + \Gamma_{-+++} + \Gamma_{----} + \Gamma_{++++} - \Gamma_{-+++} - \Gamma_{+---}) \\ &= \frac{1}{2T_1} + \frac{1}{T_\phi}. \end{aligned} \quad (76)$$

Here, we have introduced the dephasing rate  $T_\phi^{-1}$ . The relaxation rate is given by the time evolution of the *diagonal* elements, and the dephasing rate by the *off-diagonal* elements of the reduced density matrix  $\rho$ .

The factor of two in the formula connecting  $1/T_2$  and  $1/T_1$  appears to be counterintuitive, as we would expect that energy relaxation definitely also leads to dephasing, without additional factors. This physical picture is also correct, but one has to take into account that there are *two* channels for dephasing—clockwise and counterclockwise precession—which need to be added. In fact, this is the reason why the same factor of two appears in the positivity condition for the density matrix, see section 2.2. Another view is to interpret the diagonal matrix elements as classical probabilities, the absolute square of eigenfunctions of the Hamiltonian,  $|\psi_1|^2$ , whereas the off-diagonal terms constitute amplitudes,  $\psi_2^* \psi_1$ . Being squares, probabilities decay twice as fast as amplitudes. This point will be discussed further later on in the context of multi-level decoherence, Eq. (106).

The imaginary part of the Redfield tensor elements that are relevant for the dephasing rate  $\Im(R_{+---})$  provides a renormalization of the coherent oscillation frequency  $\omega_{+-}$ ,  $\delta\omega_{+-} = \Im(\Gamma_{+---} + \Gamma_{-+++})$ . If the renormalization of the oscillation frequency gets larger than the oscillation frequency itself, the Bloch–Redfield approach with its weak-coupling approximations does not work anymore. By this, we have a direct criterion for the validity of the calculation.

Finally, the stationary population is given by

$$S_{z,eq} = \frac{\Gamma_{-+++} - \Gamma_{+---}}{\Gamma_{-+++} + \Gamma_{+---}} = \tanh\left(\frac{\hbar\omega_{+-}}{2k_B T}\right), \quad (77)$$

where in the last step we have used the property of detailed balance

$$\Gamma_{nmmn} = \Gamma_{mnnm} e^{-\omega_{mn}/k_B T}, \quad (78)$$

which holds for any heat bath in thermal equilibrium and is derived, e.g. in Weiss (1999), Ingold (1998), and Callen and Welton (1951).

A different kind of derivation with the help of Keldysh diagrams for the specific case of an single-electron transistor (SET) can be found in the Appendix of Makhlin et al. (2001).

Very recent results (Thorwart et al., 2005; Gutmann, 2005) confirm that without the secular approximation, Bloch–Redfield theory preserves complete positivity only in the pure dephasing case (with vanishing coupling  $\Delta = 0$  between the qubit states). In all other cases, complete positivity is violated at short timescales. Thus, only in the pure dephasing regime is the Markovian master equation of Lindblad form (Lindblad, 1976) as typically postulated in mathematical physics. In all other cases the Lindblad theorem does *not* apply. This is not an argument against Bloch–Redfield—the Markovian shape has been obtained as an approximation which coarse-grains time, i.e. it is not supposed to be valid on short time intervals. Rather one has to question the generality of the Markov approximation (Lidar et al., 2004) at low temperature. Note, that in some cases the violation of positivity persists and one has to resort to more elaborate tools for consistent results (Thorwart et al., 2005).

### 2.3.1 Rates for the Spin-Boson model and their physical meaning

This technique is readily applied to the Spin-Boson Hamiltonian Eq. (32). The structure of the golden rule rates Eqs. (72) and (73) become rather transparent—the matrix elements of the interaction taken in the energy eigenbasis measure symmetries and selection rules whereas the time integral essentially leads to energy conservation.

In particular, we can identify the energy relaxation rate

$$\frac{1}{T_1} = \frac{\Delta^2}{E^2} S(E). \quad (79)$$

The interpretation of this rate is straightforward—the system has to make a transition, exchanging energy  $E$  with the environment using a single Boson. The factor  $S(E) = J(E)(n(E) + 1 + n(E))$  captures the density of Boson states  $J(E)$  and the sum of the rates for emission proportional to  $n(E) + 1$  and absorption proportional to  $n(E)$  of a Boson. Here,  $n(E)$  is the Bose function. The prefactor is the squared cosine of the angle between the coupling to the noise and the qubit Hamiltonian, i.e. it is maximum if—in the basis of qubit eigenstates—the bath couples to the qubit in a fully off-diagonal way. This is reminiscent of the standard square of the transition matrix element in Fermi’s golden rule.

The flip-less contribution to  $T_2$  reads

$$\frac{1}{T_\phi} = \frac{\epsilon^2}{2E^2} S(0). \quad (80)$$

It accounts for the dephasing processes which do not involve a transition of the qubit. Hence, they exchange zero energy with the environment and  $S(0)$  enters. The prefactor measures which fraction of the total environmental noise leads to fluctuations of the energy splitting, i.e. it is complementary to the transition matrix element in  $T_1$ —the component of the noise *diagonal* in the basis of energy eigenstates leads to pure dephasing. The zero frequency argument is a consequence of the Markov approximation. More physically, it can be understood as a limiting procedure involving the duration of the experiment, which converges to  $S(0)$  under the motional narrowing condition. Details of this procedure and its limitations will be discussed in the next section.

Finally, the energy shift

$$\delta E = \frac{\Delta^2}{E^2} \mathcal{P} \int d\omega \frac{J(\omega)}{E^2 - \omega^2}, \quad (81)$$

where  $\mathcal{P}$  denotes the Cauchy mean value, is analogous to the energy shift in second order perturbation theory, which collects all processes in which a virtual Boson is emitted and reabsorbed, i.e. no trace is left in the environment. Again, the prefactor ensures that the qubit makes a virtual transition during these processes. For the Ohmic case, we find

$$\delta E = \alpha E \frac{\Delta^2}{E^2} \log\left(\frac{\omega_c}{E}\right) \quad (82)$$

provided that  $\omega_c \gg E$ . Thus, the energy shift explicitly depends on the ultraviolet cutoff. In fact,  $\delta E \simeq E$  would be an indicator for the breakdown of the Born approximation. Thus, we can identify two criteria for the validity of this approximation,  $\alpha \ll 1$  and  $\alpha \log(\omega_c/E) \ll 1$ . The latter is more confining, i.e. even if the first one is satisfied, the latter one can be violated. Note that in some parts of the open quantum systems literature, the justification and introduction of this ultraviolet cutoff is discussed extensively. The spectral densities we have computed so far in the previous sections have always had an intrinsic ultraviolet cutoff, e.g. the pure reactive response of electromagnetic circuits at high frequencies.

## 2.4 ENGINEERING DECOHERENCE

The picture of decoherence we have at the moment apparently allows to engineer the decoherence properties—which we initially perceived as something deep and fundamental—using a limited set of formulae, Eqs. (79), (80) and (42), see van der

Wal et al. (2003) and Makhlin et al. (2001); these equations have been applied to designing the circuitry around quantum bits. This is, however, not the end of the story. After this process had been mastered to sufficient degree, decoherence turned out to be limited by more intrinsic phenomena, and by phenomena not satisfactorily described by the Bloch–Redfield technique. This will be the topic of the next section.

### 3 Beyond Bloch–Redfield

It is quite surprising that a theory such as Bloch–Redfield, which contains a Markov approximation, works so well at the low temperatures at which superconducting qubits are operated, even though correlation functions at low temperatures decay very slowly and can have significant power-law time tails. The main reason for this is the motional narrowing condition mentioned above, which essentially states that a very severe Born approximation, making the system–bath interaction the lowest energy/longest time in the system, will also satisfy that condition. This is analogous to the textbook derivation of Fermi’s golden rule (Sakurai, 1967; Cohen-Tannoudji et al., 1992), where the perturbative interaction is supposed to be the slowest process involved. In this section, we are going to outline the limitations of this approach by comparing to practical alternatives.

Before proceeding we would also like to briefly comment on the general problem of characterizing the environment in an open quantum system. The most general environment is usually assumed to induce a completely positive linear map (or “quantum operation”) on the reduced density matrix. The most general form of such a map is known as the Krauss operator–sum representation, although such a representation is not unique, even for a given microscopic system–bath model like the one considered here. A continuous-time master equation equivalent to a given Krauss map is provided by the Lindblad equation, but the form of the Lindblad equation is again not unique. The Lindblad equation gives the most general form of an equation of motion for the reduced density matrix that assures complete positivity and conserves the trace; however, the Markov and Born approximations are often needed to construct the specific Lindblad equation corresponding to a given microscopic model. The Markov approximation is a further additional simplification, rendering the dynamics to that of a semigroup. A semigroup lacks an inverse, in accordance with the underlying time-irreversibility of an open system. However, like the unitary group dynamics of a closed system, the semigroup elements can be generated by exponentials of non-Hermitian “Hamiltonians”, greatly simplifying the analysis. The Bloch–Redfield master equation also has a form similar to that of the Lindblad equation, but there is one important difference: Bloch–Redfield equation does not satisfy complete positivity for all values of the diagonal and off-diagonal relaxation parameters. If these parameters are calculated microscopically (or are obtained empirically),

then complete positivity will automatically be satisfied, and the Bloch–Redfield equation will be equivalent to the Lindblad equation. Otherwise inequalities have to be satisfied by the parameters in order to guarantee complete positivity.

### 3.1 PURE DEPHASING AND THE INDEPENDENT BOSON MODEL

We start from the special case  $\Delta = 0$  of the Spin-Boson model, also known as the independent Boson model (Mahan, 2000). We will discuss, how this special case can be solved exactly for a variety of initial conditions. Restricting the analysis to this case is a loss of generality. In particular, as the qubit part of the Hamiltonian commutes with the system–bath coupling, it cannot induce transitions between the qubit eigenstates. Thus,  $1/T_1 = 0$  to all orders as confirmed by Eq. (79) and  $1/T_2 = S(0)$  following Eq. (80). Still, it allows to gain insight into a number of phenomena and the validity of the standard approximations. Moreover, the results of this section have been confirmed based on a perturbative diagonalization scheme valid for gap or super-Ohmic environmental spectra (Wilhelm, 2003).

#### 3.1.1 *Exact propagator*

As the qubit and the qubit–bath coupling commute, we can construct the exact propagator of the system. We go into the interaction picture. The system–bath coupling Hamiltonian then reads

$$H_{SB}(t) = \frac{1}{2}\sigma_z \sum_j \lambda_j (a_i e^{-i\omega_j t} + a_i^\dagger e^{i\omega_j t}). \quad (83)$$

The commutator of this Hamiltonian with itself taken at a different time is a *c*-number. Consequently, up to an irrelevant global phase, we can drop the time-ordering operator  $\mathcal{T}$  in the propagator (Sakurai, 1967; Mahan, 2000) and find

$$\begin{aligned} U(t, t') &= \mathcal{T} \exp\left(-\frac{i}{\hbar} \int_{t'}^t dt' H_{SB}(t')\right) \\ &= \exp\left(\sigma_z \sum_i \frac{\lambda_i}{2\hbar\omega_i} (a_i^\dagger (e^{i\omega_i(t-t')-1}) - a_i (e^{-i\omega_i(t-t')-1}))\right). \end{aligned} \quad (84)$$

In order to work with this propagator, it is helpful to reexpress it using displacement operators  $D_i(\alpha_i) = \exp(\alpha a^\dagger - \alpha^* a)$  as

$$U(t, t') = \prod_j D_j \left( \sigma_z \frac{\lambda_j}{2\hbar\omega_j} (e^{i\omega_j(t-t')} - 1) \right). \quad (85)$$

This propagator can be readily used to compute observables. The main technical step remains to trace over the bath using an appropriate initial state. The standard

choice, also used for the derivation of the Bloch–Redfield equation, is the factorized initial condition with the bath in thermal equilibrium, i.e. the initial density matrix

$$\rho(0) = \rho_q \otimes e^{-H_B/kT}, \quad (86)$$

where we use the partition function  $Z$  (Landau and Lifshitz, 1984). The expectation value of the displacement operator between number states is  $\langle n | D(\alpha) | n \rangle = e^{-(2n+1)|\alpha|^2/2}$ . We start in an arbitrary pure initial state of the qubit

$$\rho_q = |\psi\rangle\langle\psi|, \quad |\psi\rangle = \cos \frac{\theta}{2} |0\rangle + \sin \frac{\theta}{2} e^{i\phi} |1\rangle. \quad (87)$$

Using these two expressions, we can compute the exact reduced density matrix, expressed through the three spin projections

$$\langle \sigma_x \rangle(t) = \sin \theta \cos(Et + \phi) e^{-K_f(t)}, \quad (88)$$

$$\langle \sigma_y \rangle(t) = \sin \theta \sin(Et + \phi) e^{-K_f(t)}, \quad (89)$$

$$\langle \sigma_z \rangle(t) = \cos \theta, \quad (90)$$

where we have introduced the exponent of the envelope for factorized initial conditions,

$$K_f(t) = \int \frac{d\omega}{\omega^2} S(\omega)(1 - \cos \omega t), \quad (91)$$

which coincides with the second temporal integral of the semiclassical correlation function  $S(t)$ , see Eq. (18). What does this expression show to us? At short times, we always have  $K_f(t) \propto \frac{t^2}{2} \int d\omega S(\omega)$ , which is an integral dominated by large frequencies and thus usually depends on the cutoff of  $S(\omega)$ . At long times, it is instructive to rewrite this as

$$K_f(t) = t \int d\omega \delta_\omega(t) S(\omega), \quad (92)$$

where we have introduced  $\delta_\omega(t) = 2 \frac{\sin^2 \omega t / 2}{\omega^2 t}$ , which approaches  $\delta(\omega)$  as  $t \rightarrow \infty$ . Performing this limit more carefully, we can do an asymptotic long-time expansion. Long refers to the internal time scales of the noise, i.e. the reciprocal of the internal frequency scales of  $S(\omega)$ , including  $\hbar/kT, \omega_c^{-1}$ . The expansion reads

$$K_f(t) = -t/T_2 + \log v_F + O(1/t), \quad (93)$$

with  $1/T_2 = S(0)$  as in the Bloch–Redfield result and  $\log v_F = \mathcal{P} \int \frac{d\omega}{\omega^2} S(\omega)$ . Here,  $\mathcal{P}$  is the Cauchy mean value regularizing the singularity at  $\omega = 0$ . To highlight the meaning of  $v_F$ , the visibility for factorized initial conditions, we plug this

expansion into Eq. (88) and see that  $\langle \sigma_x \rangle(t) = v_F \sin \theta \cos(Et + \phi) e^{-t/T_2+O(1/t)}$ . Thus, a long-time observer of the full dynamics sees exponential decay on a timescale  $T_2$  which coincides with the Bloch–Redfield result for the pure dephasing situation, but with an overall reduction of amplitude by a factor  $v < 1$ . This is an intrinsic loss of visibility (Vion et al., 2002; Simmonds et al., 2004). Several experiments have reported a loss of visibility, to which this may be a contribution. Note that by improving detection schemes, several other sources of reduced visibility have been eliminated (Lupascu et al., 2004; Wallraff et al., 2005).

This result allows a critical assessment of the Born–Markov approximation we used in the derivation of the Bloch–Redfield equation. It fails to predict the short-time dynamics—which was to be expected as the Markov approximation is essentially a long-time limit. In the long-time limit, the exponential shape of the decay envelope and its time constant are predicted correctly, there are no higher-order corrections to  $T_2$  at the pure dephasing point. The value of  $T_2$  changes at finite  $\Delta$ , see Leggett et al. (1987), Weiss (1999), and Wilhelm (2003). A further description of those results would however be far beyond the scope of this chapter and can be found in Wilhelm (2003). Finally, we can see how both short and long-time dynamics are related: the short-time (non-Markovian) dynamics leaves a trace in the long-time limit, namely a drop of visibility.

We now give examples for this result. In the Ohmic case  $J(\omega) = \alpha \omega e^{-\omega/\omega_c}$  at  $T = 0$ . Hence, we can right away compute  $\dot{K}_f(t)$  and obtain  $K_f(t) = \frac{\alpha}{2} \log(1 + (\omega_c t)^2)$  by a single time integral. In agreement with the formula for  $T_2$ , see Eqs. (76) and (80), the resulting decay does not have an exponential component at long time but keeps decaying as a power law, indicating vanishing visibility.

At finite temperature, the computation follows the same idea but leads to a more complicated result. We give the expression from Görlich and Weiss (1988) for a general power-law bath  $J_q(\omega) = \alpha_q \omega^q \omega_c^{1-q} e^{-\omega/\omega_c}$ ,

$$K_f(t) = 2\text{Re} \left\{ \alpha_q \Gamma(q-1) \left( 1 - (1 + i\omega_c t)^{1-s} + \left( \frac{\hbar\omega_c}{kT} \right) \times \left[ 2\zeta(s-1, \Omega) - \zeta \left( s-1, \Omega + \frac{ikTt}{\hbar} \right) - \zeta \left( q-1, \Omega - \frac{ik\tau kT}{\hbar} \right) \right] \right) \right\}, \quad (94)$$

where we have introduced  $\Omega = 1 + k_B T / \hbar \omega_0$  and the generalized Riemann zeta function, see (Abramowitz and Stegun, 1965) for the definition and the mathematical properties used in this subsection. This exact result allows to analyze and quantify the decay envelope by computing the main parameters of the decay,  $v_F$  and  $1/T_2$ . We will restrict ourselves to the scaling limit,  $\omega_c \gg 1/t, kT$ . For the Ohmic case,  $q = 1$ , we obtain at finite temperature  $1/T_2 = 2\alpha kT/\hbar$  and  $v_F = (kT/\omega_c)^\alpha$ . This result is readily understood. The form of  $T_2$  accounts for the fact that an Ohmic model has low-frequency noise which is purely

thermal in nature. The visibility drops with growing  $\omega_c$  indicating that if we keep adding high frequency modes they all contribute to lost visibility. It is less intuitive that  $v_F$  drops with lowering the temperature, as lowering the temperature generally reduces the noise. This has to be discussed together with the  $1/T_2$ -term, remembering that  $1/T_2$  is the leading and  $v_F$  only the sub-leading order of the long-time expanding Eq. (93): At very low temperatures, the crossover to the exponential long-time decay starts later and the contribution of non-exponential short time dynamics gains in relative significance. Indeed, at any given time, the total amplitude gets enhanced by lowering the temperature.

In order to emphasize these general observations, let us investigate the super-Ohmic case with  $q \geq 3$ . Such spectral functions can be realized in electronic circuits by RC-series shunts (Robertson et al., 2005), they also play a significant role in describing phonons. For  $q > 3$ , the exponential component vanishes,  $1/T_2 = 0$  and  $v_q = \exp[-2\alpha_q \Gamma(q-1)]$ . Thus, we obtain a massive loss of visibility but no exponential envelope at all. This highlights the fact that  $v$  and  $1/T_2$  are to be considered independent quantifiers of non-Markovian decoherence and that the latter accounts for environmental modes of relatively low frequency whereas  $v$  is mostly influenced by the fast modes between the qubit frequency and the cutoff.

Before outlining an actual microscopic scenario, we generalize the initial conditions of our calculation.

### 3.1.2 Decoherence for non-factorizing initial conditions

Our propagator, Eq. (85), is exact and can be applied to any initial density matrix. We start from an initial wave function

$$|\psi\rangle = |0\rangle \prod_n D(z_i^0) |0\rangle_i + |1\rangle \prod_n D(z_i^1) |0\rangle_i, \quad (95)$$

where we have introduced sets of dimensionless coefficients  $z_i^{0/1}$ . It would be straightforward to introduce  $\theta$  and  $\phi$ , which we will stay away from in order to keep the notation transparent. The factorized initial condition corresponds to  $z_i^{0/1} = 0$ .

This structure has been chosen in order to be able to obtain analytical results, using the structure of the propagator expressed in displacement operators, Eq. (85) and the multiplication rules for these operators (Walls and Milburn, 1994). Note that the choice of coherent states to entangle the qubit with is not a severe restriction. It has been shown in quantum optics in phase space, that essentially each density matrix of an harmonic oscillator can be decomposed into coherent states using the Wigner or Glauber P phase space representations, see, e.g. Schleich (2001). Physically, the initial state Eq. (95) corresponds to the qubit being in a superposition of two dressed states. Of specific significance is the initial condition which minimizes the system–bath interaction in the Hamiltonian Eq. (32), namely  $z_i^0 = -z_i^{-1} = -1$ .

We can again compute all three spin projections of the qubit. The essence of the decoherence behavior is captured in the symmetric initial state,  $z_i^0 = -z_i^1$  for all  $i$

$$\langle \sigma \rangle_x = \cos E t e^{-K(t)} \quad (96)$$

very similar to Eq. (88) in the factorized case, but now with

$$K(t) = -\frac{1}{2} \int_0^\infty \frac{d\omega}{\omega^2} J(\omega) \left[ (u(\omega) + 1)^2 + v^2(\omega) + 1 - 2(1 + u(\omega) \cos \omega t + v(\omega) \sin \omega t) \right],$$

where we have taken a continuum limit replacing the complex numbers  $z_i^0$  by the real function  $u(\omega) + iv(\omega)$ . This form connects to the factorized case by setting  $u = v = 0$ . For any other choice of  $u$  and  $v$ , the initial conditions are entangled.

We can make a few basic observations using this formula: The initial amplitude  $e^{-K(0)}$  is controlled through

$$K(0) = \int \frac{d\omega}{2\omega^2} [u^2(\omega) + v^2(\omega)], \quad (97)$$

thus for any initial condition which is more than marginally entangled (meaning that the integral is nonzero), the initial amplitude is smaller than unity. On the other hand, the time-dependence of  $K(t)$  can be completely eliminated by choosing an initial condition  $u = -1, v = 0$ . This condition minimizes the system–bath part of the total energy in the sense of variation with respect to  $u$  and  $v$ . This choice of initial state also minimizes the total energy if the oscillators are predominantly at high frequency, whereas for the global minimum one would rather choose a factorized state for the low-frequency oscillators. Physically, this corresponds to an optimally dressed state of the qubit surrounded by an oscillator dressing cloud. The overlap of these clouds reduces the amplitude from the very beginning but stays constant, such that the long-time visibility

$$v_g = \int \frac{d\omega}{2\omega^2} [(u(\omega) - 1)^2 + 1 + v^2(\omega)] \quad (98)$$

is maximum. Note that this reduces to the result for  $v_F$  for  $u = v = 0$ .

What can we learn from these results? We appreciate that initial conditions have a significant and observable effect on the decoherence of a single qubit. The choice of the physically appropriate initial condition is rather subtle and depends on the experiment and environment under consideration. A free induction decay experiment as described here does usually not start out of the blue. It is launched using a sequence of preparation pulses taking the state from a low temperature thermal equilibrium to the desired initial polarization of the qubit. Thus, from an initial equilibrium state (for some convenient setting of the qubit Hamiltonian),

the fast preparation sequence initiates nonequilibrium correlations thus shaping  $u$  and  $v$ . Furthermore, if the interaction to the environment is tunable such as in the case of the detectors discussed previously in section 2.1.2, the initial condition interpolates between factorized (rapid switching of the qubit-detector coupling) and equilibrium (adiabatic switching).

At this point, we can draw conclusions about the microscopic mechanism of the loss of visibility and other short-time decoherence dynamics. The picture is rooted on the observation that the ground state of the coupled system is a dressed state. On the one hand, as described above, the overlap of the dressing clouds reduces the final visibility. On the other hand, for nonequilibrium initial conditions such as the factorized one, there is extra energy stored in the system compared to the dressed ground state. This energy gets redistributed while the dressing cloud is forming, making it possible for an excitation in the environment with an extra energy  $\delta E$  to be created leading to a virtual intermediate state, followed by another excitation relaxing, thus releasing the energy  $\delta E$  again. It is crucial that this is *another* excitation as only processes which leave a trace in the environment lead to qubit dephasing. Higher-order processes creating and relaxing the *same* virtual excitation only lead to renormalization effects such as the Lamb shift, see Eq. (81). This explains why the loss of visibility is minimal for dressed initial conditions, where no surplus excitations are present.

The Bloch–Redfield technique is a simple and versatile tool which makes good predictions of decoherence rates at low damping. At higher damping, these rates are mostly joined by renormalization effects extending the Lamb shift in Eq. (81), see Leggett et al. (1987), Weiss (1999), and Wilhelm (2003). However, there is more to decoherence than a rate for accurate predictions of coherence amplitudes as a function of time, one has to take the non-exponential effects into account and go beyond Bloch–Redfield. Other approaches can be applied to this system such as rigorous (Born but not Markov) perturbation theory (Loss and DiVincenzo, 2003), path-integral techniques (Leggett et al., 1987; Weiss, 1999), and renormalization schemes (Kehrein and Mielke, 1998).

Note, that these conclusions all address free induction decay. There is little discussion in literature on the quality of the Bloch–Redfield theory in the presence of pulsed driving.

### 3.2 1/F NOISE

In the previous sections we have explored options how to engineer decoherence by influencing the spectral function  $J(\omega)$ , e.g. working with the electromagnetic environment. This has helped to optimize superconducting qubit setups to a great deal, down to the level where the noise intrinsic to the material plays a role. In superconductors, electronic excitations are gapped (Tinkham, 1996) and the electron phonon interaction is weak due to the inversion symmetry of

the underlying crystal everywhere except close to the junctions (Ioffe et al., 2004). The most prominent source of intrinsic decoherence is thus  $1/f$  noise.  $1/f$  noise—noise whose spectral function behaves following  $S(\omega) \propto 1/\omega$ , is ubiquitous in solid-state systems. This spectrum is very special as all the integrals in our discussion up to now would diverge for that spectrum.  $1/f$  typically occurs due to slowly moving defects in strongly disordered materials. In Josephson devices, there is strong evidence for  $1/f$  noise of gate charge, magnetic flux, and critical current, leading to a variety of noise coupling operators (see Harlingen et al. (1988) for an overview). Even though there does not appear to be a fully universal origin, a “standard” model of  $1/f$  noise has been identified (Dutta and Horn, 1981; Weissman, 1988): the fundamental unit are two-state fluctuators, i.e. two state systems which couple to the device under consideration and which couple to an external heat bath making them jump between two positions. The switching process consists of uncorrelated switching events, i.e. the distribution of times between these switches is Poissonian. If we label the mean time between switches as  $\tau$ , the spectral function of this process is  $S_{RTN} = S_0 \frac{1/\tau}{1+\tau^2\omega^2}$ . This phenomenon alone is called random telegraph noise (RTN). Superimposing such fluctuators with a flat distribution of switching times leads to a total noise spectrum proportional to  $1/f$ . Nevertheless, the model stays different from an oscillator bath. The underlying thermodynamic limit is usually not reached as it is approached more slowly: even a few fluctuators resemble  $1/f$  noise within the accuracy of a direct noise measurement. Moreover, as we are interested in very small devices such as qubits, only a few fluctuators are effective and experiments can often resolve them directly (Wakai and van Harlingen, 1987). Another way to see this is to realize that the RTN spectrum is highly non-Gaussian: a two-state distribution can simply not be fitted by a single Gaussian, all its higher cumulants of distribution are relevant. This non-Gaussian component only vanishes slowly when we increase the system size and is significant for the case of qubits.

A number of studies of models taking this aspect into account have been published (Paladino et al., 2002; Galperin et al., 2003; de Sousa et al., 2005; Faoro et al., 2005; Grishin et al., 2005; Shnirman et al., 2005). A highly simplified version is to still take the Gaussian assumption but realize that there is always a slowest fluctuator, thus the integrals in  $K_f(t)$  can be cut off at some frequency  $\omega_{IR}$  at the infrared (low frequency) end of the spectrum, i.e. using the spectral function

$$S(\omega) = \frac{E_{1/f}^2}{\omega} \theta(\omega - \omega_{IR}), \quad (99)$$

with  $\theta$  the Heaviside unit step function, we approximately find (Cottet, 2002; Shnirman et al., 2002; Martinis et al., 2003)

$$e^{-K(t)} \simeq (\omega_{IR}t)^{-(E_{1/f}t/\pi\hbar^2)^2} \quad (100)$$

so we find the Gaussian decay typical for short times—short on the scale of the correlation time of the environment, which is long as the spectrum is dominated by low frequencies—with a logarithmic correction.

At the moment, forefront research works at understanding more detailed models of  $1/f$  noise and understand the connection between the strong dephasing and a possible related relaxation mechanism at high frequencies. On the other hand, experiments work with materials to avoid  $1/f$  noise at its source. Generally, slow noise up to a certain level can be tolerated using refocusing techniques such as simple echo or the Carr-Purcell-Gill-Meiboom pulse sequence (Carr and Purcell, 1954; Falci et al., 2004; Faoro and Viola, 2004; Shiokawa and Lidar, 2004; Bertet et al., 2005b; Gutmann et al., 2005), the power and potential of which has been demonstrated both experimentally and theoretically.

#### 4 Decoherence in Coupled Qubits

To conclude, we want to outline how to go beyond a single to multiple qubits and identify the underlying challenges. On that level, much less is known both theoretically and experimentally. The variety of physically relevant Hamiltonians is larger. One extreme case is fully uncorrelated noise, e.g. originating from effects in the junctions or qubit-specific Hamiltonians,

$$H = H_{Q1} + H_{Q2} + H_{QQ} + H_{Q1B1} + H_{B1} + H_{Q2B2} + H_{B2}, \quad (101)$$

this is simply the sum of two single-qubit decoherence Hamiltonians in distinct Hilbert spaces, consisting of qubit Hamiltonians  $H_{Qi}$ ,  $i = 1, 2$ , baths  $H_{Bi}$ , qubit–bath interaction  $H_{QiBi}$  all interacting via a qubit–qubit interaction  $H_{QQ}$  alone. The other extreme case is collective noise, e.g. long-wavelength ambient fluctuations or noise shared control lines. This is described by

$$H = H_{Q1} + H_{Q2} + H_{QQ} + H_{Q1B} + H_{Q2B} + H_B, \quad (102)$$

where both qubits talk to a single bath. The distinction of baths may seem artificial, as this is a special case of Hamiltonian (101): what we really mean is that in the interaction picture there is a significant correlation between baths  $\langle H_{Q1B}(t)H_{Q2B}(t') \rangle \neq 0$ . Note, that intermediate cases between these, e.g. a partially correlated model (Storcz et al., 2005a), can be identified in the context of quantum dots.

##### 4.1 THE SECULAR APPROXIMATION

What does it take to study decoherence here or in other multilevel systems? Basically we can follow all the steps through the derivation of the Bloch–Redfield

equation given in section 2.3 up to Eq. (74) until we solve the equation. There, we have already mentioned the secular approximation without explaining its details.

The essence of the secular approximation is the separation of timescales. We go back to the interaction representation of Eq. (70), leading to

$$\dot{\rho}_{nm}^I = \sum_{kl} R_{nmkl} e^{i(\omega_{nm} - \omega_{kl})t} \rho_{kl}^I. \quad (103)$$

As the Bloch–Redfield equation is based on a Born approximation, we can expect  $|R_{ijkl}| \ll \omega_{mn}$  for all coefficients  $i, j, k, l, m, n$  with  $m \neq n$ .

In the *secular limit*, this also holds true for most frequency splittings

$$|\omega_{nm} - \omega_{kl}| \gg |R_{nmkl}| \quad (104)$$

besides the inevitable exceptions of  $n = m$ ,  $k = l$ , and  $n = k$  and  $m = l$ . Whenever condition (104) is satisfied, the time evolution induced by  $R_{nmkl}$  is certainly slower than the precession with  $\omega_{nm} - \omega_{kl}$  and averages out quickly, hence it can be dropped. So the only remaining rates are the cases just mentioned.

For  $n = k, m = l$ , we have to keep  $R_{nnmm}$ . This rate is the dephasing rate for the transition between levels  $nm$ , see Eq. (80). These rates depend on the pair of levels we chose and in general they will all be different for different choices of  $n$  and  $m$ , leading to  $N(N - 1)/2$  different  $T_2$ -rates for an  $N$ -level system.

For  $n = m$  and  $k = l$ . The set of these terms splits off from the rest of the equation, i.e. the diagonal terms of the density matrix (in the eigenstate basis) decay independent from the off-diagonal terms and obey the following set of equations

$$\dot{P}_n = \sum_n (P_m \Gamma_{m \rightarrow n} - P_n \Gamma_{n \rightarrow m}), \quad (105)$$

which is analogous to the Pauli master equation for classical probabilities. We have identified  $P_n = \rho_{nn}$ , the classical probability and the transition rates  $\Gamma_{n \rightarrow m} = R_{nnmm}$ . Equation (79) can be solved by Laplace transform, where it reduced to a matrix inversion. This leads to  $N$  different independent energy relaxation channels whose rates are the eigenvalues of the matrix form of the right hand side of Eq. (105). One of these eigenvalues is always zero representing stable thermodynamic equilibrium which does not decay. In the two-state case, this leads us to one nonvanishing  $T_1$  rate representing the only nonzero eigenvalue, given by Eq. (79). The rates generally obey the positivity constraint

$$\sum_n R_{nnmm} \leq 2 \sum_{n \neq m} R_{nnmm}, \quad (106)$$

the left hand side being the trace of the relaxation matrix, i.e. the sum over all  $T_1$ -type rates and the right hand side being the sum over dephasing rates. This reduces to  $T_2 \leq 2T_1$  in a two-state system.

In the opposite case, the case of a approximate *Liouvillian degeneracy*, we find a pair of frequencies  $|\omega_{nm} - \omega_{kl}| \ll |R_{nmkl}|$  which do not obey the conditions mentioned in the previous paragraph, such that the secular approximation does not apply to this set of levels and  $R_{ijkl}$  must be kept. In that case, the Bloch–Redfield equation can still be diagonalized numerically, identifying the relevant modes of decay (van Kampen, 1997). Note, that Liouvillian degeneracies can appear in nondegenerate systems, prominently the single harmonic oscillator. One practical example for this issue is intermediate-temperature cavity QED (Rau et al., 2004).

These concepts already found some application in the theoretical literature. We just mention the main results here. After the pioneering work (Governale et al., 2001), it was realized that the high number of rates makes the results difficult to analyze and the performance of quantum gates should be analyzed directly (Thorwart and Hänggi, 2002; Storcz and Wilhelm, 2003; Wilhelm et al., 2003). A key result is that (only) the correlated noise model, Eq. (102) permits to use symmetries and encoding into decoherence free subspaces to protect coherence (Storcz and Wilhelm, 2003; Wilhelm et al., 2003; Storcz et al., 2005c), where deviations from perfect symmetry are of relatively low impact (Storcz et al., 2005b).

## 5 Summary

In summary, we have provided an introduction to standard methods in decoherence theory as they are applied to superconducting qubits. Many of the tools and results are more general and can be applied to other damped two-state systems as well. We see that parts of the theory of decoherence—in particular the part on electromagnetic environments and Bloch–Redfield-Theory—are really well established by now, only opening the view on more subtle problems connected to memory effects and the interplay of decoherence and control.

## Acknowledgments

This work is based on numerous discussions, too many to list. It is based on our own process of learning and explaining together with other group members, such as M. Goorden, H. Gutmann, A. Käck, A. Holzner, K. Jähne, I. Serban, and J. Ferber. Very importantly, we thank G. Johannson, M. Governale, M. Grifoni, U. Weiss, G. Falci, P. Hänggi, S. Kohler, P. Stamp, L. Tian, S. Lloyd, and H. Gutmann on the theoretical as well as C.H. van der Wal, C.J.P.M. Harmans, J.E. Mooij, T.P. Orlando, J. Clarke, B.L.T. Plourde, and T.L. Robertson on the experimental side. We are very grateful to M. Flatté and I. Tifrea for organizing the NATO-ASI from which this work originates, and NATO for sponsoring it. Also, the questions of both the participants of the ASI as well as the participants

of the course “T VI: Physics of quantum computing” at LMU were very important in identifying the issues asking for explanation. We are deeply indebted to A.G. Fowler for his careful reading of the manuscript and many suggestions helping to make it at least close to pedagogical. This work was supported by the DFG through Sonderforschungsbereich 631, by ARDA and NSA through ARO grant P-43385-PH-QC, and DAAD-NSF travel grants.

## References

- Abragam, A. (1983) *Principles of Nuclear Magnetism*, Vol. 32 of *International Series of Monographs on Physics*, Oxford, Clarendon Press.
- Abramowitz, M. and Stegun, I. (eds.) (1965) *Handbook of Mathematical Functions*, New York, Dover.
- Argyres, P. and Kelley, P. (1964) Theory of spin resonance and relaxation, *Phys. Rev.* **134**, A98.
- Bertet, P., Chiorescu, I., Burkard, G., Semba, K., Harmans, C., DiVincenzo, D., and Mooij, J. (2005a) Relaxation and dephasing in a flux-qubit, *Phys. Rev. Lett.* **95**, 257002.
- Bertet, P., Chiorescu, I., Burkard, G., Semba, K., Harmans, C. J. P. M., DiVincenzo, D. P., and Mooij, J. E. (2005b) Dephasing of a superconducting qubit induced by photon noise, *Phys. Rev. Lett.* **95**, 257002.
- Blum, K. (1996) *Density Matrix Theory and Applications*, New York, Plenum.
- Brandes, T. and Kramer, B. (1999) Spontaneous emission of phonons by coupled quantum dots, *Phys. Rev. Lett.* **83**, 3021.
- Burkard, G., DiVincenzo, D., Bertet, P., Chiorescu, I., and Mooij, J. E. (2005) Asymmetry and decoherence in a double-layer persistent-current qubit, *Phys. Rev. B* **71**, 134504.
- Caldeira, A. and Leggett, A. (1981) Influence of dissipation on quantum tunneling in macroscopic systems, *Phys. Rev. Lett.* **46**, 211.
- Caldeira, A. and Leggett, A. (1983) Quantum tunneling in a dissipative system, *Ann. Phys. (NY)* **149**, 374.
- Callen, H. and Welton, T. (1951) Irreversibility and generalized noise, *Phys. Rev. B* **83**, 34.
- Carr, H. and Purcell, E. (1954) Effects of diffusion on free precession in nuclear magnetic resonance experiments, *Phys. Rev.* **94**, 630.
- Clarke, J. and Braginski, A. (eds.) (2004) *The SQUID Handbook*, Weinheim, Wiley-VCH.
- Cohen-Tannoudji, C., Diu, B., and Laloë, F. (1992) *Quantum Mechanics*, Weinheim, Wiley Interscience.
- Cottet, A. (2002) Implementation of a quantum bit in a superconducting circuit, Ph.D. thesis, Université Paris 6.
- de Sousa, R., Whaley, K., Wilhelm, F., and von Delft, J. (2005) Ohmic and step noise from a single trapping center hybridized with a Fermi sea, *Phys. Rev. Lett.* **95**, 247006.
- Dutta, P. and Horn, P. (1981) Low-frequency fluctuations in solids: 1/f-noise, *Rev. Mod. Phys.* **53**, 497.
- Falci, G., D’Arrigo, A., Mastellone, A., and Paladino, E. (2004) Dynamical suppression of telegraph and 1/f noise due to quantum bistable fluctuator, *Phys. Rev. A* **70**, R40101.
- Faoro, L. and Viola, L. (2004) Dynamical suppression of 1/f noise processes in qubit systems, *Phys. Rev. Lett.* **92**, 117905.
- Faoro, L., Bergli, J., Altshuler, B. L., and Galperin, Y. M. (2005) Models of environment and T<sub>1</sub> relaxation in Josephson charge qubits, *Phys. Rev. Lett.* **95**, 046805.
- Feynman, R. and Vernon, F. (1963) The theory of a general quantum system interacting with a linear dissipative system, *Ann. Phys. (N.Y.)* **24**, 118.

- Galperin, Y., Altshuler, B., and Shantsev, D. (2003) Low-frequency noise as a source of dephasing a qubit, *Fundamental Problems of Mesoscopic Physics: Interaction and Decoherence*, NATO-ASI, New York, Plenum.
- Geller, M., Pritchett, E., and Sornborger, A. (2006) Quantum computing with superconductors: architectures, *Manipulating Quantum Coherence in Semiconductors and Superconductors*, New York, Springer, edited by M. Flatté and I. Tîfrea.
- Giulini, D., Joos, E., Kiefer, C., Kupsch, J., Stamatescu, I.-O., and Zeh, H. D. (1996) *Decoherence and the Appearance of a Classical World in Quantum Theory*, Heidelberg, Springer.
- Goorden, M. and Wilhelm, F. (2003) Theoretical analysis of continuously driven solid-state qubits, *Phys. Rev. B* **68**, 012508.
- Görlich, R. and Weiss, U. (1988) Specific heat of the dissipative two-state system, *Phys. Rev. B* **38**, 5245.
- Governale, M., Grifoni, M., and Schön, G. (2001) Decoherence and dephasing in coupled Josephson-junction qubits, *Chem. Phys.* **268**, 273.
- Grishin, A., Yurkevich, I. V., and Lerner, I. V. (2005) Low-temperature decoherence of qubit coupled to background charges, *Phys. Rev. B (Condensed Matter and Materials Physics)* **72**, 060509.
- Gutmann, H., Kaminsky, W., Lloyd, S., and Wilhelm, F. (2005) Compensation of decoherence from telegraph noise by means of an open loop quantum-control technique, *Phys. Rev. A* **71**, 020302(R).
- Gutmann, H. PhD Thesis, Ludwig-Maximilians University Munich, (2005) Complete positivity for certain low-temperature master equations, in preparation.
- Harlingen, D. J. V., Robertson, T. L., Plourde, B. L., Reichardt, P., Crane, T., and Clarke, J. (1988) Decoherence in Josephson-junction qubits due to critical-current fluctuations, *Phys. Rev. B* **70**, 064517.
- Hartmann, L., Goychuk, I., Grifoni, M., and Hanggi, P. (2000) Driven tunneling dynamics: Bloch–Redfield theory versus path-integral approach, *Phys. Rev. E (Statistical Physics, Plasmas, Fluids, and Related Interdisciplinary Topics)* **61**, R4687–R4690.
- Hartmann, U. and Wilhelm, F. (2004) Control of decoherence through nonequilibrium between two baths, *Phys. Rev. B* **69**, 161309(R).
- Ingold, G. (1998) Dissipative quantum systems, *Quantum Transport and Dissipation*, Weinheim, Wiley-VCH.
- Ioffe, L., Geshkenbein, V., Helm, C., and Blatter, G. (2004) Decoherence in superconducting quantum bits by phonon radiation, *Phys. Rev. Lett.* **93**, 057001.
- Kehrein, S. and Mielke, A. (1998) Diagonalization of system plus environment Hamiltonians, *J. Stat. Phys.* **90**, 889.
- Kubo, R., Oda, M., and Hashitsume, N. (1991) *Statistical Physics II*, Vol. 31 of *Springer Series in Solid-State Statistical Physics*, Tokyo, Springer.
- Landau, L. and Lifshitz, E. (1982) *Mechanics*, Vol. 1 of *Course of Theoretical Physics*, Burlington, MA, Butterworth-Heinemann.
- Landau, L. and Lifshitz, E. (1984) *Statistical Physics*, Vol. 5 of *Course of Theoretical Physics*, Burlington, MA, Butterworth-Heinemann.
- Leggett, A. (2002) Testing the limits of quantum mechanics: Motivation, state of play, and prospects, *J. Phys. C* **14**, 415.
- Leggett, A., Chakravarty, S., Dorsey, A., Fisher, M., Garg, A., and Zwerger, W. (1987) Dynamics of the dissipative two-state system, *Rev. Mod. Phys.* **59**, 1.
- Lidar, D., Shabani, A., and Alicki, R. (2004) Conditions for strictly purity-decreasing quantum Markovian dynamics, quant-ph/0411119.
- Lindblad, G. (1976) On the generators of quantum dynamical semigroups, *Commun. Math. Phys.* **48**, 119.

- Loss, D. and DiVincenzo, D. (2003) Exact Born Approximation for the Spin-Boson Model, *cond-mat/0304118*.
- Lupascu, A., Verwijs, C., Schouten, R. N., Harmans, C., and Mooij, J. E. (2004) Nondestructive readout for a superconducting flux qubit, *Phys. Rev. Lett.* **93**, 177006.
- Mahan, G. (2000) *Many Particle Physics*, New York, Springer.
- Makhlin, Y., Schön, G., and Shnirman, A. (2001) Quantum-state engineering with Josephson-junction devices, *Rev. Mod. Phys.* **73**, 357.
- Martinis, J., Nam, S., Aumentado, J., Lang, K., and Urbina, C. (2003) Decoherence of a superconducting qubit due to bias noise, *Phys. Rev. B* **67**, 094510.
- Nakajima, S. (1958) On quantum theory of transport phenomena—Steady diffusion, *Prog. Theor. Phys.* **20**, 948.
- Paladino, E., Faoro, L., Falci, G., and Fazio, R. (2002) Decoherence and 1/f noise in Josephson qubits, *Phys. Rev. Lett.* **88**, 228304.
- Peres, A. (1993) *Quantum Theory: Concept and Methods*, Dordrecht, Kluwer.
- Rau, I., Johansson, G., and Shnirman, A. (2004) Cavity quantum electrodynamics in superconducting circuits: Susceptibility at elevated temperatures, *Phys. Rev. B (Condensed Matter and Materials Physics)* **70**, 054521.
- Robertson, T. L., Plourde, B. L. T., Hime, T., Linzen, S., Reichardt, P. A., Wilhelm, F. K., and Clarke, J. (2005) Superconducting quantum interference device with frequency-dependent damping: Readout of flux qubits, *Phys. Rev. B (Condensed Matter and Materials Physics)* **72**, 024513.
- Sakurai, J. (1967) *Advanced Quantum Mechanics*, New York, Addison-Wesley.
- Schleich, W. (2001) *Quantum Optics in Phase Space*, Weinheim, Wiley-VCH.
- Schrödinger, E. (1935) Die gegenwärtige Situation in der Quantenmechanik, *Naturwissenschaften* **23**, 807, 823, 844.
- Shikawa, K. and Lidar, D. A. (2004) Dynamical decoupling using slow pulses: Efficient suppression of 1/f noise, *Phys. Rev. A (Atomic, Molecular, and Optical Physics)* **69**, 030302.
- Shnirman, A., Makhlin, Y., and Schön, G. (2002) Noise and decoherence in quantum two-level systems, *Phys. Scr. T102*, 147.
- Shnirman, A., Schon, G., Martin, I., and Makhlin, Y. (2005) Low- and high-frequency noise from coherent two-level systems, *Phys. Rev. Lett.* **94**, 127002.
- Simmonds, R., Lang, K., Hite, D., Pappas, D., and Martinis, J. (2004) Decoherence in Josephson qubits from junction resonances, *Phys. Rev. Lett.* **93**, 077003.
- Storcz, M. and Wilhelm, F. (2003) Decoherence and gate performance of coupled solid-state qubits, *Phys. Rev. A* **67**, 042319.
- Storcz, M. J., Hartmann, U., Kohler, S., and Wilhelm, F. K. (2005a) Intrinsic phonon decoherence and quantum gates in coupled lateral quantum-dot charge qubits, *Phys. Rev. B (Condensed Matter and Materials Physics)* **72**, 235321.
- Storcz, M. J., Hellmann, F., Hrelescu, C., and Wilhelm, F. K. (2005b) Decoherence of a two-qubit system away from perfect symmetry, *Phys. Rev. A (Atomic, Molecular, and Optical Physics)* **72**, 052314.
- Storcz, M. J., Vala, J., Brown, K. R., Kempe, J., Wilhelm, F. K., and Whaley, K. B. (2005c) Full protection of superconducting qubit systems from coupling errors, *Phys. Rev. B (Condensed Matter and Materials Physics)* **72**, 064511.
- Thorwart, M. and Hänggi, P. (2002) Decoherence and dissipation during a quantum XOR gate operation, *Phys. Rev. A* **65**, 012309.
- Thorwart, M., Eckel, J., and Mucciolo, E. (2005) Non-Markovian dynamics of double quantum dot charge qubits due to acoustic phonons, *Phys. Rev. B* **72**, 235320.
- Tinkham, M. (1996) *Introduction to Superconductivity*, New York, McGraw-Hill.

- van der Wal, C., Wilhelm, F., Harmans, C., and Mooij, J. (2003) Engineering decoherence in Josephson persistent-current qubits, *Eur. Phys. J. B* **31**, 111.
- van Kampen, N. (1997) *Stochastic Processes in Physics and Chemistry*, Amsterdam, Elsevier.
- Vion, D., Aassime, A., Cottet, A., Joyez, P., Pothier, H., Urbina, C., Esteve, D., and Devoret, M. (2002) Manipulating the quantum state of an electrical circuit, *Science* **296**, 286.
- von Delft, J. and Schoeller, H. (1998) Bosonization for beginners—Fermionization for experts, *Ann. Phys. (Leipzig)* **7**, 225.
- Wakai, R. and van Harlingen, D. (1987) Direct lifetime measurements and interactions of charged defect states in submicron Josephson junctions, *Phys. Rev. Lett.* **58**, 1687.
- Wallraff, A., Schuster, D., Blais, A., Frunzio, L., Majer, J., Girvin, S., and Schoelkopf, R. J. (2005) Approaching Unit Visibility for Control of a Superconducting Qubit with Dispersive Readout, cond-mat/0502645.
- Walls, D. and Milburn, G. (1994) *Quantum Optics*, Berlin, Springer.
- Weiss, U. (1999) *Quantum Dissipative Systems*, No. 10 in Series in modern condensed matter physics, Singapore, World Scientific, 2nd edition.
- Weissman, M. (1988) 1/f noise and other slow, nonexponential kinetics in condensed matter, *Rev. Mod. Phys.* **60**, 537.
- Wilhelm, F. (2003) Reduced visibility in the spin-Boson model, cond-mat/0507026.
- Wilhelm, F., Storcz, M., van der Wal, C., Harmans, C., and Mooij, J. (2003) Decoherence of flux qubits coupled to electronic circuits, *Adv. Sol. St. Phys.* **43**, 763.
- Zill, D. (2000) *A First Course in Differential Equations*, Florence, KY, Brooks Cole.
- Zurek, W. (1993) Preferred states, predictability, classicality and the environment-induced decoherence, *Prog. Theor. Phys.* **89**, 281.
- Zwanzig, R. (1960) Ensemble method in the theory of irreversibility, *J. Chem. Phys.* **33**, 1338.

## INDEX

- Aharonov–Bohm phase, 39, 184  
angular momentum quenching, 37, 39, 40
- Bell states, 45  
Bloch–Redfield theory, 211–216, 218–221, 224, 226–228
- charge representation, 177  
CNOT operation, 31, 182  
Cooper pairs, 172, 173, 176, 177, 184  
  charging energy, 173  
critical current, 173, 174, 208, 225
- dephasing, 19, 162, 215–217, 221, 224, 226, 227  
dressed states, 189, 222  
dynamic nuclear polarization, 152, 153
- electron spin  
  g factor, 19, 27, 36–40, 45, 87, 111–113, 115, 125, 134, 135, 140, 143, 145, 155, 163, 164  
entanglement, 1, 42  
exchange interaction, 2, 25, 26, 46, 130
- Faraday rotation, 42, 43, 45, 99, 132, 133, 135, 161  
  conditional, 43, 44
- gate charge, 177, 225
- Hanle measurements, 131–133, 138, 140, 149, 150, 154, 155, 157
- hyperfine interaction, 25, 30, 98–108, 110–112, 115, 119, 120, 130, 162
- inversion asymmetry, 7  
  from applied electric field, 23  
  from bulk symmetry, 24, 139  
  from graded composition, 23  
  from interfaces, 22, 24  
  from strain, 139
- ionic spins, 2, 25, 45
- Jaynes–Cummings model, 188, 189  
Josephson energy, 184, 202, 203  
Josephson equations, 173, 174  
Josephson junction, 171, 187, 188, 190, 200, 207, 208
- Kerr effect, 154, 155, 157  
Kerr rotation, 87, 98, 99, 133, 140, 141, 143–147, 149, 151, 155
- magnetic fields  
  internal, 7, 134, 136, 139, 141, 144  
  nuclear, 99, 111–114, 116, 119, 120
- magnetic semiconductors, 18
- Markov approximation, 211, 216–218, 221
- microcavity, 2, 42, 44
- nanomechanical resonator, 187–192
- nanostructure, 21, 22, 24, 45, 97–101, 103, 108, 109, 111, 116, 117, 119, 120, 125
- nuclear spin, 25, 46, 97–102, 106–121, 130, 152, 154, 155, 157, 162, 202
- nuclear spin coherence, 98
- nuclear spin diffusion, 106, 108, 119
- nuclear spin dynamics, 98–101, 107, 119, 120
- nuclear spin relaxation, 98, 101, 103–107, 109–111, 115, 119–121
- optical selection rules  
  bulk zincblende semiconductors, 130  
  quantum dots, 33, 43  
  quantum wells, 131
- phase difference, 172, 173
- pseudospin, 28–31, 35
- quantum computation, 2, 25, 32, 33, 40, 46, 98, 172, 174, 191
- quantum dots, 2, 21, 25, 29, 32, 33, 36–38, 40, 42, 45, 46, 98, 108, 120, 125, 160, 161  
  self-assembled, 33
- quantum error correction, 1, 42

- quantum information processing, 31, 97, 134, 183  
 quantum memory register, 188, 191  
 quantum well, 5, 6, 19, 21–24, 33, 34, 36, 37, 40, 45, 83, 98, 99, 103, 108, 120, 123, 124, 144, 145, 147, 163  
 qubit couplings  
   resonator-based, 172  
 qubit pair, 172  
 qubit states, 172, 216  
 qubit subspace, 175, 177  
 qubits  
   charge, 172, 176, 177, 180, 182, 185–187  
   electron spin, 160  
   flux, 171, 177–180, 185, 205, 206  
   nuclear spin, 2  
   phase, 171  
 Rabi frequency, 30, 189, 190  
 rotating wave approximation, 188–191  
 single electron transistor, 45  
 spin coherence, 14, 18–24, 30, 37, 97, 98, 129, 130, 137, 146, 147, 149, 150, 160  
 spin coherence times, 21  
 spin Coulomb drag, 64, 66, 72, 78, 88, 89, 92, 93  
 spin decoherence  
   precessional decoherence, 19, 21, 130, 160  
 spin diffusion  
   upstream and downstream lengths, 16, 18, 72  
 spin drag, 84, 86  
   coefficient, 84  
 spin dynamics, 25  
 spin Hall effect, 59, 86, 93, 129, 139–144, 147, 148, 150  
 spin light-emitting diodes, 33  
 spin mass, 82–86, 93  
 spin susceptibility, 64, 66, 79, 80  
 spin transport, 2, 5, 8, 17, 33, 93, 148  
   ballistic, 6  
   drift–diffusion, 10, 16–18, 55, 57–60, 63, 72, 86, 88, 93, 135, 136, 144, 147, 149–151  
   Einstein ratio, 13, 53, 54, 56, 63, 72, 94, 201  
   spin current, 5, 7  
 spin valve, 66, 69, 72  
 spin–boson model, 204  
 spin–orbit interaction, 7, 20, 25, 26, 37, 39, 41, 55, 58, 87–89, 160  
 spin–photon coupling  
   AC Stark effect, 40  
   entanglement, 42, 43  
 spintronics, 129  
 SQUID, 171, 177, 178, 180, 184, 186, 207, 208  
 teleportation, 2, 42, 44, 45  
 two-dimensional electron gas, 32, 77, 79, 86, 144–148